FATIGUE BEHAVIOR OF A SiC/SiC COMPOSITE AT 1000 °C IN AIR AND STEAM

THESIS

Knauf, Michael, Captain, USAF
AFIT/GAE/ENY/10-D01

DEPARTMENT OF THE AIR FORCE
AIR UNIVERSITY

AIR FORCE INSTITUTE OF TECHNOLOGY

Wright-Patterson Air Force Base, Ohio

Report Documentation Page

Form Approved
OMB No. 0704-0188

1. REPORT DATE	2. REPORT TYPE	3. DATES COVERED
01 DEC 2010		**00-00-2009 to 00-00-2010**

4. TITLE AND SUBTITLE	5a. CONTRACT NUMBER
Fatigue Behavior of a SiC/SiC Composite at 1000 ?C in Air and in Steam	5b. GRANT NUMBER
	5c. PROGRAM ELEMENT NUMBER
6. AUTHOR(S)	5d. PROJECT NUMBER
	5e. TASK NUMBER
	5f. WORK UNIT NUMBER
7. PERFORMING ORGANIZATION NAME(S) AND ADDRESS(ES) **Air Force Institute of Technology,2950 Hobson Way,WPAFB,OH,45433-7765**	8. PERFORMING ORGANIZATION REPORT NUMBER
9. SPONSORING/MONITORING AGENCY NAME(S) AND ADDRESS(ES)	10. SPONSOR/MONITOR'S ACRONYM(S)
	11. SPONSOR/MONITOR'S REPORT NUMBER(S)

12. DISTRIBUTION/AVAILABILITY STATEMENT
Approved for public release; distribution unlimited

13. SUPPLEMENTARY NOTES

14. ABSTRACT

Tension-tension fatigue behavior of a prototype Silicon Carbide/Silicon Carbide (SiC/SiC) ceramic matrix composite (CMC) material was investigated at 1000 ?C in laboratory air and in steam environments. The material consists of a SiC matrix reinforced with CG NICALON? fibers woven in an eight harness satin weave (8HSW) and coated with a BN/SiC dual-layer interphase. The composite was manufactured by a Polymer Infiltration and Pyrolysis (PIP) process. A seal coat of SiC and elemental boron was applied to the test specimens after machining. The tensile stress-strain behavior was investigated and the tensile properties were measured at 1000 ?C. Tension-tension fatigue behavior was studied for fatigue stresses ranging from 60 to 100 MPa. The fatigue limit (based on a run-out condition of 2 x 105 cycles) was 80 MPa, which is 59% of the Ultimate Tensile Strength (UTS). The material retained 82% of its tensile strength. The presence of steam significantly degraded the fatigue performance at 1000 ?C. In steam the fatigue limit dropped below 60 MPa (44% UTS). Microstructural analysis revealed severe oxidation occurring in the specimens tested in steam, which resulted in accelerated damage development and failure. Through quantitative and qualitative analysis, the damage and premature failure of the composite in the steam environment is believed to be due to oxidation embrittlement. This material also showed considerably worse performance than similar SiC/SiC composites with a great deal of variability between specimens cut from different panels. The possibility exists that inadequate process control may be behind the degraded performance of the material and the panel-to-panel variability in performance.

15. SUBJECT TERMS

16. SECURITY CLASSIFICATION OF:			17. LIMITATION OF ABSTRACT	18. NUMBER OF PAGES	19a. NAME OF RESPONSIBLE PERSON
a. REPORT **unclassified**	b. ABSTRACT **unclassified**	c. THIS PAGE **unclassified**	**Same as Report (SAR)**	**166**	

AFIT/GAE/ENY/10-D01

FATIGUE BEHAVIOR OF A SiC/SiC COMPOSITE AT 1000 °C IN AIR AND STEAM

THESIS

Presented to the Faculty

Department of Aeronautics and Astronautics

Graduate School of Engineering and Management

Air Force Institute of Technology

Air University

Air Education and Training Command

In Partial Fulfillment of the Requirements for the

Degree of Master of Science in Aeronautical Engineering

Michael Knauf, B.S.

Captain, USAF

December 2010

AFIT/GAE/ENY/10-D01

FATIGUE BEHAVIOR OF A SiC/SiC COMPOSITE AT 1000 °C IN AIR AND STEAM

Michael Knauf, B.S.

Captain, USAF

Approved:

_____	_____
Marina Ruggles-Wrenn, PhD (Chairman)	Date
_____	_____
Geoff Fair, PhD (Member)	Date
_____	_____
Eric D. Swenson, PhD (Member)	Date

Abstract

Tension-tension fatigue behavior of a prototype Silicon Carbide/Silicon Carbide (SiC/SiC) ceramic matrix composite (CMC) material was investigated at 1000 °C in laboratory air and in steam environments. The material consists of a SiC matrix reinforced with CG NICALON™ fibers woven in an eight harness satin weave (8HSW) and coated with a BN/SiC dual-layer interphase. The composite was manufactured by a Polymer Infiltration and Pyrolysis (PIP) process. A seal coat of SiC and elemental boron was applied to the test specimens after machining. The tensile stress-strain behavior was investigated and the tensile properties were measured at 1000 °C. Tension-tension fatigue behavior was studied for fatigue stresses ranging from 60 to 100 MPa. The fatigue limit (based on a run-out condition of 2×10^5 cycles) was 80 MPa, which is 59% of the Ultimate Tensile Strength (UTS). The material retained 82% of its tensile strength. The presence of steam significantly degraded the fatigue performance at 1000 °C. In steam the fatigue limit dropped below 60 MPa (44% UTS). Microstructural analysis revealed severe oxidation occurring in the specimens tested in steam, which resulted in accelerated damage development and failure. Through quantitative and qualitative analysis, the damage and premature failure of the composite in the steam environment is believed to be due to oxidation embrittlement. This material also showed considerably worse performance than similar SiC/SiC composites with a great deal of variability between specimens cut from different panels. The possibility exists that inadequate process control may be behind the degraded performance of the material and the panel-to-panel variability in performance.

Acknowledgements

I would like to express my sincere appreciation to Dr. Marina Ruggles-Wrenn, whose assistance and guidance enabled the completion of this research. Additionally I would like to thank Dr. Geoff Fair for providing the materials, SEM support, and hours of discussion. I would also like to thank my final committee member, Dr. Eric Swenson. Finally I would like to thank the AFIT Materials Testing Laboratory staff including John Hixenbaugh, Sean Miller, Barry Page, and Chris Zickefoose for assisting me in the operation of the machines as well as Ryan Check and the rest of my friends and family for their continued support during this effort.

Table of Contents

List of Figures

List of Tables

FATIGUE BEHAVIOR OF A SiC/SiC COMPOSITE AT 1000 °C IN AIR AND STEAM

I. Introduction

Fueled by mounting military and commercial demands, technological advances in materials are occurring at an ever-increasing pace. Material properties such as strength, toughness, stiffness, corrosion resistance and high temperature use are at the forefront of increased performance requirements. Traditionally metal components are being replaced by advanced composites such as Ceramic Matrix Composites (CMCs), which can meet higher performance in jet turbines and rocket motors. Gains in the form of increased thrust, efficiency and more stoichiometric combustion reducing NO_x and CO emissions are all promised, and are based on CMCs' abilities to deliver on higher operating temperatures, 30-50% lower densities versus traditional materials and adequate fracture toughness to prevent catastrophic failure [23:1, 1:287, 7:1]. Indeed, following the cancellation of the NASA High Speed Civil Transport and Enabling Propulsion Materials program, NASA introduced the Ultra Efficient Engine Technology (UEET) Program to investigate future technology for the eventual production of low-emission civilian engines [7:2]. But while these composites have great potential, consistently reproducible properties between batches is more difficult to achieve than with metallic parts performing the same roles. Current research must not only focus on increasing performance properties, but also on reproducibility and consistent properties. Alongside these advances also come demands from users for decreased cost and decreased production time. CMCs can very much be cost-prohibitive and can also take weeks to produce [19:2625, 27:160]. Even with these challenges, the performance gain introduced by this class of material is exceedingly promising.

Currently, turbines in jet aircraft produce very large inefficiencies due to the high levels of cooling necessary to ensure the metal parts do not reach their melting temperature. The turbine burner efficiency in the equation below illustrates that one way to increase the efficiency of the burner section, η_b, would be to increase the total temperature within the burner, T_{T4}.

$$\eta_b = \frac{1}{\dot{m}_f h}\left[\left(\dot{m} + \dot{m}_f\right)C_{p,t}T_{T4} - \dot{m}C_{p,c}T_{T3}\right] \quad \textbf{(1.1)}$$

Here, $\dot{m}$ and $\dot{m}_f$ are the mass flow of air and fuel, respectively, h is the heating value of the fuel, and C_pT_T is the stagnation enthalpy at various turbine stages.

Efficiency is one factor that increases with increased temperature; however, specific thrust also increases with an increase in burner temperature, as seen in Figure 1 and the equation below. This equation is for a ramjet/scramjet; turbo-machines follow the same principle, although in a more complicated form.

$$Specific\ Thrust = \frac{F}{\dot{m}} = a_0 M_0\left[\sqrt{\frac{\tau_\lambda}{\tau_r}} - 1\right], \tau_\lambda = \frac{T_{T4}}{T_{T0}}\frac{C_{p,t}}{C_{p,c}} \quad \textbf{(1.2)}$$

Here, F is the force generated by the machine, and $\dot{m}$ is the mass flow of the air and fuel, a_0 is the speed of sound, M_0 is the mach number, τ_r is a function of the specific heat of the fluid and the mach number, and C_pT_T is the stagnation enthalpy at various stages.

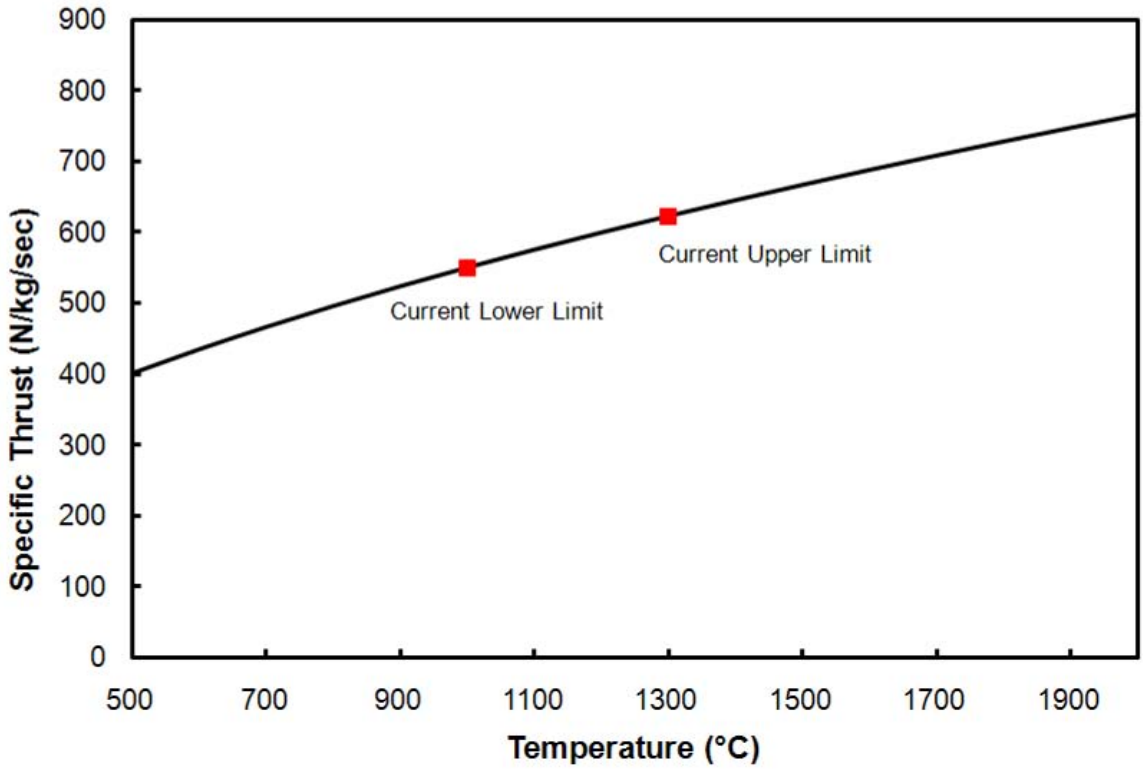

Figure 1: Specific thrust of a ramjet/scramjet as a function of temperature

Rocket engines are also poised to make significant gains through the use of materials which can maintain increased temperatures within the combustion chamber, T_c. Figure 2 illustrates the dependence of specific impulse (I_{sp}, a measure of a rocket's efficiency, as defined in the equation below) on combustion chamber temperature; the specific impulse values for the Saturn V and Delta IV rockets are provided for comparison purposes.

$$I_{sp} = \frac{\sqrt{2C_pT_o}}{g_0} \tag{1.3}$$

Here, C_pT_c is the stagnation enthalpy and g_0 is the gravity constant.

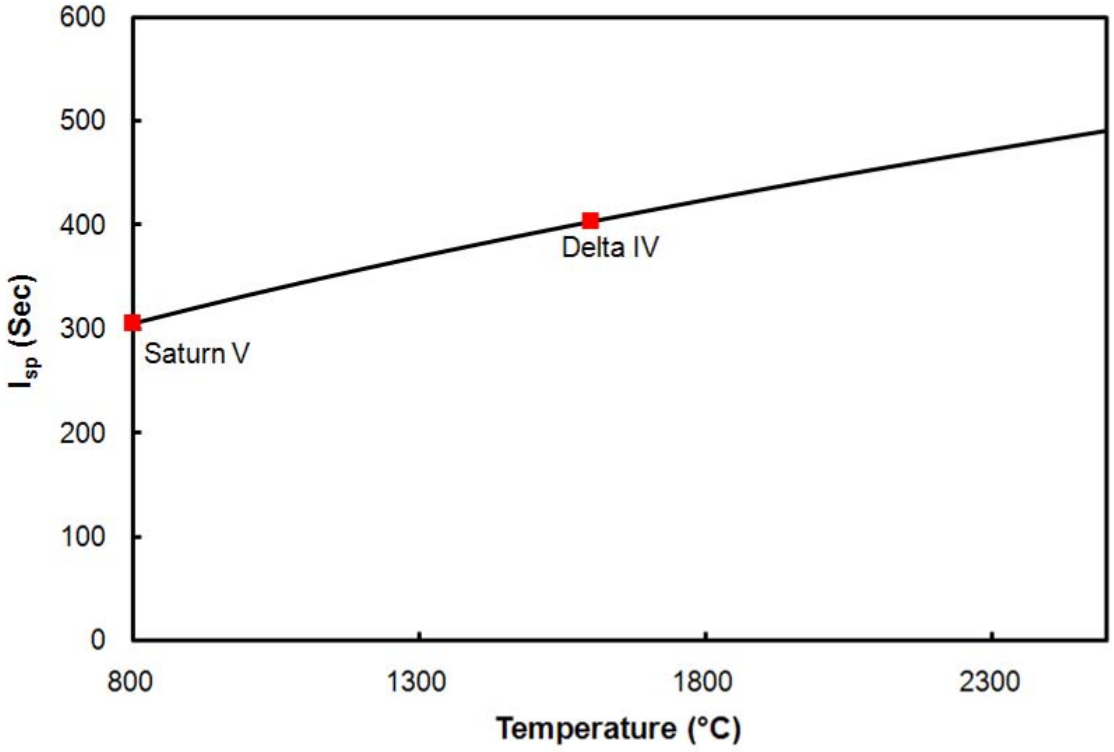

Figure 2: I_{sp} as a function of chamber temperature, T_c

The environments within all of these machines not only produce very high temperatures, but also provide high stresses, high frequency loading and a great deal of oxygen. The oxygen occurs in the forms of air, steam, and other combustion products. A suitable replacement for engine parts must be able to withstand these difficult demands while at high temperatures. Advanced Ceramic Matrix Composites show great promise to achieve these demands.

II. Background

2.1 Ceramic-Matrix Composite Overview

Although most ceramics have very high temperature tolerances, most also suffer from very low fracture toughness, which stems from insufficient energy dissipation methods within the ceramic itself [5:3]. Ceramic Matrix Composites combine ceramic fibers and a ceramic matrix to produce a material that not only has high temperature capabilities, but which also allows for greatly improved fracture toughness. This is done through innovative energy dissipation techniques focused around reducing crack propagation by introducing obstacles in the form of coated fibers to absorb and block further crack growth [6:8]. Ceramic fibers are generally coated with an interphase, which allows both the necessary stress transfer and the ability to slip and allow for detachment from the matrix. As a result a crack that formed in the matrix cannot propagate through the interphase to the fiber after the fiber and matrix debond. This either effectively stops the crack or bridges to another crack previously formed. The right-hand composite in Figure 3 below illustrates a crack propagating through a material with a strong interface causing brittle fracture throughout and thus has low fracture toughness. The left-hand composite demonstrates however a weak interface and therefore is able to absorb a great deal of crack growth in many regions without catastrophic failure [3:148]. As stress in the composite rises the load transfers to the fibers; as fibers begin to fail independent of one another, frictional pullout and sliding occur between the fiber and interphase after which the composite fails. The optimization of this failure mechanism has been the subject of a great deal of research.

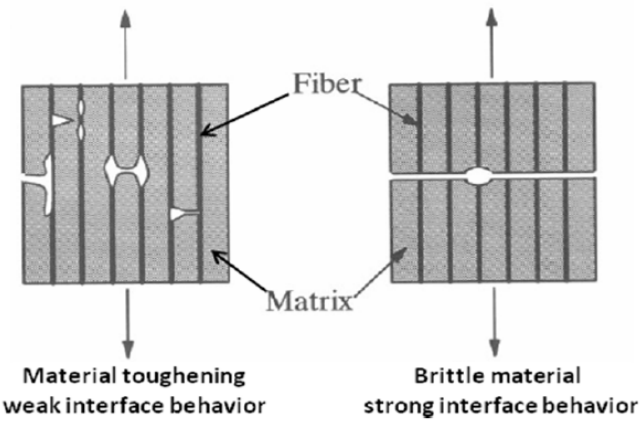

Figure 3: Examples of the crack propagation effects of weak and strong interfaces. Reproduced with permission.

A feature of CMCs, compared to other types of composites, is that the failure strain of the matrix is normally lower than that of the fiber; as such, the matrix will generally fail first. Because of this feature, induced matrix cracking stresses are redistributed around fibers, reducing stress concentration sites and consequently increasing toughness [22:3065]. During the first load cycle while under a cyclic fatigue load, matrix cracks will be formed and will begin propagating throughout the composite as cycles continue; often though these microcracks will eventually discontinue and remain inactive during additional cyclic loading [22:3068].

CMCs are classified as containing either oxide or non-oxide matrices and reinforcements. Oxide-oxide materials contain metal oxides and because of this are very resistant to additional oxidation. They are also more prone to creep however and exhibit lower strengths and elastic moduli. Non-oxide/non-oxide CMCs-such as the silicon carbide/silicon carbide CMC studied in this research-have limited initial oxygen content, prove better in creep resistance, and show greater strength and elastic modulus values [6:8]. But these materials are also very susceptible to oxidation

at high temperature, and especially so when exposed to oxygen-rich environments. The matrix and interphase therefore provide an additional function of protecting the fibers from oxidation [32:2].

Recent research efforts have investigated the effects of air and steam environments at high temperatures on SiC/SiC composites with interesting results. Large decreases in strength and stiffness have been reported due to the oxidizing effects of steam, while other materials exhibited little to no effect [32:7, 5:27, 6:54, 31]. The primary goal of this report is to characterize—using similar techniques as previous researchers—a new material that was produced through a PIP process.

2.2 Chemical Vapor Deposition/Chemical Vapor Infiltration

Chemical Vapor Deposition/Chemical Vapor Infiltration (CVD/CVI) is a process that is used to deposit different coatings on reinforcement material through a chemical reaction and/or decomposition of a gaseous chemical and the fiber [3:119]. Chemical Vapor Deposition refers to a process which is used to deposit a coating onto a bulk material, while Chemical Vapor Infiltration refers to a process which penetrates into a porous body and deposits a coating. CVI is often the method of choice for depositing solid materials on ceramic fibers, as its depositions are fairly uniform in composition and thickness [27:159]. During CVI, a permeable preform is produced and placed inside a furnace, after which it is heated to 1000-1200 °C. During this time, chemical vapors or gases are forced into the chamber and coat the reinforcement material by either decomposing or reacting with the material. The chemical reactions in below are examples of common CVI coatings producing both SiC and BN.

$$CH_3SiCl_{3(g)} \rightarrow SiC_{(s)} + 3HCl_{(g)}$$

$$BX_{3(g)} + NH_{3(g)} \rightarrow BN_{(s)} + 3HX_{(g)} \quad \textbf{(2.1)}$$

where X = F, Cl

Throughout the CVI process, matrix or interphase material grows on the reinforcement in a radial fashion until an acceptable porosity is achieved. But a problem arises in the use of CVI- while the matrix is being deposited, the deposition favors the outer edges of the reinforcement, effectively sealing off the inner areas of the reinforcement [2:482]. When used for the production of SiC/SiC materials, this method obtains at best about 15% matrix porosity. This method has been shown to be effective in producing non-oxide materials (such as SiC/SiC), and also shows promise in forming oxide-oxide materials. [17:410]

2.3 Polymer Infiltration and Pyrolysis

The process of Polymer Infiltration and Pyrolysis, or PIP, uses liquid polymers to penetrate through the small openings between fibers, after which they are chemically decomposed at high temperatures to transform the polymer into a ceramic [11:5]. Often used to compliment initial CVI processes to decrease matrix porosity, PIP processes are relatively inexpensive and produce acceptable porosity results [27:159]. A common preceramic polymer used in the PIP process is KiON Defense Technology's Ceraset polyureamethylvinylsilazane. Under the Ceraset PIP process, a fiber preform is infiltrated with Ceraset, which is then cured at temperatures around 90-190 °C. After curing, the preform undergoes pyrolysis at temperatures up to 1400 °C [16:1]. Argon and nitrogen environments are generally required to produce the desired amorphous matrix composition

while gases such as H_2 and CO are created. Through the pyrolysis action, a great deal of volume is lost and therefore the PIP process must generally be repeated five to ten times before a satisfactory porosity is achieved [2:480]. To produce acceptable porosity levels while minimizing densification cycles, concepts such as pre-impregnating the initial polymer with a SiC powder slurry-so as to rapidly introduce a greater amount of SiC in the preform-have been suggested [27:159]. Due to the shrinkage during crystallization of the polymer that is inherent of the PIP process, microcracks are readily seen throughout the matrices of PIP materials [26:2211]. After the last pyrolysis cycle, the composite can be heat treated again to a higher temperature, e.g., above 1400 °C for Ceraset, to produce a crystalline phase [2:480, 16:1].

2.4 Interphase Coatings

In producing a composite that will be as strong as possible, the load must be held primarily by the strong fibers while the matrix itself holds the composite together, transfers the loads between all fibers and protects the fibers from the environment. Generally, the failure strain of a matrix is lower than the failure strain of the fiber; when this is the case, the matrix will begin cracking well before the composite fails. Additionally if the composite is to be used at extreme temperatures, oftentimes the dissimilarity of coefficients of thermal of expansion also produce microcracking. Thus the interphase, or region between the fiber and the matrix, must be engineered as to allow debonding [27:162]. If the matrix does not break away, it will transfer the crack formed in the matrix to the fiber, resulting in a cascading matrix/fiber cracking effect that will conclude in a brittle fracture of the composite [3:147]. To prevent this result, coatings are deposited on the fibers before the matrix is introduced to allow for fiber/matrix debonding and sliding. This sliding effect is

essential, as the ultimate strength, failure strain, matrix crack spacing and material toughness are all affected by the fiber/matrix sliding friction [19:2604]. Additional considerations must also be taken into account to ensure that microcracking will not introduce oxygen to the fiber if using a non-oxide fiber. If oxygen is allowed through the matrix to the fiber, it can react with the SiC and form silica (SiO_2), which causes strong bonds to form between multiple fibers, as well as between fibers and the matrix. These bonds produce a loss of independence between the fibers and premature failure will occur [7:80]. As a result, a single (or multiple) coating(s) must be selected to both ensure debonding between matrix and fiber, as well as provide protection to the fiber from environmental attack.

Carbon in the form of graphite had long been the interphase of choice, as it has excellent inherent lubrication qualities. But when exposed to oxidation it readily volatizes into CO and CO_2, leaving the fibers open to oxidation and bridging. Therefore, to increase the oxidation resistance of the interphase, boron nitride (BN) was introduced as an alternative coating showing greater (although still far from perfect) oxidation resistance than carbon. BN is a natural alternative to carbon because, like carbon, it also enjoys excellent lubrication properties that result from its similar hexagonal layered crystal structure by allowing perfect cleavage across the basal (0001) plane [19:2610, 7:4, 19:2614]. This cleavage is especially important because crack deflection occurs along the atomic planes within the interphase itself. If the interphase is not bonded well to the fiber, the load transfer effect from the microcracks within the interphase will be greatly diminished and the fibers will have greater potential exposure to the oxidative environment. If maintained, however, the countless and exceedingly small cracks with even smaller breaches for oxygen infiltration will continue to protect the fiber from the environment, ultimately ensuring the CMC retains its strength and fracture toughness [27:162].

When oxygen reaches BN through cracks in the matrix, boron oxide (B_2O_3, i.e. boria) forms in both the area occupied formerly by the interphase and within matrix cracks, where the boria may then react with the SiC fibers and matrix, which leads to the formation of borosilicate glass, although volatilization of the BN has been observed and even under certain circumstances oxygen had no effect on the BN [25:2777, 14:1]. When this layer of boron oxide is formed, it produces a glassy sealant at temperatures as low as 490 °C [21:232] and effectively prevents additional oxygen from penetrating through to the fiber; as such, it has the potential to self-heal [9:143, 27:162]. Additionally, BN and SiC (SiC being the primary component of both CG NICALON™ fibers and the matrix material for the tested composite) are stable when in contact with each other, making BN a natural choice as a protective coating [9:143]. It is important to find the optimal coating thickness, as research involving NICALON™ fibers coated with BN and then SiC showed that too thin of BN coatings resulted in early failure due to inadequate fiber/matrix debonding, while too thick of a coating resulted in early failure due to interlaminar shear [9:144].

Most current interfacial coatings, such as boron nitride and carbon, react and degrade readily with air and water vapor; therefore, a thin coating of matrix material such as SiC can be applied to the coating to prevent any degradation during handling. This coating is generally applied immediately after the initial protective coating is applied to the fibers through a CVI process. As the material is deposited on the composite, this top layer of SiC will simply become a part of the matrix. [2:460]

2.5 Matrix Overcoats

Oftentimes after the final CVI or PIP process has been completed a final thick coating is applied to the CMC to further improve its resistance to oxidation in harsh environments. This coating is generally a layer of matrix material deposited to seal the residual porosity common to both CVI and PIP processes [27:163]. Additionally, if net-shape products are too difficult to produce, such as the specimens used in monotonic and fatigue testing, machining to create the final shape must take place. This machining however re-exposes the inner matrix and fibers and another coating must be introduced to the specimen [31].

The considerable amount of matrix material on the outside of the composite can provide a self healing layer under ideal circumstances. If the composite is under a constant stress or is being cycled very slowly, while also being at temperatures above approximately 900 °C, the silica formed on the coating layer will actually flow to fill in the cracks produced and seal the inner composite from environmental attack. But if the temperatures are lower than 900 °C the highly viscous silica will be unable to move into the cracks. Furthermore, if the fatigue frequency is too great, the silica will not have enough time to form this protective layer [27:163].

2.6 Environmental Attack and Oxidation

During high-stress fatigue, matrix cracking is generally considered saturated after the first cycle; during low-stress fatigue, however, the cracking of the matrix takes considerably longer to form. During and after saturation has occurred, these cracks within the matrix detach and debond from the 90° weft fibers, which then become excellent channels for crack propagation and, hence, environmental attack [22:96]. Once open to the effects of oxygen, the SiC matrix and fibers tend to

either volatize (vaporize) or oxidize through the formation of SiO_2. After the formation of the silica (often, in the form of scales), it may then react with other gasses to form $SiO_{(g)}$ and $Si(OH)_{4(g)}$, as well as other $Si(OH)_{x(g)}$ species [30:1817]. The equation below illustrates some of the more common chemical transformations related to oxidation and environmental attack within common SiC/SiC CMCs while being tested in air.

$$SiC_{(s)} + 2O_{2(g)} \rightarrow SiO_{2(s)} + CO_{2(g)}$$

$$SiC_{(s)} + 3/2O_{2(g)} \rightarrow SiO_{2(s,l)} + CO_{(g)} \quad \textbf{(2.2)}$$

For CMCs being used within combustion chambers, one of the main byproducts of the combustion process is water vapor. Additionally, if these materials are to be used in aircraft, they would naturally be flown through rain and snow, introducing additional moisture content. As previously mentioned, the presence of steam within the environment significantly increases the degradation of non-oxide CMCs [32:7, 5:27, 31], in part, because of an increased rate of silica growth [24:212]. The viscosity of silica decreases with increasing temperature. The presence of water further decreases the viscosity of silica by breaking some of the Si-O-Si bonds in the glass structure. In turn the lower viscosity of the material facilitates mass transport of the oxidizing species through the glass leading to increased oxidation rates. Water vapor also increases the rate of BN oxidation. When in a low water vapor environment this is done by first producing boria, which is then converted to borosilicate glass through a chemical reaction with oxidation products of the SiC fibers and matrix. But if the environment has a relatively high water vapor content, volatile HBO_2, H_3BO_3 and $H_3B_3O_6$ chemicals are produced directly between chemical reactions of BN and H_2O [19:2610]. Boria has a similar mass transport effect on silica, again by breaking the bonds of the silica and thereby reducing the viscosity of the material.

III. Material and Test Specimen

3.1 Material

The material used for these experiments is a Ceramic Matrix Composite consisting of a Silicon Carbide matrix and Ceramic Grade (CG) NICALON™ fibers, and was manufactured by the Materials and Electrochemical Research (MER) Corporation of Tucson, AZ. The material underwent a Chemical Vapor Infiltration (CVI) process to produce the interphase and a Polymer Infiltration and Pyrolysis (PIP) process to produce the matrix within the composite. This material is composed of tows in an eight harness satin weave (8HSW), is a dark brown color due to a final impregnation of both SiC and elemental boron, has a fiber volume fraction of 21.5% and has an average density of 2.10 g/cm^3. When heated to 1000 °C in air, the material becomes black, smooth and glassy; however, when heated in steam, it becomes white with oxidation and residue with no glassy surface visible to the unaided eye. It also occasionally lost pieces of the matrix coating due to flaking.

This material was produced by using a new CVI/PIP method as well as attempting a net-shape process. MER's primary goal was to achieve less than 5% porosity in less than four PIP cycles and thereby reduce the cost of the finished product. MER coated the fibers in BN and then SiC using CVI techniques [20:36-37]. After this step, the fabric was laid up in a preceramic polymer bath including 2 μm SiC powder [20:72]. The reason to pre-impregnate the matrix with powdered SiC was that if SiC was already present within the slurry, the SiC infiltration process would take fewer cycles to produce an acceptable porosity result [27:159]. After the composite was laid up, it was then pyrolyzed, causing the preceramic polymer to transform into a pure SiC matrix. After pyrolization, the plates were again infiltrated with the polymer (without additional SiC

powder) and pyrolyzed. This procedure was repeated for a total of three cycles. After these three cycles the porosity was deemed to be sufficient. A fourth and final coating deposition was performed with the preceramic polymer and combined boron particles to improve resistance to oxidation at elevated temperatures; this served to seal the machined dogbone specimens.

The CG NICALON™ fibers used in the material (produced by Nippon Carbon Company, Ltd. of Japan) consist of β-SiC crystals as well as an amorphous composition of Silicon, Carbon and Oxygen. The composition by weight of Si:C:O is 52%:37%:12%, which leads to very high strength and modulus properties at high temperatures under harsh conditions [28:2]. The manufacturer also recommends a BN coating to achieve optimum CMC properties.

The interphase chosen for MER's CMC was a layer of Boron Nitride (BN), followed by a layer of Silicon Carbide (SiC). BN and SiC were deposited through a CVI chemical reaction onto 192 separate 8HSW CG NICALON™ plies. The 192 plies represented 24 groups of 8 plies each. The CVI reaction produced average group weight gains between 3.6% and 6.9%. Because of this, in an attempt to maintain the most consistent property results, the plies from the highest weight-gain group and the lowest weight-gain group were interwoven with one another to produce the 16-ply panel S1. Plies from the second-highest and second-lowest weight-gain groups were then paired to produce panel S2 and so on to produce 12 panels. This method resulted in an average weight gain of approximately 5%. Panel S5's two groups of plies had thicknesses of approximately 0.15 μm and 0.21 μm. The diminishing difference between plies continued until panel S11's two ply groups had thicknesses of approximately 0.17 μm and 0.18 μm [20:213, 20:169, 28:2, 3:36]. Interestingly, the density also increased with panel number; this indicates that the porosity decreased immediately as the weight gain differences were minimized.

3.2 Test Specimen Preparation

Five specimens were cut from each of six panels, resulting in a total of 30 test specimens. These specimens were received from MER with a dog-bone type geometry. Dimensions of each specimen are given in Table 1 below.

Table 1: Original specimen dimensions

Specimen #	WIDTH (mm)	DEPTH (mm)	CROSS SECTIONAL AREA (mm^2)
S10A	3.39	5.04	17.10
S10B	3.37	5.08	17.10
S10C	3.35	5.05	16.95
S10D	3.34	4.99	16.67
S10E	3.37	5.04	16.97
S11A	3.44	4.84	16.65
S11B	3.38	4.93	16.65
S11C	3.43	5.00	17.16
S11D	3.34	4.97	16.59
S11E	3.49	5.07	17.70
S5A	3.51	4.74	16.60
S5B	3.53	4.86	17.17
S5C	3.57	4.85	17.31
S5D	3.47	4.78	16.56
S5E	3.45	4.72	16.32
S7A	3.42	5.33	18.22
S7B	3.51	5.33	18.70
S7C	3.42	5.08	17.35
S7D	3.51	5.17	18.12
S7E	3.51	5.17	18.12
S8A	3.34	5.16	17.22
S8B	3.43	4.94	16.94
S8C	3.40	4.93	16.77
S8D	3.37	4.90	16.50
S8E	3.37	4.86	16.37
S9A	3.34	4.94	16.50
S9B	3.31	4.84	16.04
S9C	3.37	4.85	16.33
S9D	3.38	4.83	16.30
S9E	3.38	4.80	16.22

Less than one unit cell of the weave is seen within the very thin gage section of the specimen. In doing so the material properties of the specimen may have been inadvertently degraded due to this lack of constraint.

Fiberglass tabs 1/16” thick were glued onto the ends of the specimens using M-Bond 200 Adhesive and M-Bond 200 Catalyst-C manufactured by Vishay Micro Measurements. These tabs provided a cushioning layer between the material and the hydraulic grips used in testing to avoid inadvertent early failure in the gripped areas. Figure 4, below, shows a specimen prior to testing.

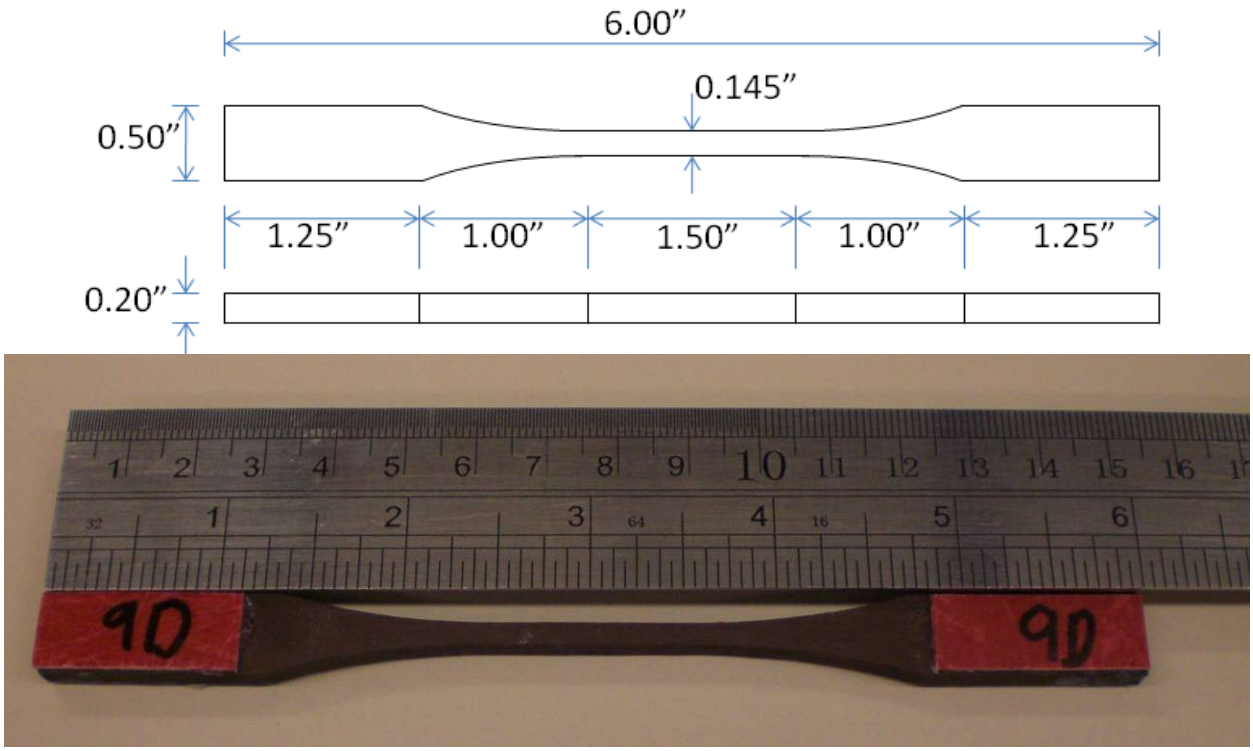

Figure 4: Specimen dimensional drawing (top) and specimen prior to testing (bottom)

IV. Experimental Arrangements and Procedures

4.1 Test Equipment and Setup

Mechanical testing was performed using an MTS 810 Material Test System 5,000 lb capacity servo-hydraulic machine controlled by a Flextest 40 digital controller and a PC loaded with MTS Station Manager/Multipurpose Testware software, as seen in Figure 5. An MTS extensometer with six-inch alumina legs was used to measure strain. Both the top and bottom sets of wedges were cooled with 15 °C water by a Neslab Coolflow Refrigerated Recirculator, Model HX-75. This ensured the grips would stay at acceptable temperature levels, while the purpose-built rail furnace was at elevated temperatures. When steam was used, it was generated with an Amteco Chromalox 2110 Steam Generator and distilled water.

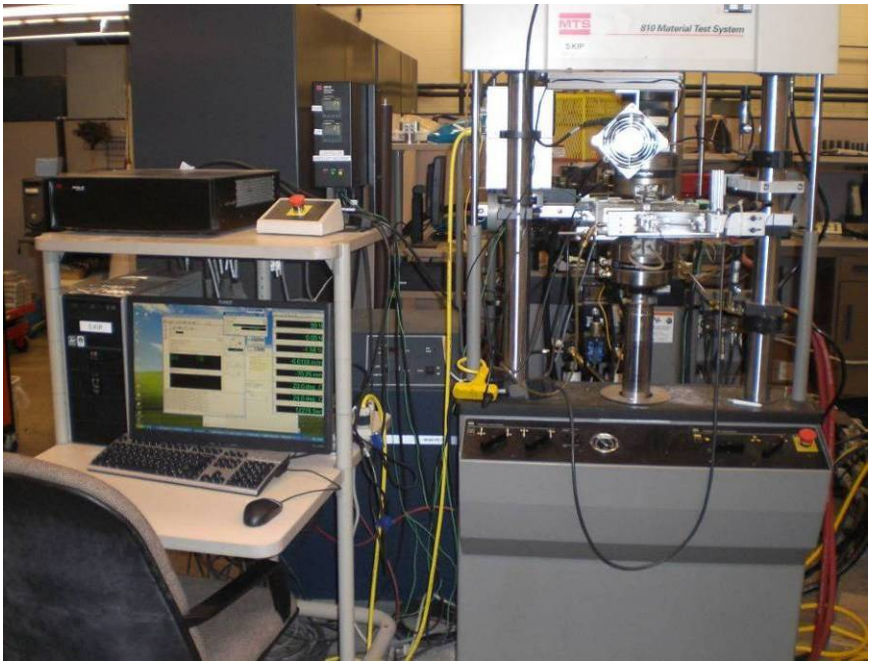

Figure 5: MTS 5 kip machine setup

Prior to placement into the MTS machine, each specimen was loaded into a “susceptor,” a small ceramic cylinder designed primarily to keep a steam environment present within the cylinder, and thus within the test section, while keeping non-saturated air out. But these susceptors were also found to provide a great deal of insulation around the test section and therefore, after the susceptor (enclosing the test section) warmed to a steady state temperature, there was very little temperature fluctuation within the test section. Because of this quality, the susceptor was utilized for both steam and laboratory air tests. Figure 6 is an example of a susceptor loaded into the right half of the furnace with a specimen inserted.

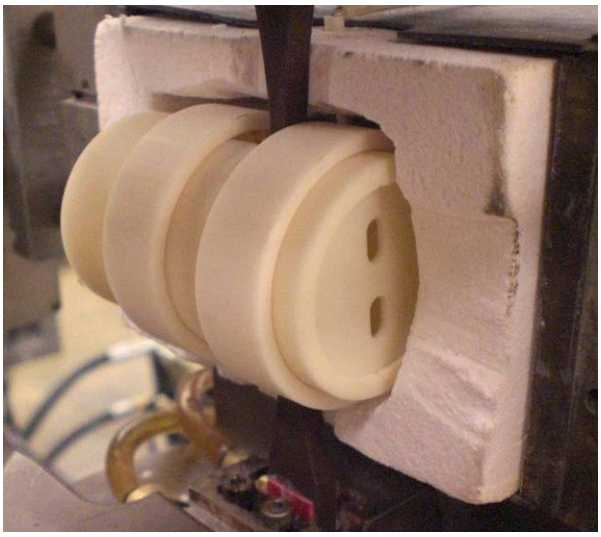

Figure 6: Specimen loaded into ceramic susceptor

After placing the specimen into the susceptor, the top portion of the specimen was gripped into the hydraulic wedges of the MTS machine and the furnace was slid into place and securely tightened with multiple bolts to ensure a tight insulation fit. Gripping pressure was set to 8 MPa. At this point, the top grip held the final load of the assembly and the load cell was zeroed electronically on the computer to ensure that the MTS machine would put the correct load on the

specimen. The machine was commanded to load zero newtons of force, the bottom grip was activated, and the specimen was ready to be tested.

4.2 Test Procedures

Prior to any testing, multiple temperature calibration cycles were performed using the exact test setup for both air and steam scenarios. The single exception to this was the lack of an extensometer, as the holes in the susceptor normally used for the extensometer legs were needed for threading the thermocouples. The temperature necessary to maintain 1000 °C at the test section was found to be 1065 °C in air and 1084 °C in steam. Temperatures axially along the loading direction were also measured to ensure there was no significant temperature gradient; at approximately one-half inch above and below the center of the test section, it was found the specimen was about three to four degrees cooler and therefore the gradient was not significant. This small gradient, as well as the need to maintain higher furnace temperatures than those at which the specimen was tested, was due primarily to heat losses in the space between the furnace heating elements and the specimen, as well as the thermal conductance between the specimen and the 15 °C grips.

Three types of tests were carried out: a monotonic tension to failure test, a cyclic tension-tension to failure fatigue test in a laboratory air environment and a cyclic tension-tension to failure fatigue test in a steam environment. All three of these scenarios produced invaluable information as to the properties of the material.

4.2.1 Monotonic Testing

Specimens from each of the six panels were tested in a monotonic tension to failure test. Each specimen was loaded into the susceptor, clamped into the wedges and readied with the furnace, wedge cooling water and extensometer. An MTS program was written to take the specimen up to 1000 °C under a force control mode (so as to not induce any compressive loads due to thermal expansion) and it then dwelt for 20 minutes as a thermal soak time. After the 20 minutes were finished, the program then began to tension the specimen at a constant displacement rate of 0.05 mm/s until failure. Data recorded included measured strain, measured and commanded force, measured and commanded displacement, measured and commanded temperature between both furnace sides and time. Data was acquired at 0.01 second intervals. Immediately after failure the bottom half of the specimen was removed from the heat to prevent any additional oxidation caused at high temperatures to occur on the fracture surface.

4.2.2 Fatigue Test

Specimens that underwent fatigue testing were loaded in the same fashion as the monotonic tension specimens, with the exception of those in steam environments, which had a ceramic steam tube positioned between the steam generator and the rear of the susceptor to provide a continual slow steady stream of steam. The generic program heated the specimen to 1000 °C and dwelt at this temperature for no less than 20 minutes; more time was added if the temperature ever moved outside of the control tolerance of 5 °C during the thermal soak. It then brought the specimen to 10% of the maximum load, as determined by the test scenario, over a period of 30 seconds, after which it began cycling with the ratio R (minimum to maximum stress) equal to 0.1 at 1.0 Hz. If run

out was achieved (one instance), the program would unload the specimen and perform a tension to failure test at a displacement rate of 0.05 mm/s to test the retained strength. Once the specimen failed, the furnace temperature was immediately brought down to ambient temperature, or in the case of steam, to 300 °C, to prevent condensation formation. Data recorded included measured strain, measured and commanded force, measured and commanded displacement, measured and commanded temperature between both furnace sides and time. This data was recorded during warm-up at 0.25 second intervals, during cyclic testing at 0.10 second intervals during cycles 1-25, every tenth cycle from 30 to 100, every hundredth cycle from 100 to 1,000, every thousandth cycle from 1,000 to 10,000 and every ten-thousandth cycle from 10,000 to 200,000. This data was also recorded as single data points at each maximum and each minimum value of each cycle. Finally, if run out was achieved, data was taken at 0.01 second intervals during the tension to failure test. This data collection process ensured that enough data would be gathered to provide meaningful results.

4.3 Microstructural Examination

Following failure, each test specimen was marked T (for “top”) or B (for “bottom”) and carefully organized to ensure no damage would occur to the fracture surface. The sides of each half were then photographed under a Zeiss stereomicroscope shown in Figure 7. Fracture surfaces of one of the halves of each specimen were subsequently cut off with a diamond blade and mounted on SEM pin mounts. Additional material from the same half was then cut and mounted into conductive 1 ¼” phenolic pucks (Buehler number 20-3112-501) using a Buehler SimpliMet 2000. These were then polished according to the suggested polishing guide for SiC/SiC ceramic matrix composites [10:231] using a Buehler EcoMet/AutoMet 300. The process is outlined in Table 2,

below, although in practice, the forces were reduced by half and the time spent in each process was equal to two-thirds of the maximum recommended time. SEM micrographs were taken using a FEI Company Quanta 200 and a FEI Company Quanta 200 3D, shown in Figure 8, below.

Figure 7: Zeiss Stereomicroscope used in microstrucural examination

Table 2: Materialographic preparation process used as recommended for SiC materials

Traditional SiC/SiC Polishing Method

Grind/Polish	Plane Grind	Fine Grind 1	Fine Grind 2	Fine Grind 3	Polish 1	Polish 2	Polish 3
Disk/Cloth	SiC Paper	SiC Paper	Ultrapad	Ultrapad	Texmet 2500	Texmet 2500	Chemomet
Grit (P)/Grain Size (µm)	P400	P600	15 µm	9 µm	6 µm	3 µm	0.1 µm
Lubricant	Water	Water	Suspension	Suspension	Suspension	Suspension	Suspension
Rotation Disk (rpm)	300	300	150	150	150	150	150
Rotation Holder (rpm)	150	150	150	150	150	150	150
Comp/Contra	Contra	Comp	Comp	Comp	Comp	Comp	Comp
Force Per Specimen (lb)	7	7	7	7	7	5	2
Time (min)	5	2-10	6-15	6-15	5-30	10-60	1-10

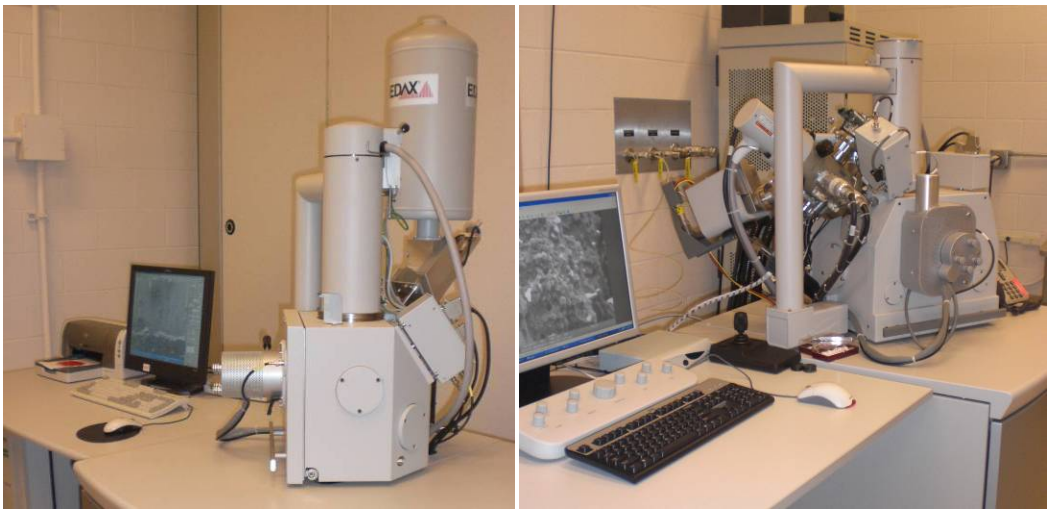

Figure 8: FEI Co. Quanta 200 (left) and Quanta 200 3D (right) Scanning Electron Microscopes used in microstrucural examination

V. Results and Discussion

5.1 Chapter Overview

Results of the experimental investigation are presented in this chapter. Section 5.2 provides a summary of thermal strains and coefficients of thermal expansion obtained for all specimens tested in this study. Results produced in six monotonic tension to failure tests are given in Section 5.3. Section 5.4 presents results obtained in fatigue tests conducted at 1000 °C in air, while Section 5.5 offers a brief discussion of the effects of prior fatigue at 1000 °C in air on tensile properties and stress-strain behavior of the CG NICALON™/BN/SiC composite. Results of the fatigue tests conducted at 1000 °C in steam are discussed in Section 5.6. Sections 5.7-5.10 provide a qualitative analysis of the microstructure of the MER CG NICALON™/BN/SiC virgin material and of the microstructure of the material subjected to mechanical tests. Optical and scanning electron

microscope (SEM) micrographs depicting characteristics of the microstructure are presented, which illustrate the different damage and failure mechanisms observed in this study.

Specimen alphanumeric identification contain reference to the batch ("S"), panel number (5, 7, 8, 9, 10 or 11), and specimen letter designation (A, B, C, D or E). For example, specimen S10D came from batch S, panel 10 and was the fourth of five specimens cut from that panel. Specimens from panels 5, 7, 8 and 9 were generally not tested in fatigue because specimens from these panels exhibited low ultimate tensile strength (UTS).

All test results performed in this study are summarized in Table 3. All tests were conducted at 1000 °C. All fatigue tests were carried out with the ratio R (minimum stress to maximum stress) of 0.1 at the frequency of 1.0 Hz.

Table 3: Summary of test results for CG NICALON™/BN/SiC composite at 1000 °C

Specimen	Maximum Stress (MPa)	Elastic Modulus (GPa)	Cycles to Failure (N)	Time to Failure (h)	Failure Strain (%)	Ultimate/ Retained Strength (MPa)
Tensile Tests						
S5A	-	42.2	-	-	0.209	98.6
S7C	-	49.1	-	-	0.229	104
S8D	-	50.3	-	-	0.232	106
S9A	-	48.4	-	-	0.266	114
S10D	-	59.1	-	-	0.279	136
S11B	-	49.1	-	-	0.263	124
Fatigue in Air						
S7B	80	47.2	34,652	9.63	0.552	-
S10B	80	50.6	200,000*	55.56	0.558	111.5
S11E	100	56.6	168,255	46.74	0.382	-
Fatigue in Steam						
S11A	60	54.7	194,930	54.15	0.683	-
S11D	70	57.0	65,154	18.10	0.283	-
S10E	70	51.8	126,593	35.16	0.391	-
S8E	80	49.7	46,621	12.95	0.404	-
S10A	80	47.6	73,084	20.30	0.422	-
S11C	100	54.5	17,587	4.89	0.232	-

*Run out, failure of specimen did not occur when the test was terminated

5.2 Thermal Expansion

In all tests a specimen was heated to test temperature of 1000 °C at a rate of 1 °C/s then held at 1000 °C for no less than 20 minutes prior to testing. During the temperature increase the load was held at zero to allow for thermal expansion. Analyzing the data collected from this phase of the test reveals that the material ceased expanding in the test section within seven minutes of the furnace reaching 1000 °C, therefore 20 minutes was sufficient time for the specimen to reach thermal equilibrium.

Recorded thermal strain values were used to calculate the coefficient of linear thermal expansion, α_t, which are reported in Table 4. The coefficient of linear thermal expansion showed a weak correlation with UTS. The average coefficient of linear thermal expansion was 4.53×10^{-6}/°C. This value is consistent with values reported for similar materials [5:30,6:40].

Table 4: Thermal strain and corresponding coefficient of linear thermal expansion for CG NICALON™/BN/SiC composite measured for temperature increase from 23 °C to 1000 °C

Specimen	Thermal Strain (%)	Coefficient of Linear Thermal Expansion, α_t (10^{-6} / °C)
S5A	0.389	3.89
Average		3.89
Standard Deviation		N/A
S7B	0.428	4.28
S7C	0.467	4.67
Average		4.48
Standard Deviation		0.28
S8D	0.459	4.59
S8E	0.472	4.72
Average		4.66
Standard Deviation		0.09
S9A	0.473	4.73
Average		2.41
Standard Deviation		N/A
S10A	0.423	4.23
S10B	0.462	4.62
S10C	0.472	4.72
S10D	0.408	4.08
S10E	0.479	4.79
Average		4.49
Standard Deviation		0.31
S11A	0.481	4.81
S11B	0.498	4.98
S11C	0.440	4.40
S11D	0.484	4.84
S11E	0.417	4.17
Average		4.64
Standard Deviation		0.34

5.3 Monotonic Tension

Specimens from each of the six panels were tested in tension to failure at a rate of 0.05 mm/s at 1000 °C in air. Results are presented in Table 5 and in Figure 9. The average elastic modulus was 49.7 GPa, the average UTS was 114 MPa and the average failure strain was 0.25%. However, these averages are not necessarily representative of this material. The UTS obtained for specimens from panel 5 is only 72% of the UTS obtained for specimens from panel 10. This inconsistency in the strength values exhibited by specimens from different panels severely limited the usefulness of the specimens from panels that produced lower strength values in characterizing fatigue behavior of this composite. Notably the panels with lower numbers also had greater differences in average weight gains between the plies when processed as well as lower densities. These differences evidently had an effect on the overall strength of the material in these panels.

The stress-strain curves in Figure 9 are nearly linear to failure and do not show an obvious proportional limit, which is the stress at which point the linear relationship between the stress and strain ceases [33:102, 1:288]. In ceramic composites this generally corresponds to the point where the matrix begins to crack, and the majority of the load transfers to the fibers [5:42]. Typically tensile stress-strain curves obtained for ceramic composites with a dense matrix exhibit a bi-linear behavior. Although uncommon, the nearly linear stress-strain curves produced by the CG NICALON™/BN/SiC material have been observed in very porous SiC/SiC PIP composites, though are more typical for an oxide-oxide composite with an exceptionally weak matrix [26:2215, 15:596]. The contribution of the fibers to the overall modulus was approximately 45.1 GPa per specimen, giving further credence to the weak matrix concept as the modulus in most specimens was rarely significantly above this value.

Table 5: Summary of tensile properties for the CG NICALON™/BN/SiC composite at 1000 °C

Specimen	Elastic Modulus (GPa)	Ultimate Tensile Strength (MPa)	Failure Strain (%)
S5A	42.2	98.6	0.232
S7C	49.1	104	0.266
S8D	50.3	106	0.279
S9A	48.4	114	0.263
S10D	59.1	136	0.25
S11B	49.1	124	
Average	49.70	113.77	

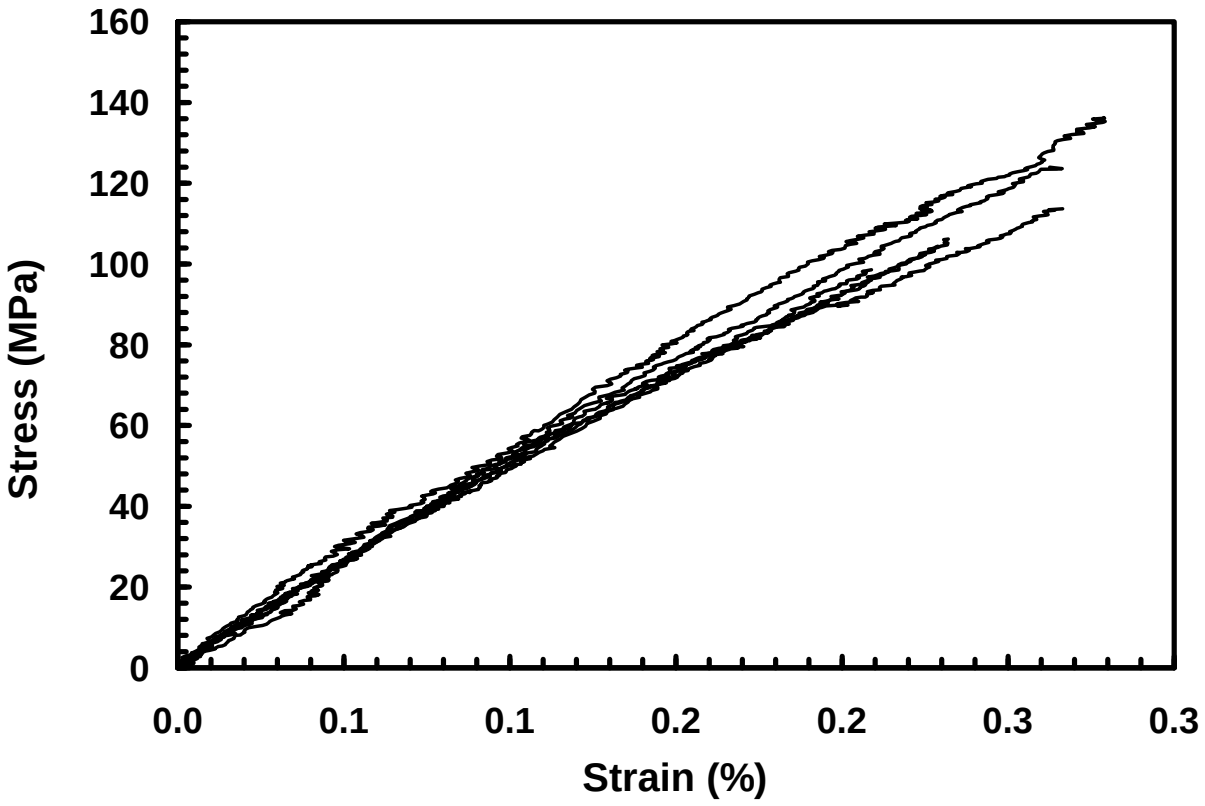

Figure 9: Tensile stress-strain curves obtained for CG NICALON™/BN/SiC composite at 1000 °C in air

It is instructive to compare the tensile results obtained for the CG NICALON™/BN/SiC composite at 1000 °C in this study with the tensile results for HI-NICALON™/SiC at 1200 °C reported by Christensen [5:32] and tensile results for HI-NICALON™/HyprSiC at 1200 °C reported by Delapasse [6:40]. It is recognized that CG NICALON™ fibers have a higher UTS (3.0 GPa) [28:2] than the HI-NICALON™ fibers (2.8 GPa) [12:2]. Therefore in a low-oxidation environment of a tension test to failure, which is completed in less than an hour, as a minimum comparable failure stress and failure strain values should be produced by the three aforementioned composites. However, as seen in Figure 10, this is not the case. The tensile strength values produced by the CG NICALON™/BN/SiC composite are significantly lower than those produced by the composites reinforced with the HI-NICALON™ fibers. Note a nearly bi-linear nature of the stress-strain curves obtained for the CMCs reinforced with the HI-NICALON™ fibers.

The stress-strain curves obtained for the CG NICALON™/BN/SiC composite are nearly parallel to the stress-strain curves obtained for the composites reinforced with the HI-NICALON™ fibers after the proportional limit. This observation suggests that there was little contribution from the matrix in the case of the CG NICALON™/BN/SiC composite and that the matrix may not be sufficiently dense. It is also noteworthy that the failure strain produced by the CG NICALON™/BN/SiC composite was approximately equal to that produced by the HI-NICALON™/SiC CMC. The failure strain values reported for the CG NICALON™ fibers and the HI-NICALON™ fibers in literature [28:2, 12:2] are 1.43% and 1.04%, respectively. As seen in Figure 10, the failure strains obtained for the HI-NICALON™/PyC/HyprSiC composite are closer to this value than the failure strains obtained for the two composites with the BN fiber coating and the SiC matrix. This suggests that the interphase material and/or processing may have significantly degraded the performance of the fibers.

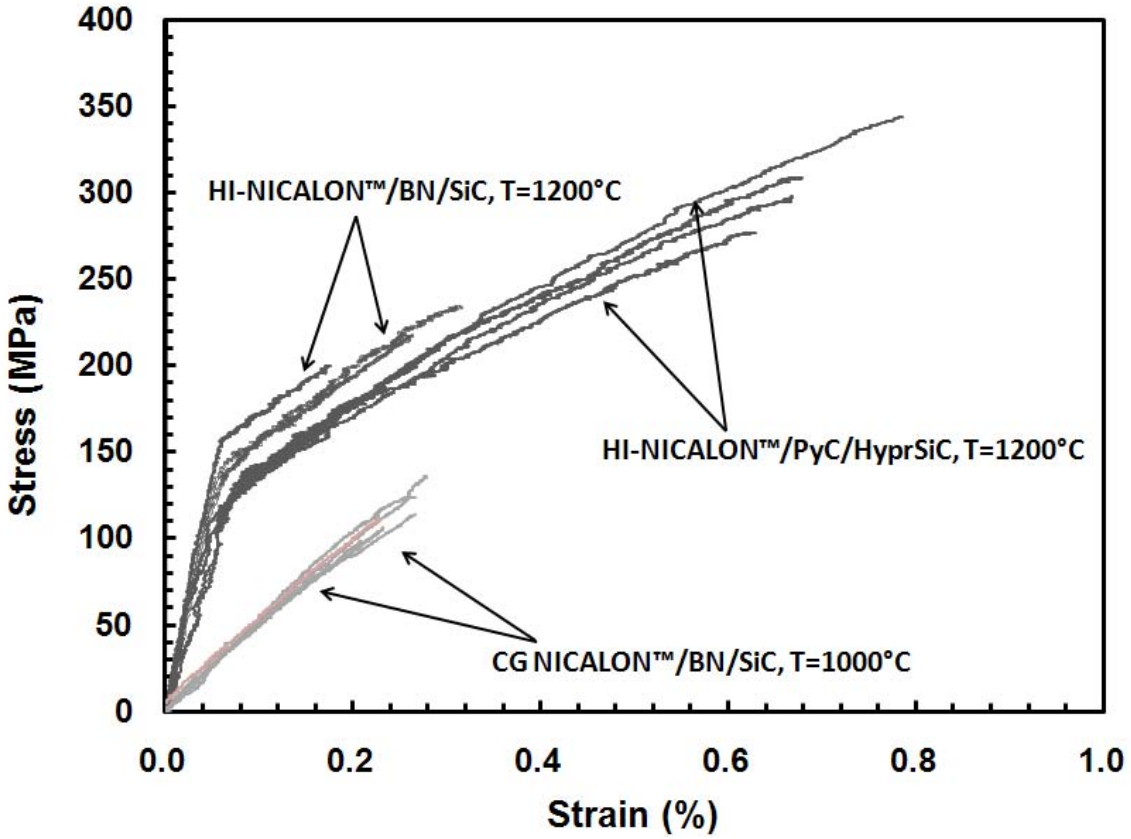

Figure 10: Tensile stress-strain curves obtained for HI-NICALON™/SiC and HI-NICALON™/HyprSiC ceramic composites at 1200 °C in air, and for CG NICALON™/BN/SiC ceramic composite at 1000 °C in air. Data for HI-NICALON™/SiC from Christensen [5:32]. Data for HI-NICALON™/HyprSiC from Delapasse [6:40].

5.4 Tension-Tension Fatigue at 1000˚C in Air

Three fatigue tests were conducted with the ratio R (minimum to maximum stress) of 0.1 at a frequency of 1.0 Hz, at 1000 °C in laboratory air. Two tests were conducted with the maximum stress of 80 MPa and one with the maximum stress of 100 MPa. Fatigue run out of 200,000 cycles was achieved in one of the 80 MPa tests. The specimen that achieved run-out was subjected to a

tensile test to failure at 1000 °C in air to determine the retained strength and stiffness. Results of the fatigue tests performed at 1000 °C in air are summarized in Table 6.

Table 6: Summary of fatigue results for CG NICALON™/BN/SiC composite at 1000 °C in laboratory air

Specimen	Maximum Stress (MPa)	Elastic Modulus (GPa)	Cycles to Failure (N)	Time to Failure (h)	Failure Strain (%)
S7B	80	47.2	34,652	9.63	0.552
S10B	80	50.6	200,000*	55.56	0.558
S11E	100	56.6	168,255	46.74	0.382

*Run out, failure of specimen did not occur when the test was terminated

As discussed earlier the low tensile strength was exhibited by specimens from panels 5-9. A dramatic difference in UTS produced by specimens from different panels is also reflected in cyclic lives produced in two 80 MPa tests. Specimen S10B achieved a run-out of 200,000 cycles while specimen S7B failed after only 34,652 cycles.

Of interest in cyclic fatigue is the reduction in stiffness (hysteresis modulus determined from the maximum and minimum stress-strain data points during a load cycle), reflecting the damage development during fatigue cycling. Normalized modulus (i.e. modulus normalized by the modulus obtained in the first cycle) is plotted vs. fatigue cycles in Figure 11. It is seen that the normalized modulus values remain approximately 1.0 during the entire lifetime of both specimens. This result suggests that little fatigue damage has occurred to the fibers and that the material is strongly fiber-dominated.

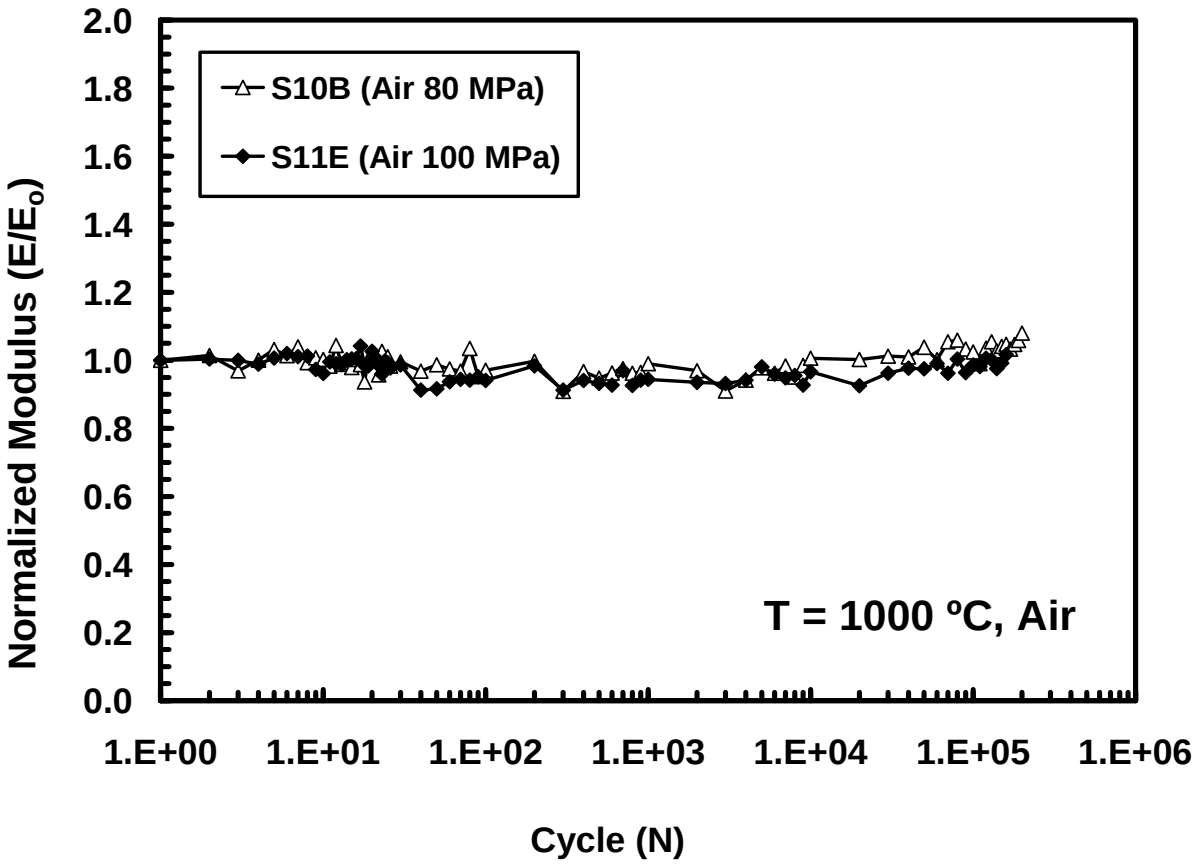

Figure 11: Normalized modulus vs. fatigue cycles at 1000 °C in air

Figure 12 below displays the strain accumulated with fatigue cycles. Continuous strain accumulation with cycling suggests progressive damage development, which is contrary to the conclusion suggested by the normalized modulus data in Figure 11. These are two different indications of damage development. Evaluating change in the normalized modulus with fatigue cycles characterizes damage development by evaluating stiffness degradation. Evaluating strain accumulation with cycles characterizes accumulation of permanent strain.

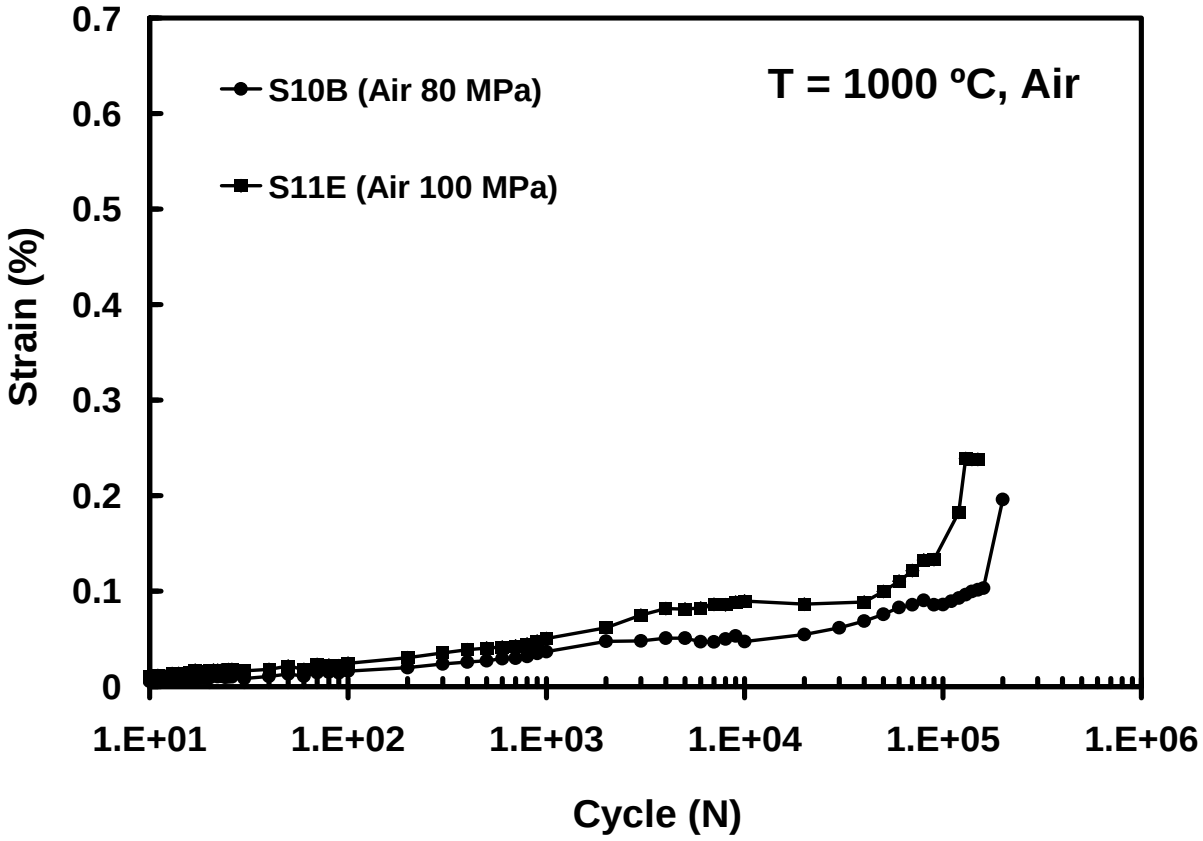

Figure 12: Strain accumulation vs. fatigue cycles at 1000 °C in air

It is recognized that weave-stretching and realignment can occur in a woven composite [4:1229]. Chawla [4:1229] studied two NICALON™ fabric-reinforced SiCON matrix composites, where the matrix composition was varied by the addition of SiC and BN particulate fillers to maximize densification and minimize shrinkage during the PIP process. This material, after being subjected to tension-tension fatigue with the maximum stress of approximately 70% of its UTS for 10^7 cycles was tested in tension to failure where it exhibited an increase in the Young's Modulus, failure strain and ultimate tensile strength. It was determined that the transverse tows within the weave realigned themselves to provide these improved tensile properties. This process of realignment of the transverse fiber bundles also leads to stretching of the weave (along the loading

direction) and shrinking of the weave (perpendicular to the loading direction), schematically depicted in Figure 13 [4:1229].

The CG NICALON™/BN/SiC composite did not exhibit loss of normalized modulus with cycling. On the contrary, a slight increase in the normalized modulus was observed just prior to failure. The realignment of the transverse fiber bundles and stretching of the weave would explain the increase in strain accumulation with cycles due to an actual increase in length of the composite. This phenomenon would also explain why the increase in strain was not accompanied with a decrease in normalized modulus. Furthermore, a slight decrease in cross sectional area was observed for specimens that failed in fatigue, further giving credence to the likelihood of the realignment of the transverse fiber bundles and stretching of the weave in the composite. The extremely thin gage section of the material may be the cause of this phenomenon.

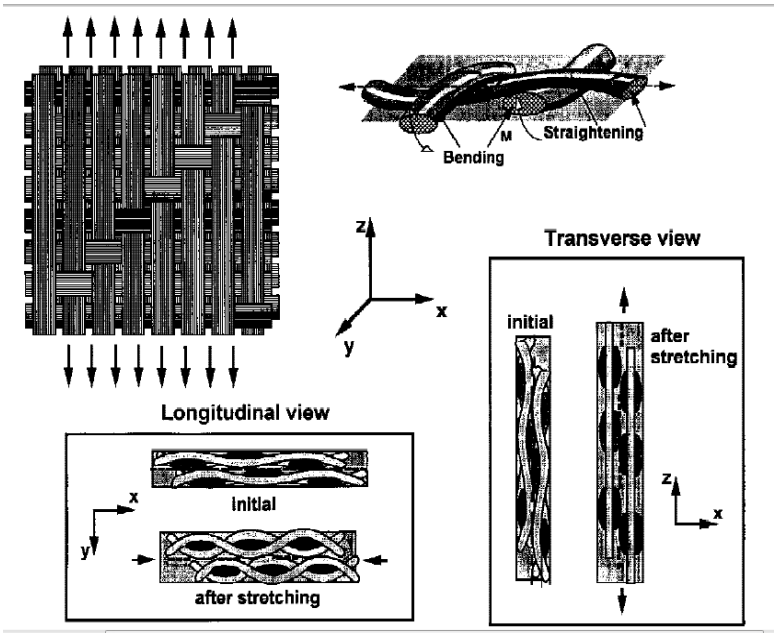

Figure 13: Schematic of the stretching of the weave and realignment of transverse fiber bundles likely to occur during fatigue of CG NICALON™/BN/SiC composite [4:1229]. Reproduced with permission.

Evolution of the hysteresis response with fatigue cycles at 1000 °C in air is typified in Figure 14. Results in Figure 14 reveal that ratcheting, defined as progressive accumulation of strain with increasing number of cycles, continues throughout the test. Figure 14 also shows that the hysteretic modulus remains nearly unchanged throughout the test. These general results are comparable to the other stress-strain hysteresis graphs of materials fatigued in air.

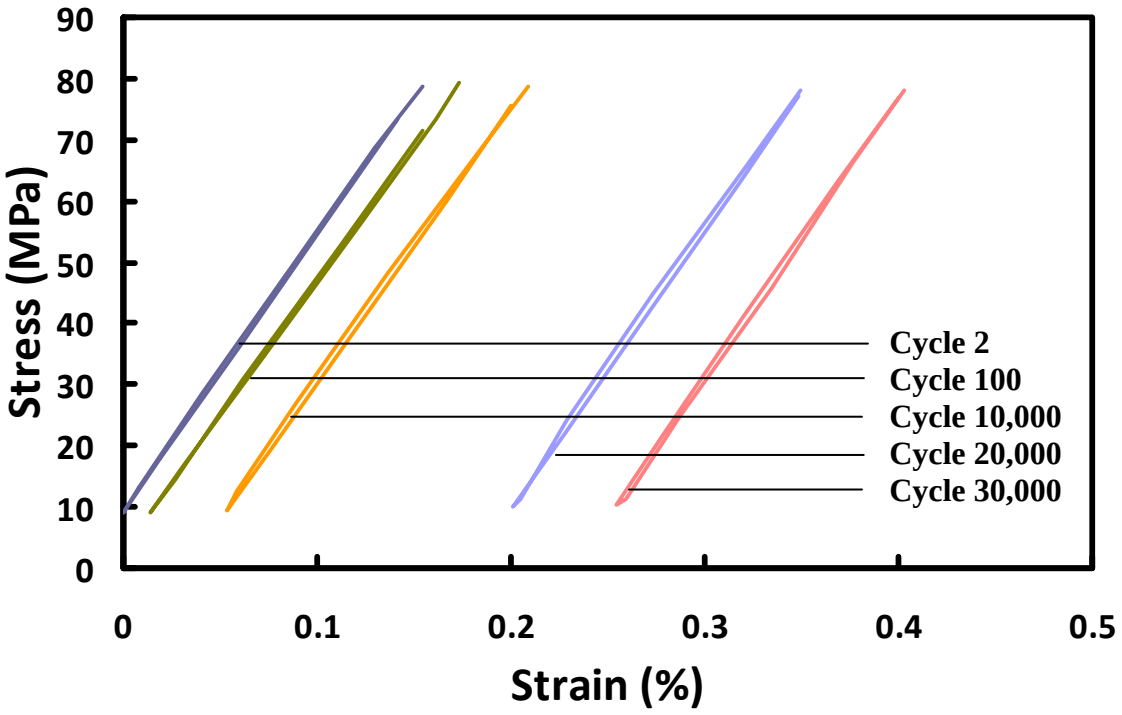

Figure 14: Evolution of stress-strain hysteresis response with fatigue cycles at 1000 °C in air (Specimen S10B, σ_{max} = 80 MPa).

Maximum and minimum strain as a functions of cycle number for the 80 MPa fatigue test conducted at the frequency of 1.0 Hz at 1000 °C in air are shown in Figure 15. The two curves are essentially parallel indicating that the composite does not exhibit cyclic hardening or softening.

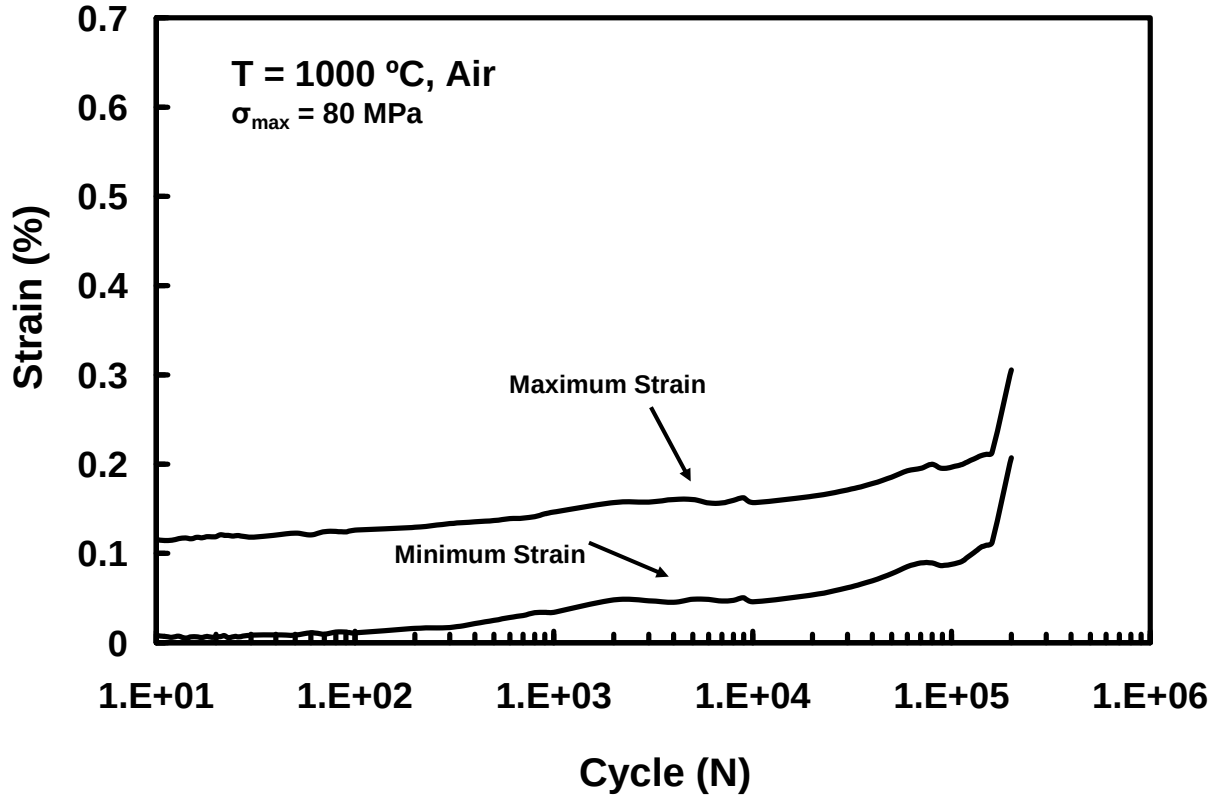

Figure 15: Maximum and minimum strains vs. fatigue cycles for specimen S10B at 1000 °C in air (f = 1.0 Hz, σ_{max} = 80 MPa).

5.5 Effect of Prior Fatigue on Tensile Properties and Tensile Stress-Strain Behavior

Only one specimen subjected to fatigue with the maximum stress of 80 MPa achieved the run-out of 200,000 cycles at 1000 °C in air. After achieving fatigue run-out this specimen was tested in tension to failure to determine its retained properties as summarized in Table 7. The specimen retained 82% of the tensile strength and nearly 97% of its modulus. By retaining its modulus the material further exhibits strong indications the fibers within the CMC straightened and were not damaged throughout the testing. Prior fatigue had minimal effect on the failure strain. The tensile stress-strain curve obtained for specimen S10B subjected to prior fatigue at 1000 °C in air is presented in Figure 16 together with the tensile stress-strain curves for the as-processed material. It is seen that prior fatigue had little effect on tensile stress-strain behavior. Apparently no significant damage occurred in the composite during fatigue loading.

Table 7: Retained properties of CG NICALOON™/BN/SiC specimen S10B subjected to prior fatigue at 1000 °C in air

Maximum Stress (MPa)	Retained Strength (MPa)	Strength Retention (%)	Retained Modulus (GPa)	Modulus Retention (%)	Failure Strain (%)
80	111.5	82	56.1	96.7	0.558

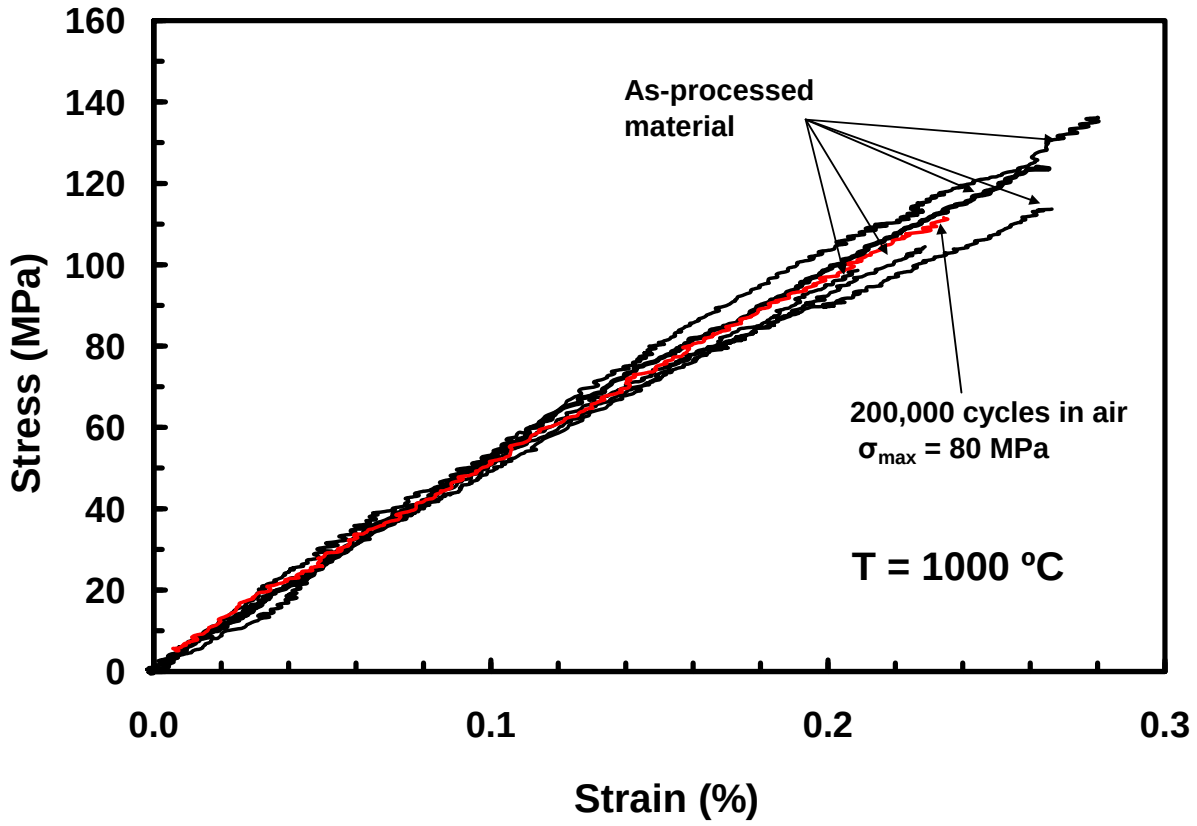

Figure 16: Effect of prior fatigue at 1000 °C on tensile stress-strain behavior of the CG NICALON™/BN/SiC composite.

5.6 Tension-Tension Fatigue at 1000˚C in Steam

Six fatigue tests were conducted with the ratio R (minimum to maximum stress) of 0.1 at a frequency of 1.0 Hz at 1000 °C in a steam environment. The maximum cyclic stresses ranged from 60 to 100 MPa. Fatigue run out of 200,000 was not achieved at 1000 °C in steam. Results of the fatigue tests performed at 1000 °C in steam are summarized in Table 8. Results of fatigue tests at 1000 °C in air are included in Table 8 for comparison.

Table 8: Summary of fatigue results for CG NICALON™/BN/SiC composite at 1000 °C in laboratory air and in steam environment

Specimen	Maximum Stress (MPa)	Elastic Modulus (GPa)	Cycles to Failure (N)	Time to Failure (h)	Failure Strain (%)	Retained Strength (MPa)
Fatigue in Air						
S7B	80	47.2	34,652	9.63	0.552	-
S10B	80	50.6	200,000*	55.56	0.558	111.5
S11E	100	56.6	168,255	46.74	0.382	-
Fatigue in Steam						
S11A	60	54.7	194,930	54.15	0.683	-
S11D	70	57	65,154	18.10	0.283	-
S10E	70	51.8	126,593	35.16	0.391	-
S8E	80	49.7	46,621	12.95	0.404	-
S10A	80	47.6	73,084	20.30	0.422	-
S11C	100	54.5	17,587	4.89	0.232	-

The degradation in fatigue life due to the presence of steam is immediately noticeable. The results in Table 8 are consistent with those reported by other researchers [32:7, 5:27, 6:54, 31]. The fatigue limit in steam is less than 60 MPa, while the fatigue limit in air was 80 MPa. The reduction in cyclic life due to steam was 90% in the 100 MPa fatigue test and at least 64% in the 80 MPa fatigue test. Figure 17 compares stress vs. cycles to failure (S-N) curves obtained at 1000 °C in air and in steam. The negative effect of steam on the fatigue life of the material is evident.

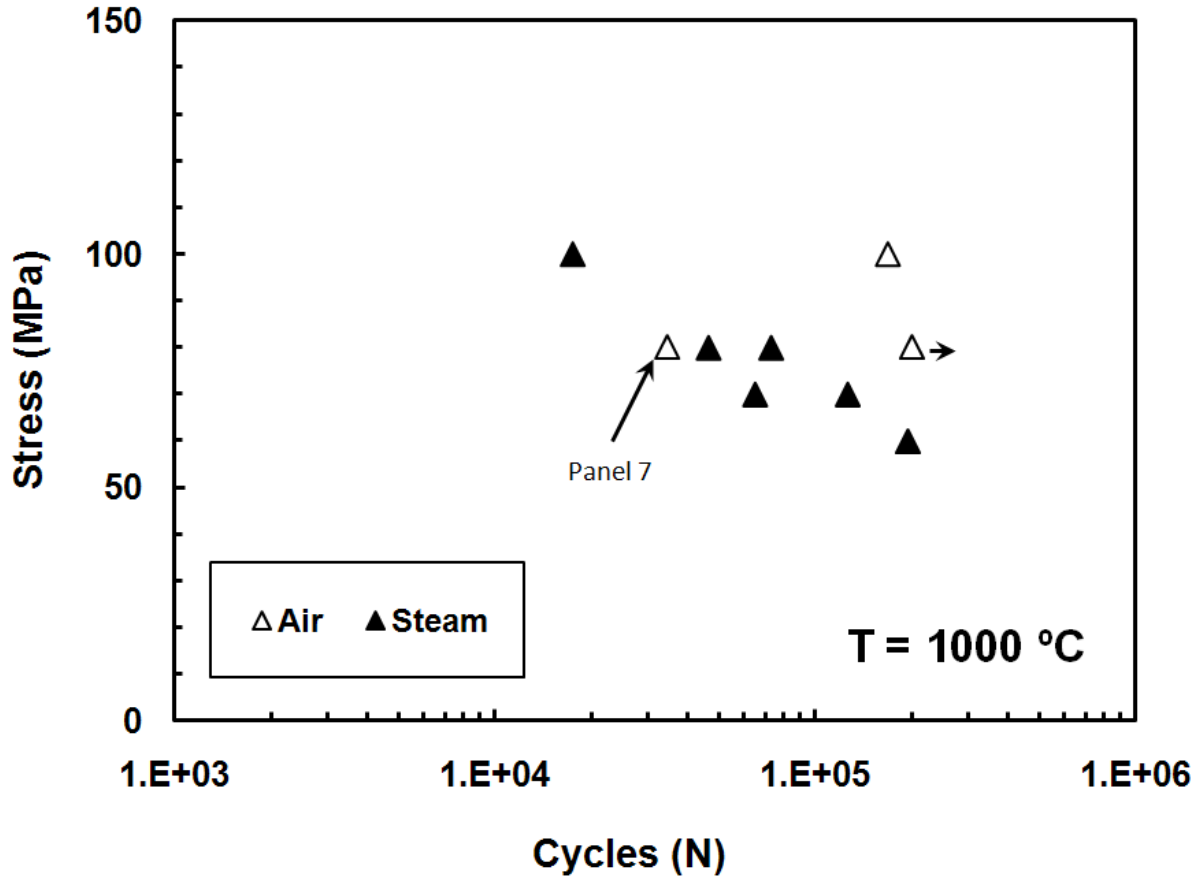

Figure 17: Fatigue S-N curves for CG NICALON™/BN/SiC composite at 1000 °C in air and in steam. Arrow indicates that failure of specimen did not occur when the test was terminated.

The stress vs. cycles to failure (S-N) curves are presented again in Figure 18, where the maximum cyclic stresses are normalized by the UTS of the particular composite panel in order to reduce data scatter. As expected, the correlation remains and fatigue life decreases with increasing stress. The presence of steam degrades fatigue resistance.

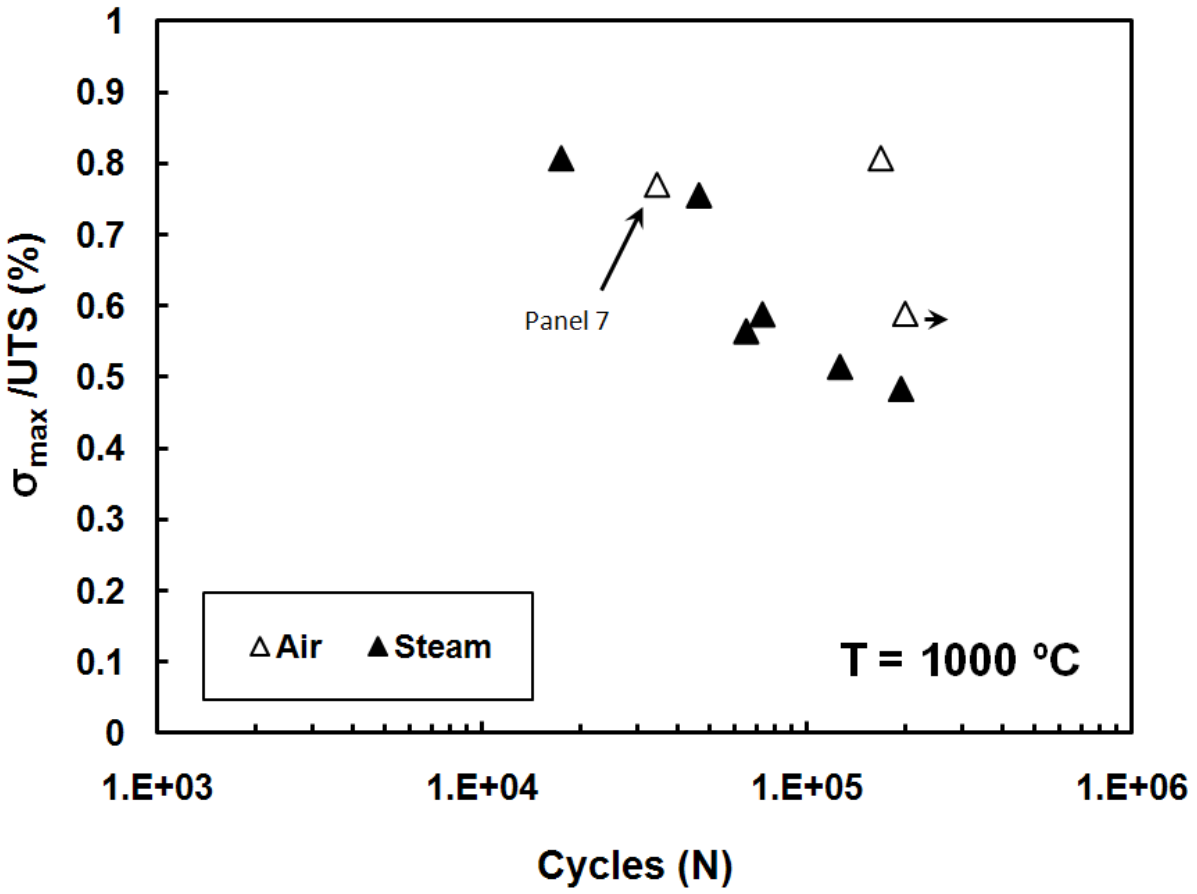

Figure 18: Normalized maximum stress vs. cycles to failure for CG NICALON™/BN/SiC composite at 1000 °C in air and in steam.

As was the case at 1000 °C in air, there is little change in normalized modulus with fatigue cycles at 1000 °C in steam (see Figure 19). The 60 MPa and 70 MPa tests performed in steam represent an exception. In the case of these tests, the normalized modulus remained approximately 1.0 during the test, but dropped significantly just prior to fracture. Specimen S11A, tested with the maximum stress of 60 MPa, failed after 194,930 cycles and showed a modulus loss of nearly 23%. Specimen S10E, tested with the maximum stress of 70 MPa, failed after 126,593 cycles and showed a modulus loss of 21%.

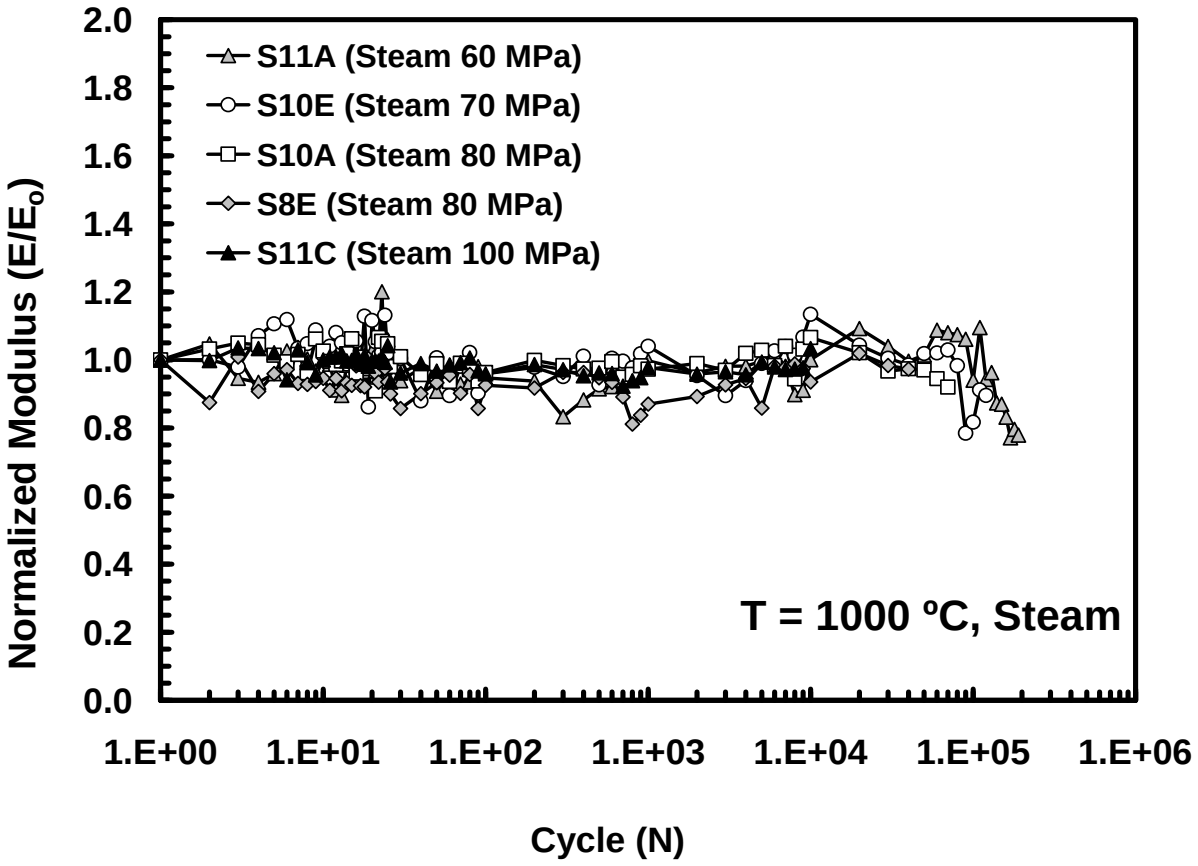

Figure 19: Normalized modulus vs. fatigue cycles at 1000 °C in steam

A considerably greater amount of strain was accumulated during fatigue tests conducted at 1000 °C in steam than during similar tests performed in air (see Figure 20). Larger strains were accumulated in tests conducted with lower maximum stresses. At 1000 °C in steam, the largest amount of strain (0.68%) was accumulated in the 60 MPa test, and the lowest amount of strain (0.23%) was accumulated in the 100 MPa test. Typically lower strain accumulation with fatigue cycles suggests that less damage has occurred. However, in this case low strain accumulations are more likely due to early bundle failures leading to specimen failure.

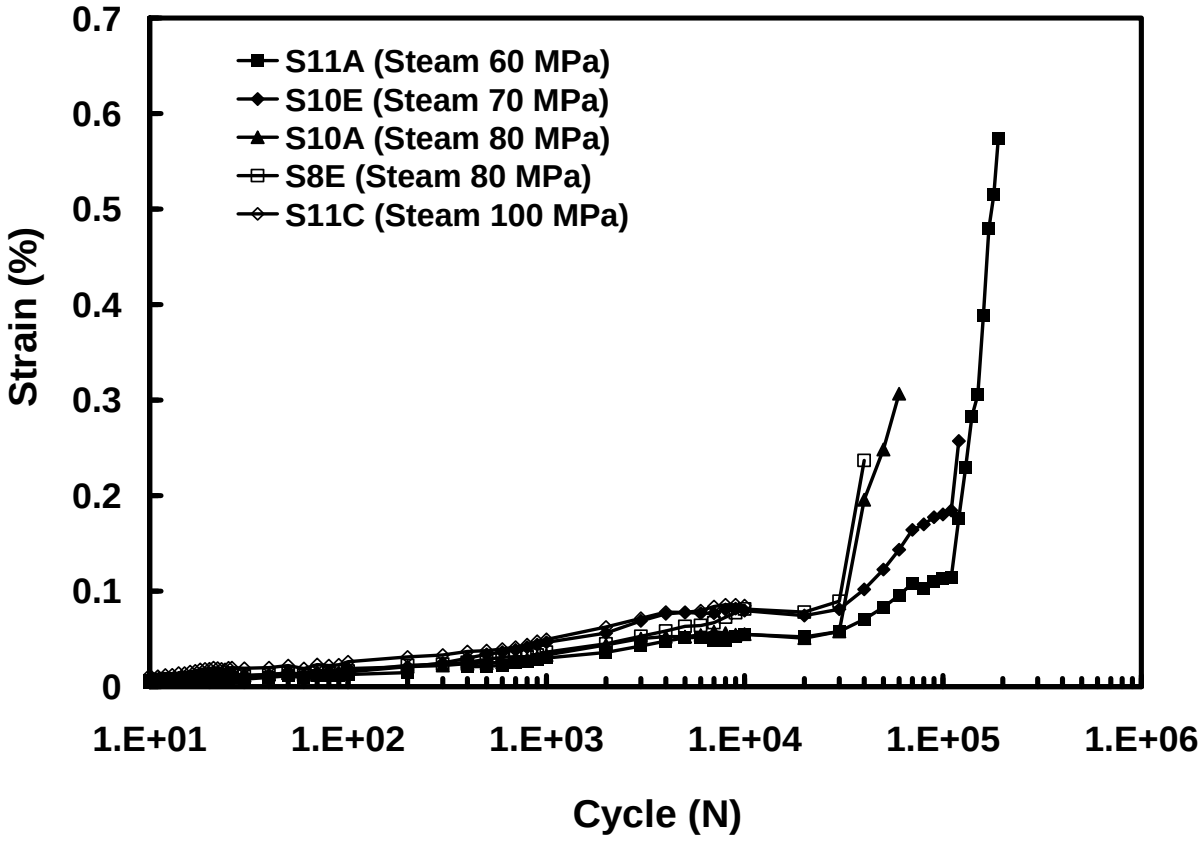

Figure 20: Strain accumulation vs. fatigue cycles at 1000 °C in steam

Evolution of the hysteresis response with fatigue cycles at 1000 °C in steam is typified in Figures 21 and 22. Results obtained for specimen S11A tested with the maximum stress of 60 MPa are shown in Figure 21, and results obtained for specimen S11C tested with the maximum stress of 100 MPa are presented in Figure 22. The hysteresis stress-strain loops in Figures 21 and 22 reveal that ratcheting takes places continuously throughout the test. Furthermore, the hysteretic modulus appears to change little with fatigue cycling. It is apparent that the material exhibits little to no cyclic softening or hardening, which further supports the notion that the realignment of the transverse fiber bundles and stretching of the weave were responsible for much of the strain accumulation.

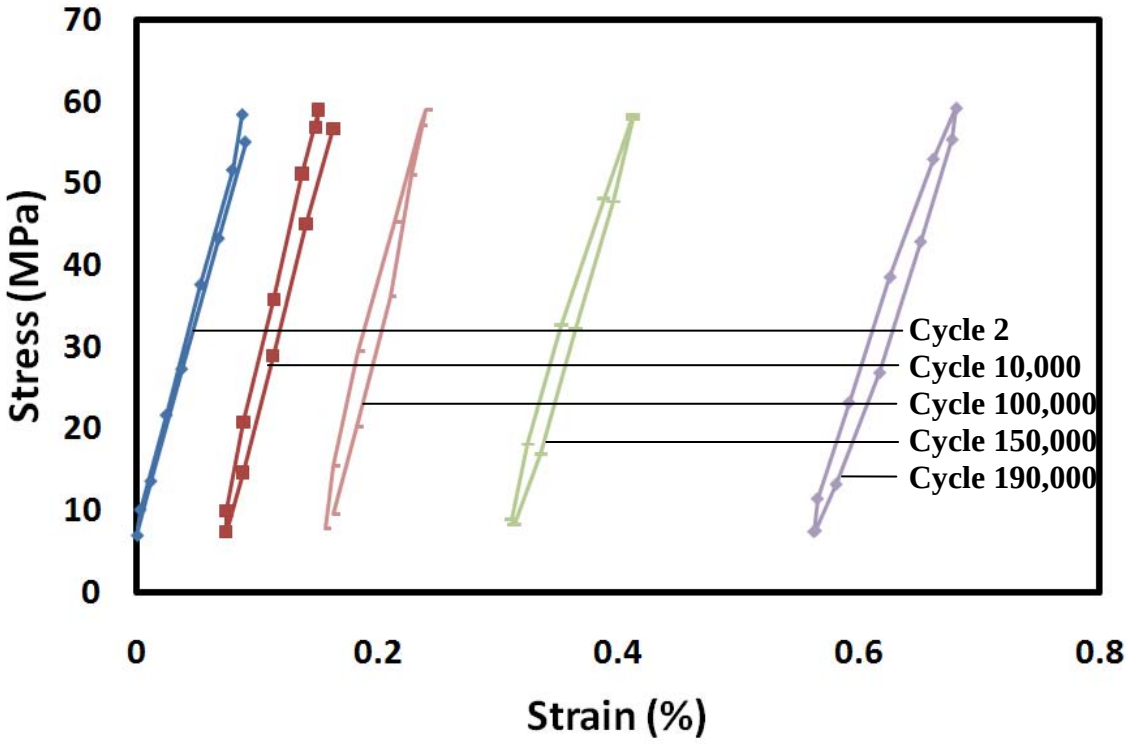

Figure 21: Evolution of stress-strain hysteresis response with fatigue cycles at 1000 °C in steam (Specimen S11A, σ_{max} = 60 MPa).

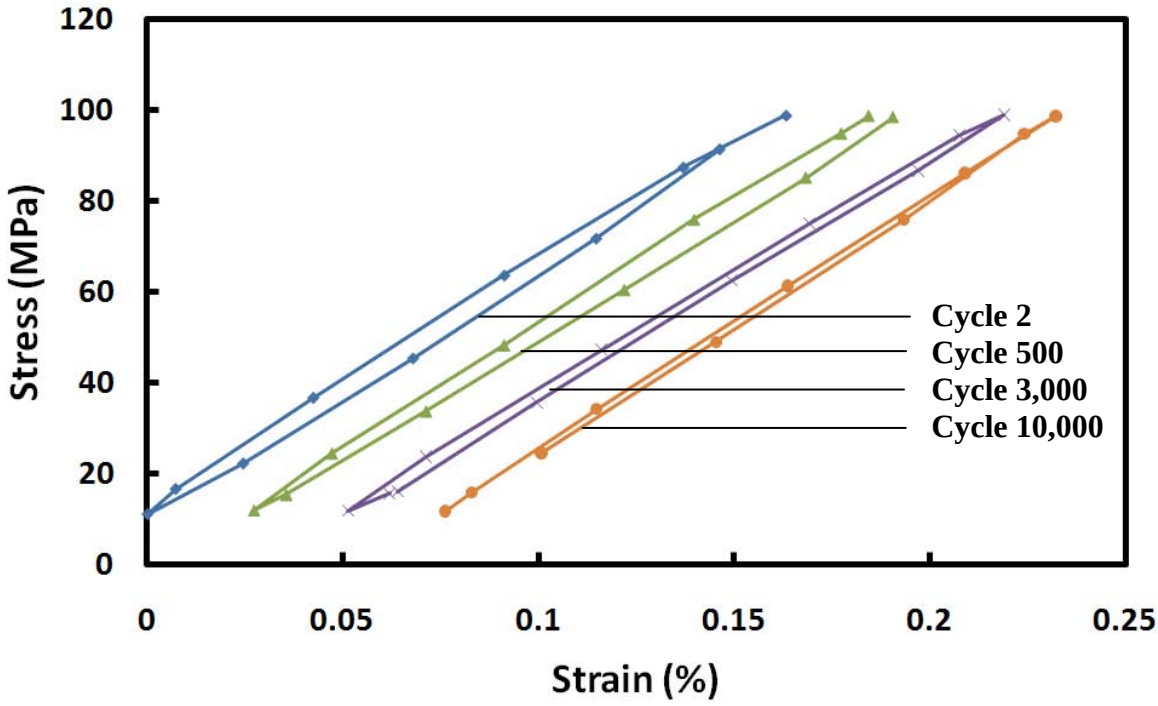

Figure 22: Evolution of stress-strain hysteresis response with fatigue cycles at 1000 °C in steam (Specimen S11C, σ_{max} = 100 MPa).

Evolution of the maximum and minimum strains with fatigue cycles at 1000 °C in steam is typified in Figures 23 and 24. Results obtained for specimen S11A tested with the maximum stress of 60 MPa are shown in Figure 23, and results obtained for specimen S10A tested with the maximum stress of 80 MPa are presented in Figure 24. It is noteworthy that although the strains continue to increase, each pair of curves in Figures 23 and 24 remains parallel throughout the test. These results suggest that there is little change in the stiffness of the composite. The material neither hardens nor softens during fatigue cycling as indicated by the plots in Figures 23 and 24, and also by the normalized modulus vs. fatigue cycles plot in Figure 19.

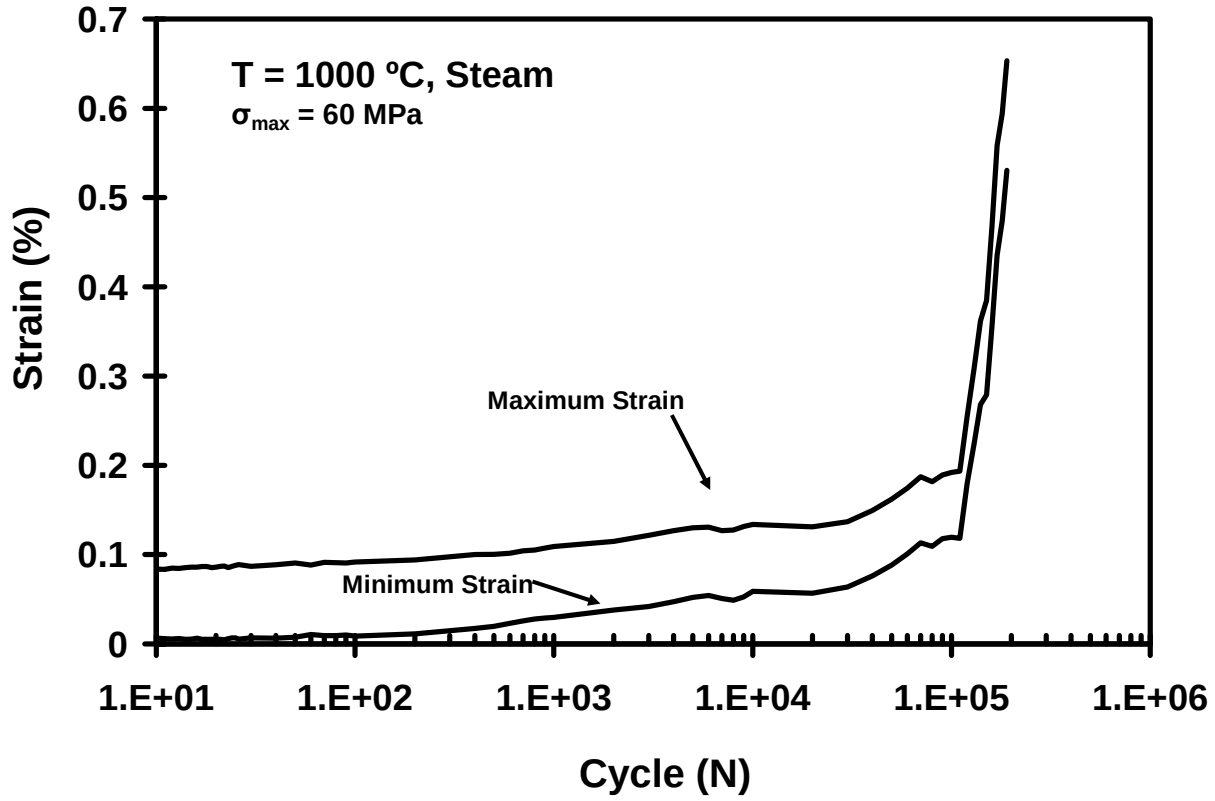

Figure 23: Maximum and minimum strains vs. fatigue cycles for specimen S11A at 1000 °C in steam (f = 1.0 Hz, σ_{max} = 60 MPa).

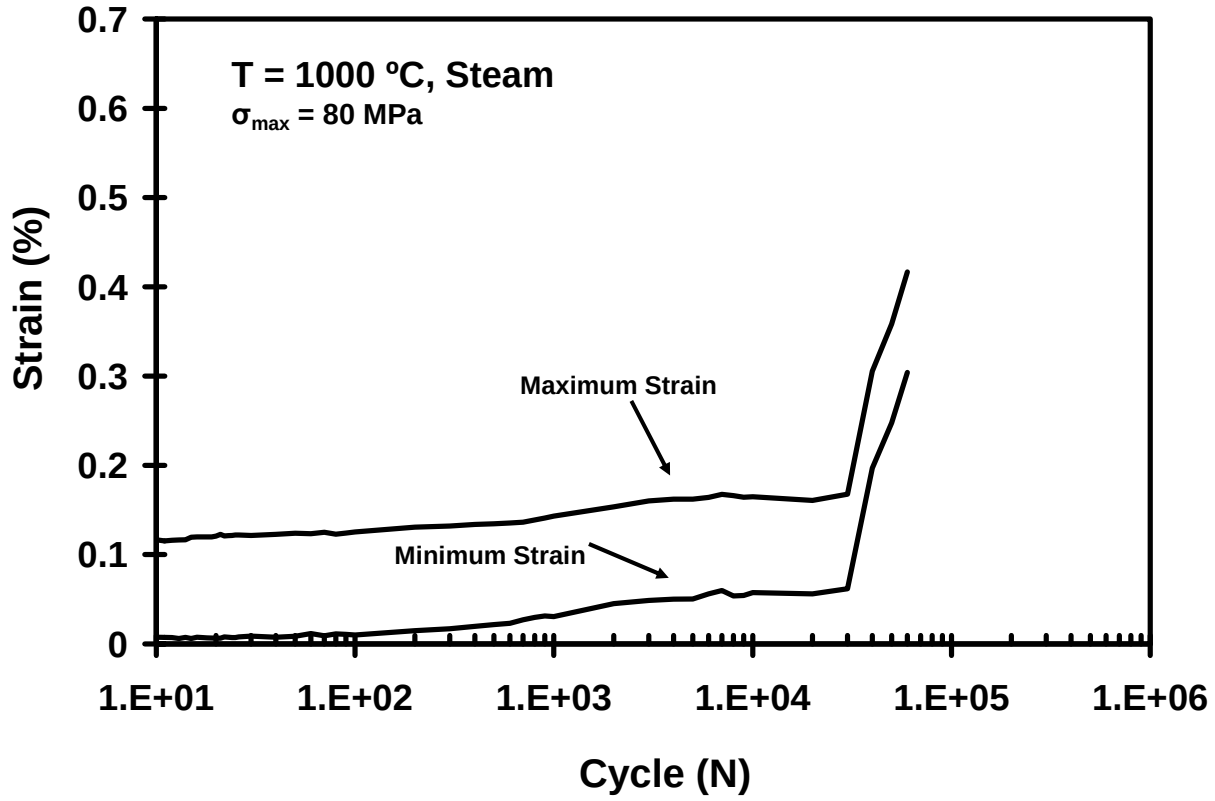

Figure 24: Maximum and minimum strains vs. fatigue cycles for specimen S10A at 1000 °C in steam (f = 1.0 Hz, σ_{max} = 80 MPa).

One of the most remarkable features of the specimens tested in steam is through-thickness swelling of the test section. Note that this effect was not observed for specimens tested in air. Figure 25 shows specimen S11A subjected to the 60 MPa test at 1000 °C in steam, which failed after 194,930 cycles. The dotted line marks the initial thickness of the specimen, making through-thickness swelling caused by testing at 1000 °C in steam readily apparent. A specimen tested in fatigue at 1000 °C in air is shown nearby for comparison. Note that the specimen tested in air exhibits no through-thickness swelling. Additionally, specimens tested in steam and air exhibited very little change in width (see Figure 26).

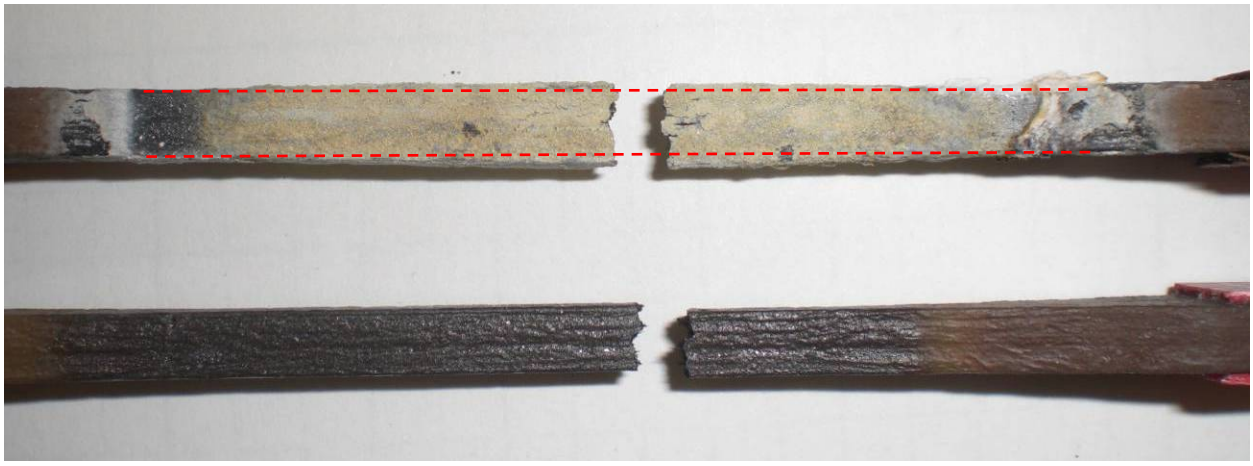

Figure 25: Side view of the specimens tested in fatigue at 1000 °C in steam (top) and in air (bottom). Through-thickness swelling of the specimen tested in steam is evident.

Figure 26: Front view of specimens tested in fatigue at 1000 °C in steam (top) and in air (bottom) showing no swelling regardless of test environment.

To quantify the changes in the specimen test section due to testing at 1000 °C in steam, the initial and final width and thickness of the test specimens are given in Table 9 together with the initial

and final cross-sectional area measurements. Generally, the cross-sectional area increased with time spent in the steam environment. The largest increase in the cross-sectional area (approximately 30%) was observed for the specimen S11A, which also spent the greatest amount of time in steam (54.2 h).

Table 9: Summary of initial and final width, thickness, and cross-sectional area for CG NICALON™/BN/SiC specimens subjected to monotonic and fatigue tests at 1000 °C in air and in steam

Specimen	Initial Width (mm)	Initial Thickness (mm)	Initial Cross Sectional Area (mm^2)	Top/ Bottom	Final Width (mm)	Final Depth (mm)	Final Cross Sectional Area (mm^2)	Change in Cross Sectional Area (%)
Tension Tests								
S5A	3.51	4.74	16.60	T	3.51	4.76	16.69	0.54
				B	3.45	4.81	16.63	0.14
S7C	3.42	5.08	17.35	T	3.59	5.00	17.98	3.63
				B	3.54	5.04	17.86	2.94
S8D	3.37	4.90	16.50	T	3.38	4.97	16.78	1.68
				B	3.37	4.91	16.54	0.26
S9A	3.34	4.94	16.50	T	3.44	4.99	17.18	4.10
				B	3.51	5.00	17.54	6.29
S10D	3.34	4.99	16.67	T	3.40	4.95	16.86	1.12
				B	3.35	4.95	16.61	-0.39
S11B	3.38	4.93	16.65	T	3.38	4.89	16.52	-0.77
				B	3.35	4.97	16.65	0.02
Fatigue in Air								
S7B	3.51	5.33	18.70	T	Failure outside TS			N/A
				B	Failure outside TS			N/A
S10B	3.37	5.08	17.10	T	3.48	5.05	17.59	2.88
				B	3.38	5.03	16.99	-0.63
S11E	3.49	5.07	17.70	T	3.47	5.04	17.48	-1.22
Fatigue in Steam								
				B	3.43	5.14	17.64	-0.34
S11A	3.44	4.84	16.65	T	3.57	6.12	21.85	31.18
				B	3.53	6.11	21.57	29.51
S11D	3.34	4.97	16.59	T	3.52	5.66	19.93	20.14
				B	3.39	5.61	19.03	14.76
S10E	3.37	5.04	16.97	T	3.51	6.06	21.23	25.14
				B	3.47	5.98	20.74	22.22
S8E	3.37	4.86	16.37	T	3.40	5.38	18.33	11.96
				B	3.39	5.17	17.53	7.07
S10A	3.39	5.04	17.10	T	3.39	5.80	19.68	15.11
				B	3.43	5.85	20.08	17.43
S11C	3.43	5.00	17.16	T	3.29	4.95	16.29	-5.05
				B	3.31	4.93	16.33	-4.81

Figure 27 shows that at 1000 °C in steam the specimen cross sectional area increases with fatigue cycles. It appears that fatigue cycling in steam is causing delamination between the plies of the composite near the fracture location.

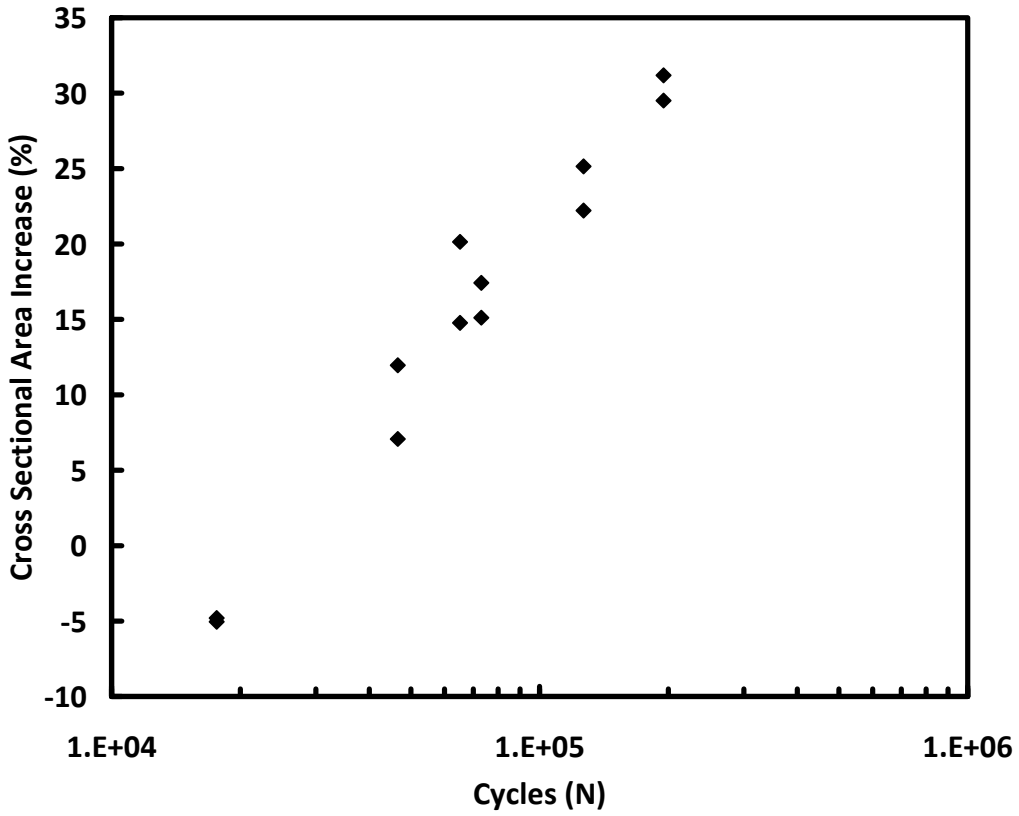

Figure 27: Change in cross sectional area of CG NICALON™/BN/SiC specimens with fatigue cycles at 1000 °C in steam

5.7 Microstructural Characterization of the As-Processed CG NICALON™/BN/SiC Composite

Cross sections of material from all six panels were cut perpendicular to the fiber direction, mounted in phenolic pucks and polished according to the method described in Section 4.3 to be

examined under the Scanning Electron Microscope (SEM). All six panels exhibited the same general features including poor polishing characteristics, no obvious layering of the CVI coatings, large voids, slight differences in fiber diameter and a heterogeneous matrix when observed at high magnification. Additionally all panels also showed an abundance of microcracks within the matrix.

Many iterations were performed in determining the highest quality polishing process with mediocre results at best. However, if a matrix is very weak or sparse and does not have hardness similar to that of the fibers the polishing process becomes very difficult [8]. Therefore it can be inferred that the matrix of this NICALON™/BN/SiC composite was comparatively weak. This conclusion corresponds very well with the tensile stress-strain curves with no obvious proportional limit, which also suggested a weak matrix. Figure 28 shows fiber and matrix degradation due to polishing, illustrating the low strength of the matrix.

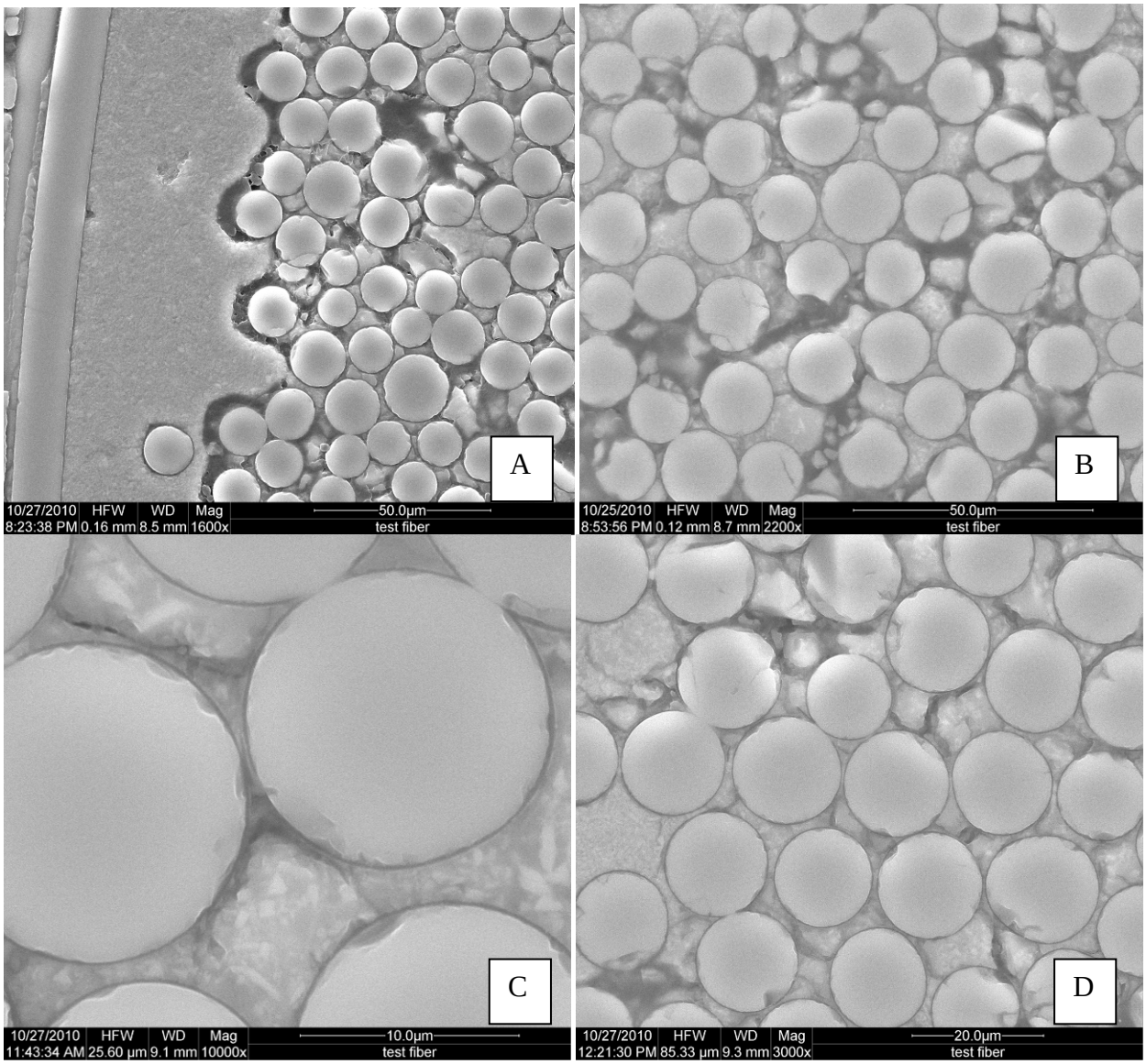

Figure 28: SEM micrographs of the as-processed CG NICALON™/BN/SiC composite showing fiber and matrix degradation due to low matrix strength in: (A) panel 5, (B) panel 8, (C) panel 9 and (D) panel 10, with panel 10 showing the least degradation.

As mentioned earlier, boron nitride (BN) is a soft, dry lubricant and as such when undergoing polishing may cleave away from the surface leaving an empty concentric circle around each fiber. This phenomenon has been observed in similar composites utilizing a BN/SiC

interphase [5:46] and is apparent in the composite studied in this research. The gaps left by the BN CVI fiber coating, which appear as black rings around each fiber in Figure 29, are consistent with the 150-210 nm thickness of the fiber coating reported by the composite manufacturer.

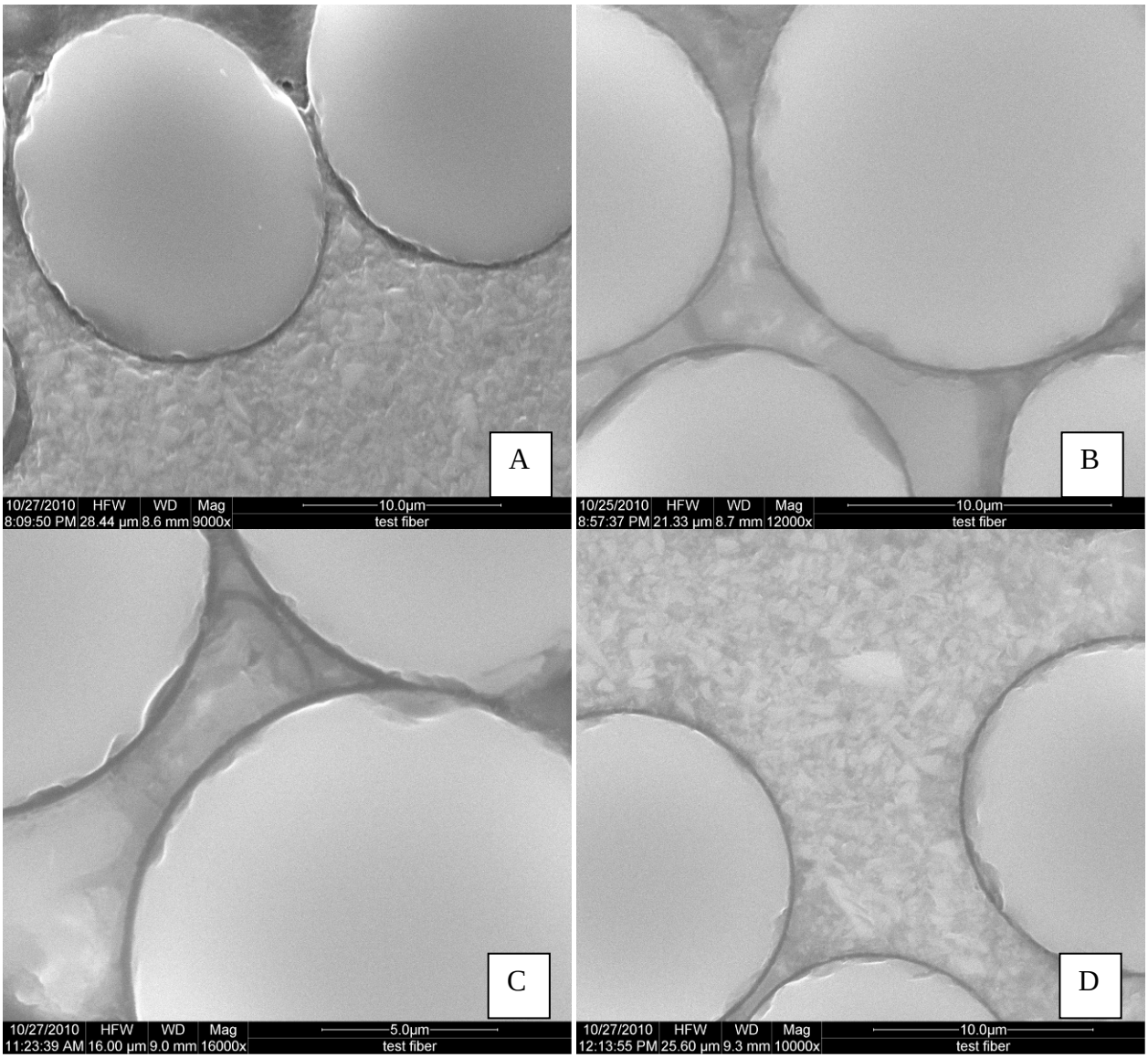

Figure 29: SEM micrographs of the as-processed CG NICALON™/BN/SiC composite showing absence of BN fiber coating in: (A) panel 5, (B) panel 8, (C) panel 9 and (D) panel 10.

Large voids are apparent throughout the composite, putting into question the effectiveness of the modified PIP process used to manufacture this CMC and offering possible reasons for its poor mechanical performance. Additionally, when comparing randomly chosen views in Figure 30 it is seen that the "weaker" panels generally have more voids. For example, panel 7 (Figure 30A) has considerably more voids than panel 10 (Figure 30D). Panel 7 exhibited comparatively low UTS, while panel 10 had the highest UTS. Therefore, it is reasonable to conclude that as the matrix density increases so does the tensile strength of the composite. Figure 30 illustrates the occurrences of voids in different panels. Note the darker areas, which are residue from the phenolic used in mounting the composite; voids appear as actual holes in the CMC.

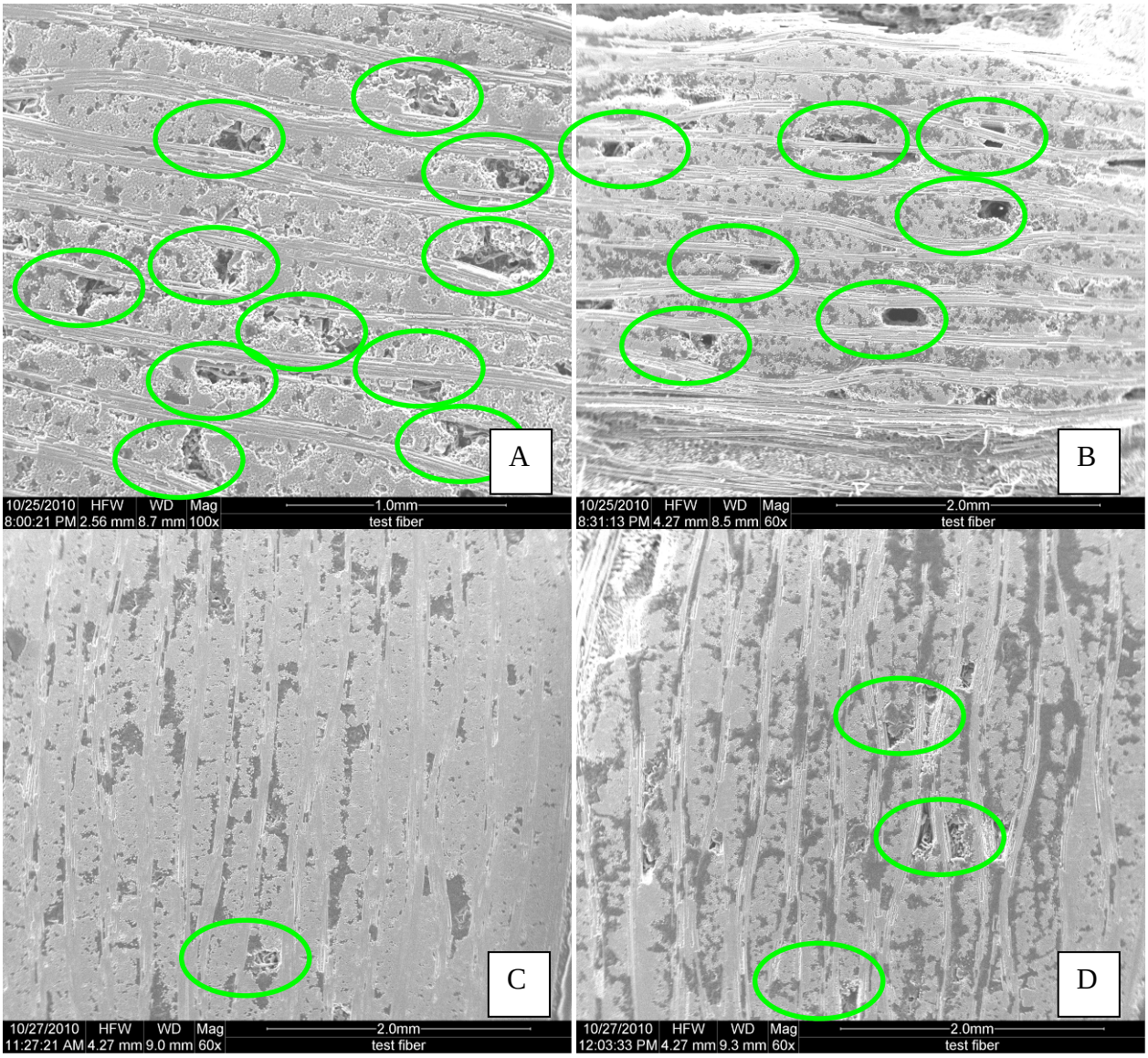

Figure 30: SEM micrographs of the as-processed CG NICALON™/BN/SiC composite showing voids in: (A) panel 7, (B) panel 8, (C) panel 9 and (D) panel 10.

CG NICALON™ fibers have a reported average diameter of 14 μm [28:2] which Figure 31 confirms, although there is variability in diameter between fibers. This variability in diameter is relatively small and can be neglected. Interestingly, the same high magnification micrographs in Figure 31 show 2-μm SiC particles densifying the matrix. The SiC powder appears to have mixed

well with the matrix but due to the large voids present throughout the composite this method may have only helped to densify the matrix in the tight spaces between the fibers while not producing equally good results in the areas with large initial voids before the PIP process began. The SiC powder was introduced in order to develop a process that required fewer infiltration cycles. However, the micrographs of the as-processed composite suggest that this goal was not met.

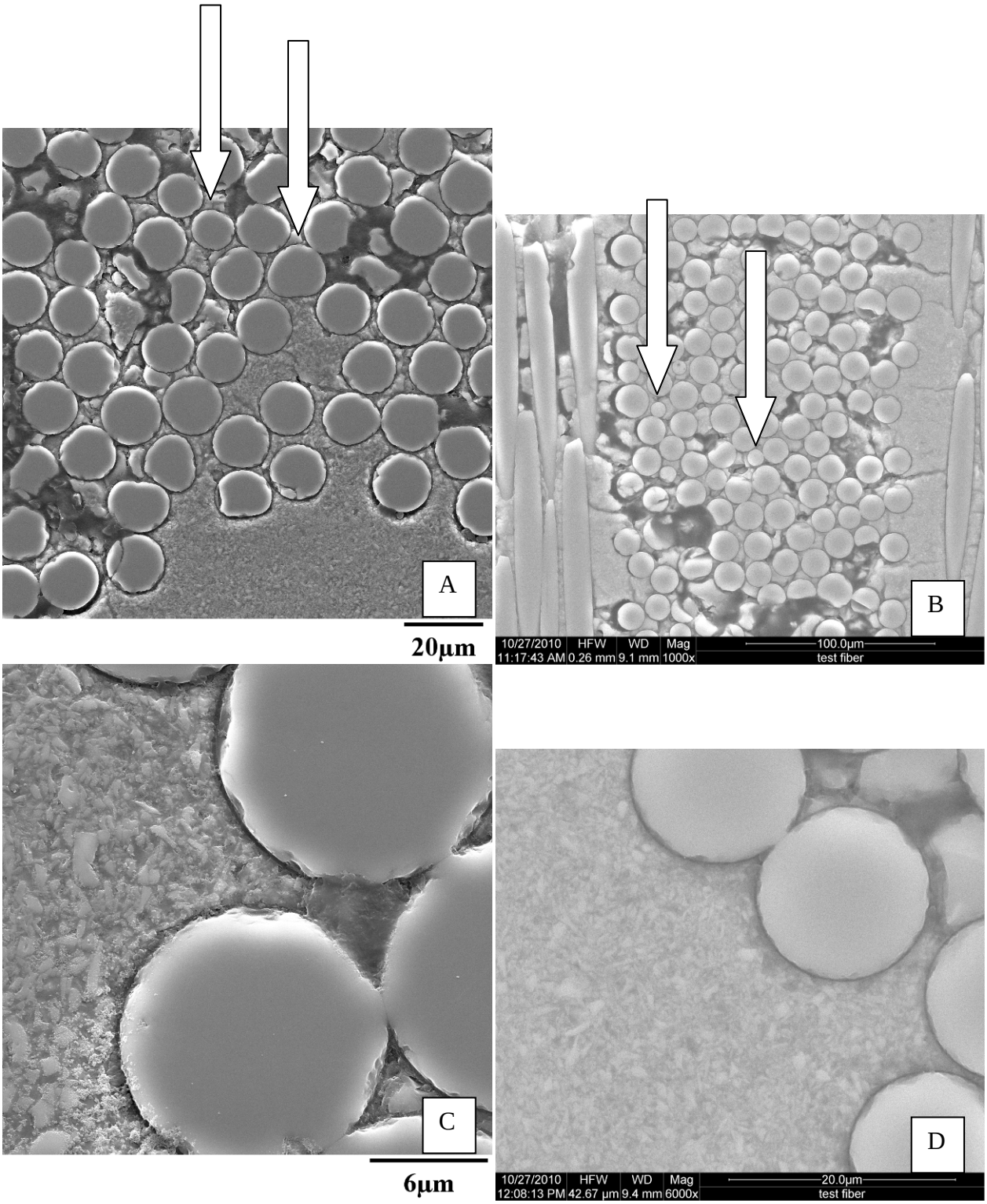

Figure 31: SEM micrographs of the as-processed CG NICALON™/BN/SiC composite showing non-uniform CG NICALON™ fibers in: (A) panel 5, (B) panel 9 and SiC particles in: (C) panel 5 and (D) panel 10.

As discussed earlier, the PIP process causes crystallization and shrinkage during the pyrolysis steps resulting in many microcracks, which are apparent in the matrix of the as-processed material shown in Figure 32.

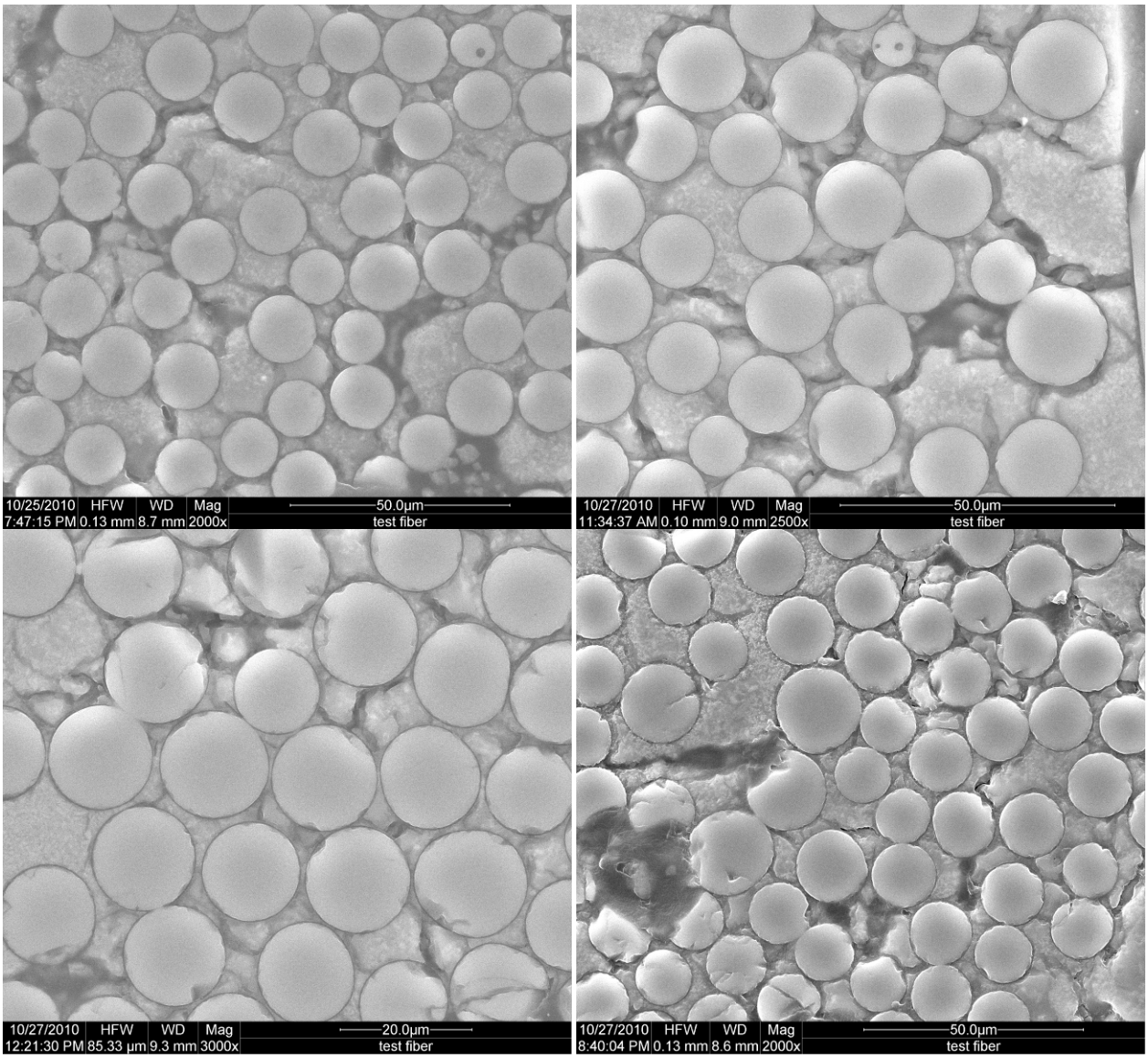

Figure 32: SEM micrographs of the as-processed CG NICALON™/BN/SiC composite showing abundant matrix microcracks in: (A) panel 7, (B) panel 9, (C) panel 10 and (D) panel 11.

5.8 Microstructural Characterization of CG NICALON™/BN/SiC Specimens Tested in Tension to Failure at 1000 °C in Air

One specimen from each panel was subjected to a monotonic tension test at 1000 °C in air. Presented in this section are optical micrographs, scanning electron micrographs of the fracture surfaces, and scanning electron micrographs of polished samples cut perpendicular to the loading direction. Specimens generally displayed a nearly flat fracture surface demonstrating coupled failure between the plies and therefore no delamination [13:1049].

Specimen S5A, which exhibited the lowest UTS, produced a rather jagged fracture surface with some fiber pullout as seen in the optical micrographs in Figure 33. A composite image in Figure 34 shows an appreciable amount of fiber pullout with no obvious signs of oxidation. Entire tows can be seen pulling out of the fracture surface in Figure 34. Fiber pullout can also be seen in higher magnification SEM micrographs in Figures 35 A and B. Figure 35 C shows an area of brittle fracture evidenced by coordinated fiber failure. Figure 35 D shows matrix cracking around fibers, suggesting that the matrix was weak.

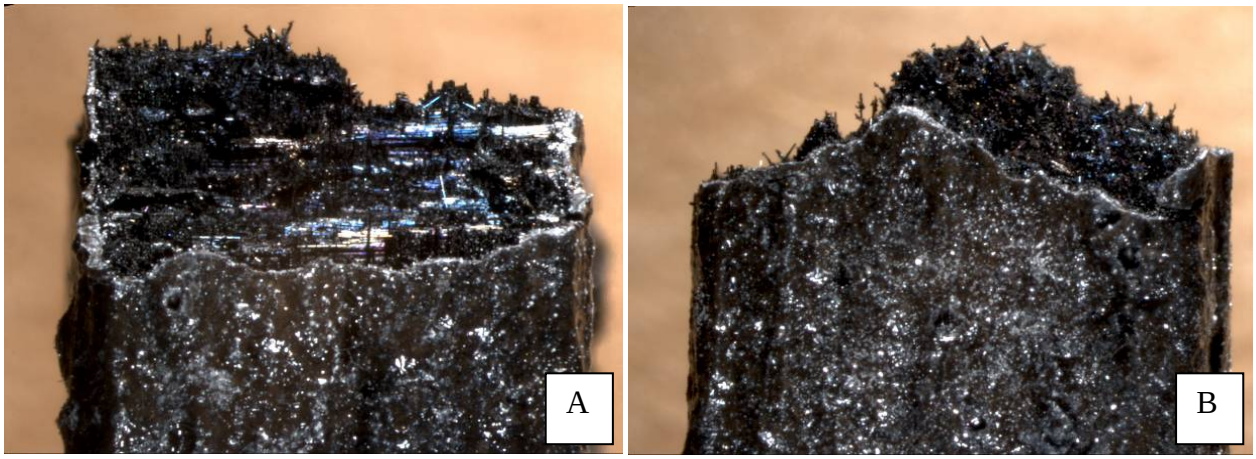

Figure 33: Optical micrographs of specimen S5A, front (A) and side (B), subjected to tensile test to failure at 1000 °C in air. Fracture surface normal to the applied load. (UTS = 98.6 MPa, E = 42.2 GPa).

Figure 34: Optical micrographs of specimen S5A, front (A) and side (B), subjected to tensile test to failure at 1000 °C in air. Fracture surface normal to the applied load. (UTS = 98.6 MPa, E = 42.2 GPa).

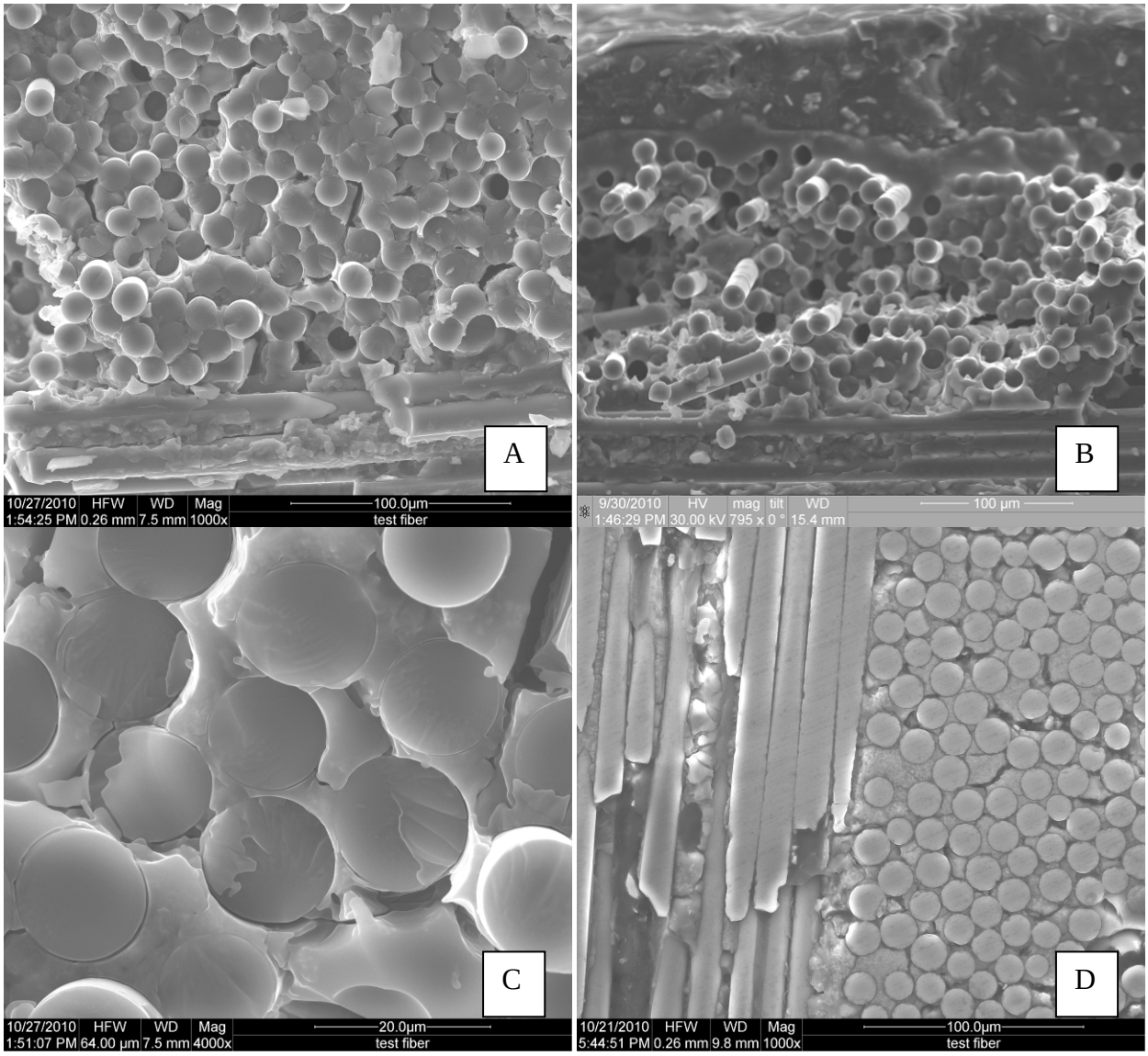

Figure 35: SEM micrographs of specimen S5A subjected to tensile test to failure at 1000 °C. Fracture surface normal to the applied load.

Optical micrographs of specimen S7C in Figure 36 show a relatively flat fracture surface with some localized areas of relatively long fiber pullout. The SEM micrograph in Figure 37 displays a considerable number of large voids as well as small areas of fiber pullout. Higher

magnification views of fiber pullout are also seen in Figures 38 A and B. Figures 38 C and D offer a rare view of interphase left on the fiber. The cleaving of the BN interphase is evident. The micrographs in Figures 38 C and D show an approximately 200 nm interphase coating, within the nominal 150-210 nm coating reported by the CMC manufacturer.

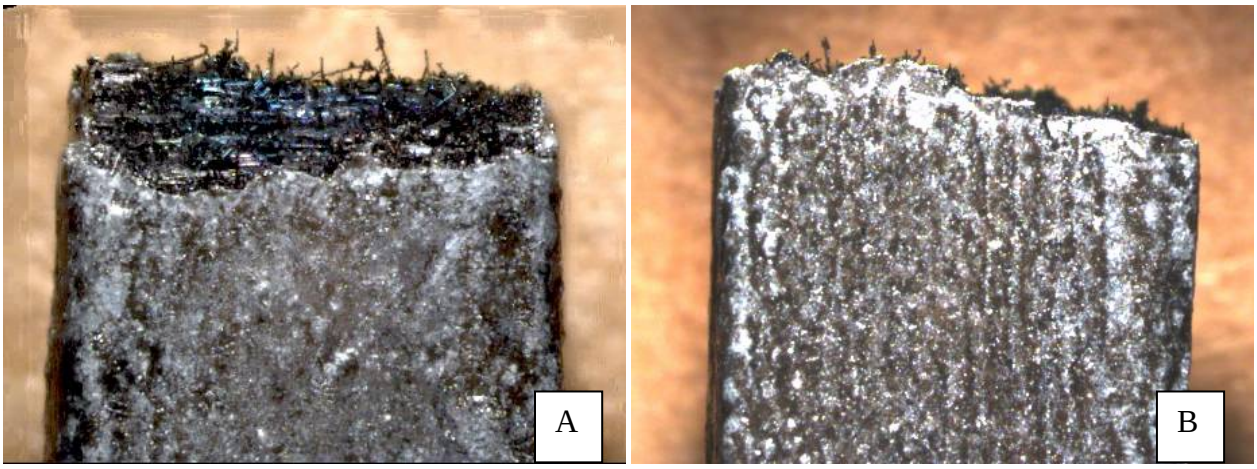

Figure 36: Optical micrographs of specimen S7C, front (A) and side (B), subjected to tensile test to failure at 1000 °C in air. Fracture surface normal to the applied load. (UTS = 104 MPa, E = 49.1 GPa).

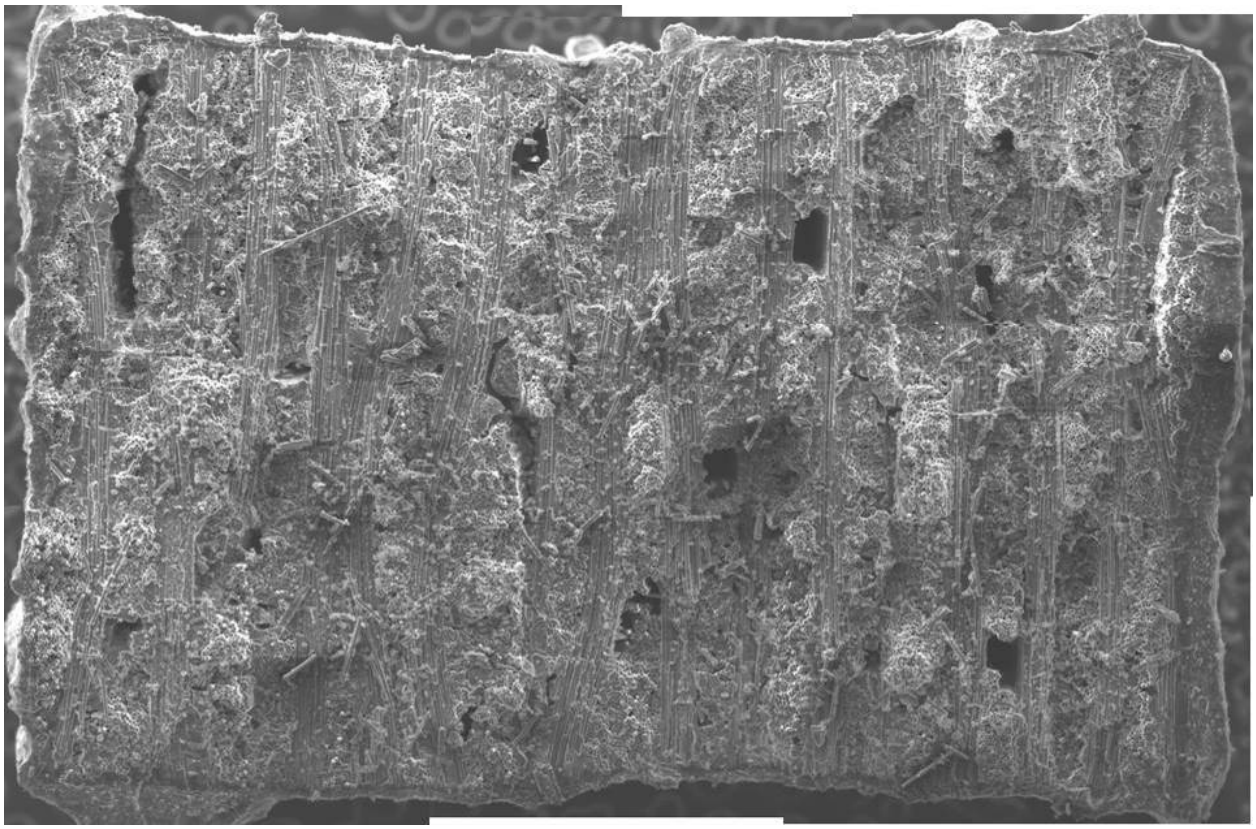

Figure 37: SEM composite micrograph of specimen S7C produced in a tensile test to failure at 1000 °C. Fracture surface normal to the applied load.

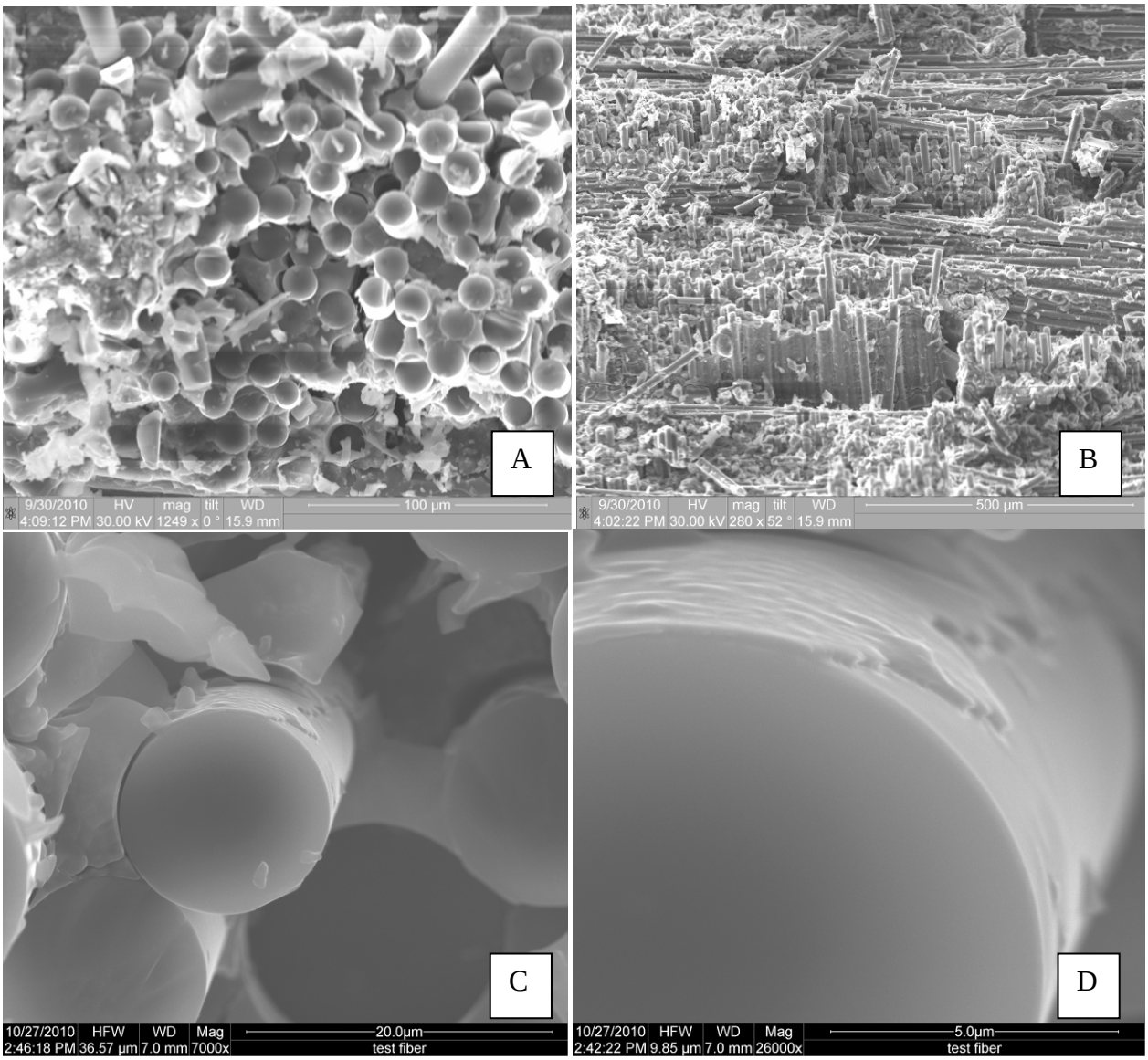

Figure 38: SEM micrographs of specimen S7C subjected to tensile test to failure at 1000 °C. Fracture surface normal to the applied load.

Optical micrographs of specimen S8D in Figure 39 show a flat fracture surface with some areas of relatively long fiber pullout. An abundance of large voids and some small areas of fiber pullout are seen in the composite image in Figure 40. A higher magnification view of fiber pullout

as well as an instance of an unusually small CG NICALON™ fiber are seen in Figure 41 A. An additional illustration of fiber pullout is given in Figure 41 B.

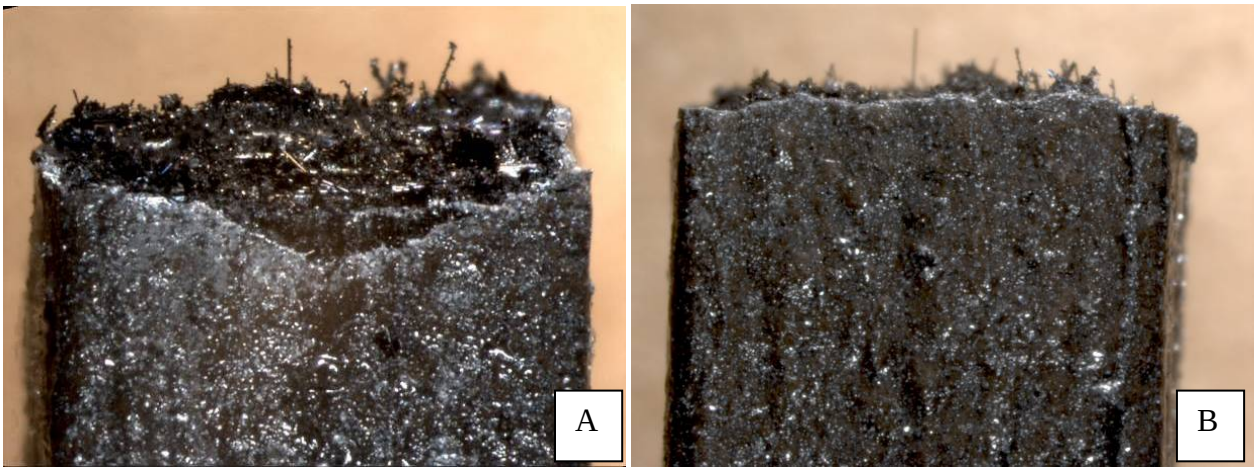

Figure 39: Optical micrographs of specimen S8D, front (A) and side (B), subjected to tensile test to failure at 1000 °C in air. Fracture surface normal to the applied load. (UTS = 106 MPa, E = 50.3 GPa).

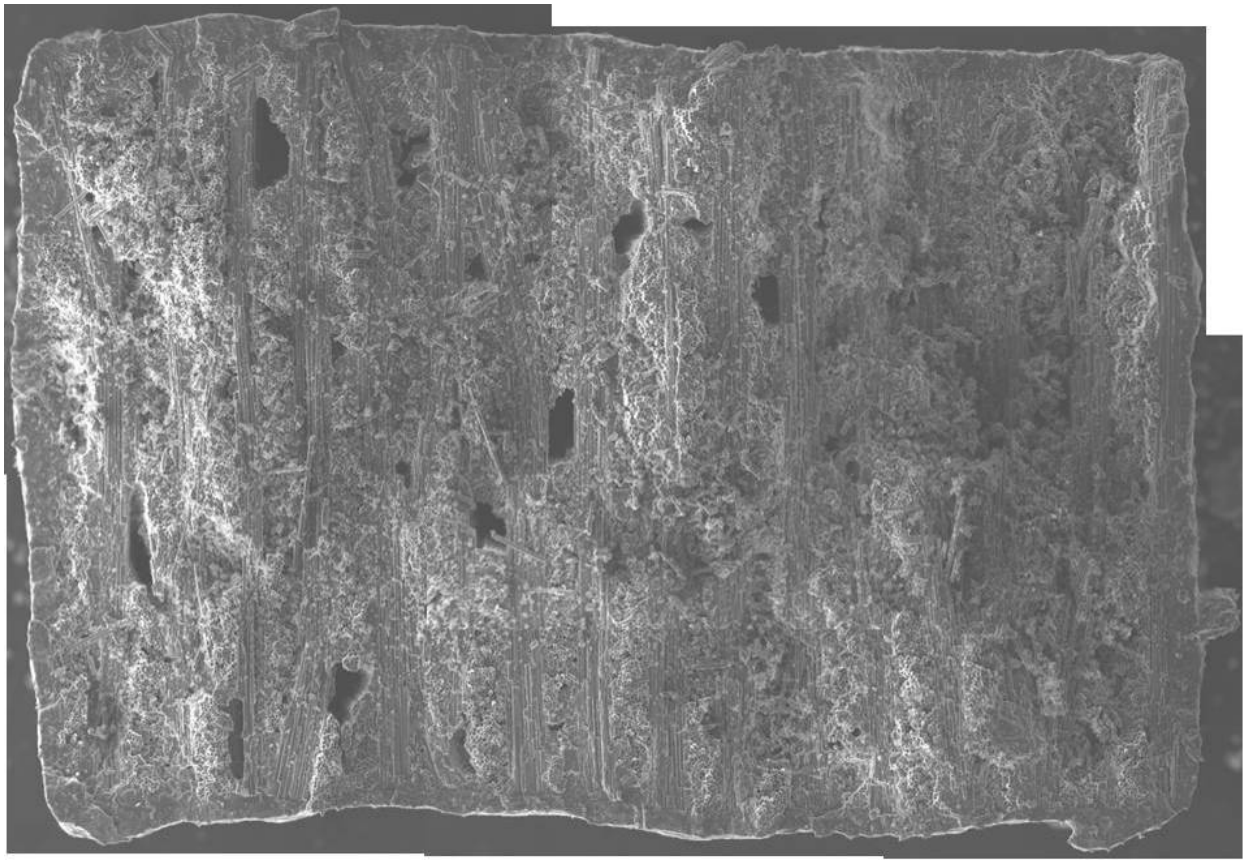

Figure 40: SEM composite micrograph of specimen S8D produced in a tensile test to failure at 1000 °C. Fracture surface normal to the applied load.

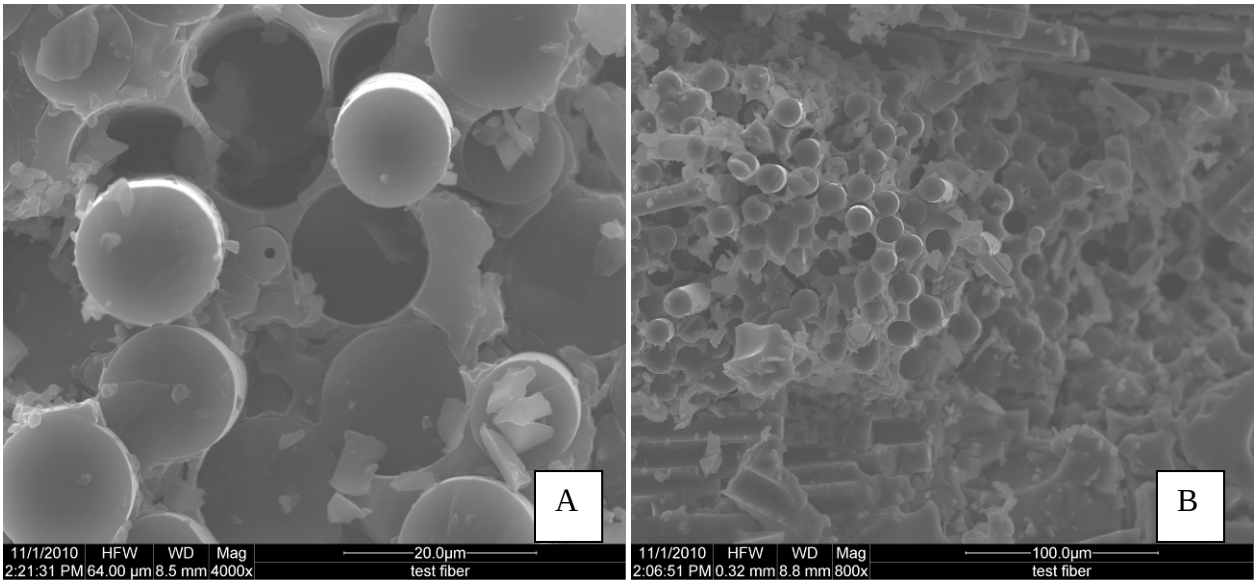

Figure 41: SEM micrographs of specimen S8D subjected to tensile test to failure at 1000 °C. Fracture surface normal to the applied load.

Optical micrographs of specimen S9A in Figure 42 show an irregular fracture surface with some instances of relatively long fiber pullout. Figure 43 shows considerably fewer voids than were seen in previous specimens while still showing considerable fiber pullout. Figure 44 A clearly shows the thin BN ring around each fiber. Figure 44 B shows some fiber pullout and most notably crack deflection, again showing a desirable relatively weak fiber-matrix interface.

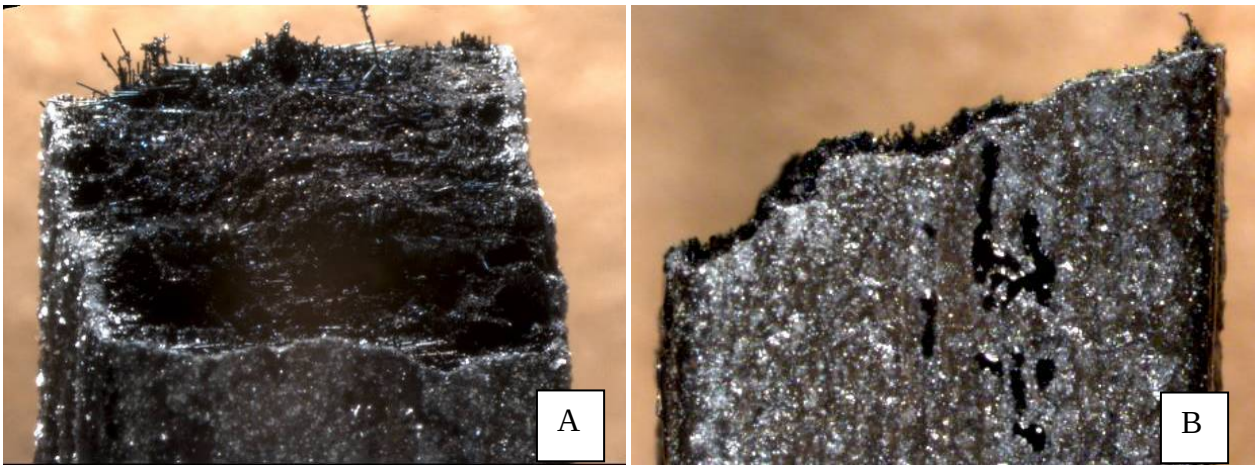

Figure 42: Optical micrographs of specimen S9A, front (A) and side (B), subjected to tensile test to failure at 1000 °C in air. Fracture surface normal to the applied load. (UTS = 114 MPa, E = 48.4 GPa).

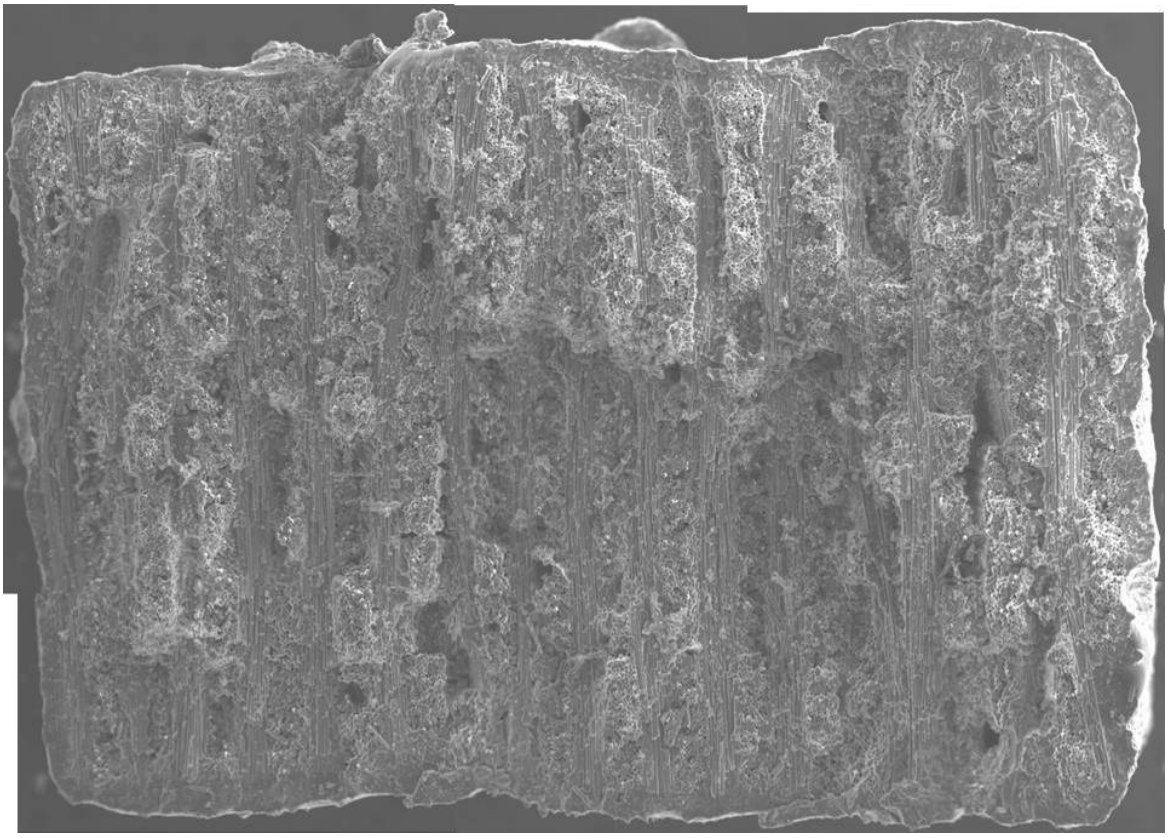

Figure 43: SEM composite micrograph of specimen S9A produced in a tensile test to failure at 1000 °C. Fracture surface normal to the applied load.

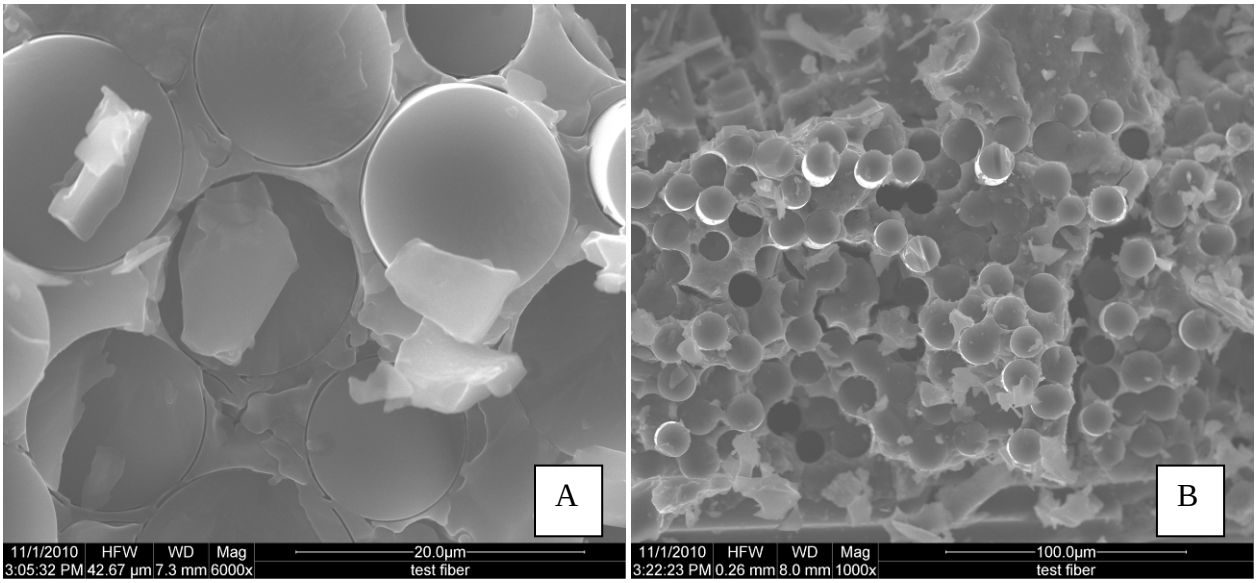

Figure 44: SEM micrographs of specimen S9A subjected to tensile test to failure at 1000 °C. Fracture surface normal to the applied load.

Optical micrographs of specimen S10D, from the panel with the highest UTS, are seen in Figure 45. Note a few instances of relatively long fiber pullout. Very few large voids are seen in Figure 46 suggesting that the percentage of area occupied by voids plays a major role in raising or lowering the tensile strength of the material. Areas of fiber pullout are seen in Figures 47 A, B and C. Figure 47 D shows a general view of the polished surface of the material.

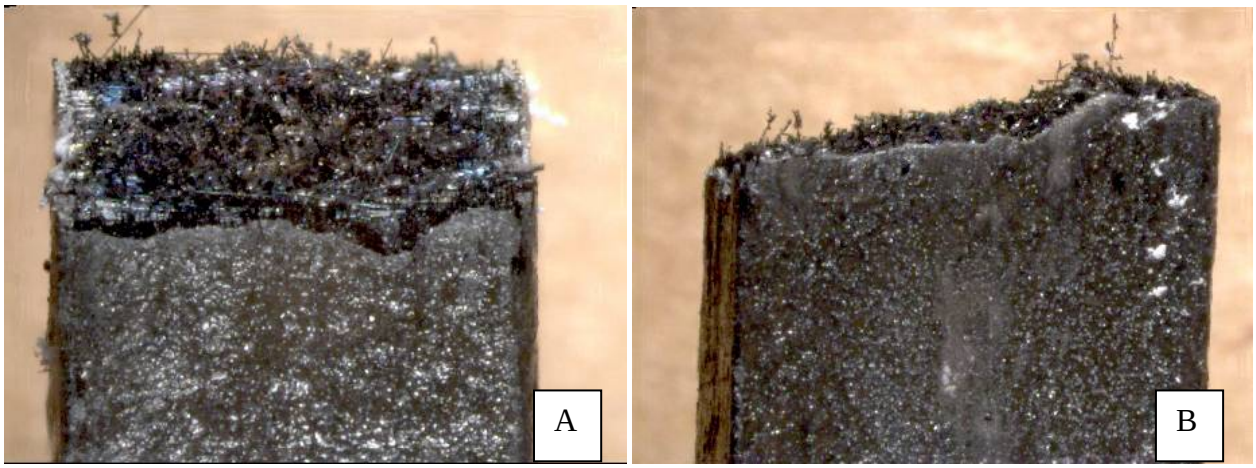

Figure 45: Optical micrographs of specimen S10D, front (A) and side (B), subjected to tensile test to failure at 1000 °C in air. Fracture surface normal to the applied load. (UTS = 136 MPa, E = 59.1 GPa).

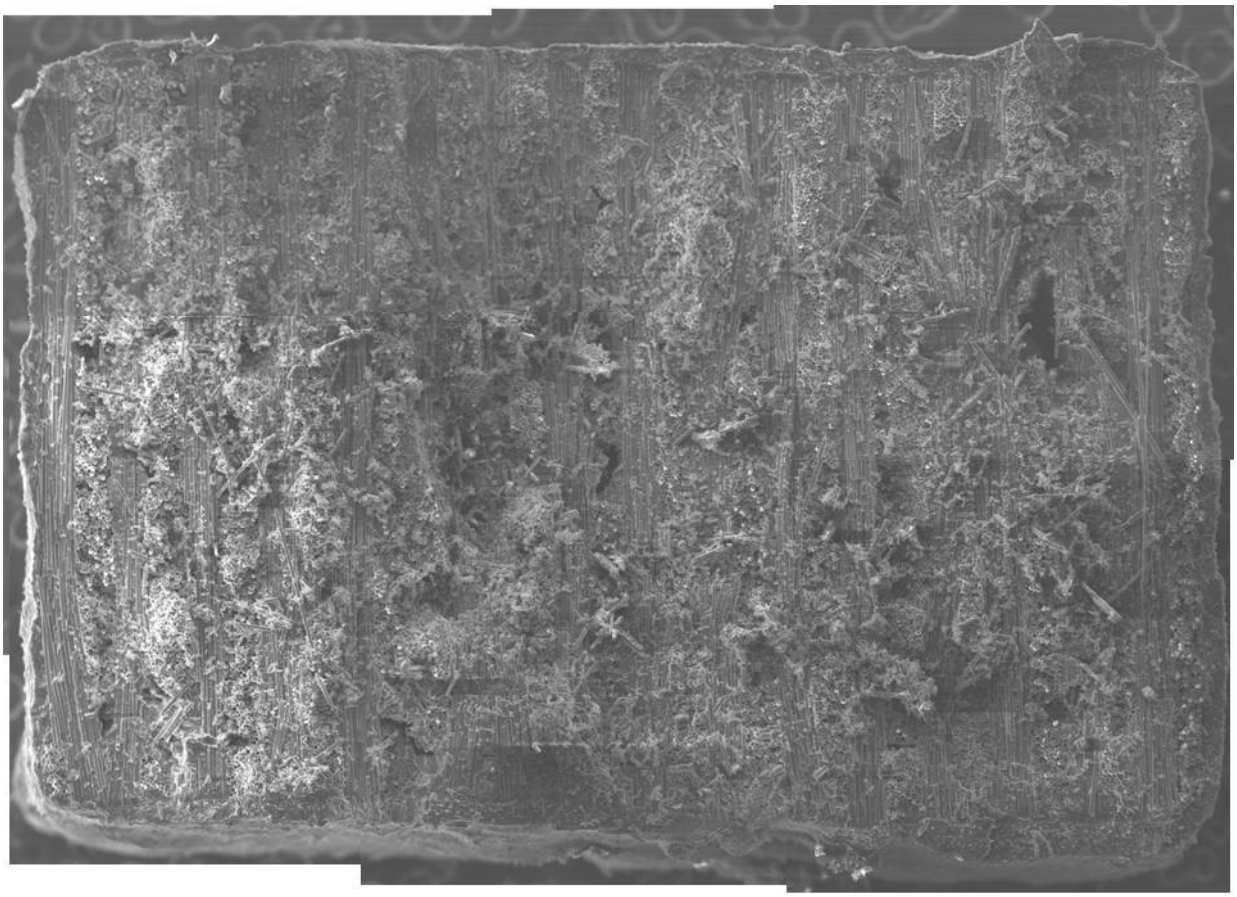

Figure 46: SEM composite micrograph of specimen S10D produced in a tensile test to failure at 1000 °C. Fracture surface normal to the applied load.

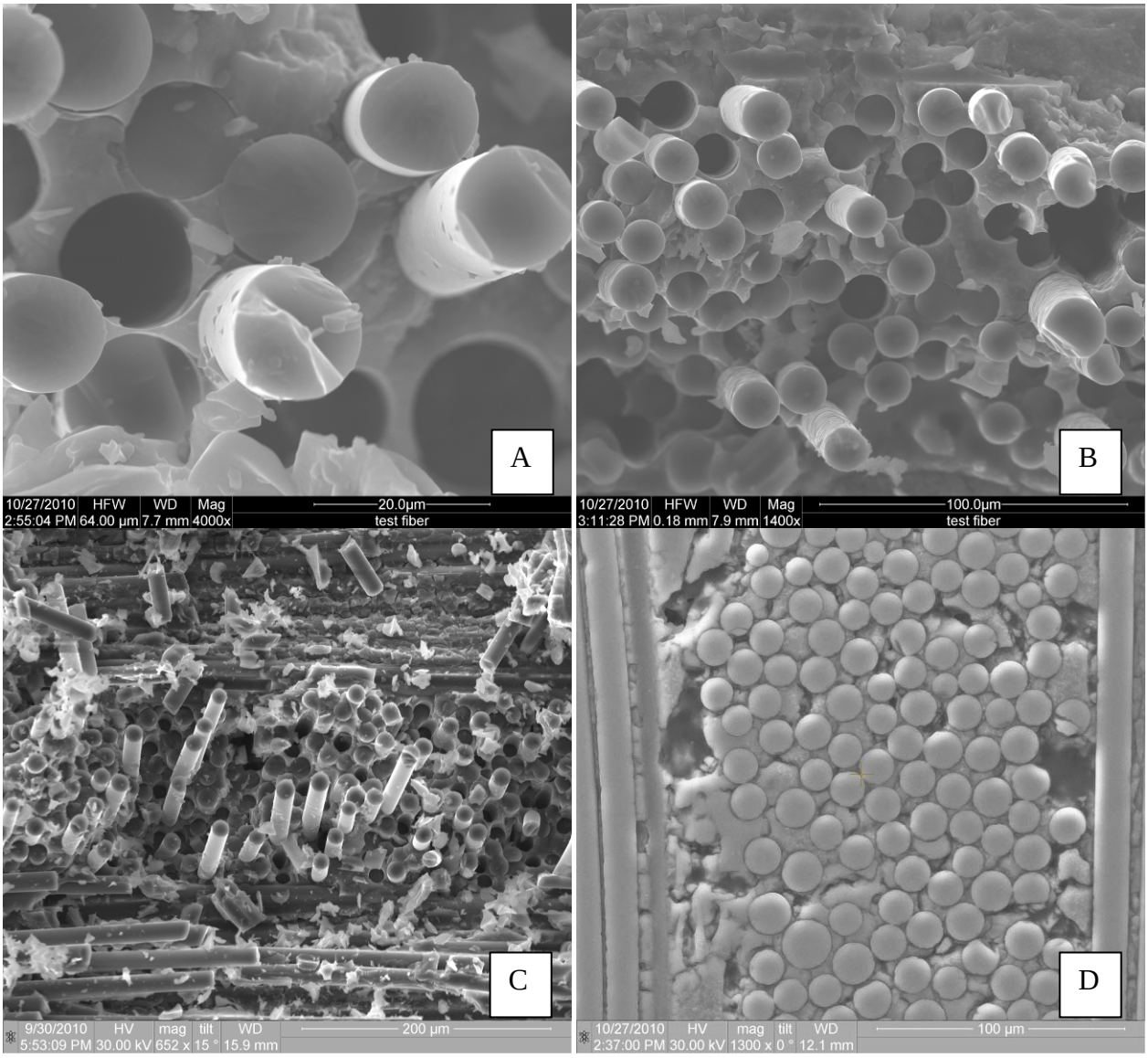

Figure 47: SEM micrographs of specimen S10D subjected to tensile test to failure at 1000 °C. Fracture surface normal to the applied load.

Optical micrographs of specimen S11B in Figure 48 show relatively long fiber pullout. The composite image in Figure 49 shows relatively few voids as expected from the high tensile strength

exhibited by specimens cut from panel 11. The image in Figure 49 also shows substantial fiber pullout. Higher magnification views of the fiber pullout are also seen in Figures 50 A, B and C.

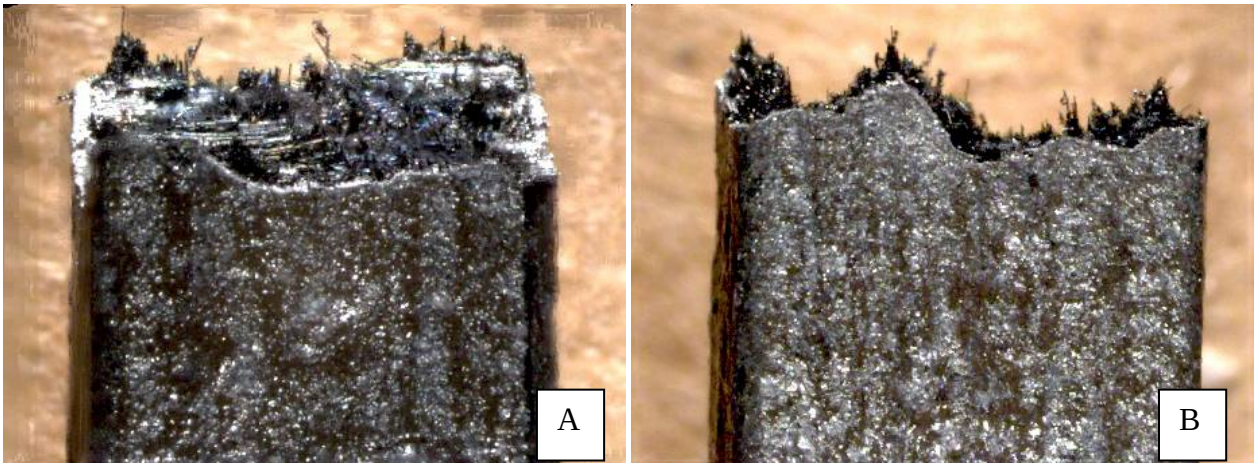

Figure 48: Optical micrographs of specimen S11B, front (A) and side (B), subjected to tensile test to failure at 1000 °C in air. Fracture surface normal to the applied load. (UTS = 124 MPa, E = 49.1 GPa).

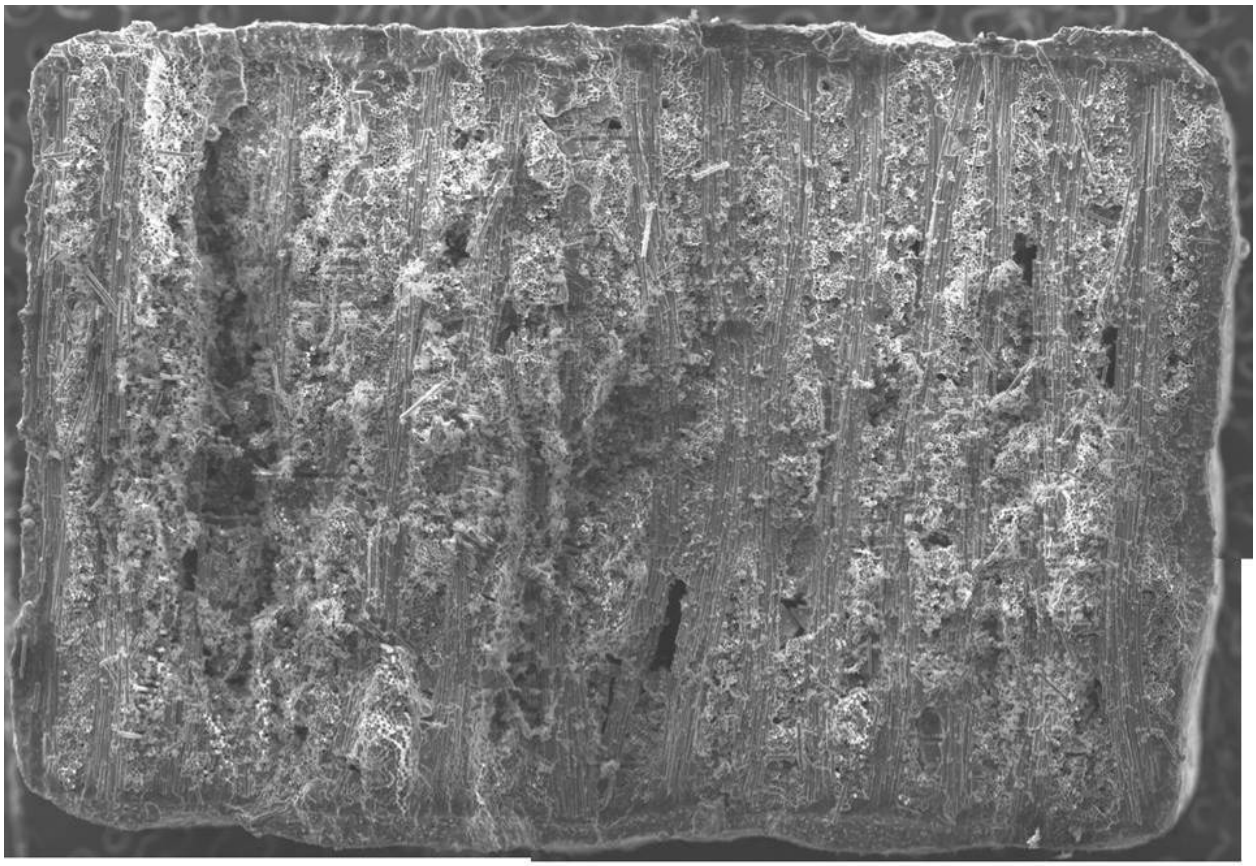

Figure 49: SEM composite micrograph of specimen S11B produced in a tensile test to failure at 1000 °C. Fracture surface normal to the applied load.

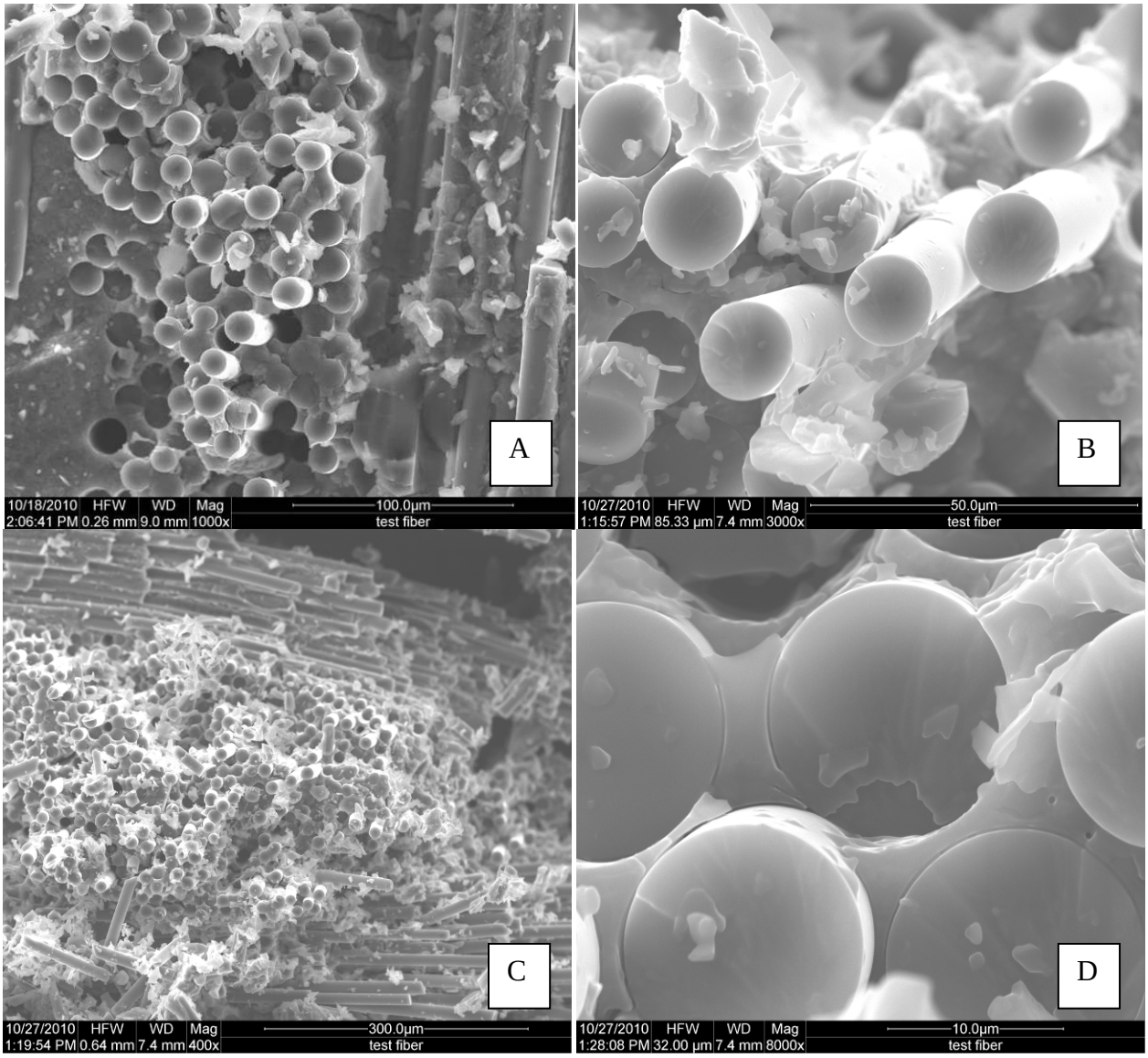

Figure 50: SEM micrographs of specimen S11B subjected to tensile test to failure at 1000 °C.

Fracture surface normal to the applied load.

5.9 Microstructural Characterization of CG NICALON™/BN/SiC Specimens Tested in Fatigue at 1000 °C in Air

Three specimens were subjected to fatigue tests at 1000 °C in air. Specimens S7B and S10B were tested with the maximum stress of 80 MPa while specimen S11E was tested with the maximum stress of 100 MPa. All specimens produced a fairly flat fracture surface demonstrating coupled failure between the plies and therefore no delamination [13:1049]. Optical micrographs of specimen S7B in Figure 51 show a fracture surface similar to those produced in the monotonic tensile tests although very little fiber pullout can be seen. Figure 52, a composite image of the entire fracture surface, shows a surface comparable in regards to void density to that of specimen S7C tested in tension to failure. Figure 53 A shows multiple cracks with a dominant crack propagating through both the 0° tow and the 90° tow, indicating a strong matrix/fiber bond which suggests a poor interphase. Additionally two voids, common to this specimen, are seen in the center and on the right hand side of the micrograph. Figure 53 B shows some very minor pullout as well as signs of brittle fracture on the fiber face. Figure 53 C illustrates the minor fiber pullout in stark contrast to that seen on the fracture surfaces produced in tension tests. Figure 53 D shows a micrograph of a polished section normal to the loading direction, where multiple cracks on the 90° tow are visible, again suggesting a strong matrix/fiber interface. Little to no oxidation was observed on the fracture surface of this specimen most likely due to its relatively short lifetime of less than 10 hours.

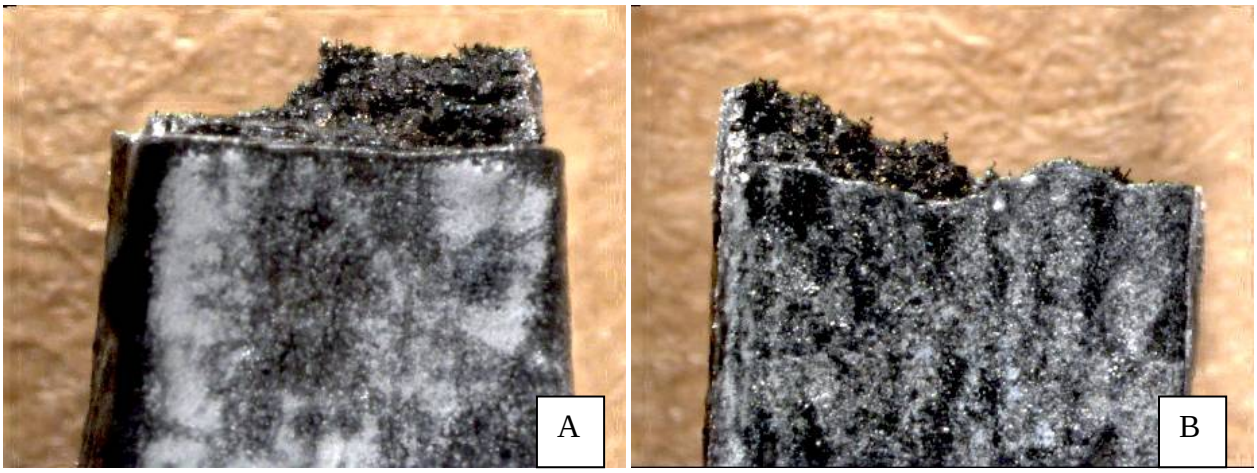

Figure 51: Optical micrographs of specimen S7B, front (A) and side (B), subjected to fatigue at 1000 °C in air (f = 1.0 Hz, σ_{max} = 100 MPa, N_f = 17,587). Fracture surface normal to the applied load.

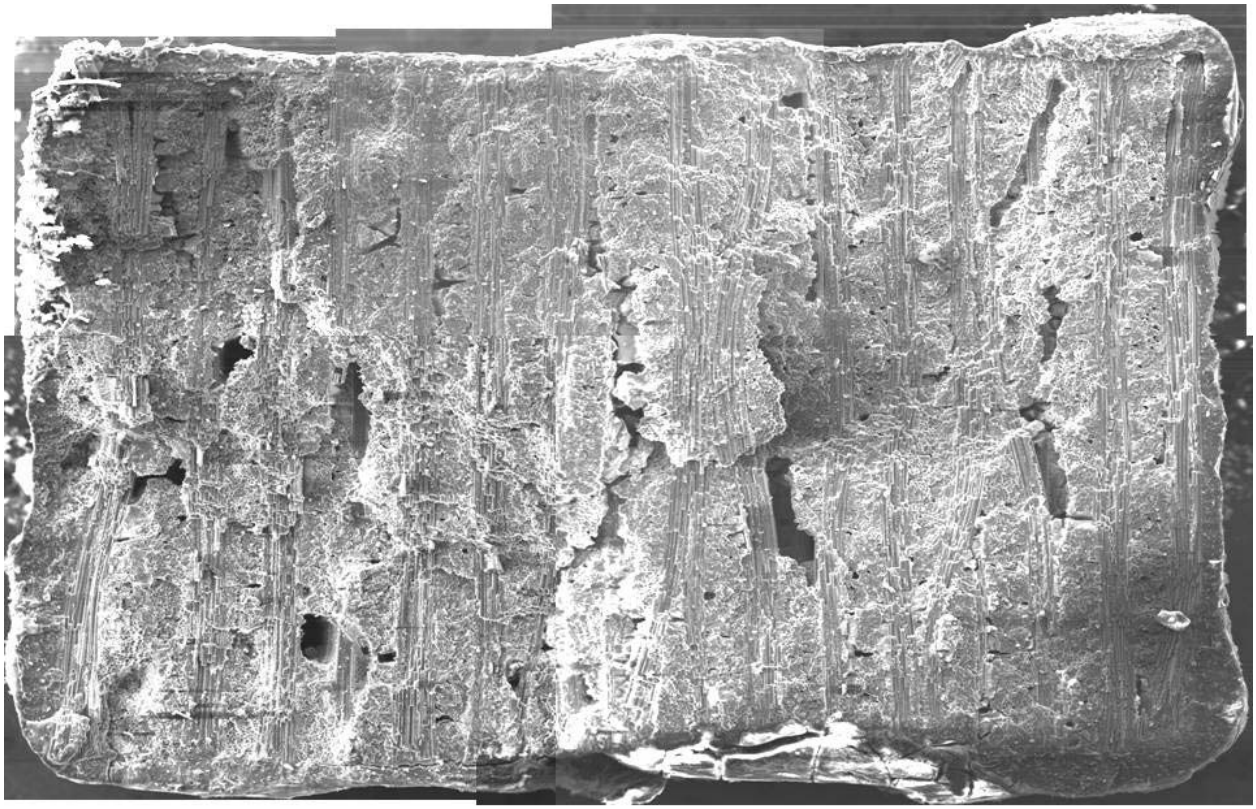

Figure 52: SEM composite micrograph of specimen S7B subjected to fatigue at 1000 °C in air (f = 1.0 Hz, σ_{max} = 80 MPa, N_f = 34,652). Fracture surface normal to the applied load.

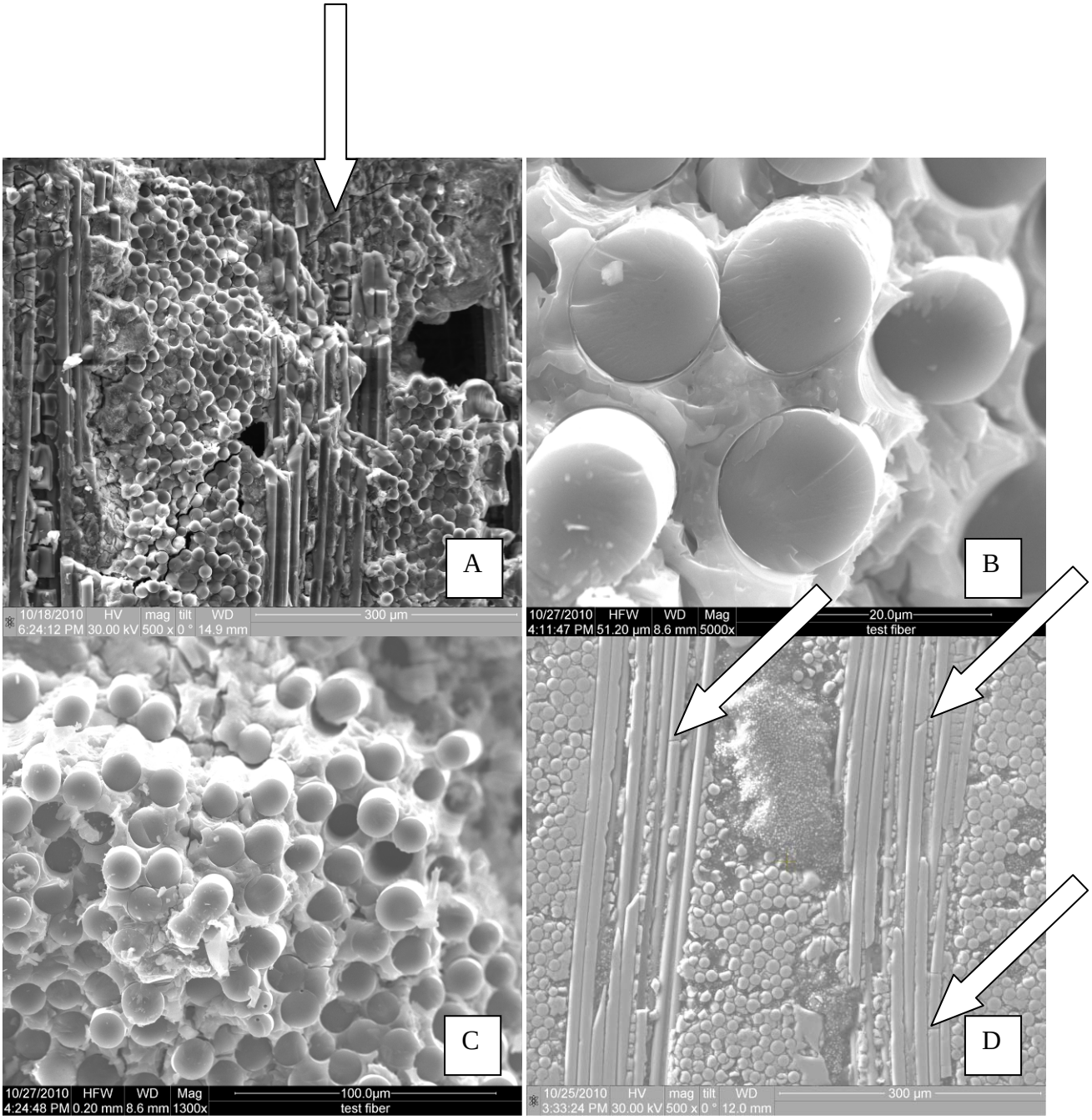

Figure 53: SEM micrographs of specimen S7B subjected to fatigue at 1000 °C in air (f = 1.0 Hz, σ_{max} = 80 MPa, N_f = 34,652). Fracture surface normal to the applied load.

Specimen S10B was the only specimen to achieve a run-out of 200,000 cycles at 1000 °C in air. Figures 54-56 depict the fracture surface of specimen S10B produced in a tension test to failure preceded by 200,000 fatigue cycles. Figure 54 shows an optical micrograph of the very flat fracture

surface with virtually no fiber pullout. A composite image in Figure 55 also reveals the very flat fracture surface. Figure 56 A shows some minimal fiber pullout. Figure 56 B shows only minor signs of oxidation in the fracture surface (see the circled area). In some scattered areas the interphase has been eaten away and replaced by small areas of glassy phase. However, this minimal oxidation did not seem to affect the final performance of the material significantly. Figure 56 C shows a crack propagating around the 0° fibers, illustrating crack deflection. Very minor signs of oxidation are also visible (see the circled region). Note that this micrograph depicts the portion of the fracture surface at the edge of the specimen (the seal coat of matrix material can be seen at the bottom of the micrograph). The very minor oxidation seen in the fracture surface of this specimen was of the "picture frame" type, where the outer edges were oxidized, and the inner areas were left free of oxidation. The micrograph of the polished surface in Figure 56 D reveals not only a pathway for the environmental attack, but shows some minor signs of oxidation as well.

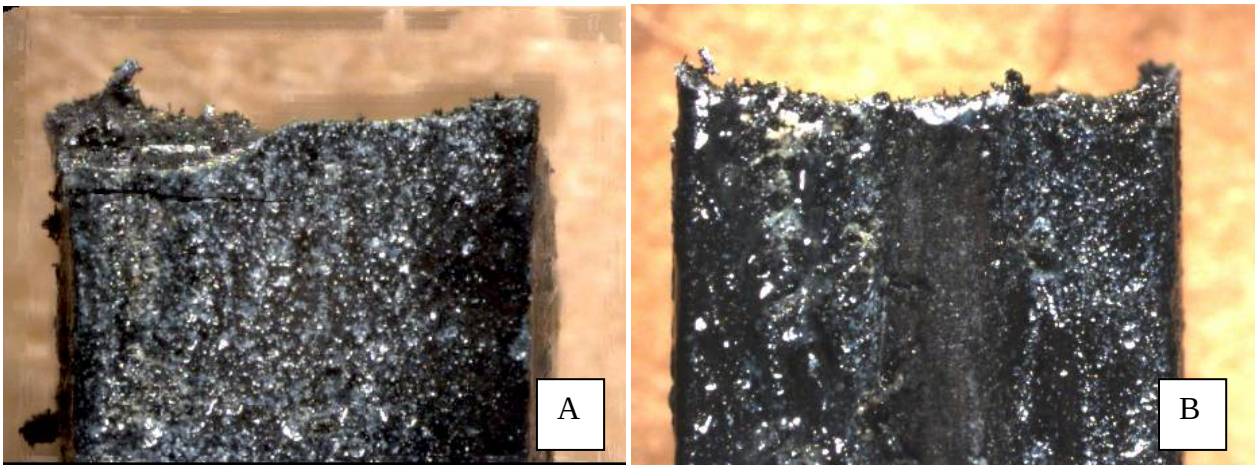

Figure 54: Optical micrographs of specimen S10B, front (A) and side (B), subjected to fatigue and a subsequent tensile test to failure at 1000 °C in air (f = 1.0 Hz, σ_{max} = 80 MPa, N_f = 200,000). Fracture surface normal to the applied load.

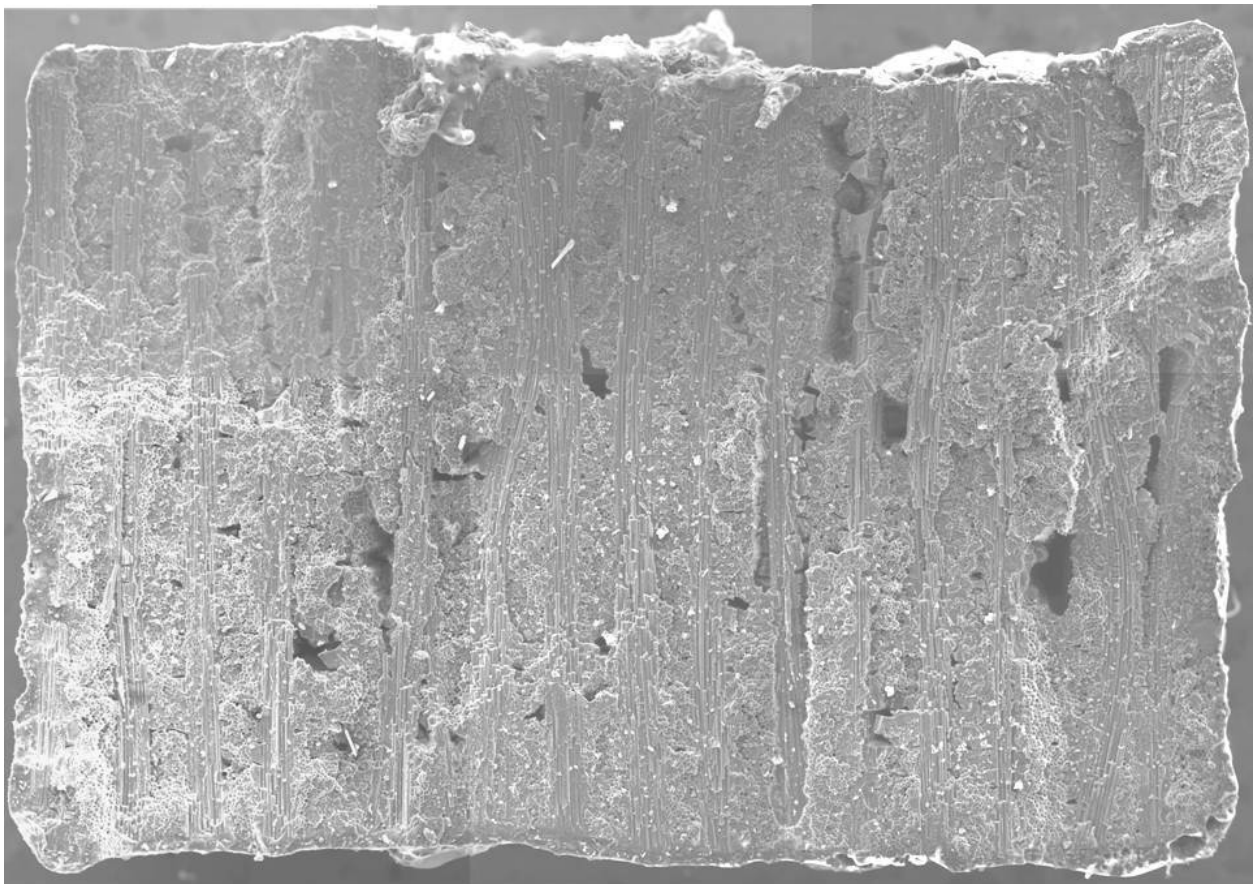

Figure 55: SEM composite micrograph of specimen S10B subjected to fatigue and a subsequent tensile test to failure at 1000 °C in air (f = 1.0 Hz, σ_{max} = 80 MPa, N_f = 200,000). Fracture surface normal to the applied load.

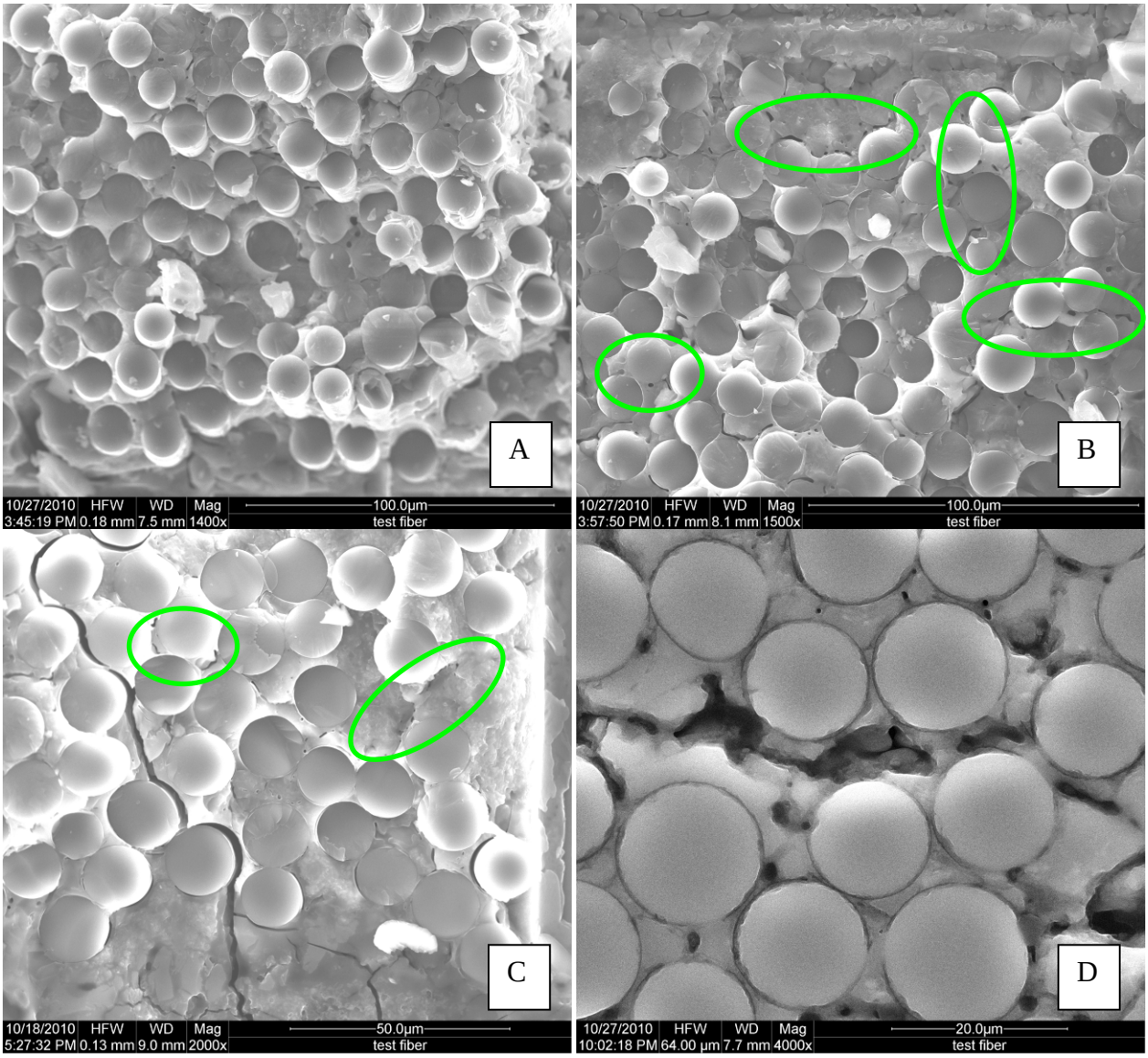

Figure 56: SEM micrographs of specimen S10B subjected to fatigue and a subsequent tensile test to failure at 1000 °C in air (f = 1.0 Hz, σ_{max} = 80 MPa, N_f = 200,000). Fracture surface normal to the applied load.

Figures 57-59 show the fracture surface of specimen S11E, which survived 168,255 fatigue cycles performed with the maximum stress of 100 MPa. Although the cyclic life of specimen S11E was slightly less than that of specimen S10B, because specimen S11E was tested with a higher

maximum stress a larger number of cracks formed during cycling, exposing more of the matrix and fibers to the oxidizing test environment. Hence a greater portion of the fracture surface of specimen S11E was oxidized, as evidenced by the SEM micrographs. The optical micrographs in Figure 57 show a predominantly flat fracture surface with no fiber pullout visible. Figure 58 shows considerably more voids than the fracture surfaces produced in tension tests on specimens cut from the same panel. SEM images in Figures 59 A and B depict higher magnification views of the composite fracture surface where some rare instances of fiber pullout may be observed. Although difficult to discern the apparent crack in Figure 59 C actually consists of fibers pulling away from each other and are only connected with small fingers of silica. Figure 59 D examines small localized areas of oxidation damage as well as the brittle fracture of the surrounding fibers. Figure 59 E shows the brittle fracture of the fibers and oxidation of the fiber/matrix interphase. Furthermore, Figure 59 E shows where silica has formed in place of the interphase as well as the glassy layer covering some of the fracture surface. Finally Figure 59 F shows a wide variety of brittle fractures, oxidation on fracture surfaces, and oxidation voids within the matrix. The presence of voids interspersed throughout the matrix without a clear pattern suggests that the matrix density was less than adequate to ensure environmental durability.

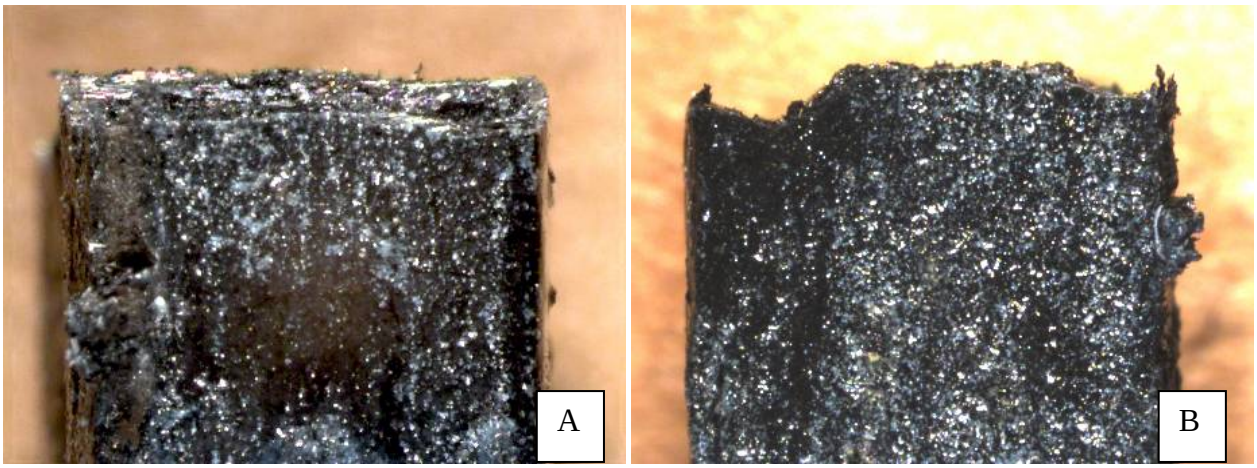

Figure 57: Optical micrographs of specimen S11E, front (A) and side (B), subjected to fatigue at 1000 °C in air (f = 1.0 Hz, σ_{max} = 100 MPa, N_f = 168,255). Fracture surface normal to the applied load.

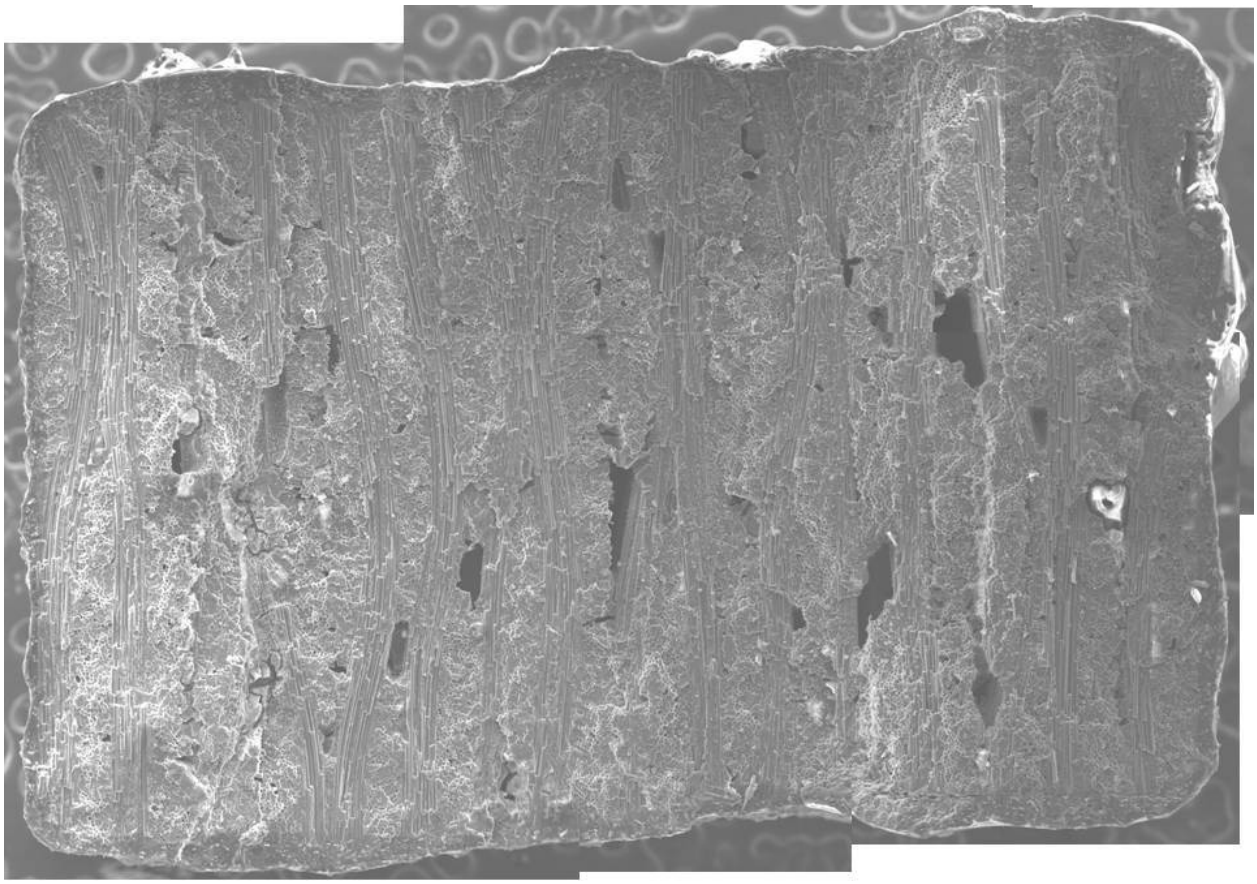

Figure 58: SEM composite micrograph of specimen S11E subjected to fatigue at 1000 °C in air (f = 1.0 Hz, σ_{max} = 100 MPa, N_f = 168,255). Fracture surface normal to the applied load.

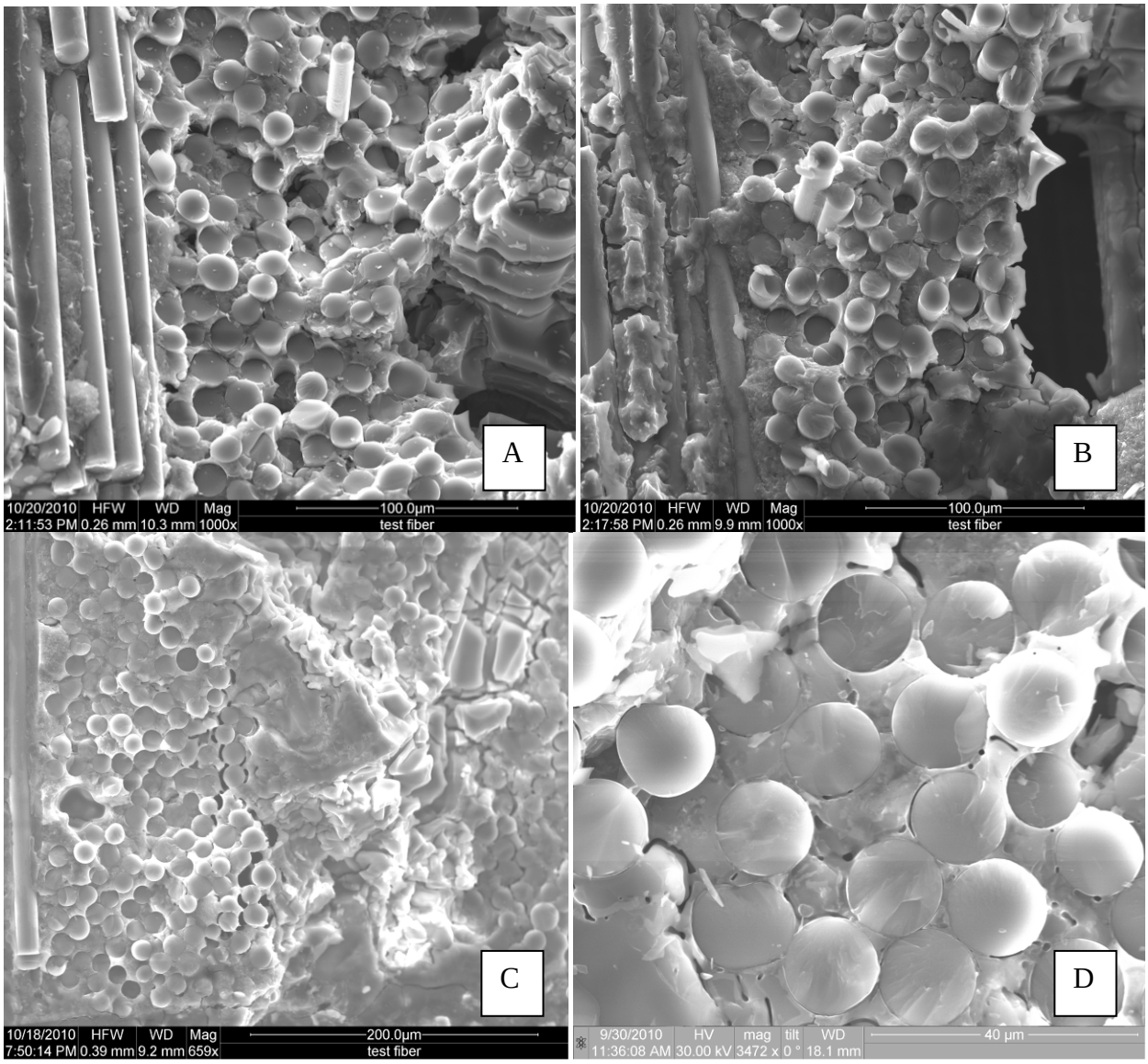
A
10/20/2010 HFW WD Mag 100.0µm
2:11:53 PM 0.26 mm 10.3 mm 1000x test fiber
B
10/20/2010 HFW WD Mag 100.0µm
2:17:58 PM 0.26 mm 9.9 mm 1000x test fiber
C
10/18/2010 HFW WD Mag 200.0µm
7:50:14 PM 0.39 mm 9.2 mm 659x test fiber
D
9/30/2010 HV mag tilt WD 40 µm
11:36:08 AM 30.00 kV 3472 x 0 ° 18.1 mm

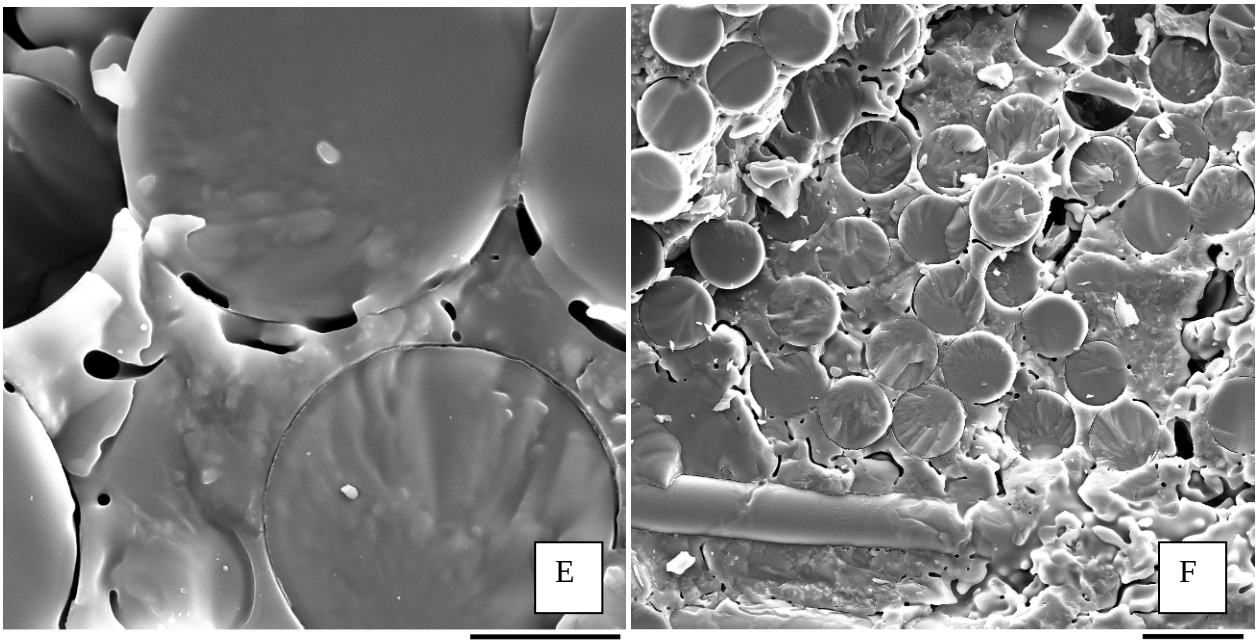

Figure 59: SEM micrographs of specimen S11E subjected to fatigue at 1000 °C in air (f = 1.0 Hz, σ_{max} = 100 MPa, N_f = 168,255). Fracture surface normal to the applied load.

5.10 Microstructural Characterization of CG NICALON™/BN/SiC Specimens Tested in Fatigue at 1000 °C in Steam

Specimens tested in steam generally produced uneven fracture surfaces, where the failure planes exhibited decoupled random failure between the plies and delamination [13:1049]. Indeed a great deal of delamination is readily seen in the micrographs presented in this Section. Additionally, the micrographs shown in this Section suggest that the matrix microcracks formed early on, allowing vaporization of the protective SiC layers and permitting oxygen ingress along the 90° fiber tows [7:4].

Figures 60-62 show the fracture surface of specimen S11A, which survived 194,930 fatigue cycles performed with the maximum stress of 60 MPa. As this specimen was exposed to a steam

environment at 1000 °C for more than 54 h, a great deal of oxidation was able to occur. Optical micrographs in Figure 60 show a white residue on the specimen surface, which are likely silica scales [30:1817]. Such white residue was observed on the surface of all specimens tested at 1000 °C in steam. Although optical micrographs of all fatigue specimens in both air and steam exhibited no visible fiber pullout, the white residue on the surfaces, uneven fracture surfaces, and increases in specimen depth among specimens tested in steam made these images considerably dissimilar. Indeed, as reported earlier, considerable changes in overall specimen thickness were noted because of significant delamination occurring between plies. In fact, most of the 16 plies can be easily identified in Figure 61, where the large gaps between the plies are readily discernable. These gaps between the plies are the primary cause for the significant increase in thickness. The ply delamination also provided wide paths for environmental attack into the composite. Figures 62 A, B, C, and D illustrate the extent of the major degradation by oxidation occurring throughout the composite. Virtually no area is free from large amounts of silica deposits. Figure 62 E depicts a large crack propagating through matrix and fibers, indicating an undesirable strong matrix-fiber bond. Figure 62 F illustrates widespread glass bubble formation throughout the composite. This oxidative feature occurred at the intersection of two 90° tows between different plies, thus a virtual highway for hot gasses to enter through. The significant damage caused by the steam environment stems from the addition of oxygen in the form of water as the primary oxidant. At 1000 °C in steam a number of chemical reactions discussed in Sections 2.2 and 2.6 take place creating among other products silicon dioxide visible in Figure 62 F [21:228, 30:1817].

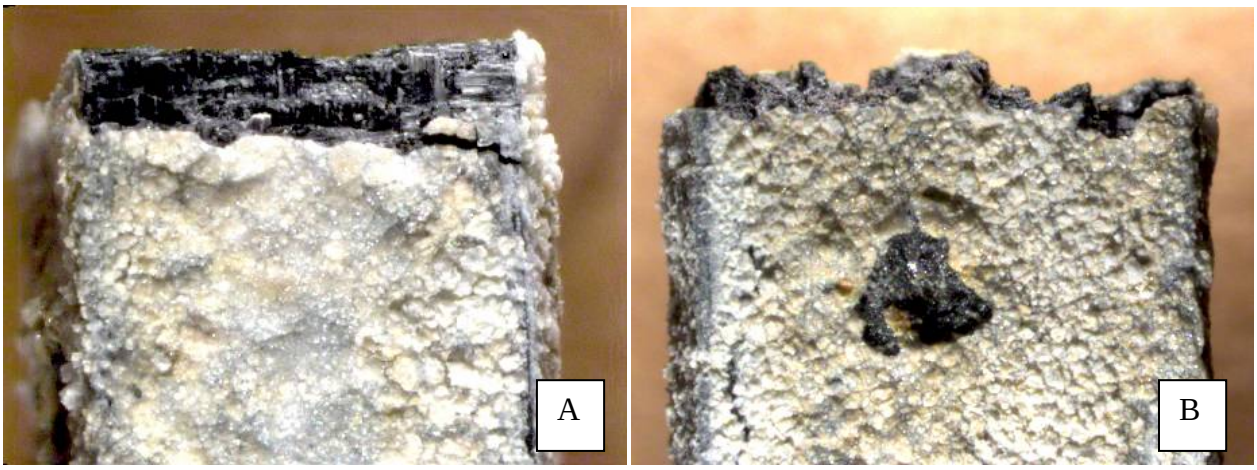

Figure 60: Optical micrographs of specimen S11A, front (A) and side (B), subjected to fatigue at 1000 °C in steam (f = 1.0 Hz, σ_{max} = 60 MPa, N_f = 194,930). Fracture surface normal to the applied load.

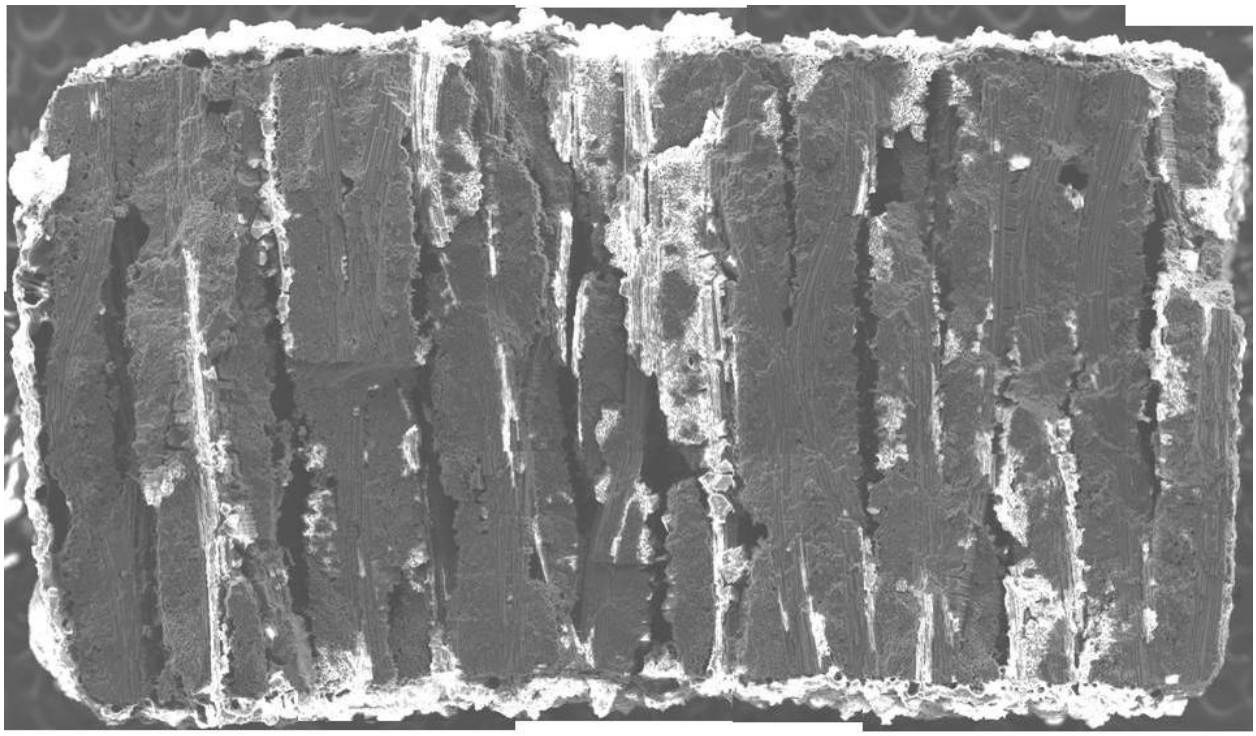

Figure 61: SEM composite micrograph of specimen S11A subjected to fatigue at 1000 °C in steam (f = 1.0 Hz, σ_{max} = 60 MPa, N_f = 194,930). Fracture surface normal to the applied load.

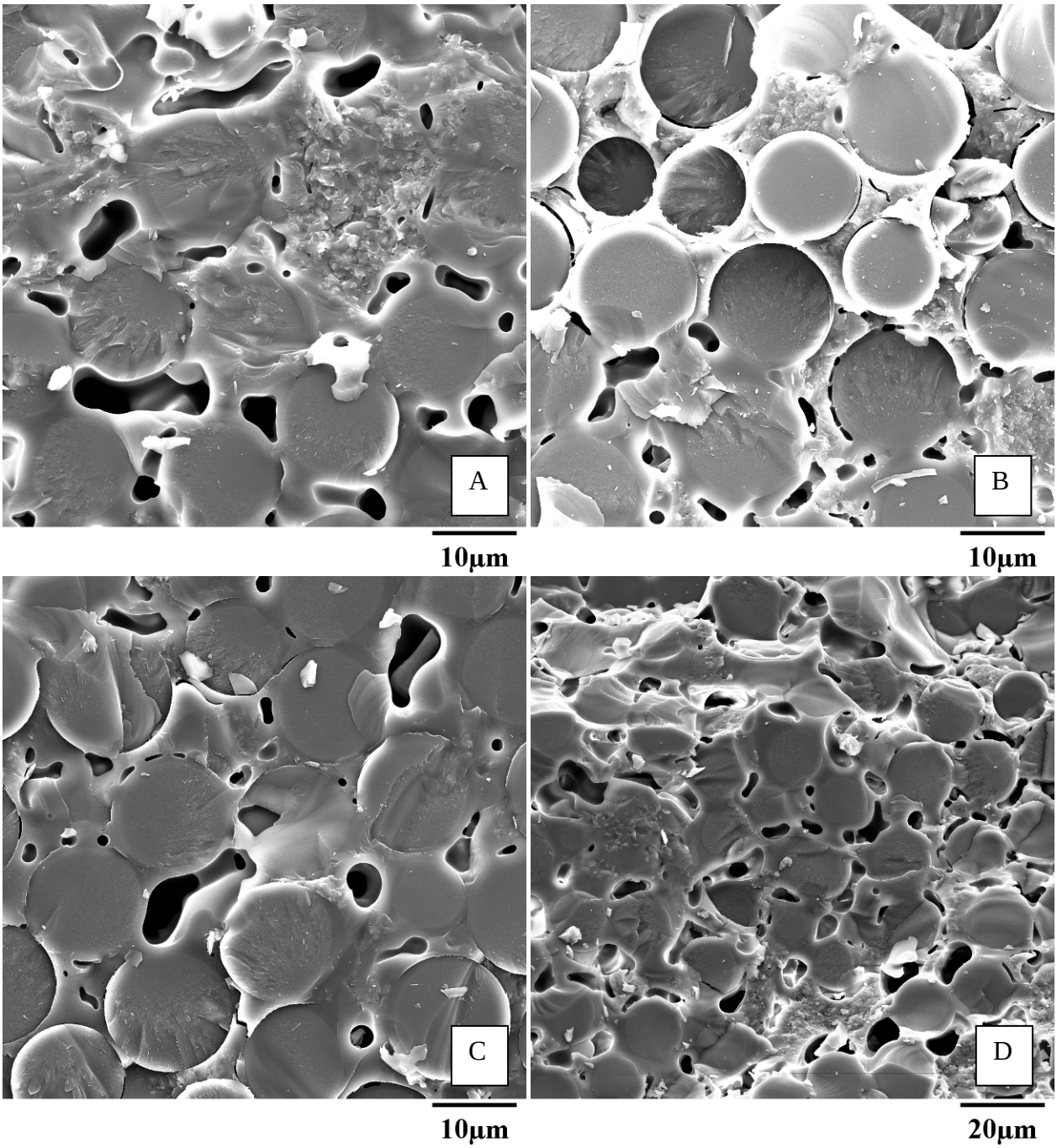
A
10µm
B
10µm
C
10µm
D
20µm

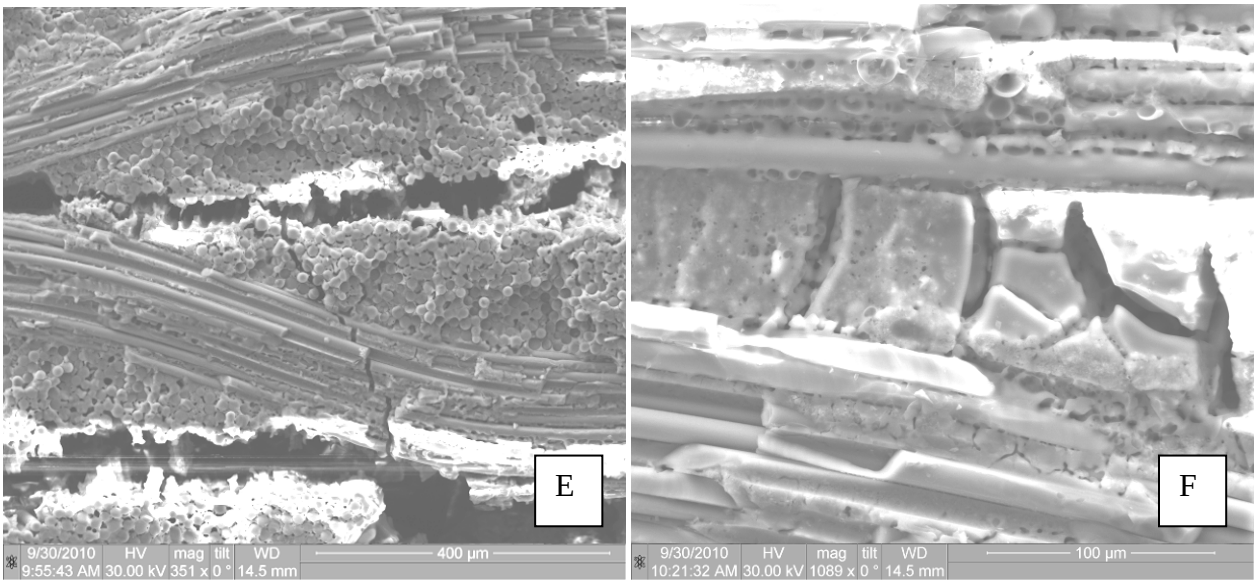

Figure 62: SEM micrographs of specimen S11A subjected to fatigue at 1000 °C in steam (f = 1.0 Hz, σ_{max} = 60 MPa, N_f = 194,930). Fracture surface normal to the applied load.

Figures 63-65 show the fracture surface of specimen S10E, which survived 126,593 fatigue cycles performed with the maximum stress of 70 MPa. The optical micrographs in Figure 63 reveal a great deal of white residue on the specimen surface as well as the stepwise fracture surface. However, although the fracture surface has a stepwise nature, it is mostly flat within each individual step. Figure 64 shows a fracture surface that is similar to that obtained for specimen S11A fatigued with the maximum stress of 60 MPa. Note ply delamination with large gaps opening between individual plies, creating pathways for the oxidizing environment to enter the interior of the composite. Figures 65 A and B illustrate the extent of degradation by oxidation throughout the composite where non-oxidized sections were incredibly difficult to locate. Figure 65 C demonstrates an interesting area of matrix oxidation. It appears that the oxidation process did not result in formation of silica glass but rather consumed much of the matrix, leaving what appear to be the original SiC particles embedded within the first PIP cycle. Figure 65 D presents a

noteworthy effect of oxidation of the fracture surface. Apparently the fibers broke before the final fracture of the composite occurred, then silica formed and covered the fractured fibers. Note that the fractured fibers are visible underneath the layer of glass. This phenomenon has been noticed in several micrographs although the effect is generally not as pronounced as in Figure 65 D. Figure 65 E also displays a glassy silica layer covering the fractured fibers with some fibers being barely discernable. Figure 65 F demonstrates a few fibers exhibiting brittle fracture and matrix undamaged by oxidation in close proximity to an area severely damaged by oxidation, as manifested by the presence of a glassy layer on the fracture surface.

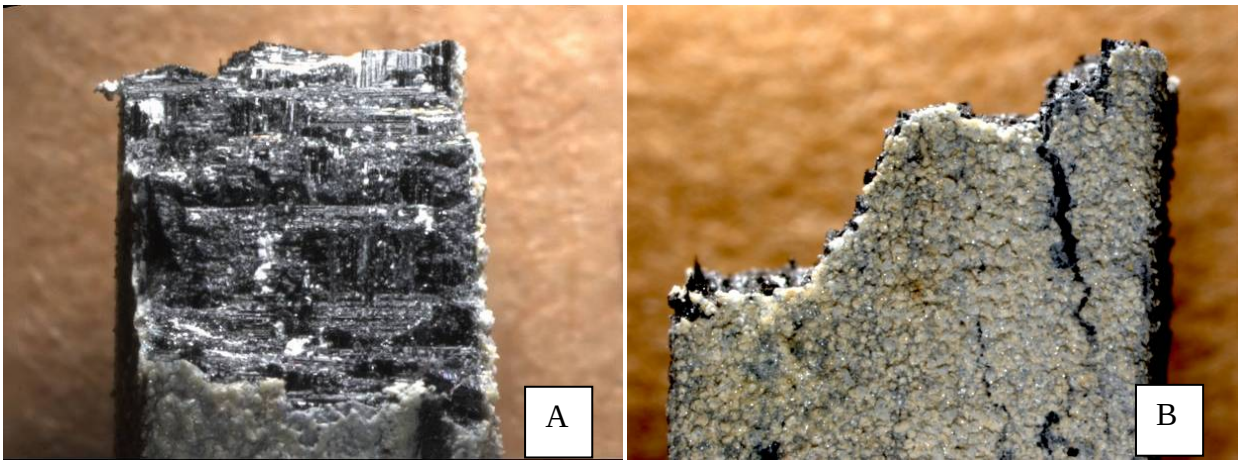

Figure 63: Optical micrographs of specimen S10E, front (A) and side (B), subjected to fatigue at 1000 °C in steam (f = 1.0 Hz, σ_{max} = 70 MPa, N_f = 126,593). Fracture surface normal to the applied load.

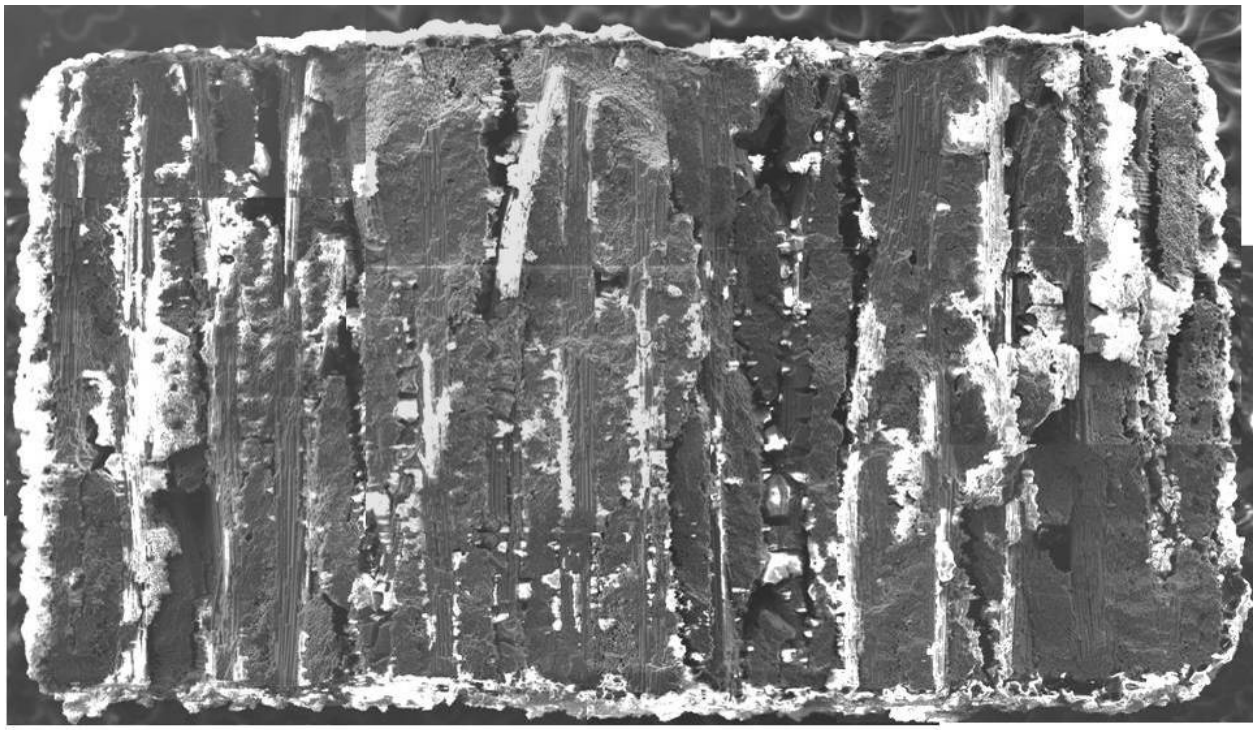

Figure 64: SEM composite micrograph of specimen S10E subjected to fatigue at 1000 °C in steam (f = 1.0 Hz, σ_{max} = 70 MPa, N_f = 126,593). Fracture surface normal to the applied load.

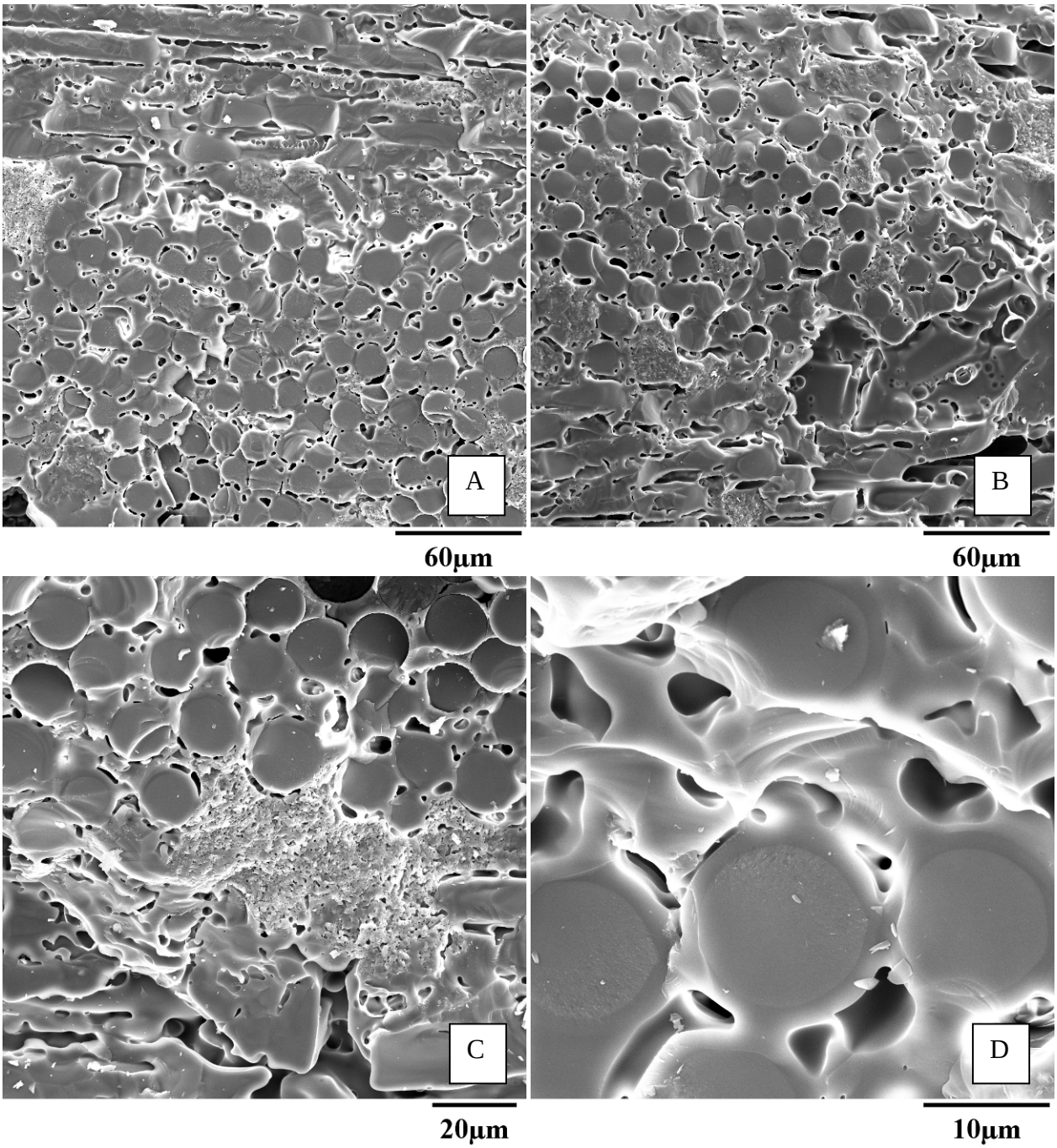
A
60µm
B
60µm
C
20µm
D
10µm

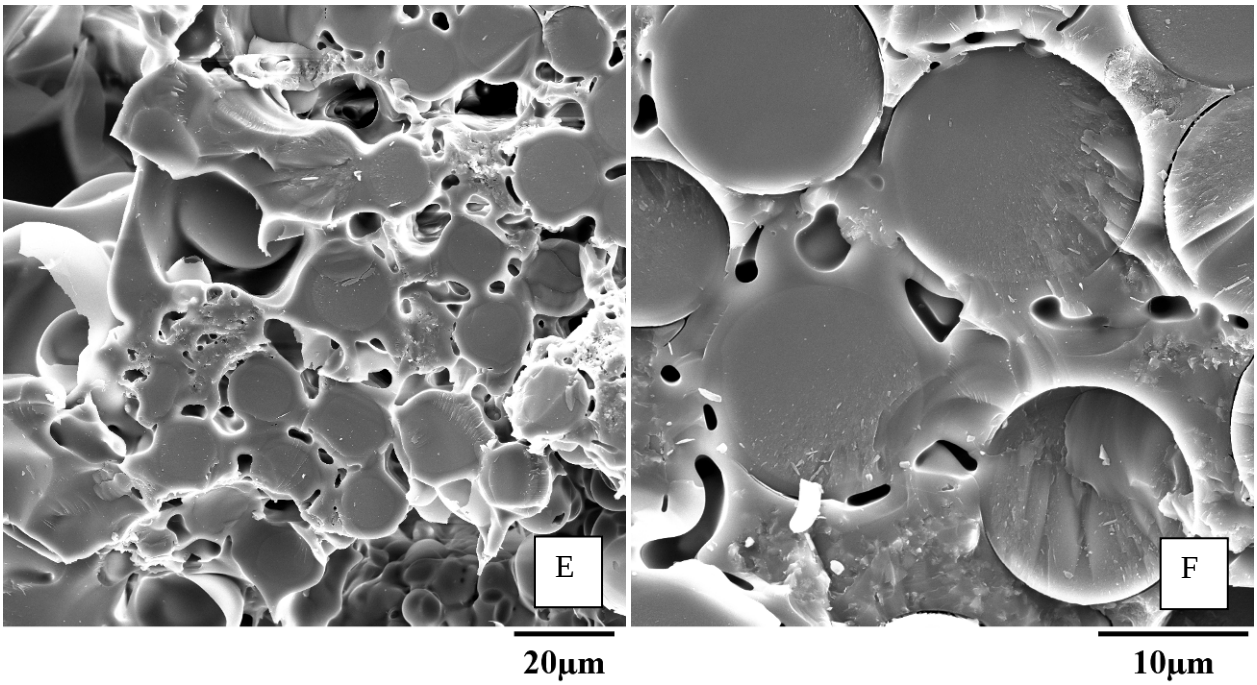

Figure 65: SEM micrographs of specimen S10E subjected to fatigue at 1000 °C in steam (f = 1.0 Hz, σ_{max} = 70 MPa, N_f = 126,593). Fracture surface normal to the applied load.

Specimen S11D was also subjected to fatigue at 1000 °C in steam with a maximum stress of 70 MPa. Unlike specimen S10E, which survived 126,593, specimen S11D failed after 65,154 cycles (thus being exposed to steam environment at 1000 °C for just over 18 h). Due to a shorter exposure to the oxidizing environment less oxidative degradation is observed. An optical micrograph in Figure 66 shows a stepwise fracture surface with the white residue covering the specimen surface. The composite image in Figure 67 reveals ply delamination characteristic of specimens tested in steam, which provides excellent pathways for the oxidizing environment to enter the interior of the composite. Figures 68 A and B, both depicting the areas of the fracture surface near the center of the specimen cross section, show the deterioration of BN fiber coating around the fibers and silica forming strong connections throughout the fiber interfaces. Note that not all areas in Figures 68 A and B are completely oxidized. This trend continues, with small non-oxidized areas being found

throughout the fracture surface suggesting that steam penetrated through the specimen prior to fracture. Figure 68 C shows silica forming as delamination is occurring; note the highly viscous molten silica forming stalactite-like patterns. Figure 68 D shows a crack penetrating directly through the 90° fibers, which illustrates the strong fiber-matrix interface. Figures 68 E and F show severe oxidation commonly seen within this composite.

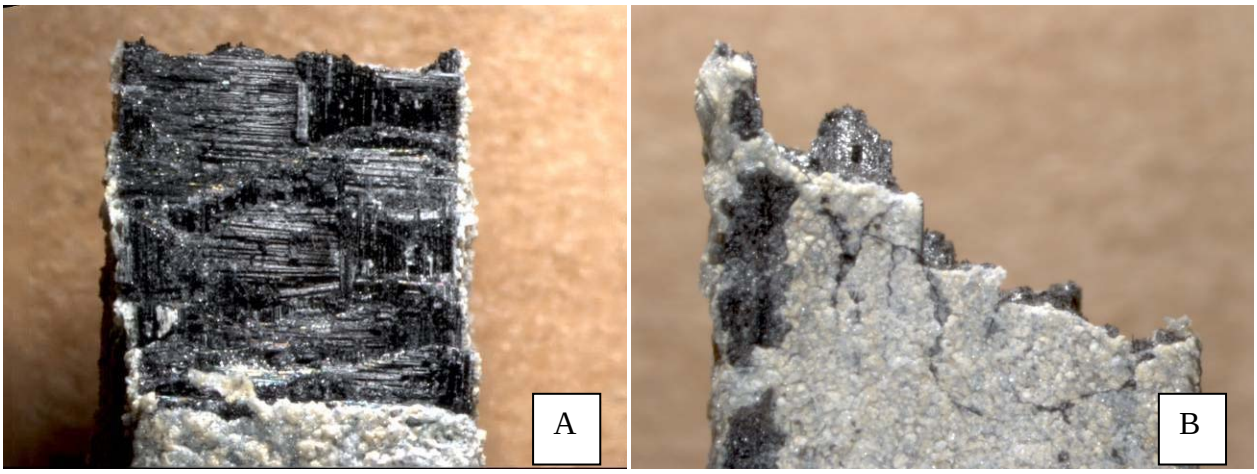

Figure 66: Optical micrographs of specimen S11D, front (A) and side (B), subjected to fatigue at 1000 °C in steam (f = 1.0 Hz, σ_{max} = 70 MPa, N_f = 65,154). Fracture surface normal to the applied load.

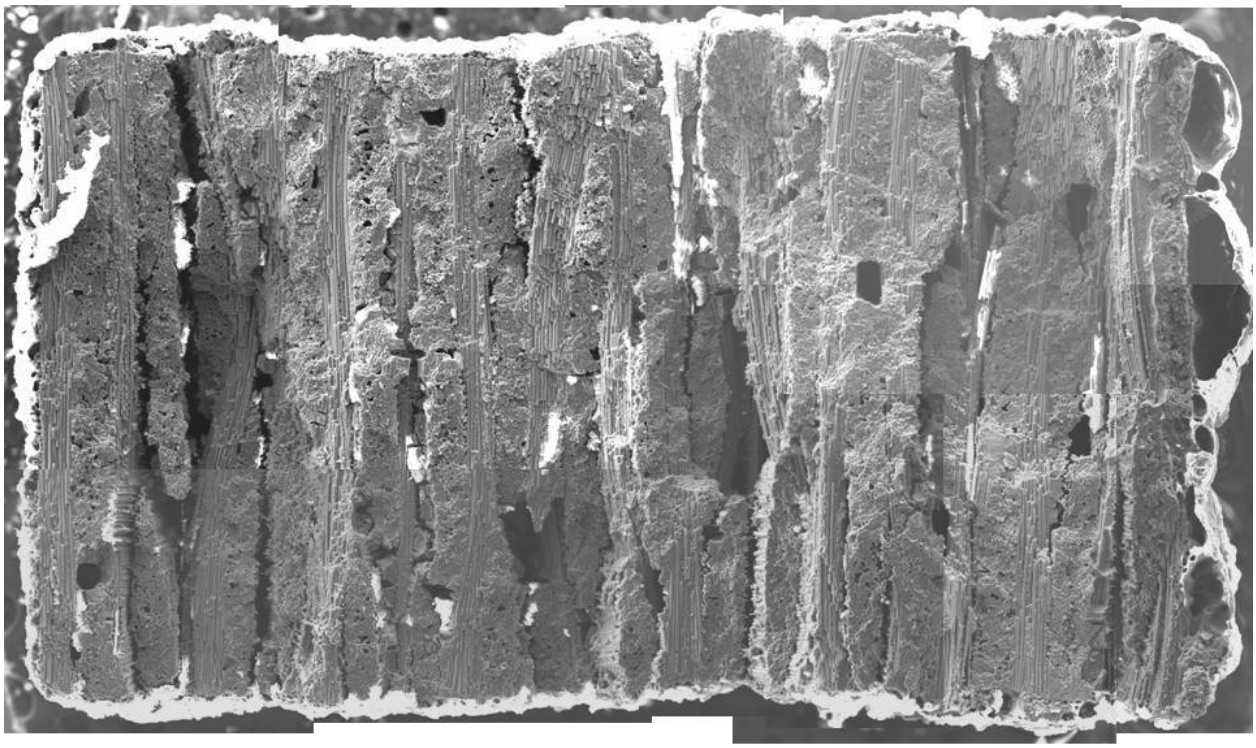

Figure 67: SEM composite micrograph of specimen S11D subjected to fatigue at 1000 °C in steam (f = 1.0 Hz, σ_{max} = 70 MPa, N_f = 65,154). Fracture surface normal to the applied load.

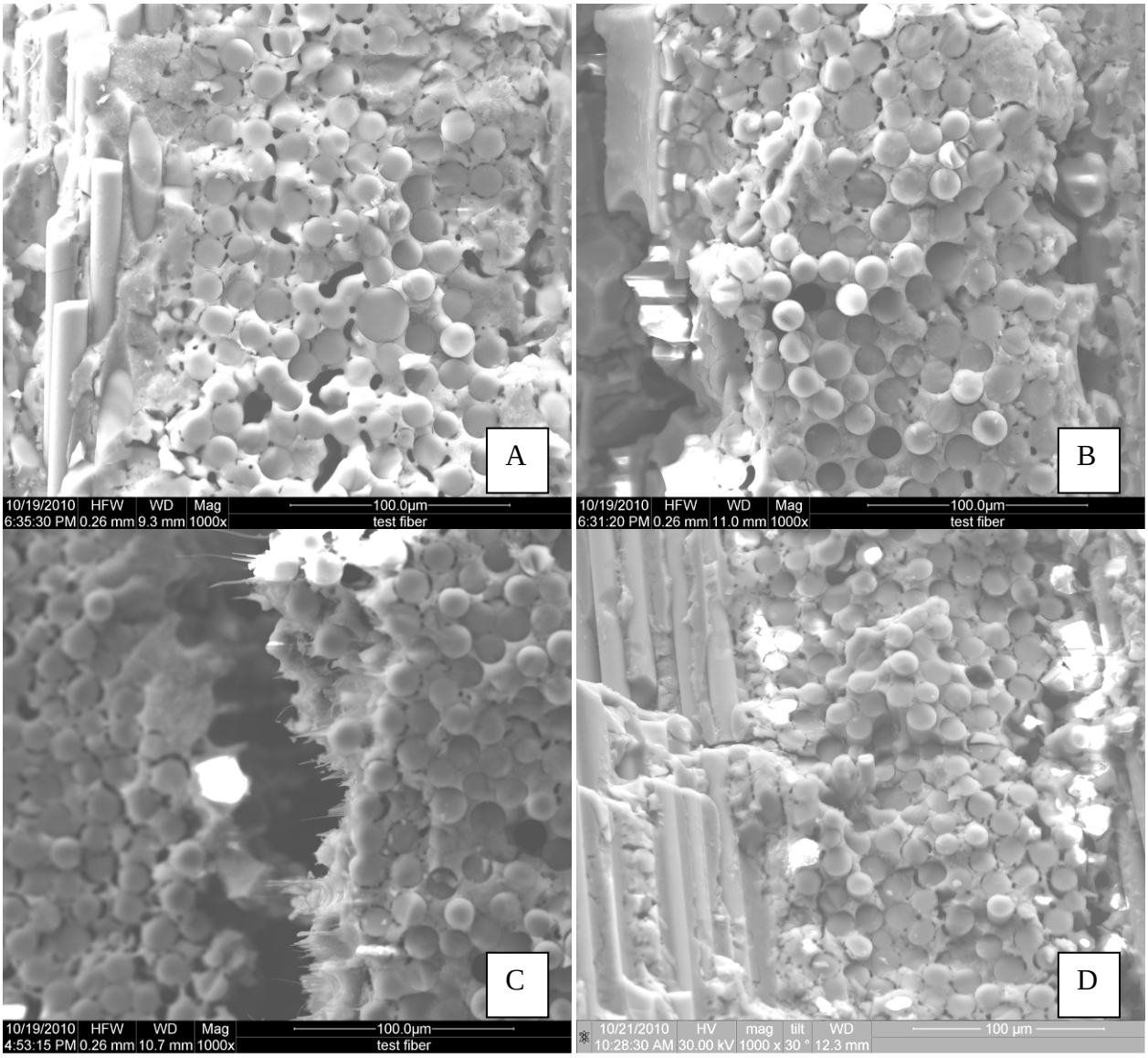
A
10/19/2010 HFW WD Mag 100.0µm
6:35:30 PM 0.26 mm 9.3 mm 1000x test fiber
B
10/19/2010 HFW WD Mag 100.0µm
6:31:20 PM 0.26 mm 11.0 mm 1000x test fiber
C
10/19/2010 HFW WD Mag 100.0µm
4:53:15 PM 0.26 mm 10.7 mm 1000x test fiber
D
10/21/2010 HV mag tilt WD 100 µm
10:28:30 AM 30.00 kV 1000 x 30 ° 12.3 mm

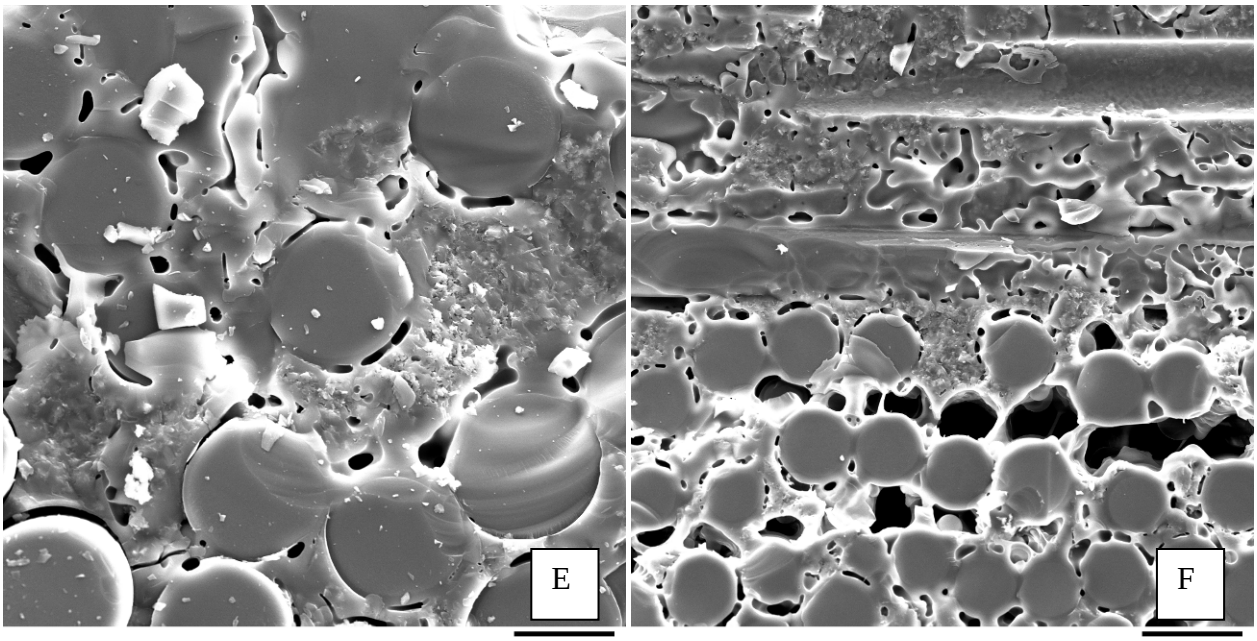

Figure 68: SEM micrographs of specimen S11D subjected to fatigue at 1000 °C in steam (f = 1.0 Hz, σ_{max} = 70 MPa, N_f = 65,154). Fracture surface normal to the applied load.

Figures 69-72 show the fracture surface of specimen S10A, which survived 73,084 fatigue cycles performed with the maximum stress of 80 MPa. Optical micrographs in Figures 69 and 70 show the white residue on the specimen surface. Note that this specimen fractured in two places, hence two fracture surfaces were formed: the first was stepwise and the second was flat. Note that only the bottom part of the specimen was examined with the SEM because this part of the specimen was removed from the hot steam environment immediately following failure and was not subject to any additional oxidation after the test was terminated. The SEM image in Figure 71 shows the high amount of delamination typical of specimens tested in steam. Severe oxidation of the entire fracture surface is also evident. A higher magnification view in Figure 72 A depicts the typical oxidation of the fracture surface with a degraded fiber-matrix interphase and a glassy layer coating the fiber fracture surfaces. Figure 72 B focuses on the glass bubbles typically seen on the 90° fibers in this

composite. A large crack seen on the left hand side represents a clear pathway for hot gasses to penetrate into the interior of the composite. Figures 72 C and D provide general views of the oxidation seen throughout the fracture surface.

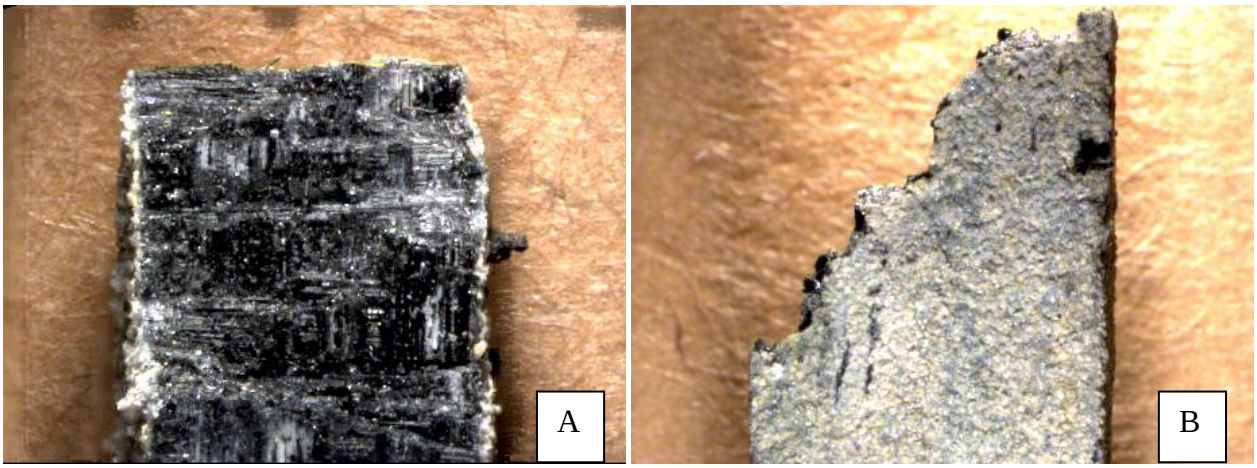

Figure 69: Optical micrographs of bottom half of specimen S10A, front (A) and side (B), subjected to fatigue at 1000 °C in steam (f = 1.0 Hz, σ_{max} = 80 MPa, N_f = 73,084). Fracture surface normal to the applied load.

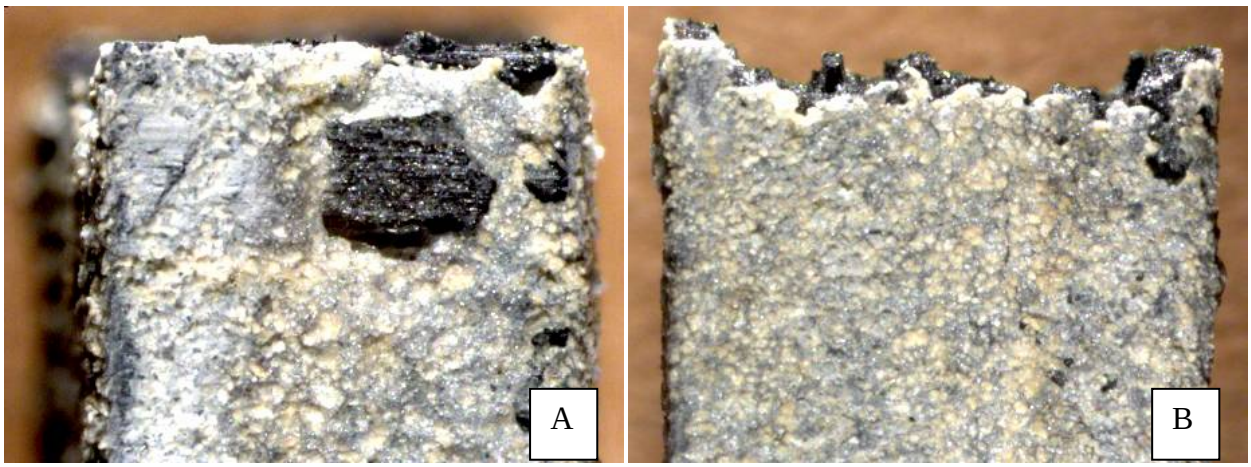

Figure 70: Optical micrographs of top half of specimen S10A, front (A) and side (B), subjected to fatigue at 1000 °C in steam (f = 1.0 Hz, σ_{max} = 80 MPa, N_f = 73,084). Fracture surface normal to the applied load.

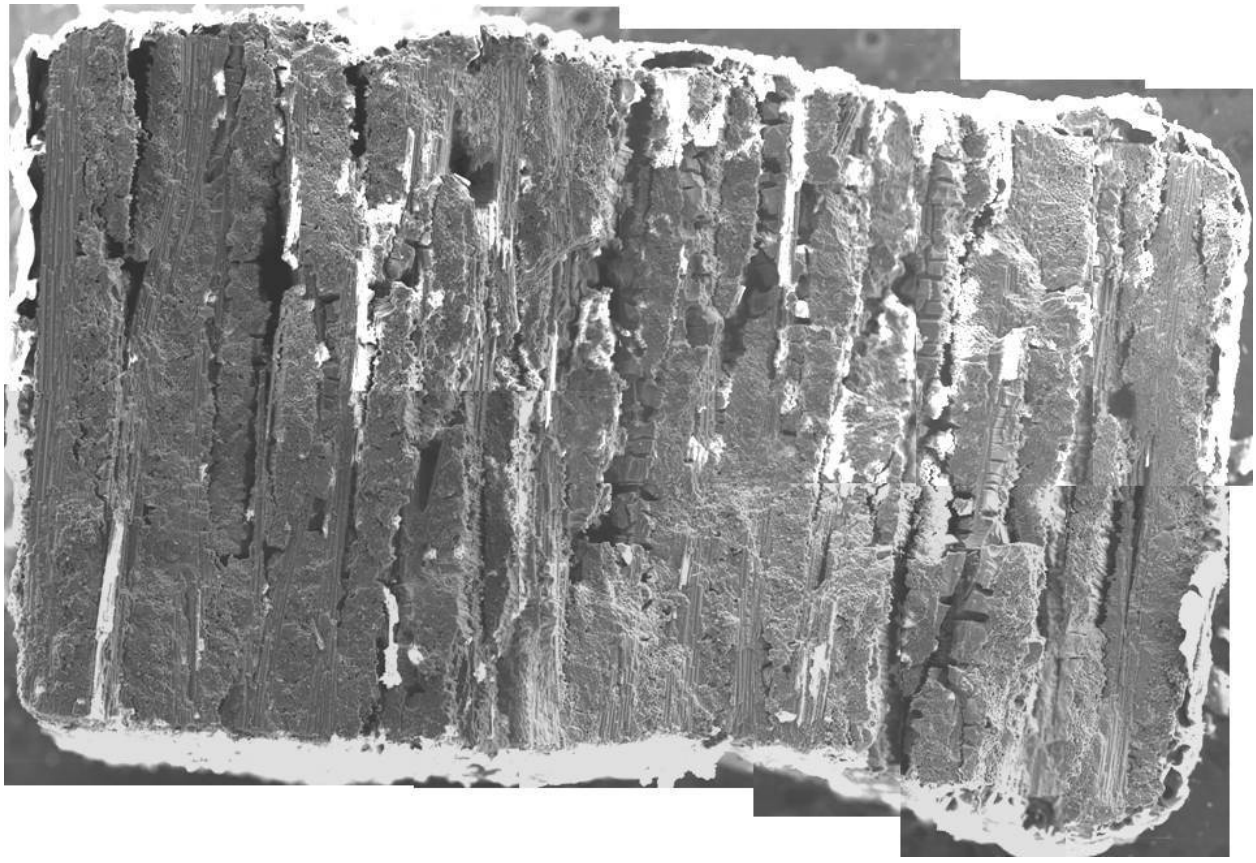

Figure 71: SEM composite micrograph of specimen S10A subjected to fatigue at 1000 °C in steam (f = 1.0 Hz, σ_{max} = 80 MPa, N_f = 73,084). Fracture surface normal to the applied load.

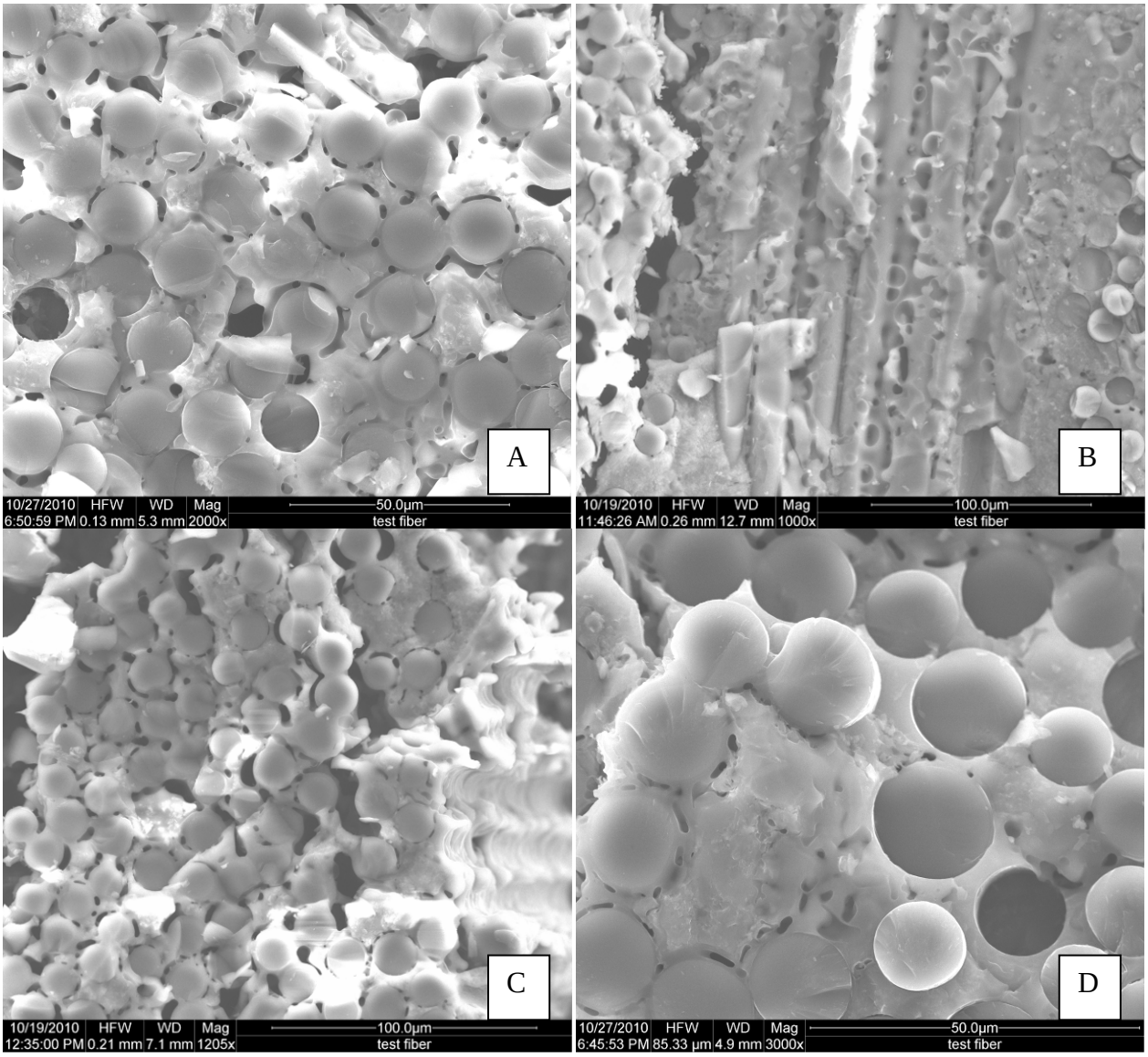

Figure 72: SEM micrographs of specimen S10A subjected to fatigue at 1000 °C in steam (f = 1.0 Hz, σ_{max} = 80 MPa, N_f = 73,084). Fracture surface normal to the applied load.

The fracture surface of specimen S8E, also subjected to fatigue with the maximum stress of 80 MPa in steam, is shown below in Figures 73-75. Having survived 46,621 cycles, specimen S8E was subjected to a steam environment at 1000 °C for just over 12 h. Considerable amounts of oxidative damage can yet be seen throughout the composite. The SEM image in Figure 74 shows

that specimen S8E exhibits considerably less delamination than other specimens tested in steam. Additionally the area above the dotted line in Figure 74 exhibits no fiber pullout while below the dotted line some minor fiber pullout is observed. Figures 75 A and B show some oxidation of the fiber/matrix interphase. Figure 75 B also shows the semi-transparent silica glass covering the fiber fracture surfaces. Figures 75 C and D present the first instances of noticeable fiber pullout, though oxidation of the matrix occurs close by as well.

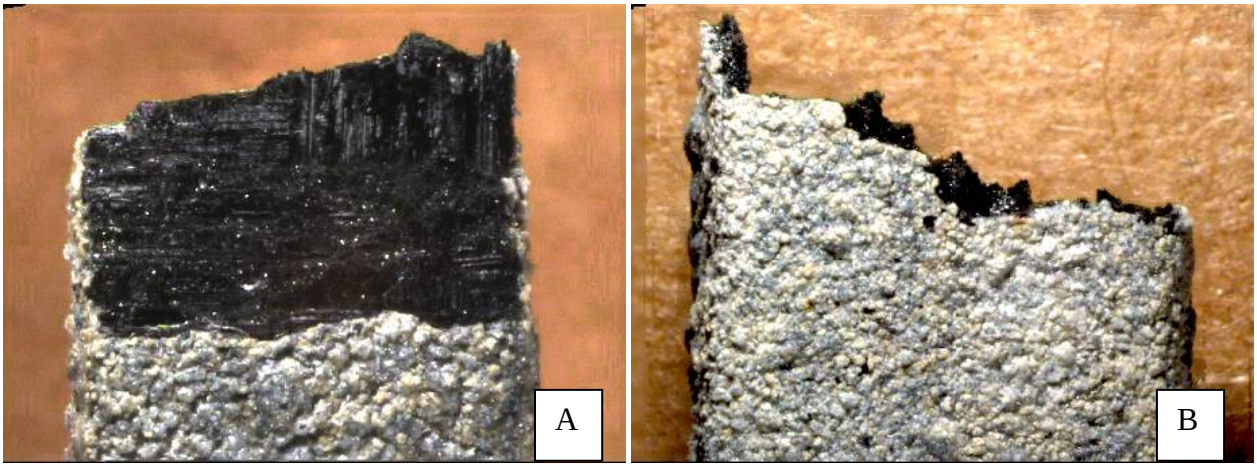

Figure 73: Optical micrographs of specimen S8E, front (A) and side (B), subjected to fatigue at 1000 °C in steam (f = 1.0 Hz, σ_{max} = 80 MPa, N_f = 46,621). Fracture surface normal to the applied load.

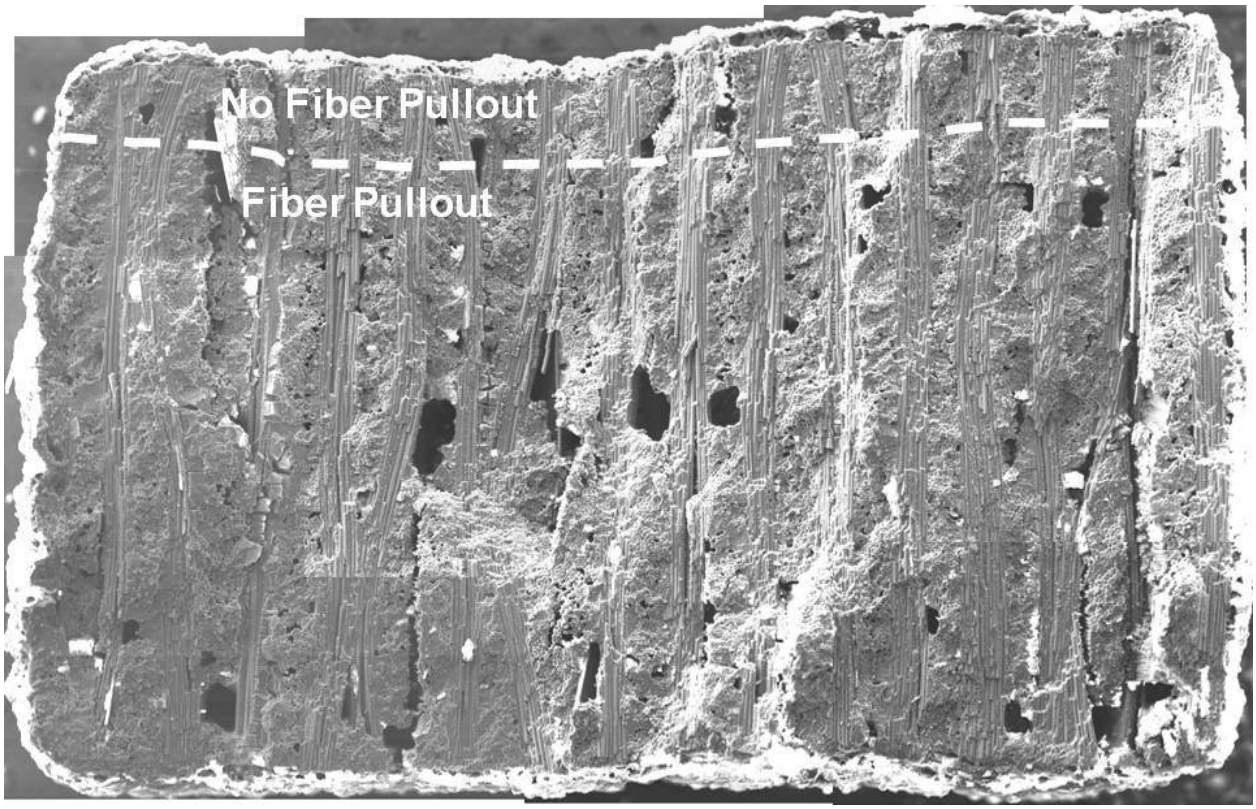

Figure 74: SEM composite micrograph of specimen S8E subjected to fatigue at 1000 °C in steam (f = 1.0 Hz, σ_{max} = 80 MPa, N_f = 46,621). Fracture surface normal to the applied load.

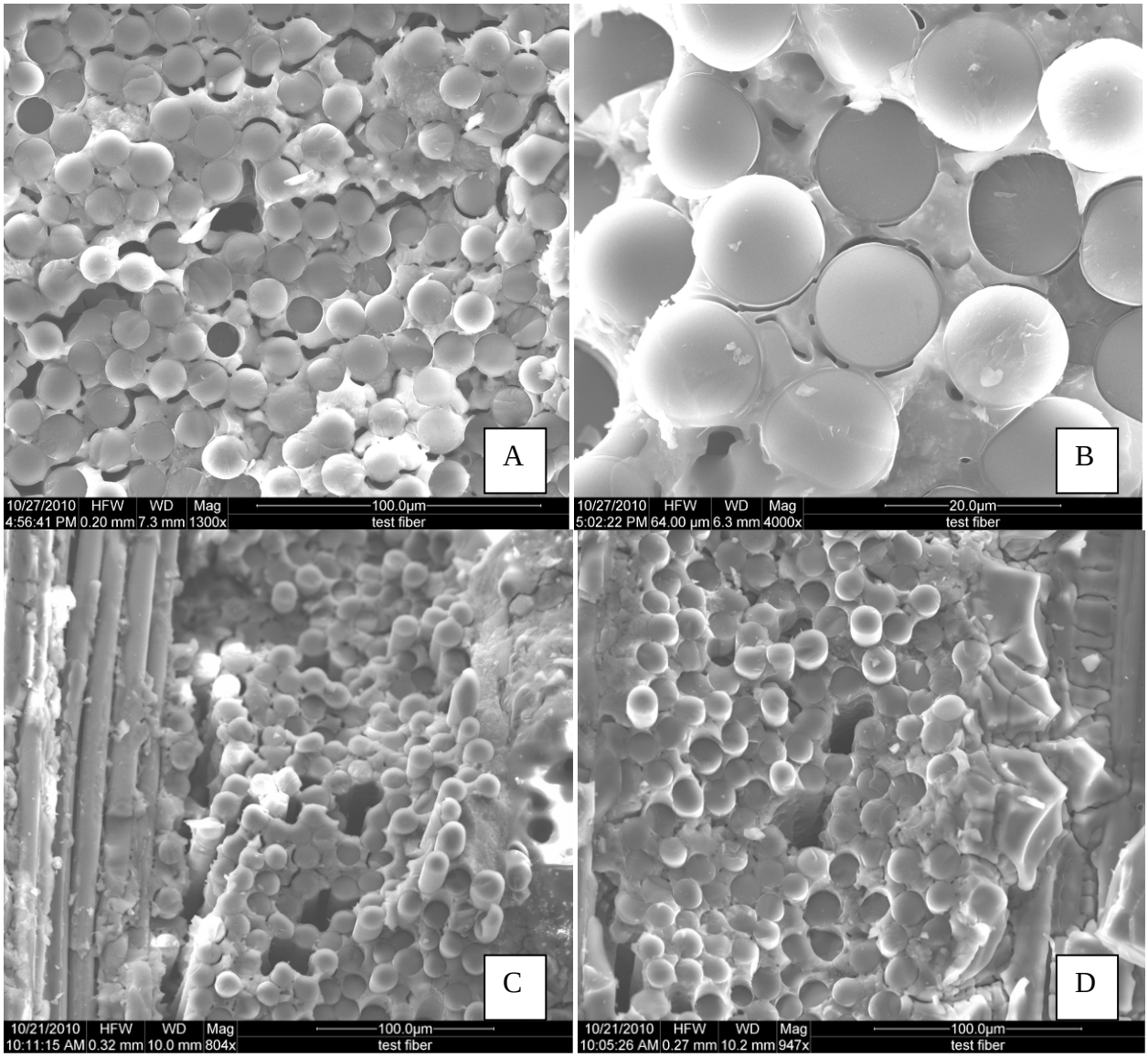

Figure 75: SEM micrographs of specimen S8E subjected to fatigue at 1000 °C in steam (f = 1.0 Hz, σ_{max} = 80 MPa, N_f = 46,621). Fracture surface normal to the applied load.

Figures 76-78 show the fracture surface of specimen S11C, which survived 17,587 fatigue cycles performed with the maximum stress of 100 MPa. Optical micrographs in Figure 76 reveal that the outer surface layer of the specimen has flaked off in large chunks, most likely due to the combination of high fatigue stress and exposure to steam. The loss of the outer surface layer

explains the reduction in cross sectional area of this specimen. Also seen in Figure 76 are minor instances of fiber pullout. However, as seen in Figures 77 and 78, flaking off of the degraded surface layer is the only major sign of oxidation within this specimen. Figure 77 shows a fracture surface similar to those produced in fatigue tests conducted in air, with a considerable amount of fiber pullout seen throughout the fracture surface. Figure 78 A shows brittle fracture of the fibers. Figures 78 B, C and D also display appreciable amounts of fiber pullout with no visible signs of oxidation.

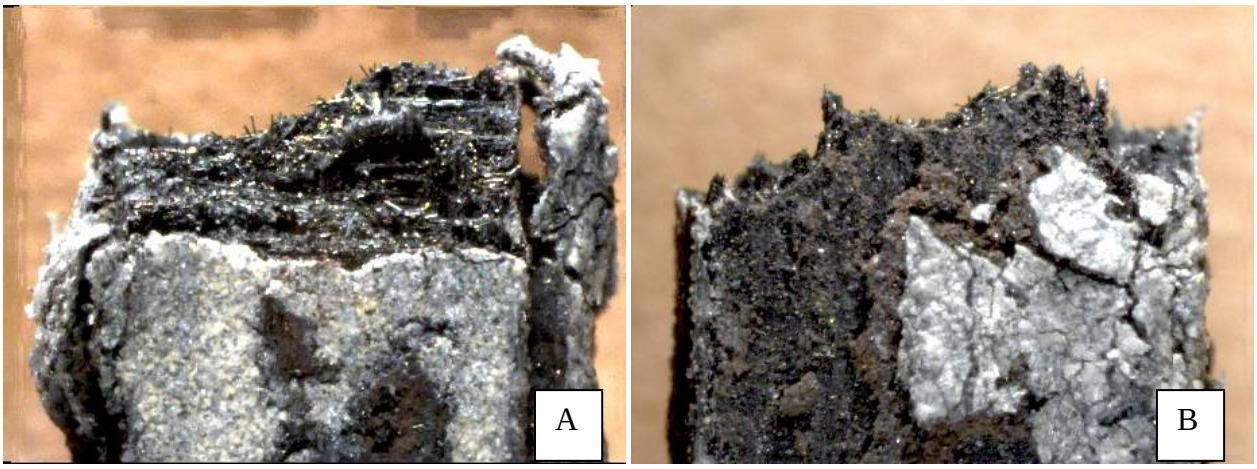

Figure 76: Optical micrographs of specimen S11C, front (A) and side (B), subjected to fatigue at 1000 °C in steam (f = 1.0 Hz, σ_{max} = 100 MPa, N_f = 17,587). Fracture surface normal to the applied load.

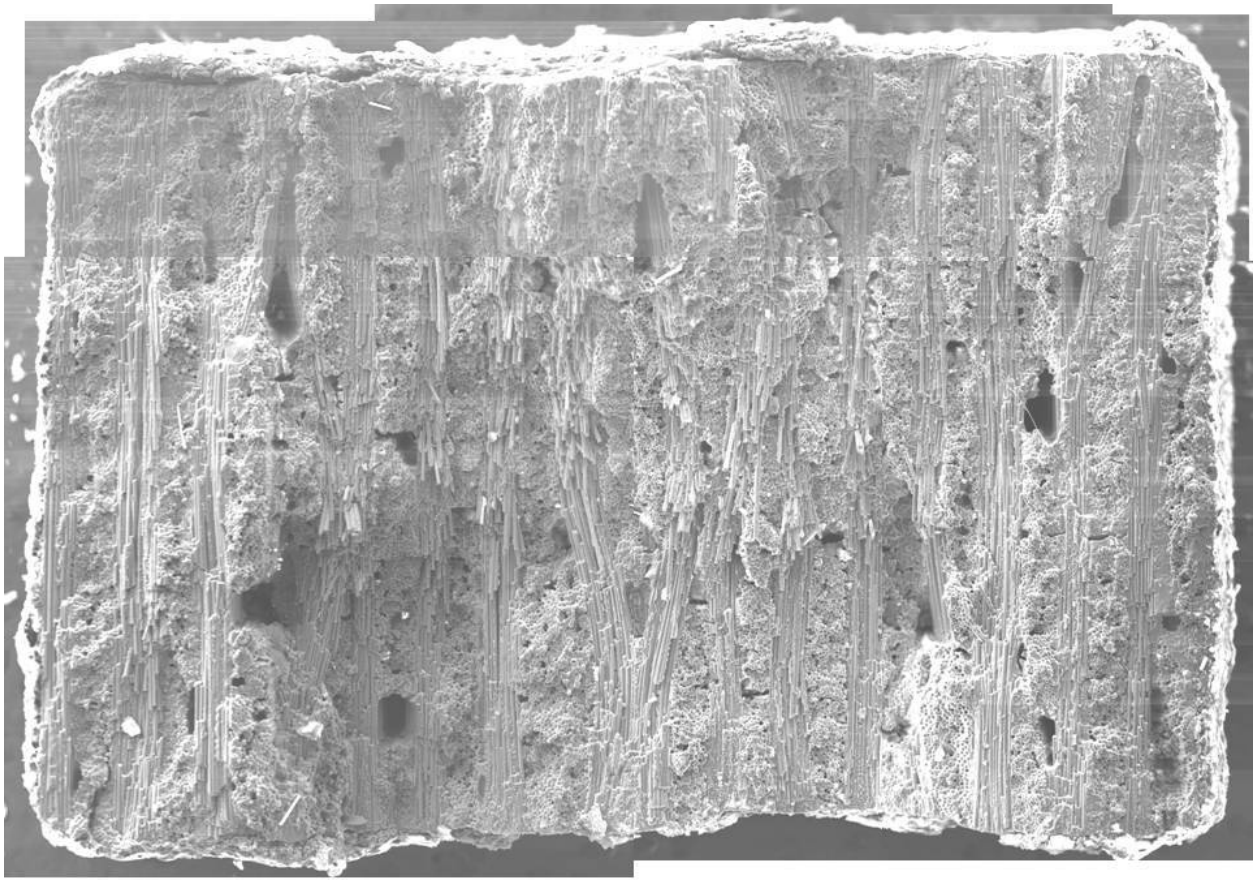

Figure 77: SEM composite micrograph of specimen S11C subjected to fatigue at 1000 °C in steam (f = 1.0 Hz, σ_{max} = 100 MPa, N_f = 17,587). Fracture surface normal to the applied load.

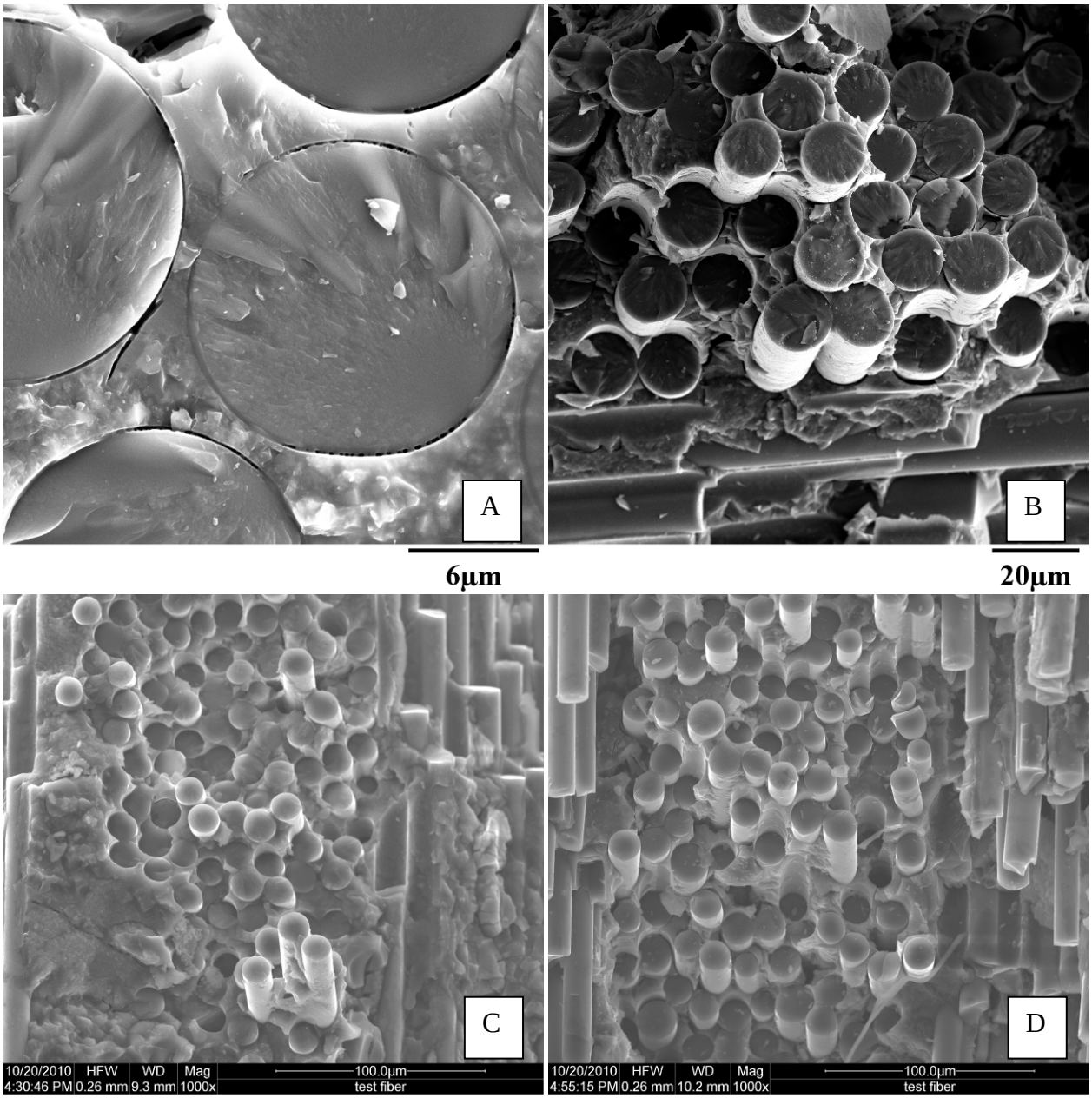

Figure 78: SEM micrographs of specimen S11C subjected to fatigue at 1000 °C in steam (f = 1.0 Hz, σ_{max} = 100 MPa, N_f = 17,587). Fracture surface normal to the applied load.

VI. Conclusions and Recommendations

6.1 Conclusions

The tensile stress-strain behavior of the CG NICALON™/BN/SiC composite was studied and the tensile properties measured at 1000 °C in laboratory air. The composite exhibited inferior tensile properties compared to other materials of this type. At 1000 °C the UTS was a low 136 MPa and the Young's Modulus was 59.1 GPa. The stress-strain behavior at 1000 °C was nearly linear elastic until failure, which is more typical for the composites with an exceptionally weak porous matrix and not for composites with a dense matrix.

Tension-tension fatigue behavior of the CG NICALON™/BN/SiC composite was studied for fatigue stress levels of 60-100 MPa at 1000 °C in laboratory air and steam environments. The fatigue limit in air (based on a run-out condition of 200,000 cycles) is 80 MPa (59% UTS at 1000 °C). The material retains 82% of its tensile strength. Surprisingly the modulus did not degrade with fatigue cycling although strain ratcheting was observed. Progressive strain accumulation with cycling may be attributed to the realignment of the transverse fiber bundles and stretching of the weave. This may have been supported by the lack of constraint given to the specimen width, with less than one unit cell of weave captured by the cut surface of each specimen.

The presence of steam significantly degraded the fatigue performance of the composite. The fatigue limit in steam is below 60 MPa (< 44% UTS at 1000 °C). Specimens subjected to fatigue in steam exhibited considerable through-thickness swelling, which caused an increase in the cross sectional area of up to 31%. No through-thickness swelling was observed for specimens subjected to fatigue in air.

Specimens cut from panels S5, S7, S8, and S9 produced considerably lower tensile strength values and exhibited lower fatigue resistance than the specimens cut from panels 10 and 11. This difference in mechanical performance is attributed to differences in fiber coating thickness (0.15-0.21 μm for panels S5, S7, S8, and S9 and 0.16-0.19 μm for panels S10 and S11) and to an increased prevalence of voids in panels S5, S7, S8, and S9. The voids introduced stress concentrations and allowed for easier ingress of oxidizing environments into the composite, leading to further oxidation and subsequently earlier failure of specimens from panels S5, S7, S8, and S9.

Fracture surfaces produced in fatigue tests performed at 1000 °C in air showed very little oxidation. Some minimal signs of oxidative degradation were observed in the fracture surface of specimen S11E (σ_{max} = 100 MPa, N_f = 168,255 cycles). However, all fracture surfaces produced in fatigue tests performed at 1000 °C in steam exhibited significant degradation by oxidation. Specimens S11C (σ_{max} = 100 MPa, N_f = 17,587 cycles) and S8E (σ_{max} = 80 MPa, N_f = 46,621 cycles), which produced fracture surfaces with significant fiber pullout represent an exception.

Minor areas of oxidation were observed on the generally non-oxidized fracture surfaces, suggesting that the protective seal coat did not seal well enough to protect the composite interior from the oxidizing environment. Additionally the continuous development of small matrix cracks further escalated this problem.

The analysis of the fatigue data and the examination of the micrographic images indicates that the matrix is not sufficiently dense, possibly due to the SiC powder infused into the matrix, or because of too few infiltration and pyrolysis cycles, or due to both. The low matrix density is manifested in the tensile stress-strain curves that lack a distinguishable proportional limit (characterizing this composite then as a fiber-dominated composite). Composite micrographs also suggest that the matrix is more porous than dense.

Considerably less oxidation occurred in the specimens that exhibited shorter fatigue lifetimes, although in this case the interior of the composite appeared to be exposed to the oxidizing environment from the start of the test either due to poor seal coats or due to microcracks forming in the seal and propagating through the seal coat into the matrix during the first few cycles.

Several levels of oxidation were observed in the fracture surfaces, which represented the severity of degradation. In the severest case it was impossible to discern the fiber fracture surfaces in high magnification SEM micrographs. In the case of moderate degradation, only minor oxidation of the BN fiber coating was observed throughout the fracture surface. In the case of the least degradation only minor oxidation was observed along the edges of the fracture surface. In the best cases, little or no oxidation was observed.

It is recognized that the art of making CMCs is still being refined. However, processing flaws cannot be overlooked as a source of inconsistent properties and inadequate performance. Fiber degradation during processing, interphases too thin or too thick, matrix porosity and many other factors all play a significant role in the production of a successful ceramic matrix composite. If any of these factors are neglected serious implications will result.

6.2 Recommendations

Additional tests to characterize fatigue response at higher and lower frequencies would be beneficial.

Appendix A

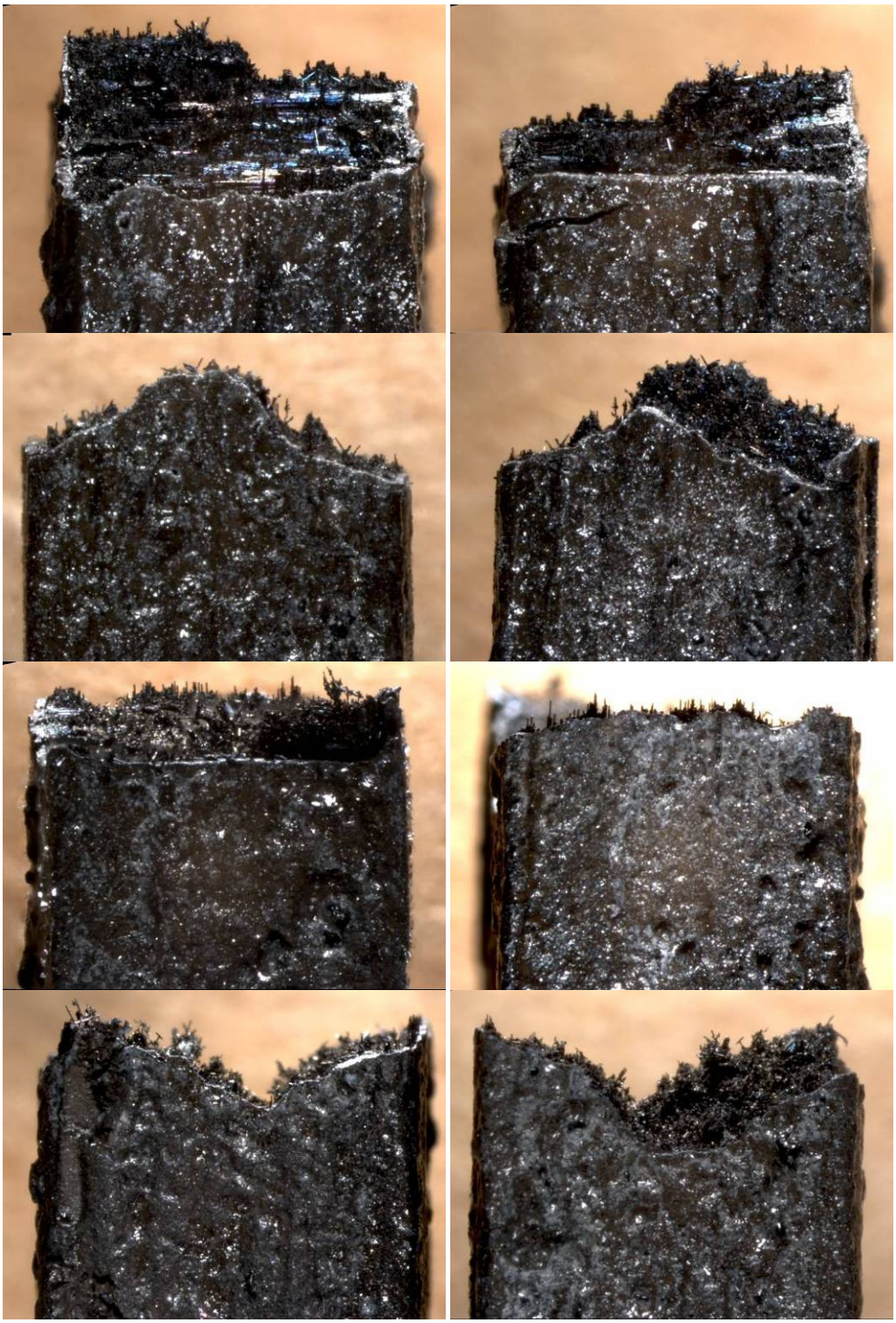

Figure 79: Optical micrographs of specimen S5A subjected to tensile test to failure at 1000 °C in air. Fracture surface normal to the applied load. (UTS = 98.6 MPa, E = 42.2 GPa).

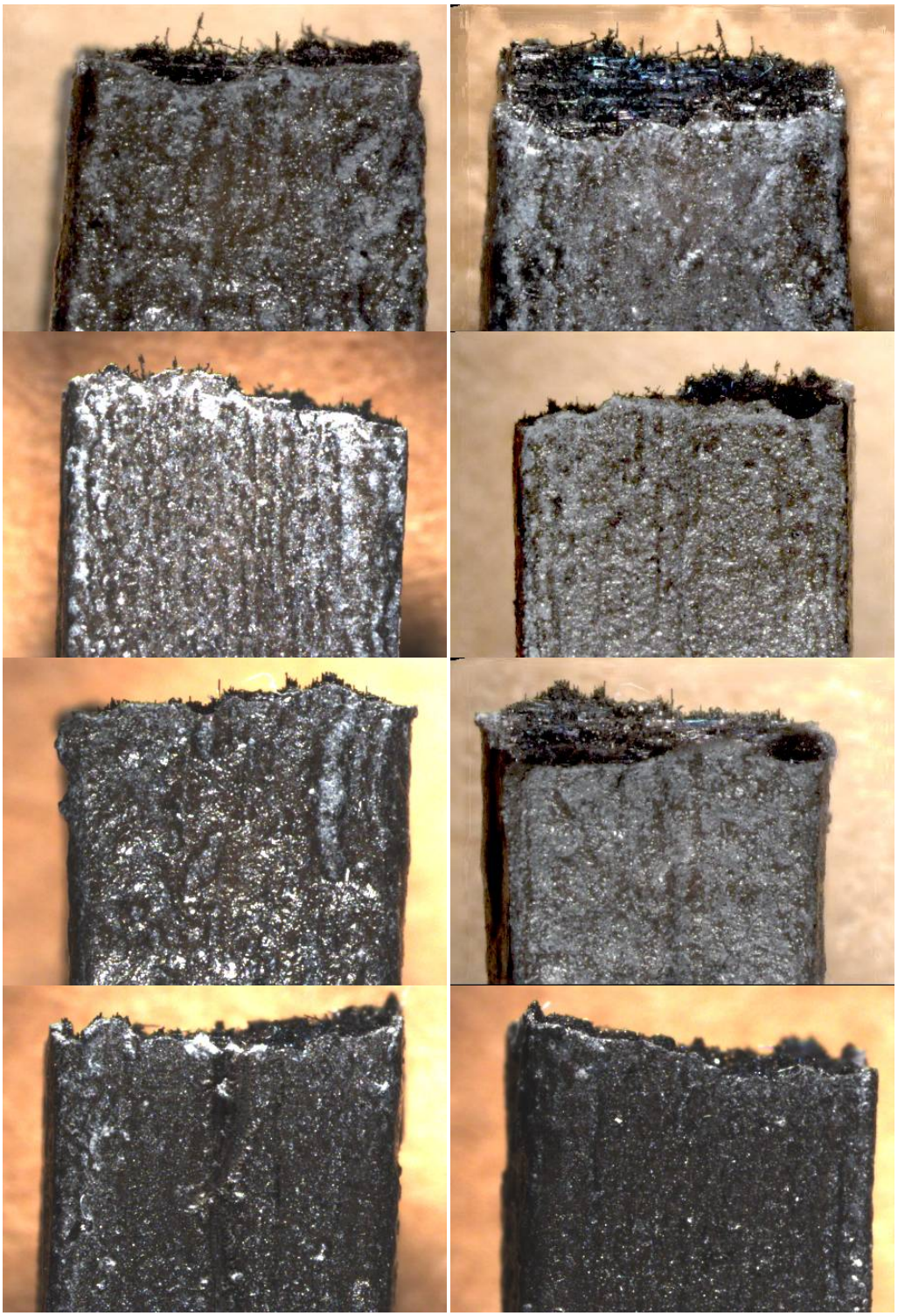

Figure 80: Optical micrographs of specimen S7C subjected to tensile test to failure at 1000 °C in air. Fracture surface normal to the applied load. (UTS = 104 MPa, E = 49.1 GPa).

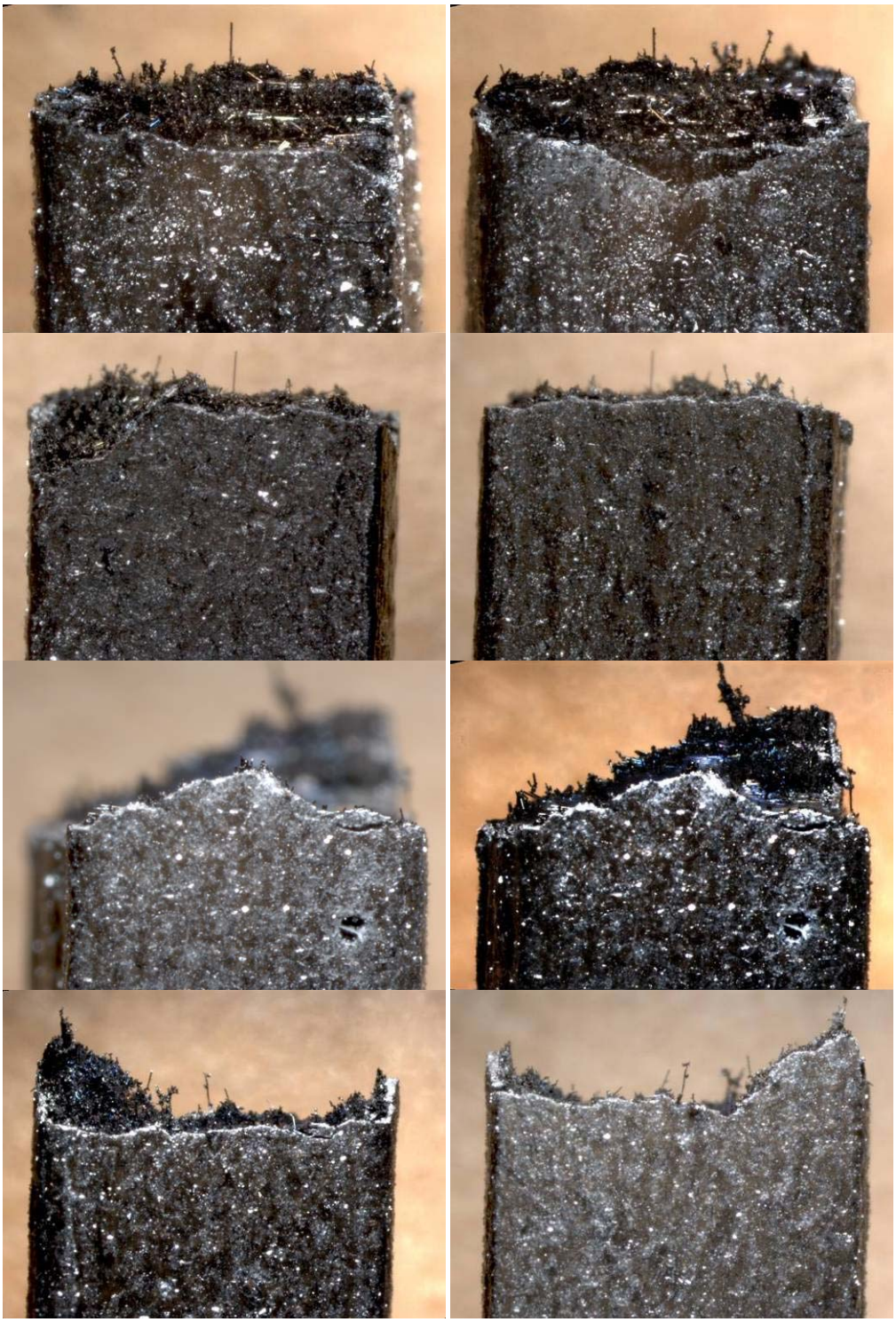

Figure 81: Optical micrographs of specimen S8D subjected to tensile test to failure at 1000 °C in air. Fracture surface normal to the applied load. (UTS = 106 MPa, E = 50.3 GPa).

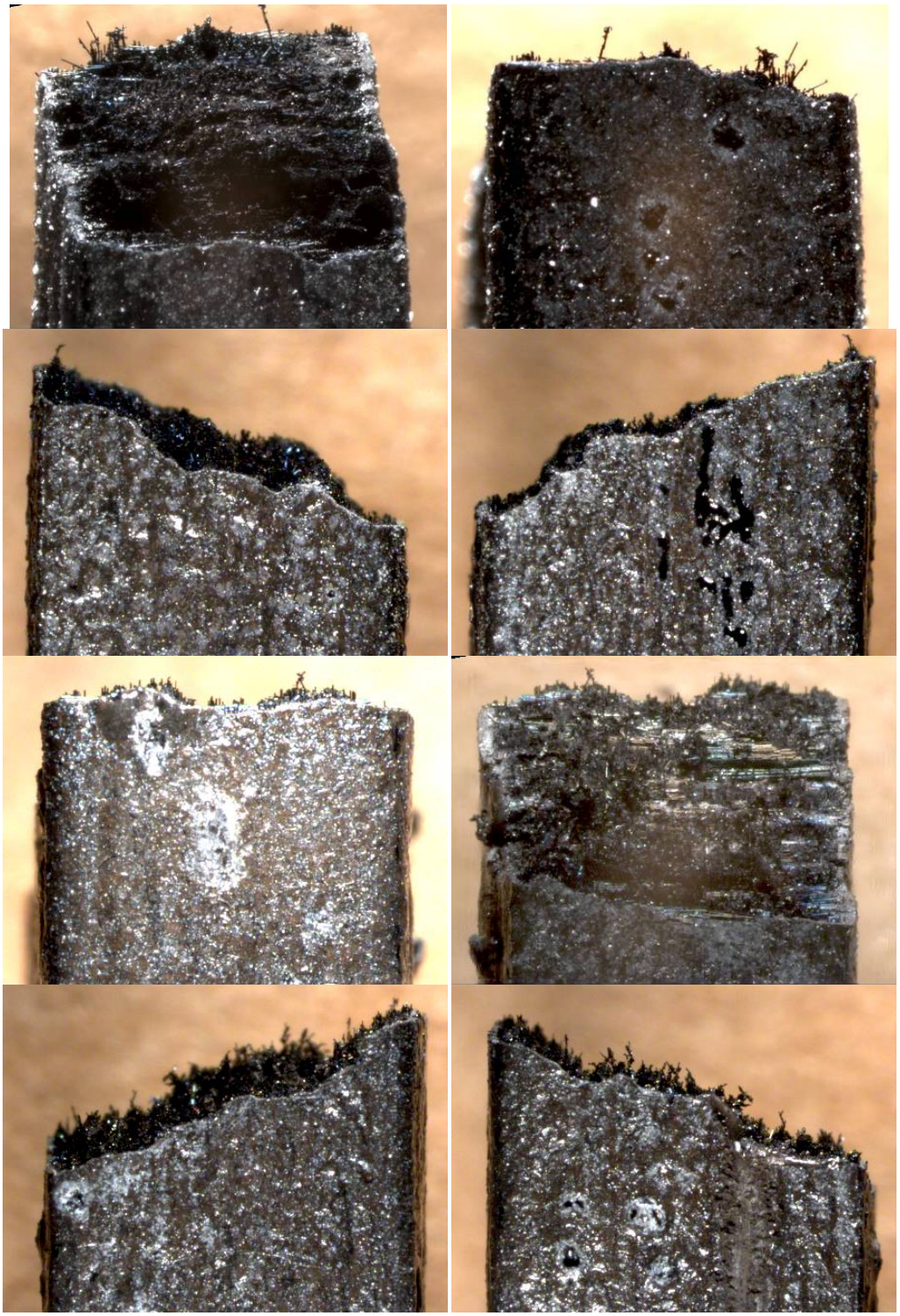

Figure 82: Optical micrographs of specimen S9A subjected to tensile test to failure at 1000 °C in air. Fracture surface normal to the applied load. (UTS = 114 MPa, E = 48.4 GPa).

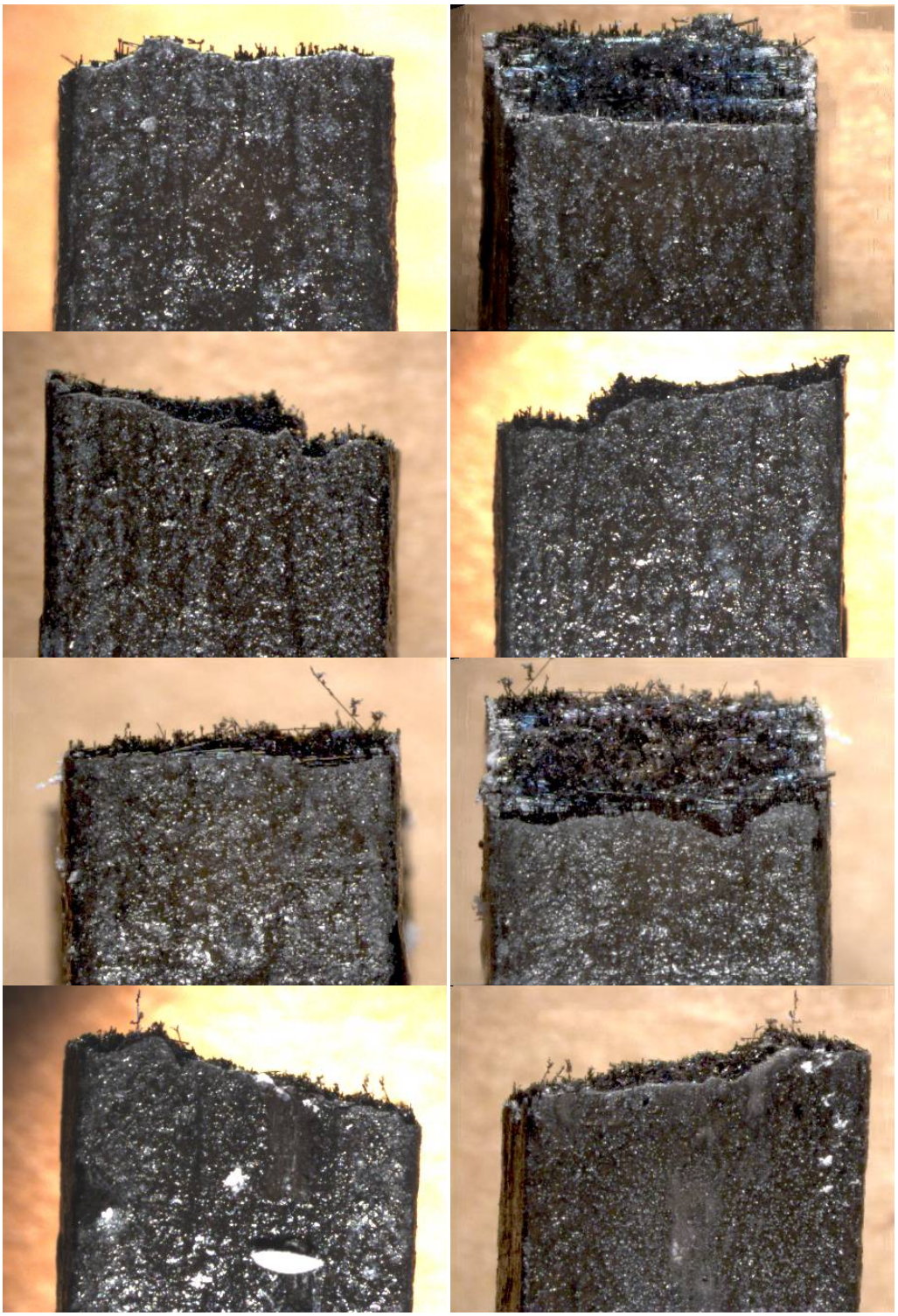

Figure 83: Optical micrographs of specimen S10D subjected to tensile test to failure at 1000 °C in air. Fracture surface normal to the applied load. (UTS = 136 MPa, E = 59.1 GPa).

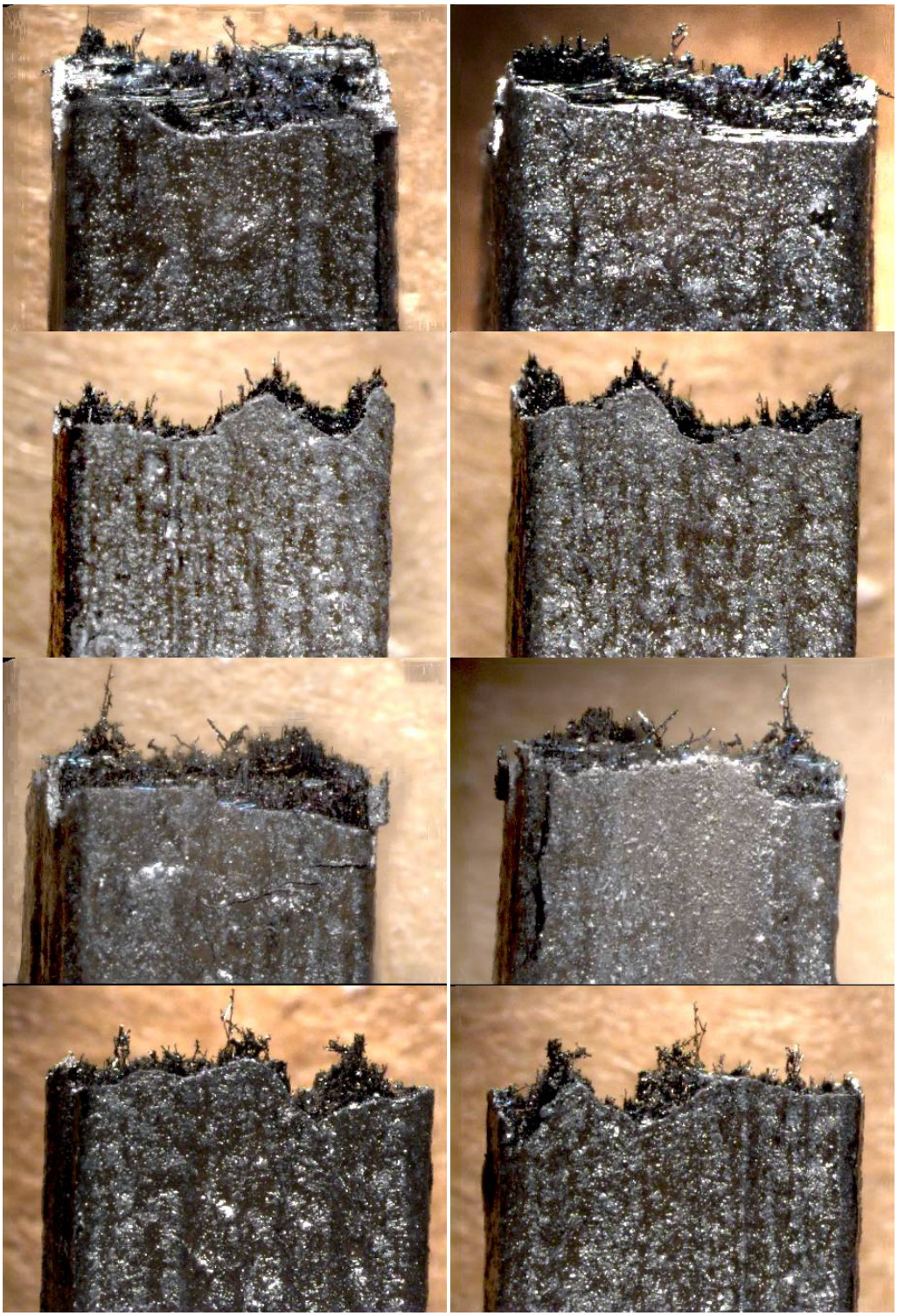

Figure 84: Optical micrographs of specimen S11B subjected to tensile test to failure at 1000 °C in air. Fracture surface normal to the applied load. (UTS = 124 MPa, E = 49.1 GPa).

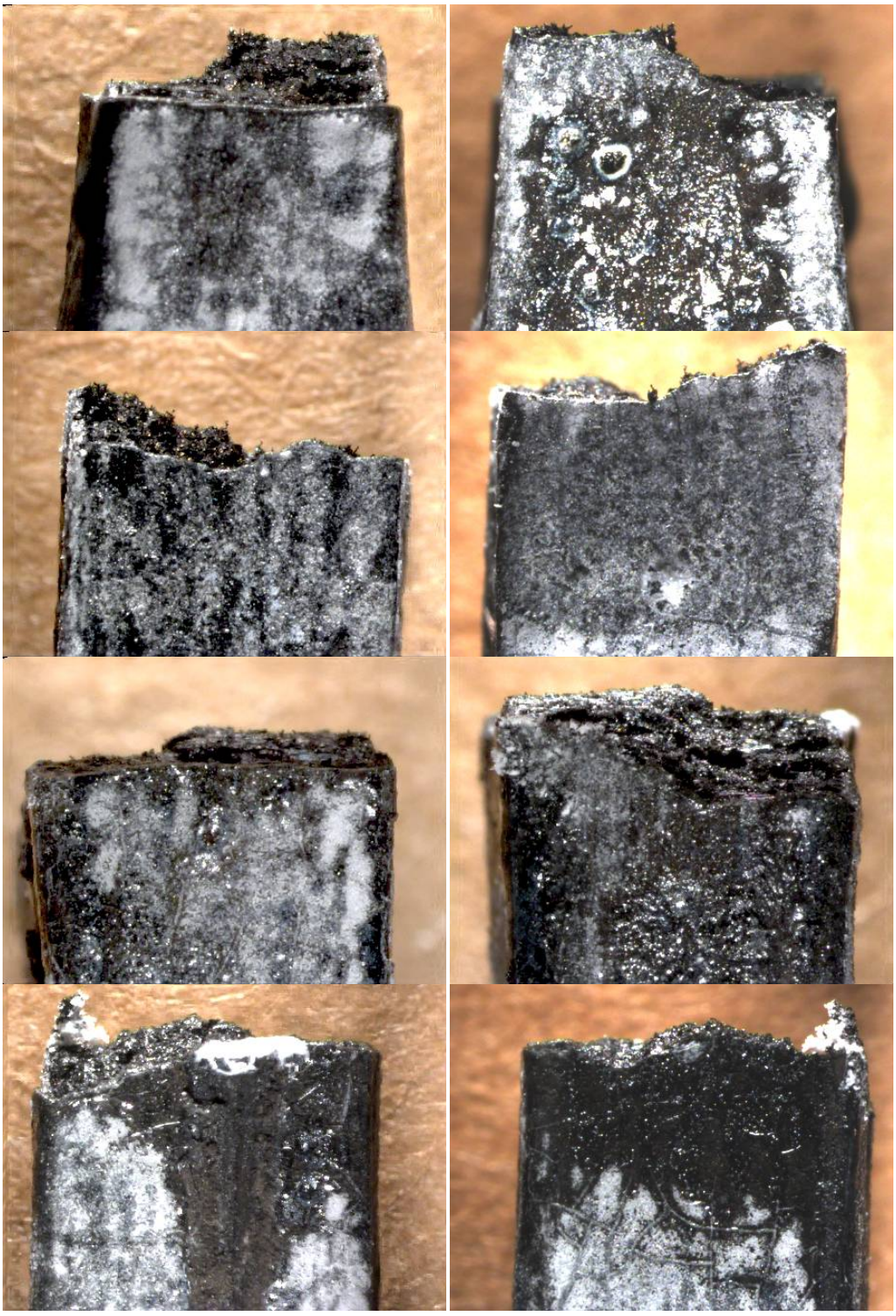

Figure 85: Optical micrographs of specimen S7B subjected to fatigue at 1000 °C in air (f = 1.0 Hz, σ_{max} = 100 MPa, N_f = 17,587).

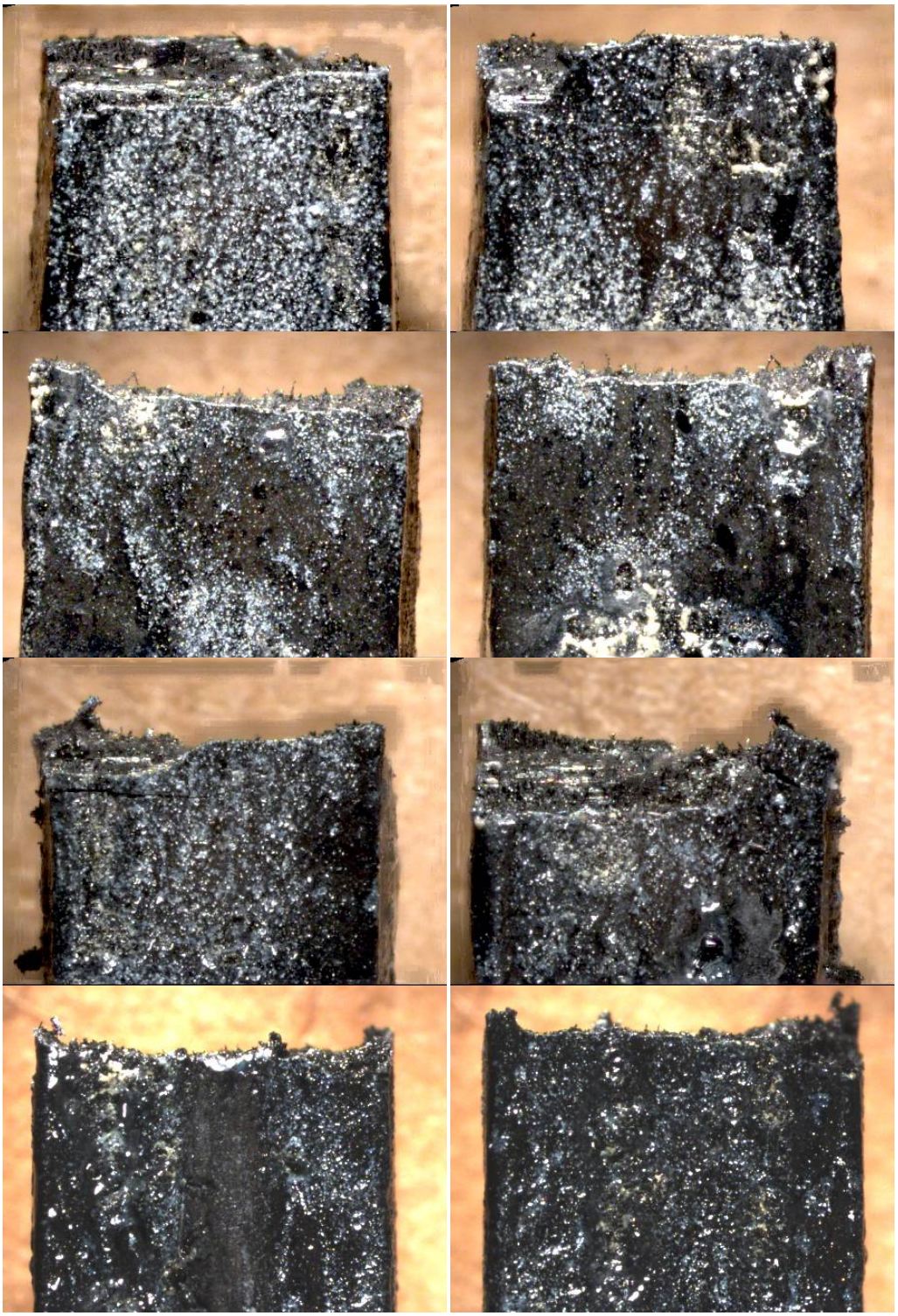

Figure 86: Optical micrographs of specimen S10B subjected to fatigue and a subsequent tensile test to failure at 1000 °C in air (f = 1.0 Hz, σ_{max} = 80 MPa, N_f = 200,000). Fracture surface normal to the applied load.

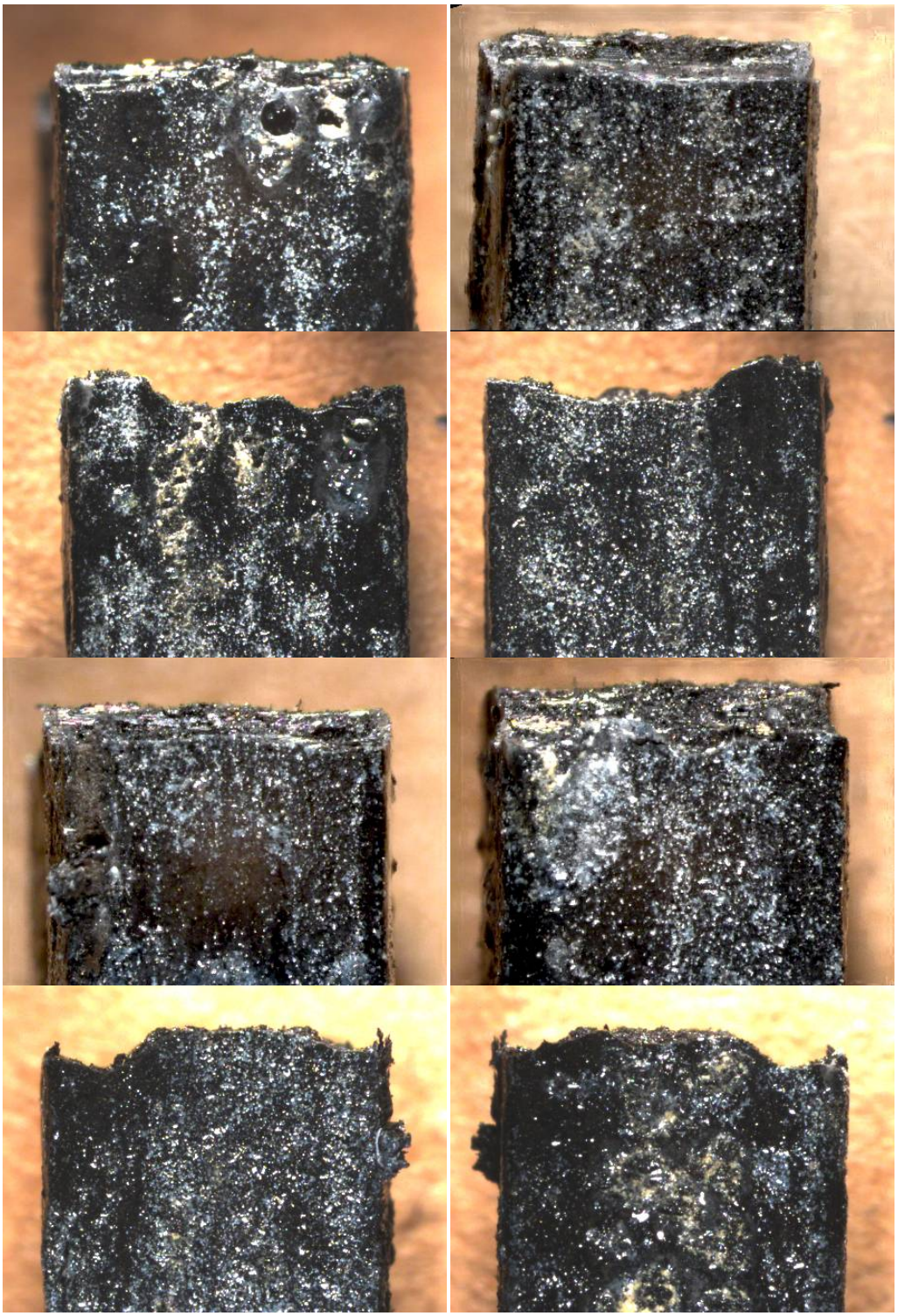

Figure 87: Optical micrographs of specimen S11E subjected to fatigue at 1000 °C in air (f = 1.0 Hz, σ_{max} = 100 MPa, N_f = 168,255). Fracture surface normal to the applied load.

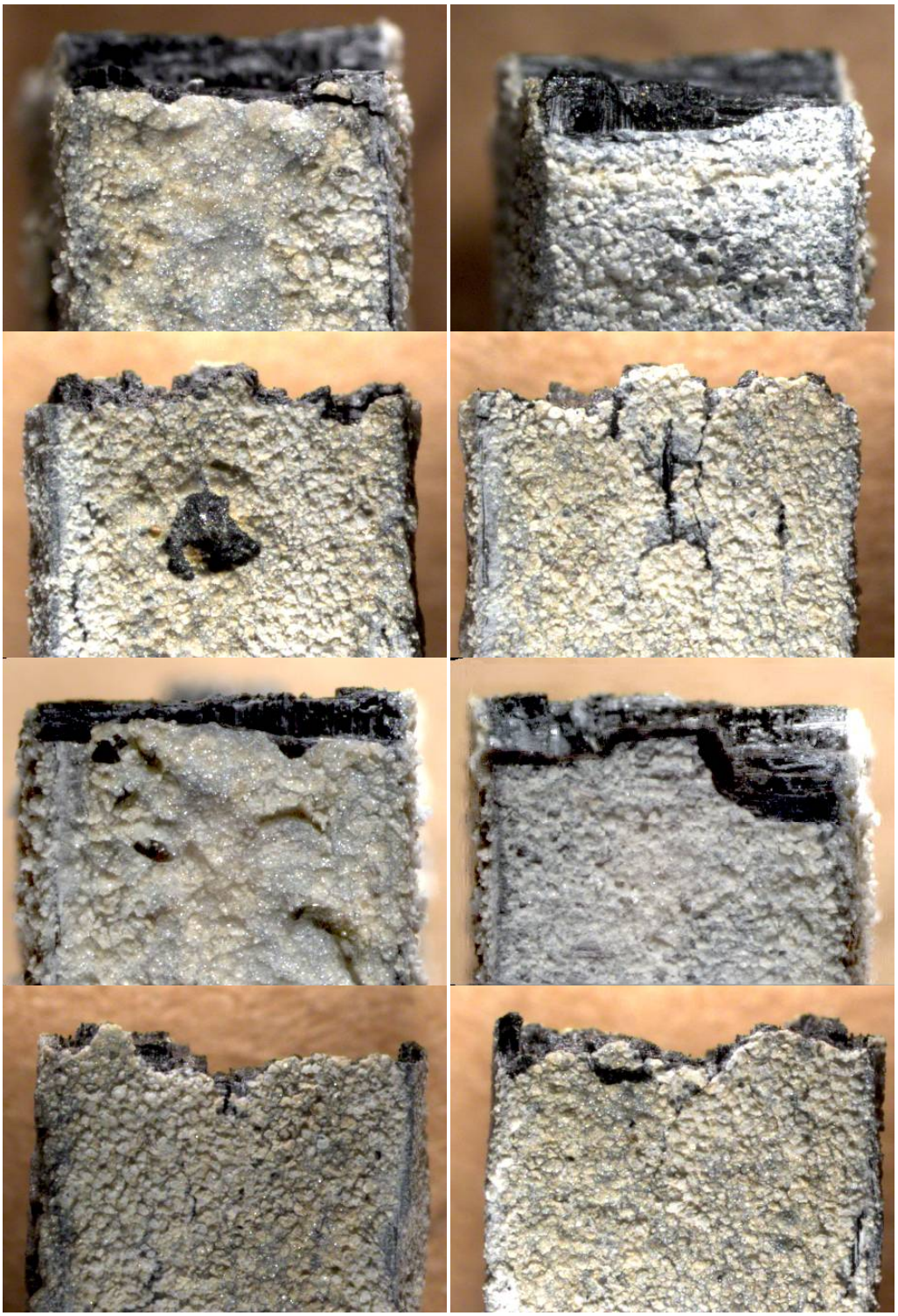

Figure 88: Optical micrographs of specimen S11A subjected to fatigue at 1000 °C in steam (f = 1.0 Hz, σ_{max} = 60 MPa, N_f = 194,930). Fracture surface normal to the applied load.

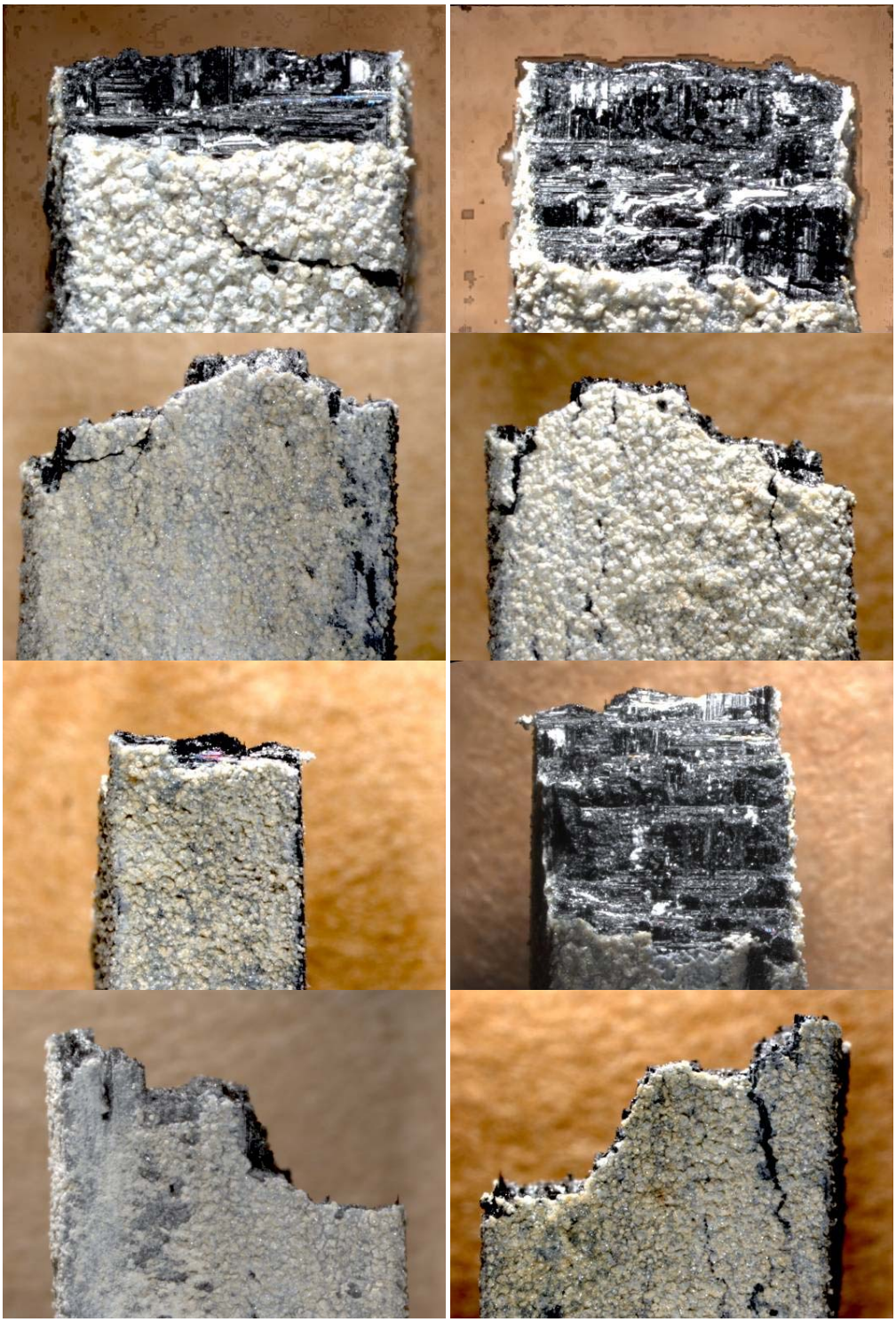

Figure 89: Optical micrographs of specimen S10E subjected to fatigue at 1000 °C in steam (f = 1.0 Hz, σ_{max} = 70 MPa, N_f = 126,593). Fracture surface normal to the applied load.

Figure 90: Optical micrographs of specimen S11D subjected to fatigue at 1000 °C in steam (f = 1.0 Hz, σ_{max} = 70 MPa, N_f = 65,154). Fracture surface normal to the applied load.

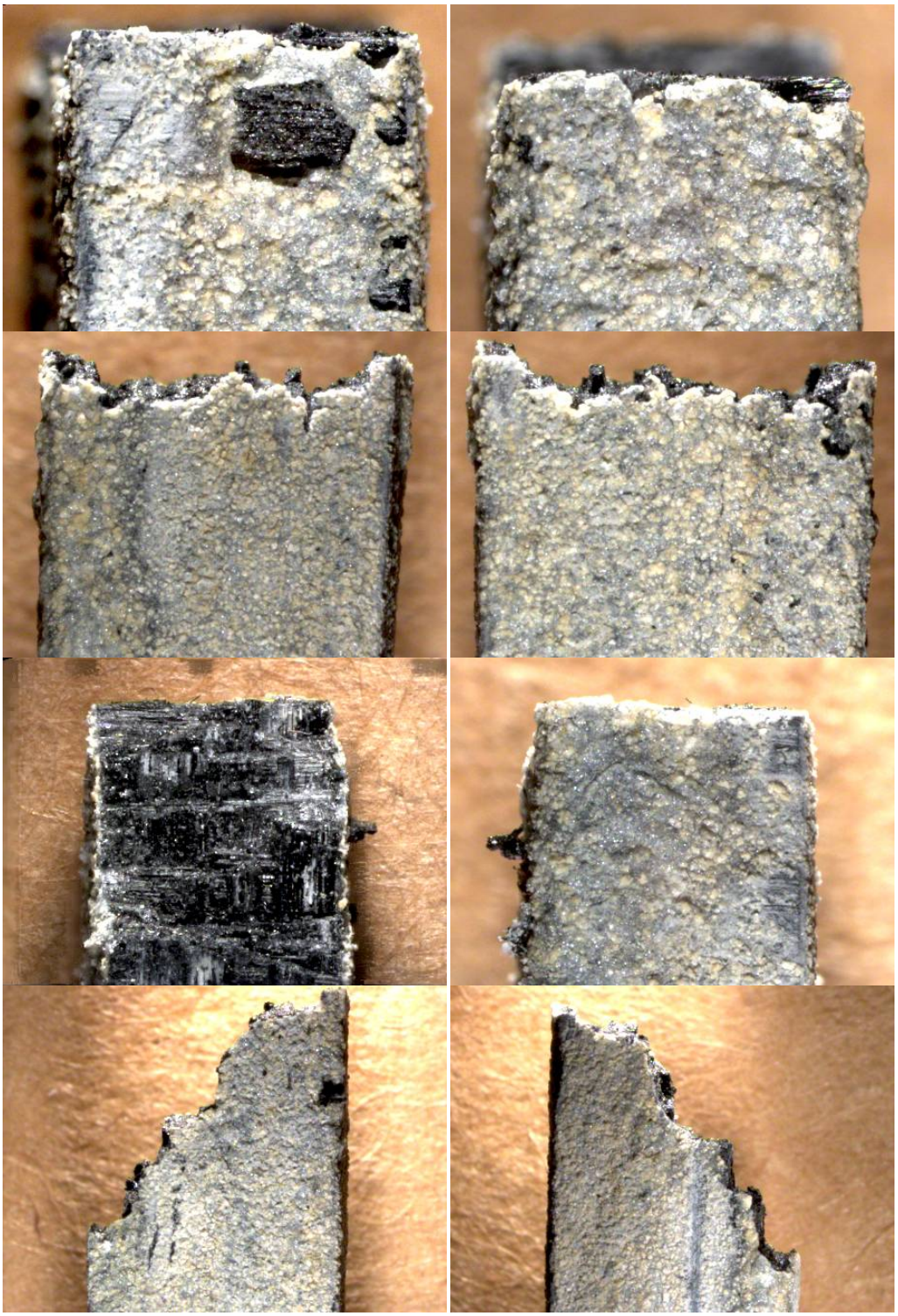

Figure 91: Optical micrographs of specimen S10A subjected to fatigue at 1000 °C in steam (f = 1.0 Hz, σ_{max} = 80 MPa, N_f = 73,084). Fracture surface normal to the applied load.

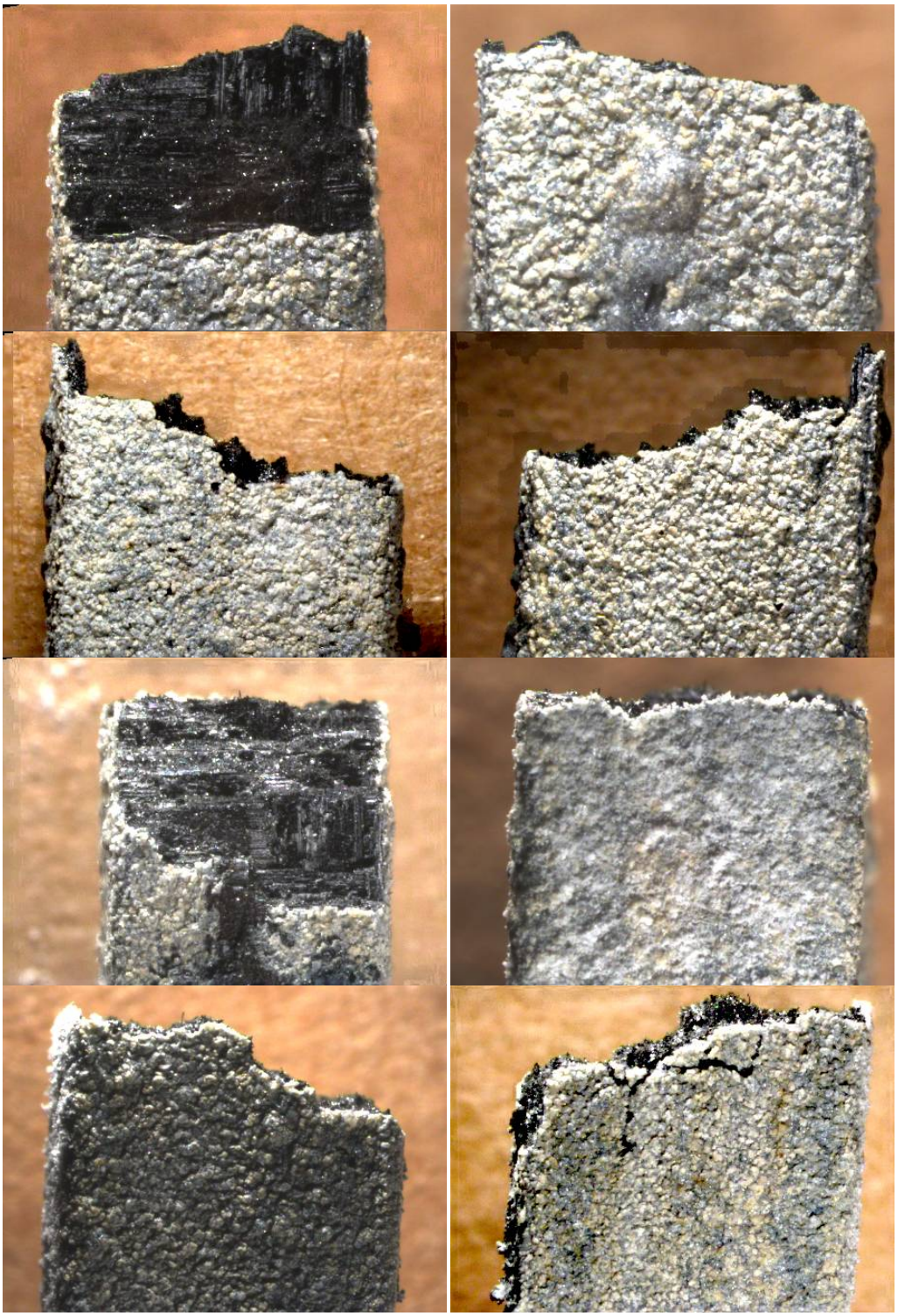

Figure 92: Optical micrographs of specimen S8E subjected to fatigue at 1000 °C in steam (f = 1.0 Hz, σ_{max} = 80 MPa, N_f = 46,621). Fracture surface normal to the applied load.

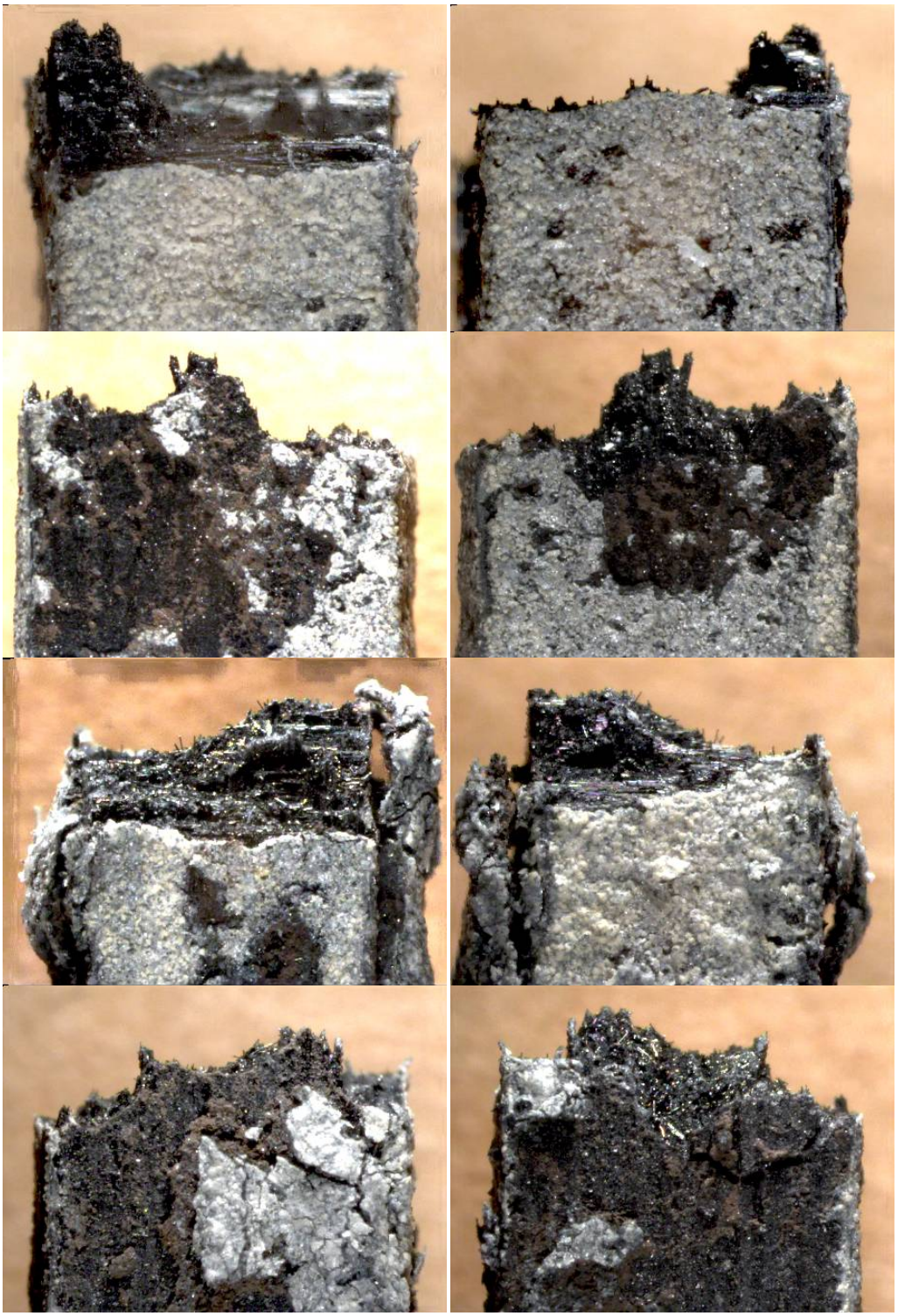

Figure 93: Optical micrographs of specimen S11C subjected to fatigue at 1000 °C in steam (f = 1.0 Hz, σ_{max} = 100 MPa, N_f = 17,587). Fracture surface normal to the applied load.

Appendix B

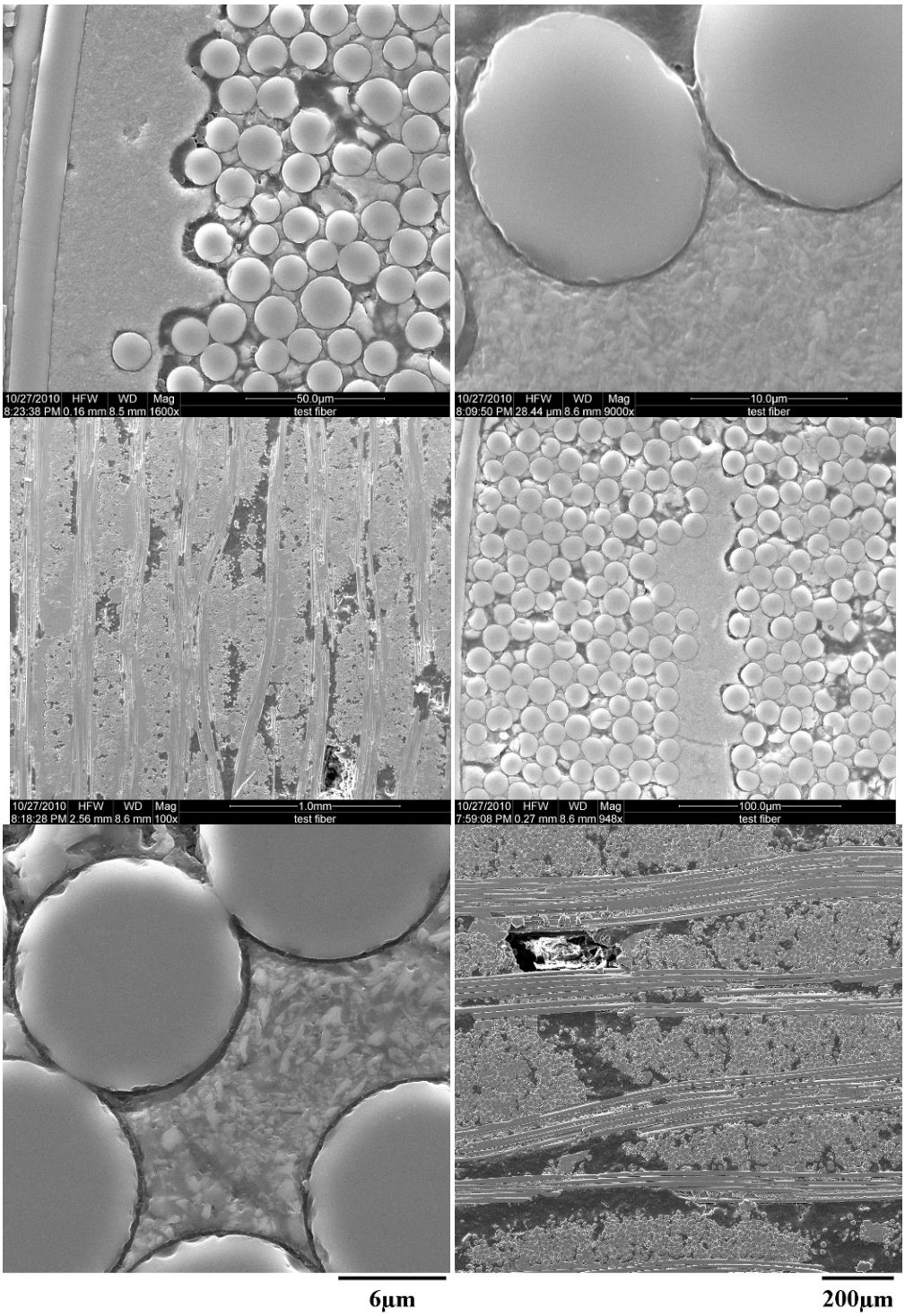

Figure 94: SEM polished micrographs of the as-processed CG NICALON™/BN/SiC composite from panel 5

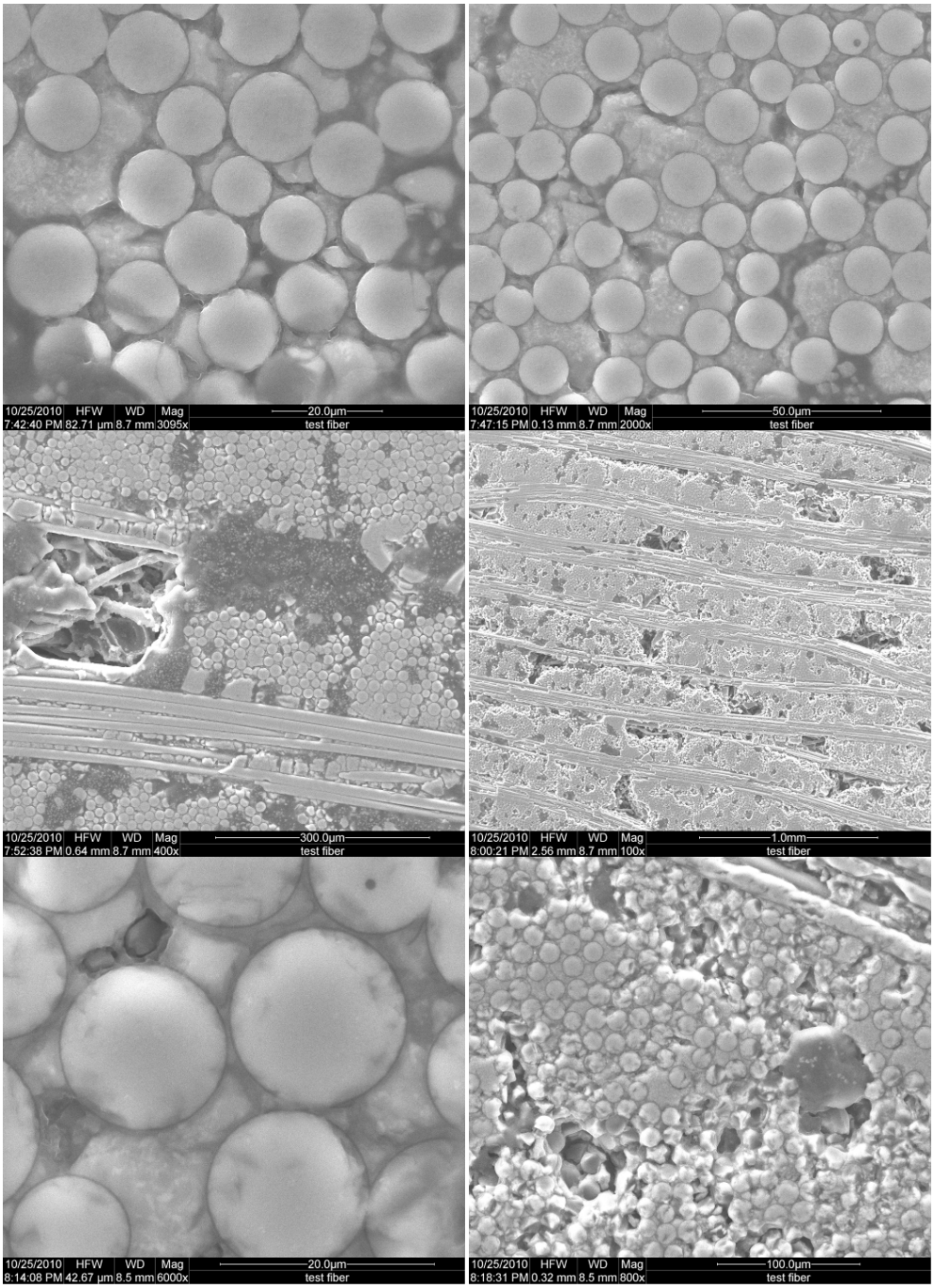

Figure 95: SEM polished micrographs of the as-processed CG NICALON™/BN/SiC composite from panel 7

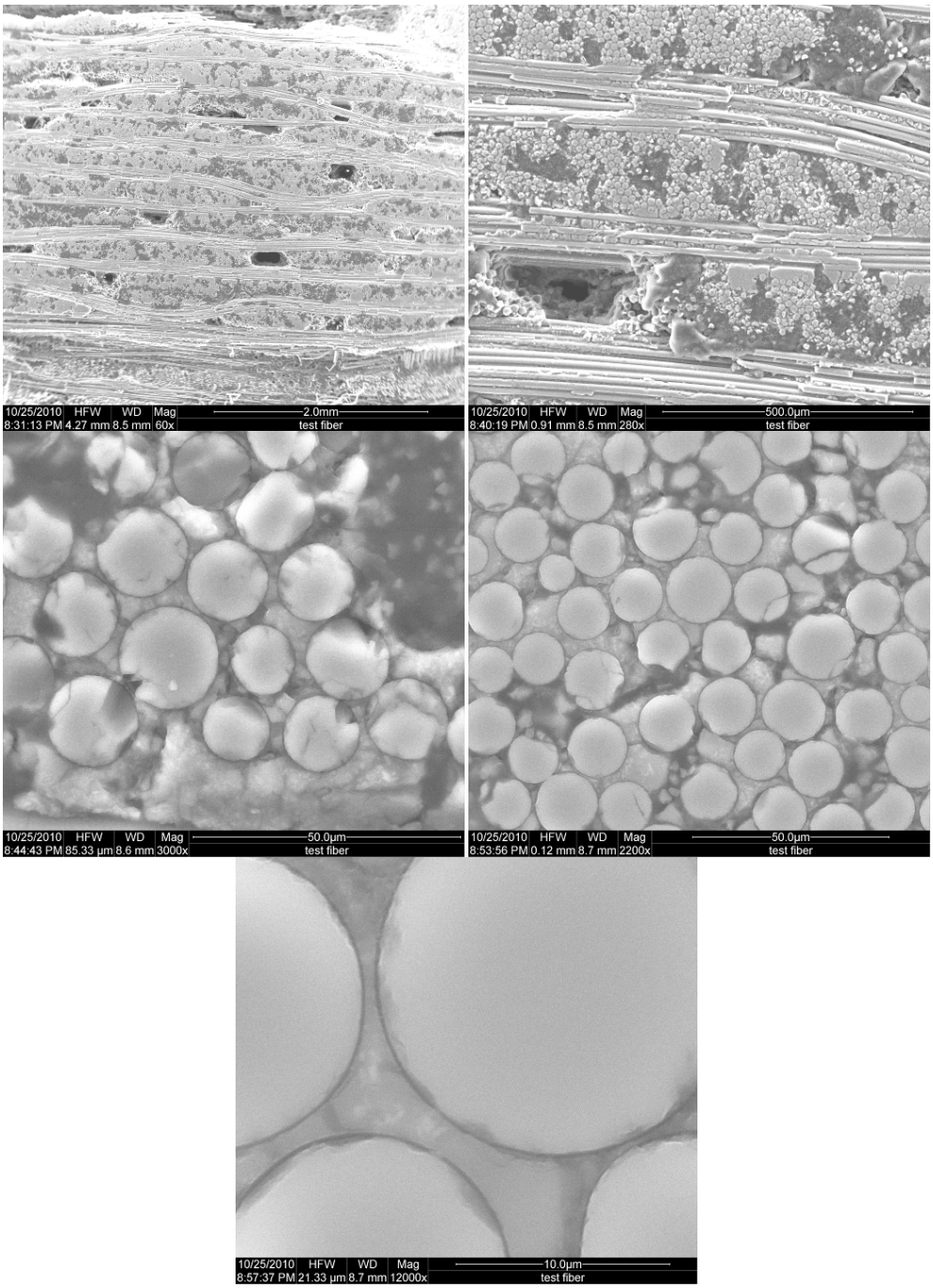

Figure 96: SEM polished micrographs of the as-processed CG NICALON™/BN/SiC composite from panel 8

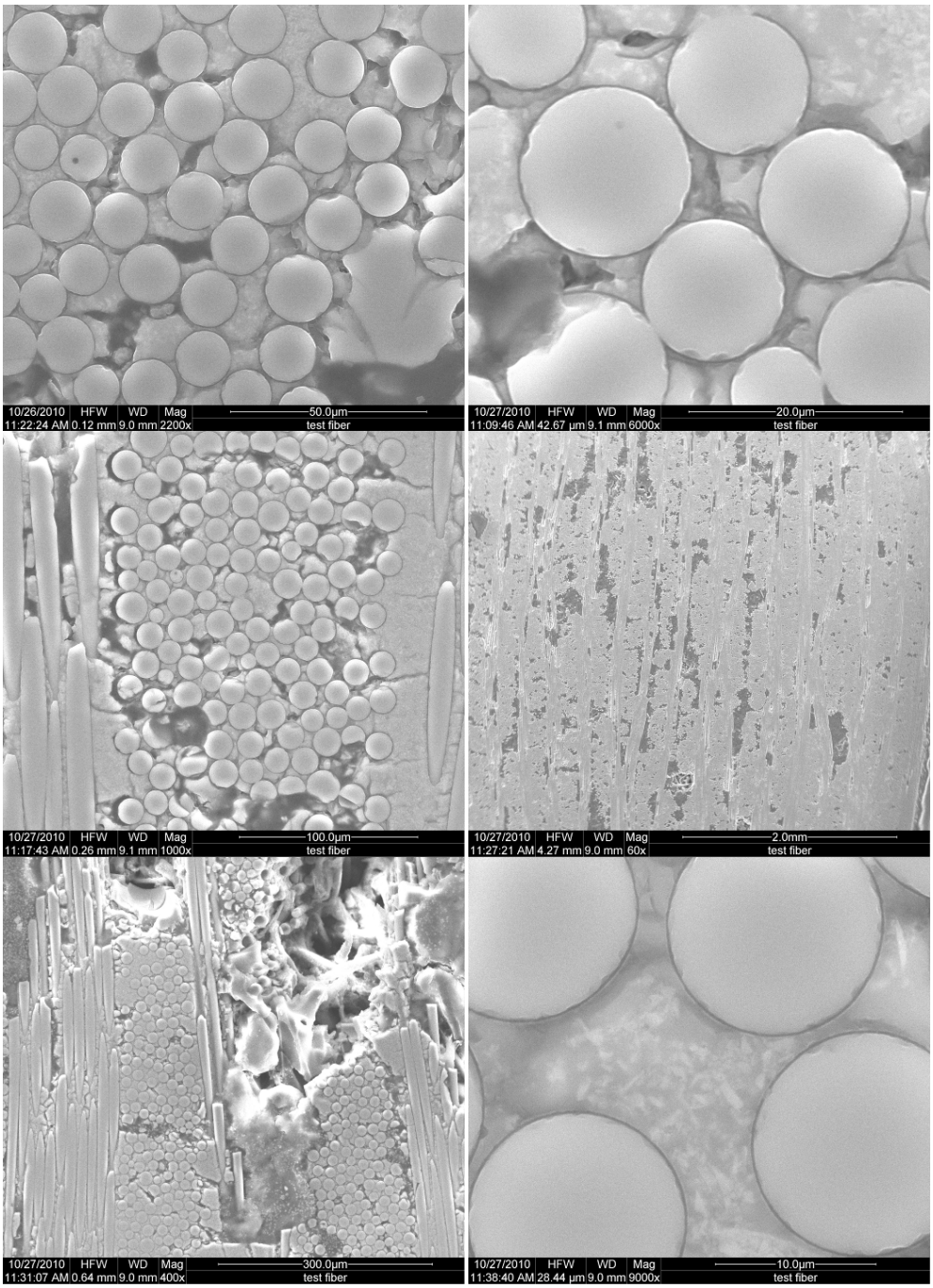

Figure 97: SEM polished micrographs of the as-processed CG NICALON™/BN/SiC composite from panel 9

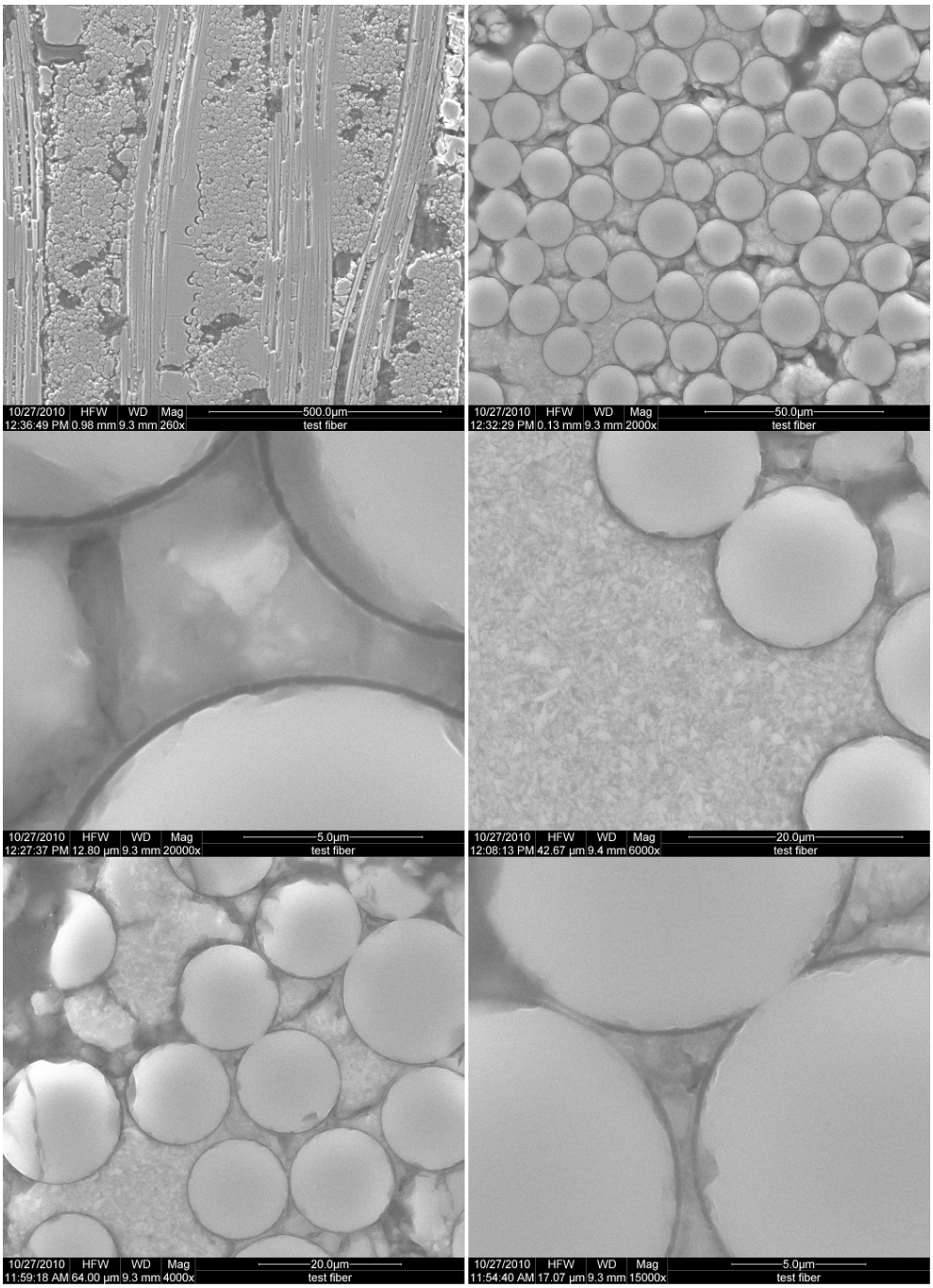

Figure 98: SEM polished micrographs of the as-processed CG NICALON™/BN/SiC composite from panel 10

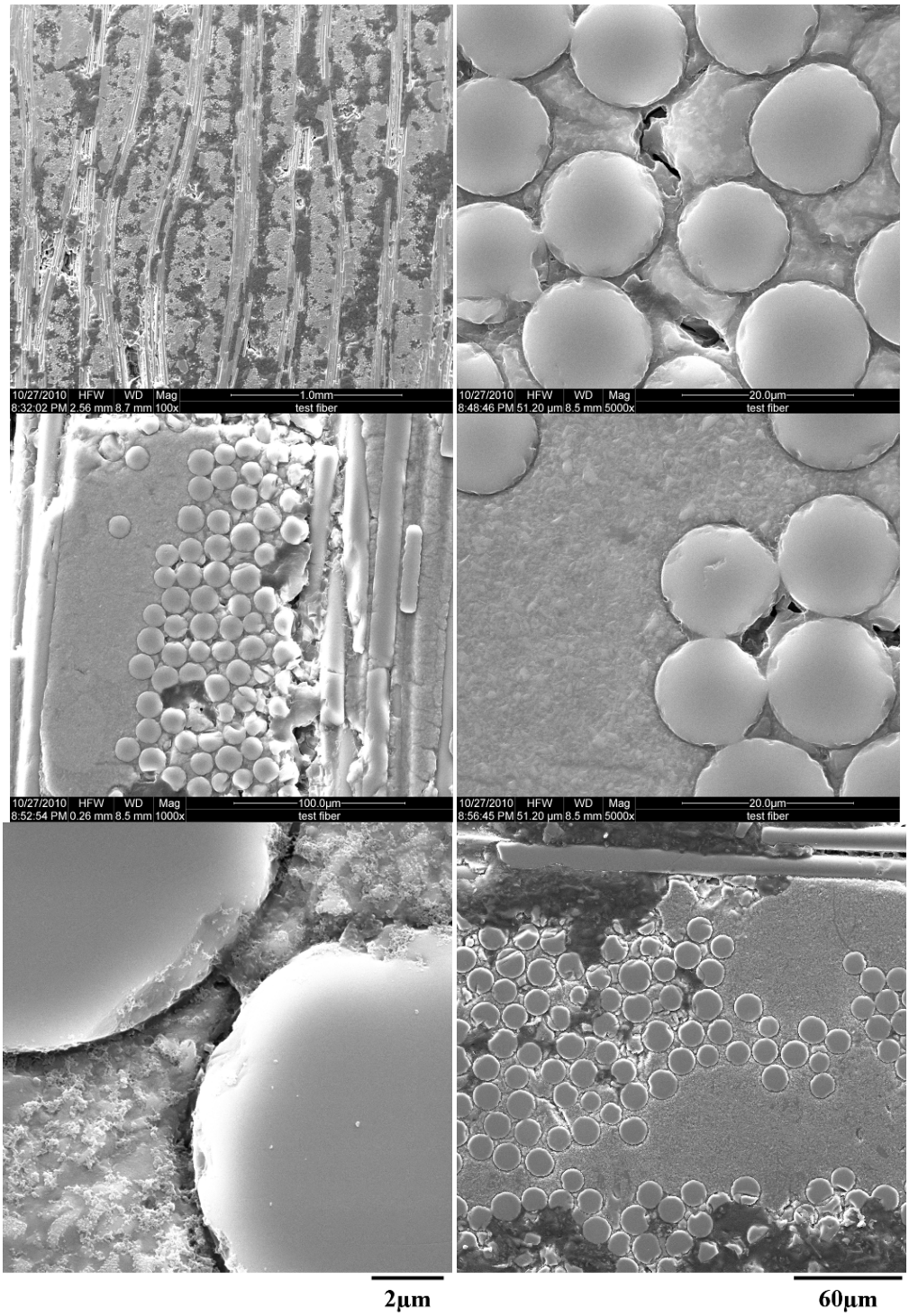

Figure 99: SEM polished micrographs of the as-processed CG NICALON™/BN/SiC composite from panel 11

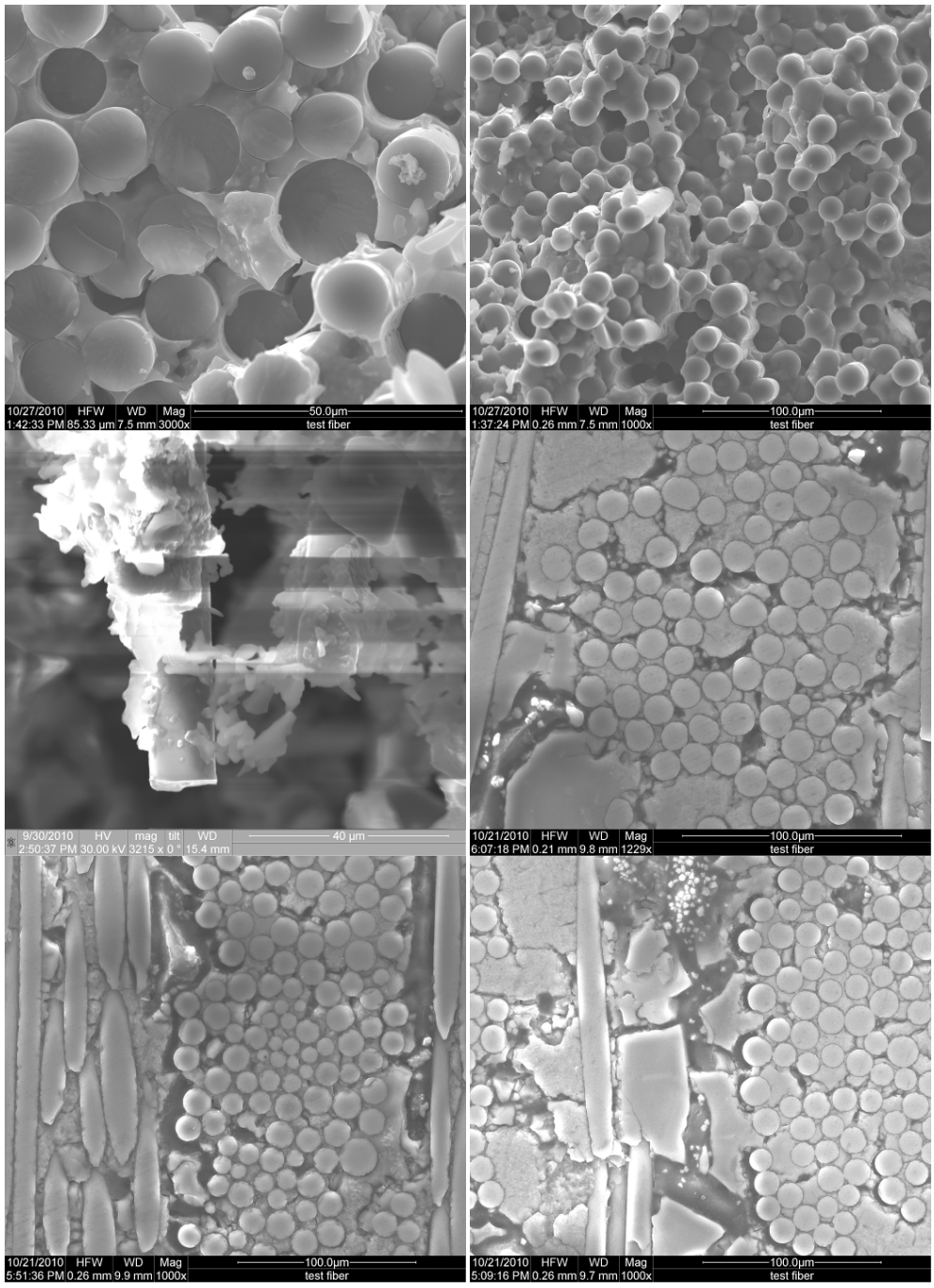

Figure 100: SEM micrographs of specimen S5A subjected to tensile test to failure at 1000 °C. Fracture surface normal to the applied load.

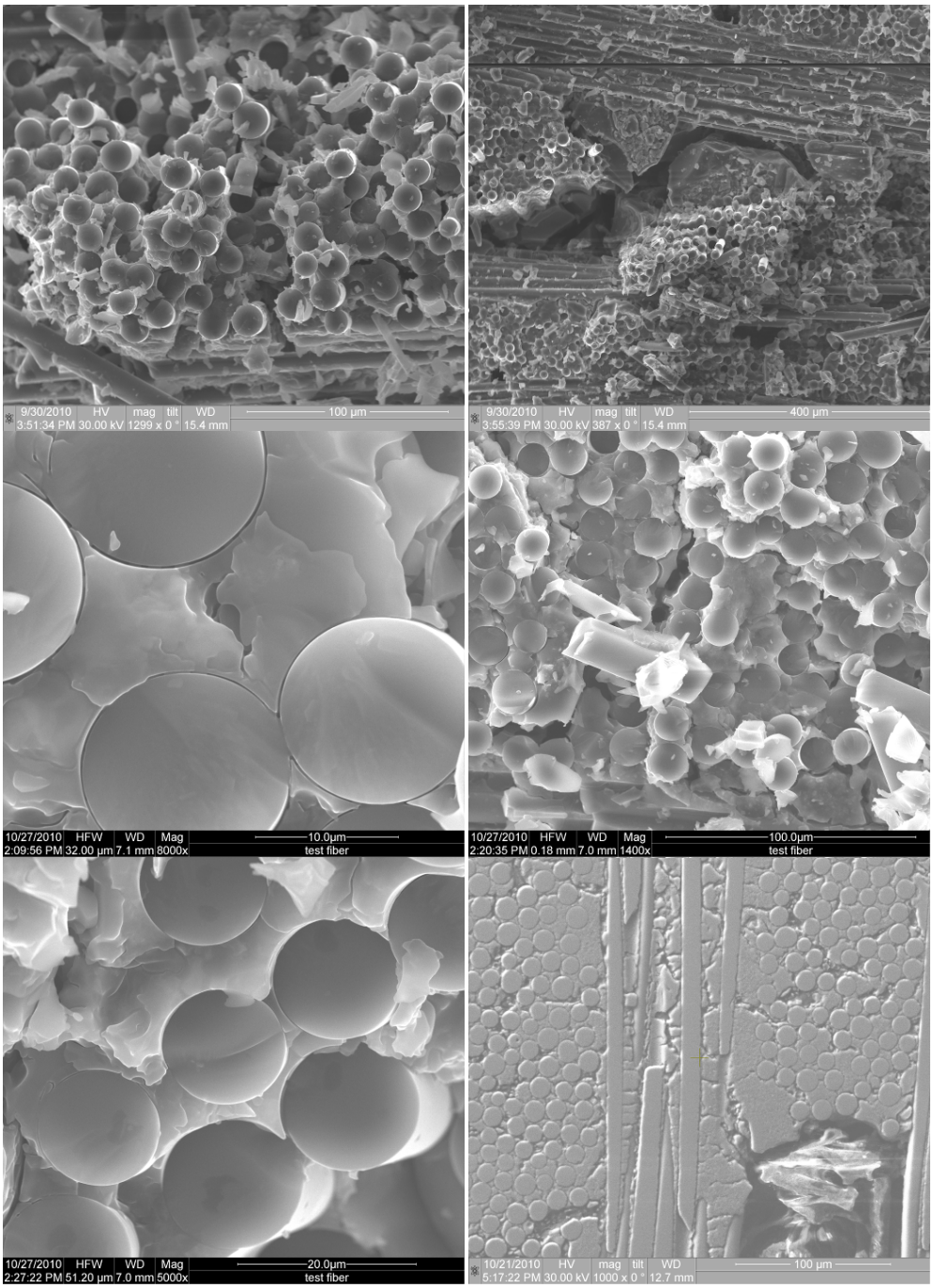

Figure 101: SEM micrographs of specimen S7C subjected to tensile test to failure at 1000 °C. Fracture surface normal to the applied load.

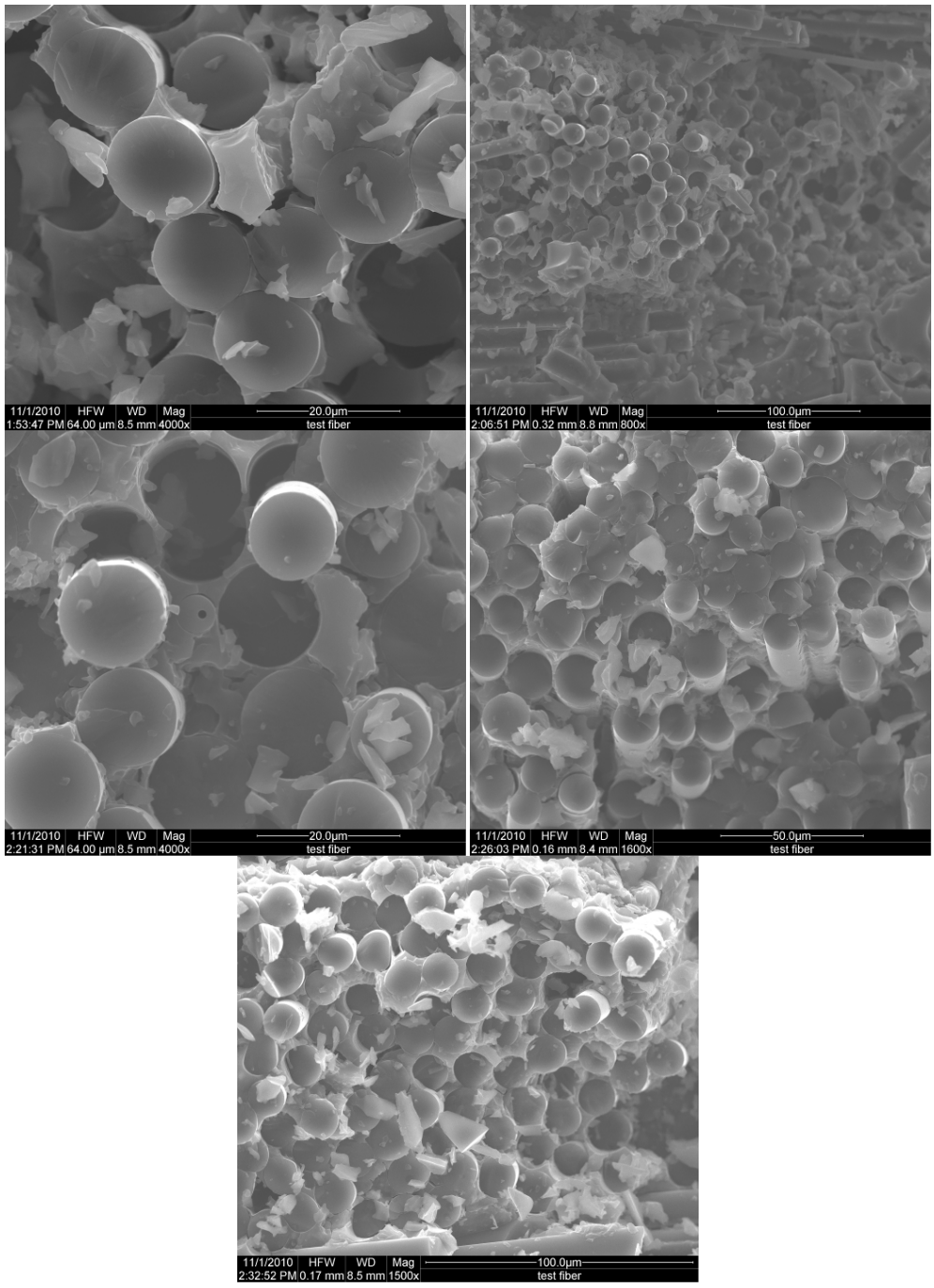

Figure 102: SEM micrographs of specimen S8D subjected to tensile test to failure at 1000 °C. Fracture surface normal to the applied load.

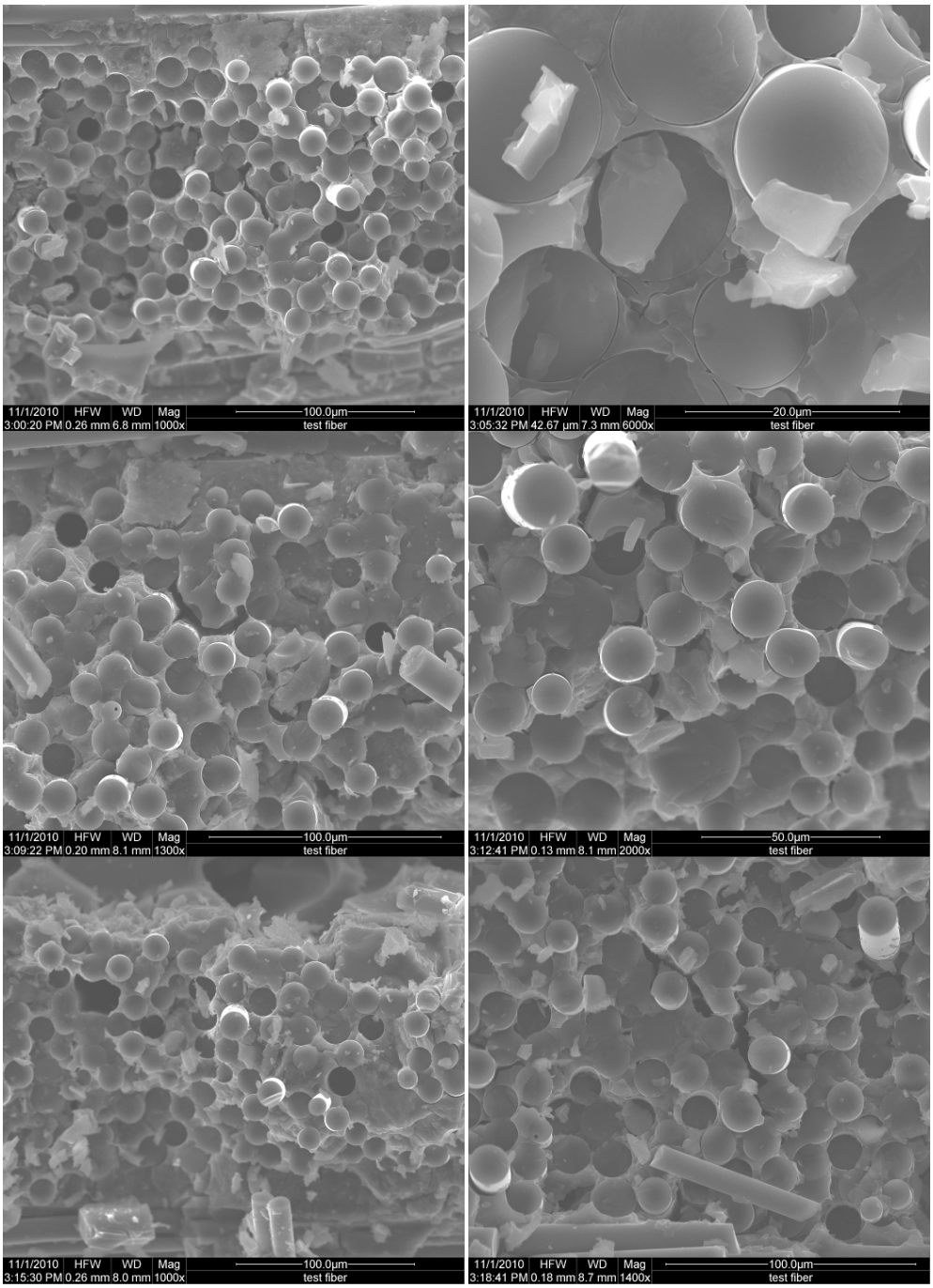

Figure 103: SEM micrographs of specimen S9A subjected to tensile test to failure at 1000 °C. Fracture surface normal to the applied load.

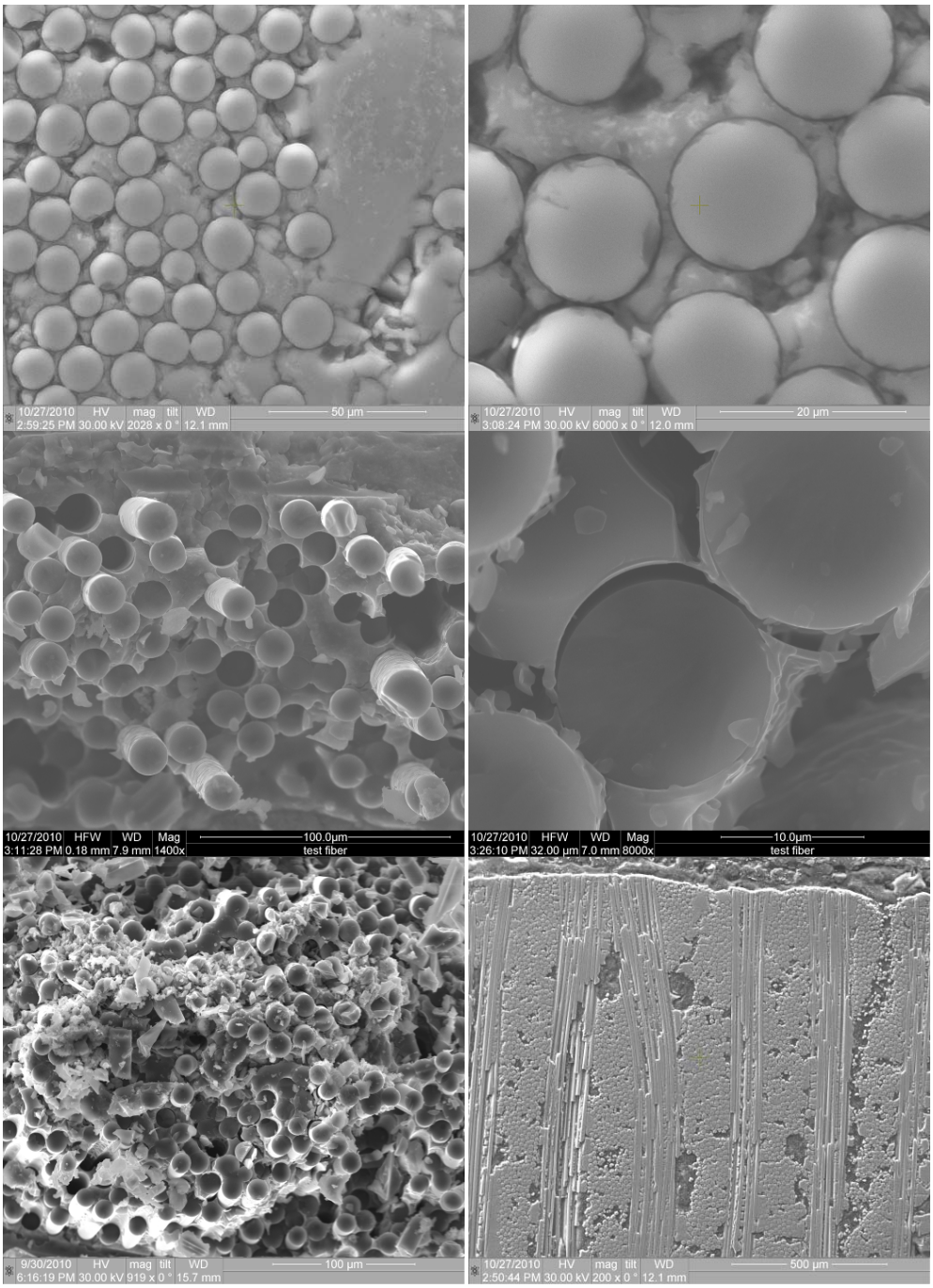

Figure 104: SEM micrographs of specimen S10D subjected to tensile test to failure at 1000 °C. Fracture surface normal to the applied load.

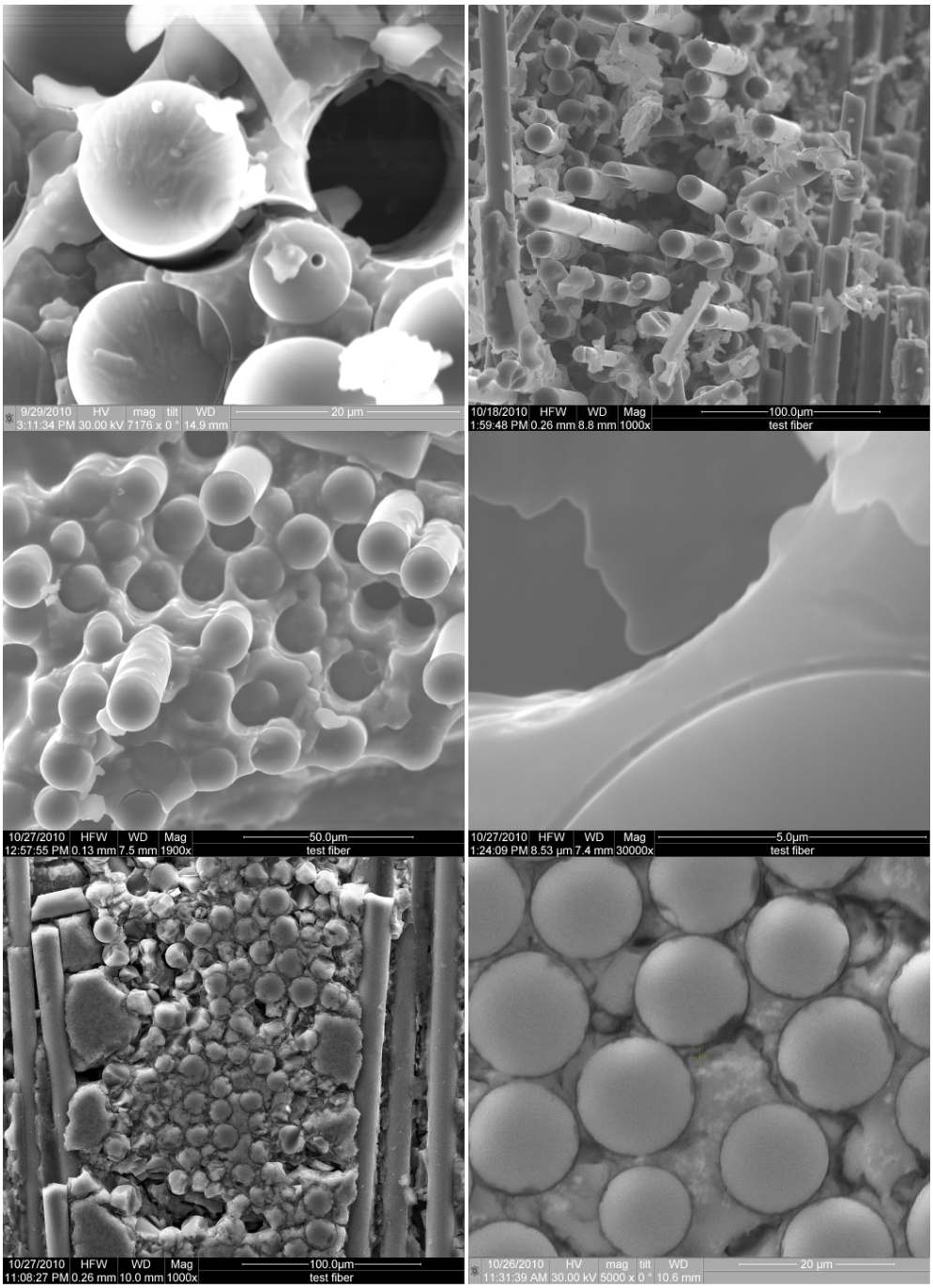

Figure 105: SEM micrographs of specimen S11B subjected to tensile test to failure at 1000 °C. Fracture surface normal to the applied load.

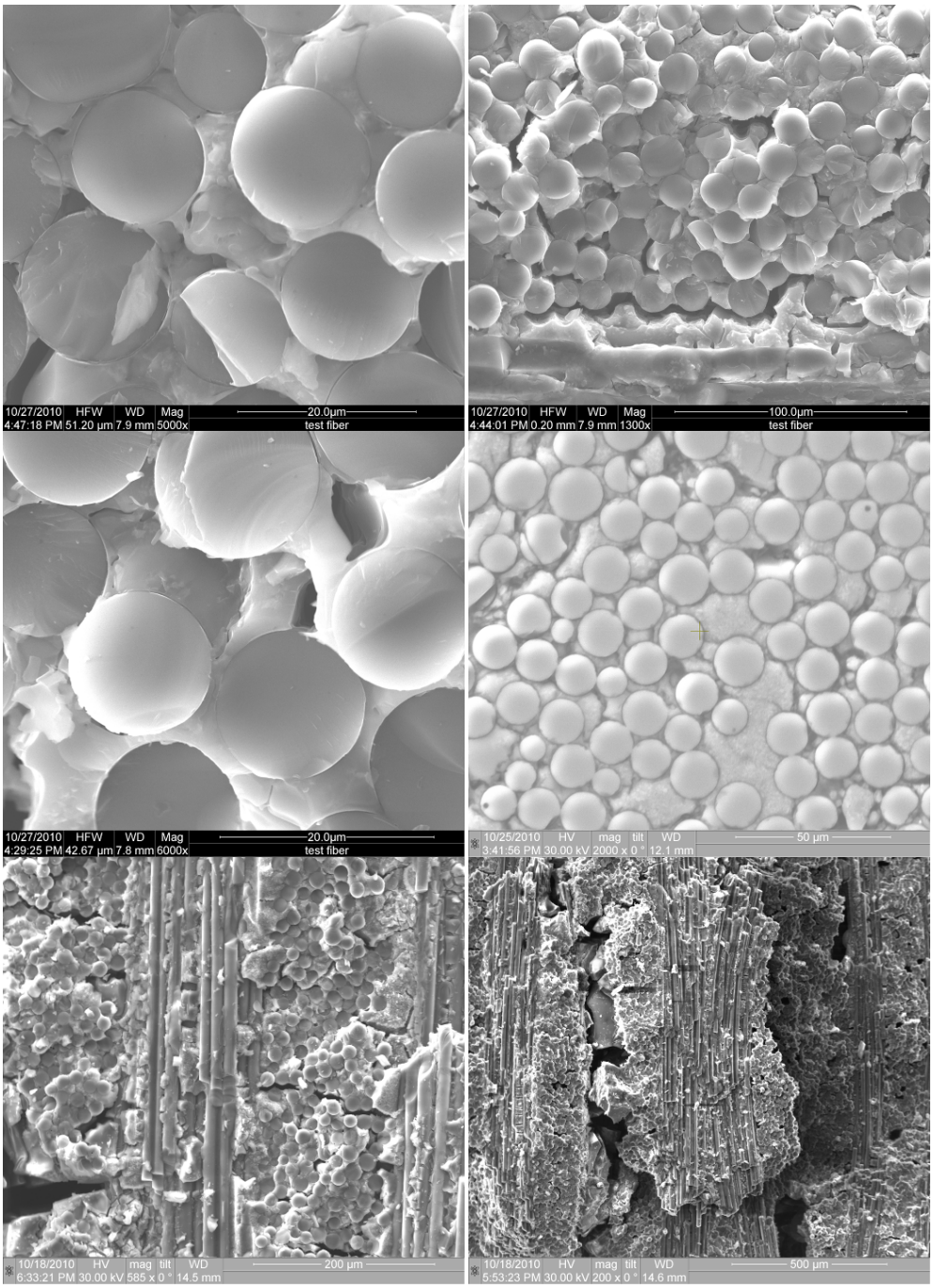

Figure 106: SEM micrographs of specimen S7B subjected to fatigue at 1000 °C in air (f = 1.0 Hz, σ_{max} = 80 MPa, N_f = 34,652). Fracture surface normal to the applied load.

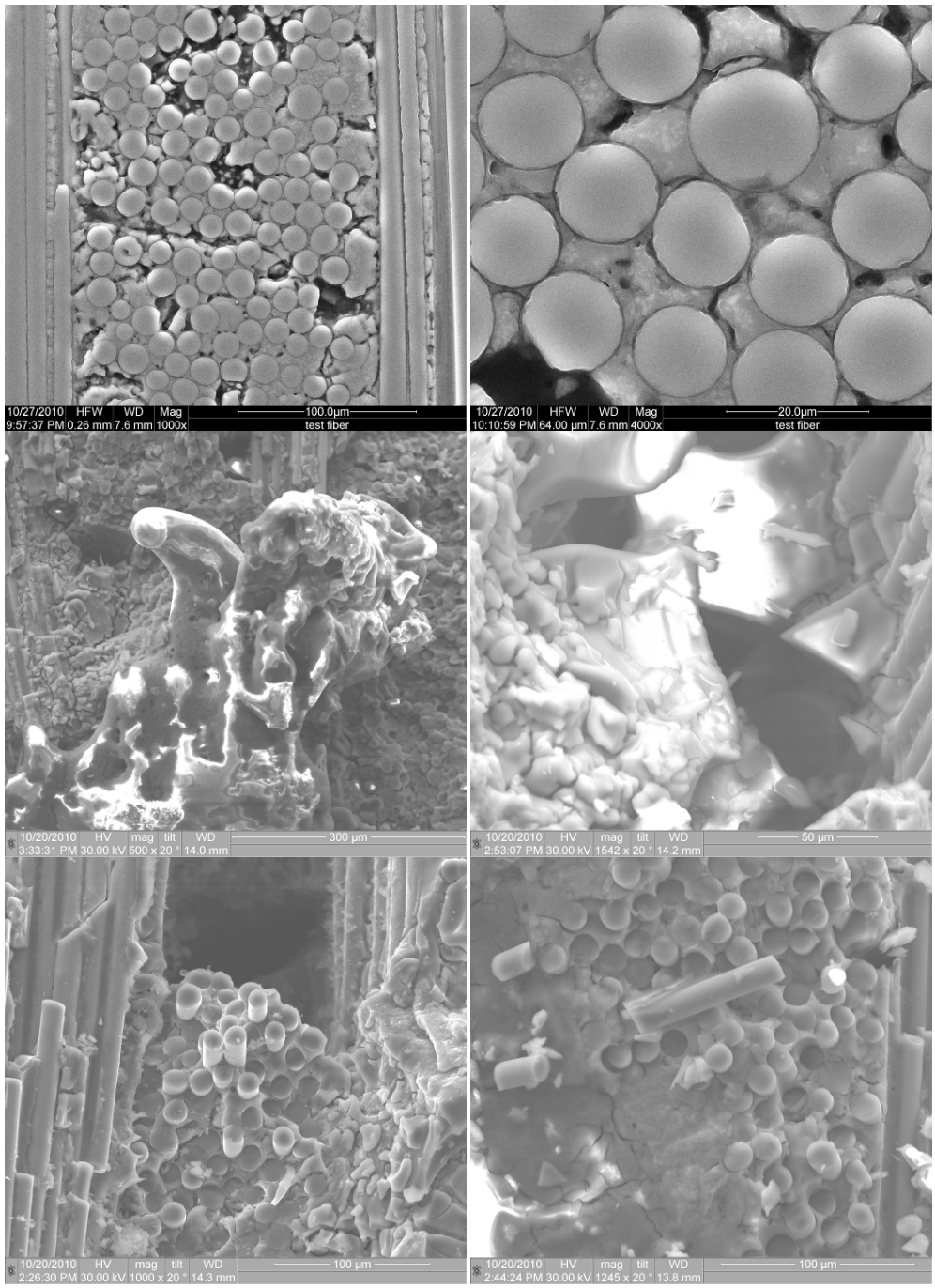

Figure 107: SEM micrographs of specimen S10B subjected to fatigue and a subsequent tensile test to failure at 1000 °C in air (f = 1.0 Hz, σ_{max} = 80 MPa, N_f = 200,000). Fracture surface normal to the applied load.

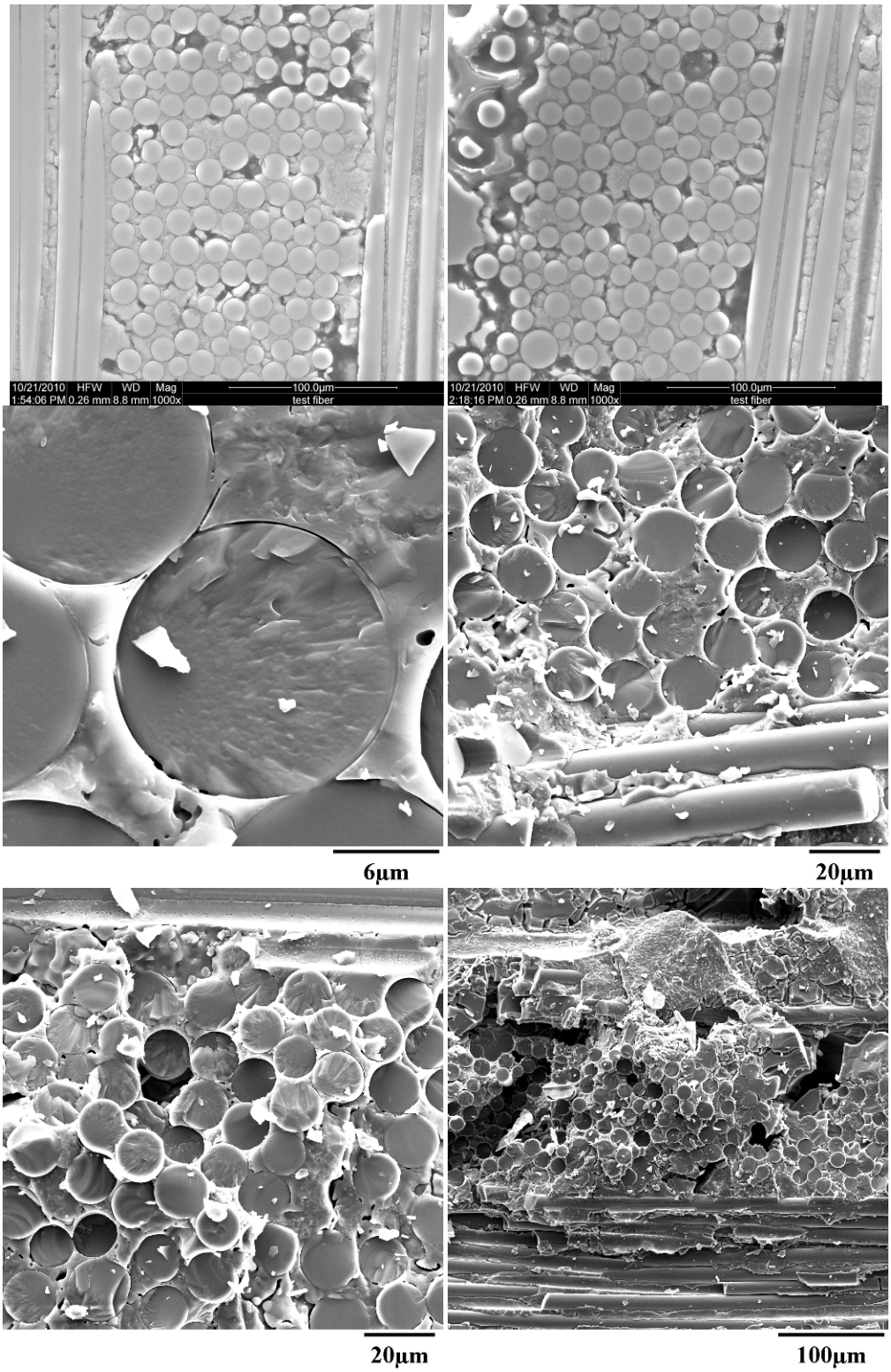

Figure 108: SEM micrographs of specimen S11E subjected to fatigue at 1000 °C in air (f = 1.0 Hz, σ_{max} = 100 MPa, N_f = 168,255). Fracture surface normal to the applied load.

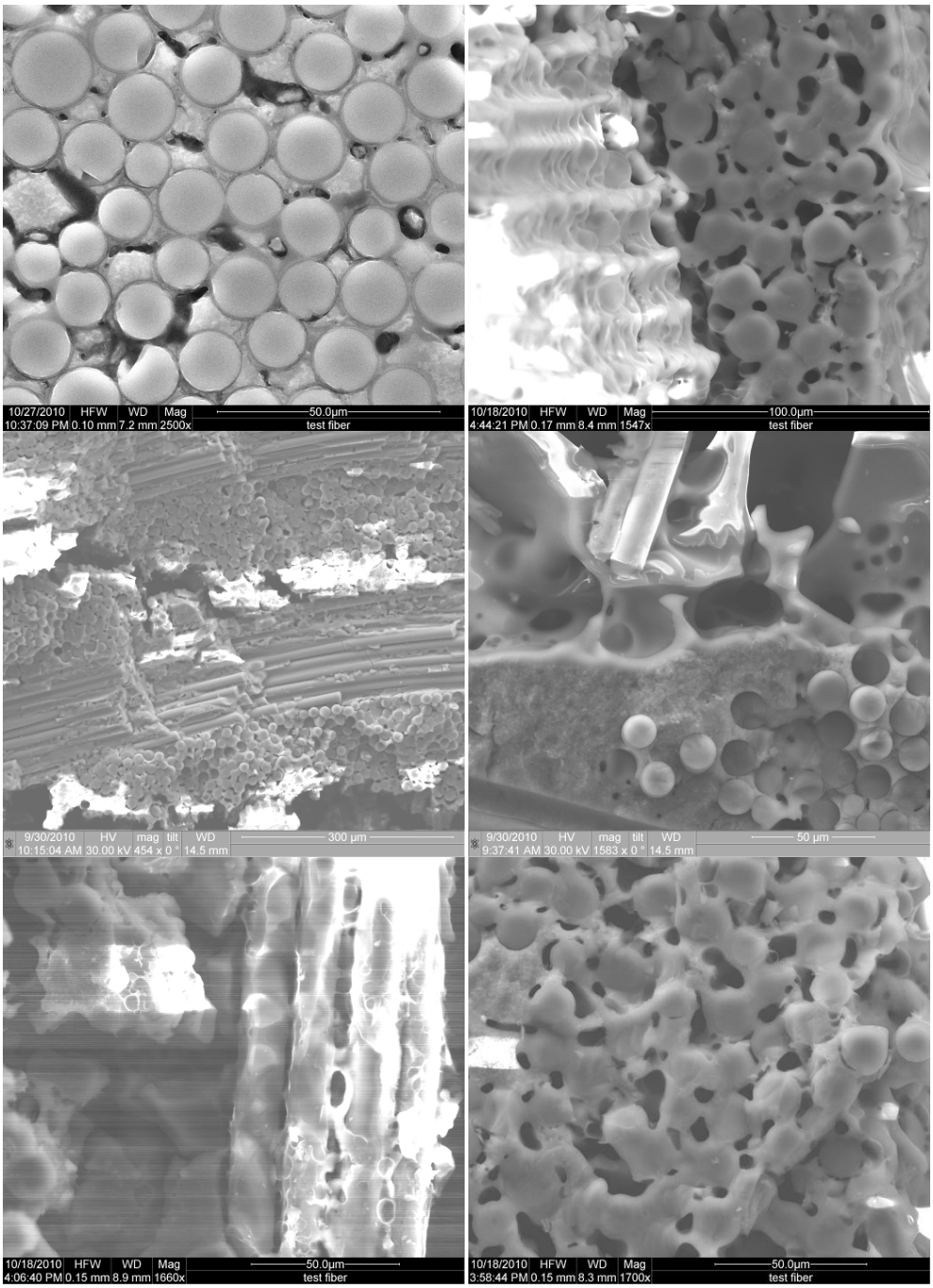

Figure 109: SEM micrographs of specimen S11A subjected to fatigue at 1000 °C in steam (f = 1.0 Hz, σ_{max} = 60 MPa, N_f = 194,930). Fracture surface normal to the applied load.

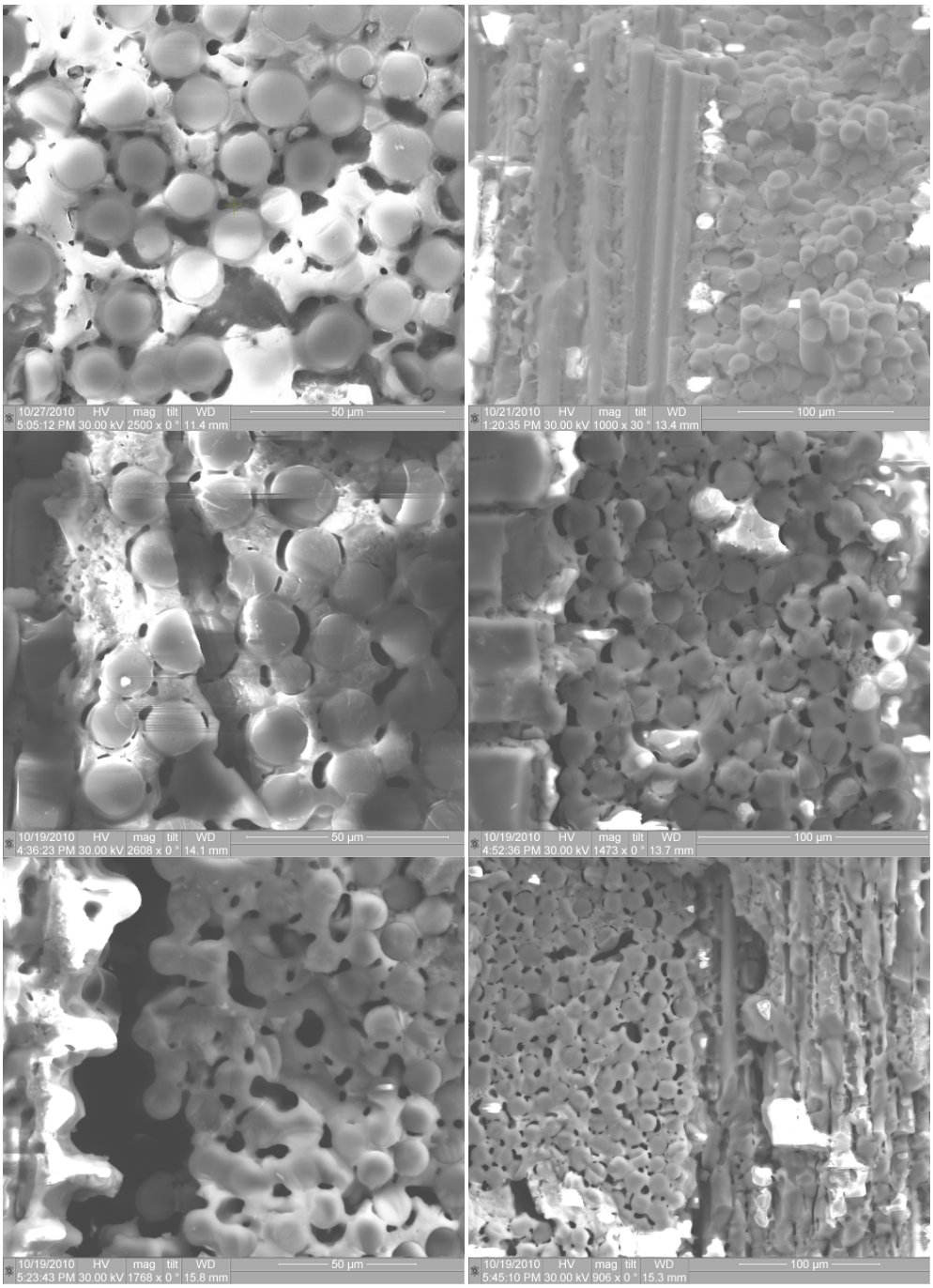

Figure 110: SEM micrographs of specimen S10E subjected to fatigue at 1000 °C in steam (f = 1.0 Hz, σ_{max} = 70 MPa, N_f = 126,593). Fracture surface normal to the applied load.

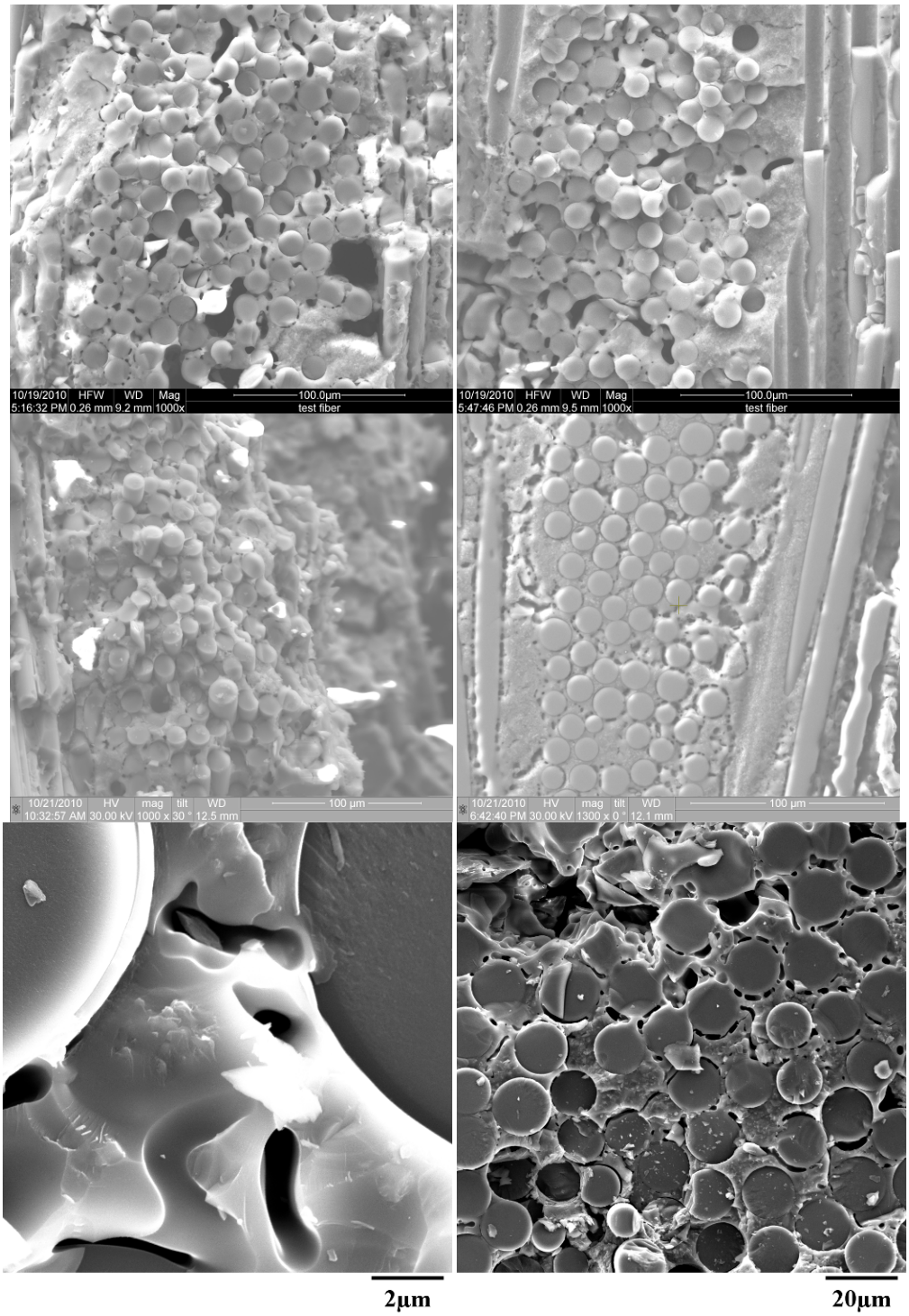

Figure 111: SEM micrographs of specimen S11D subjected to fatigue at 1000 °C in steam (f = 1.0 Hz, σ_{max} = 70 MPa, N_f = 65,154). Fracture surface normal to the applied load.

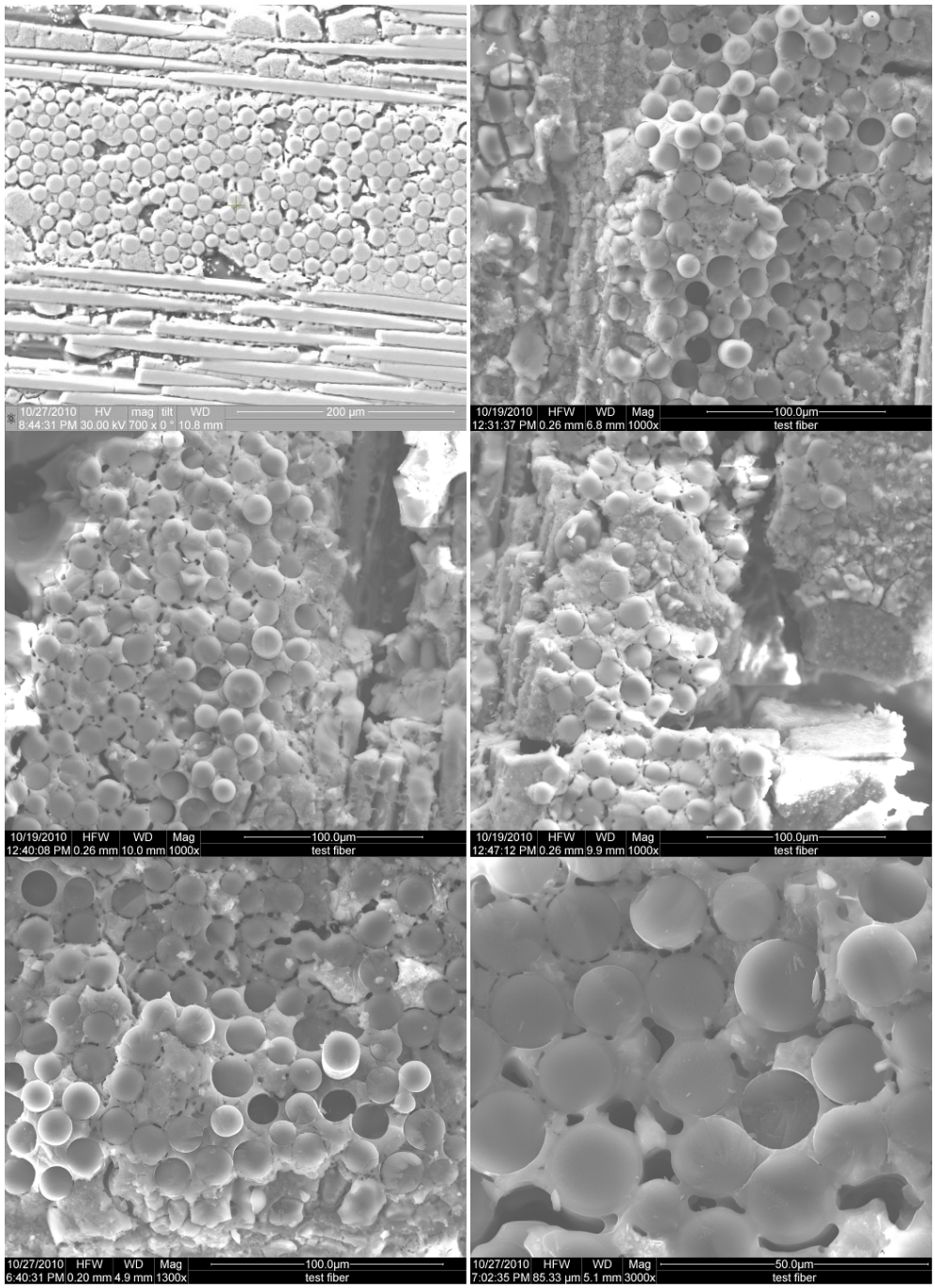

Figure 112: SEM micrographs of specimen S10A subjected to fatigue at 1000 °C in steam (f = 1.0 Hz, σ_{max} = 80 MPa, N_f = 73,084). Fracture surface normal to the applied load.

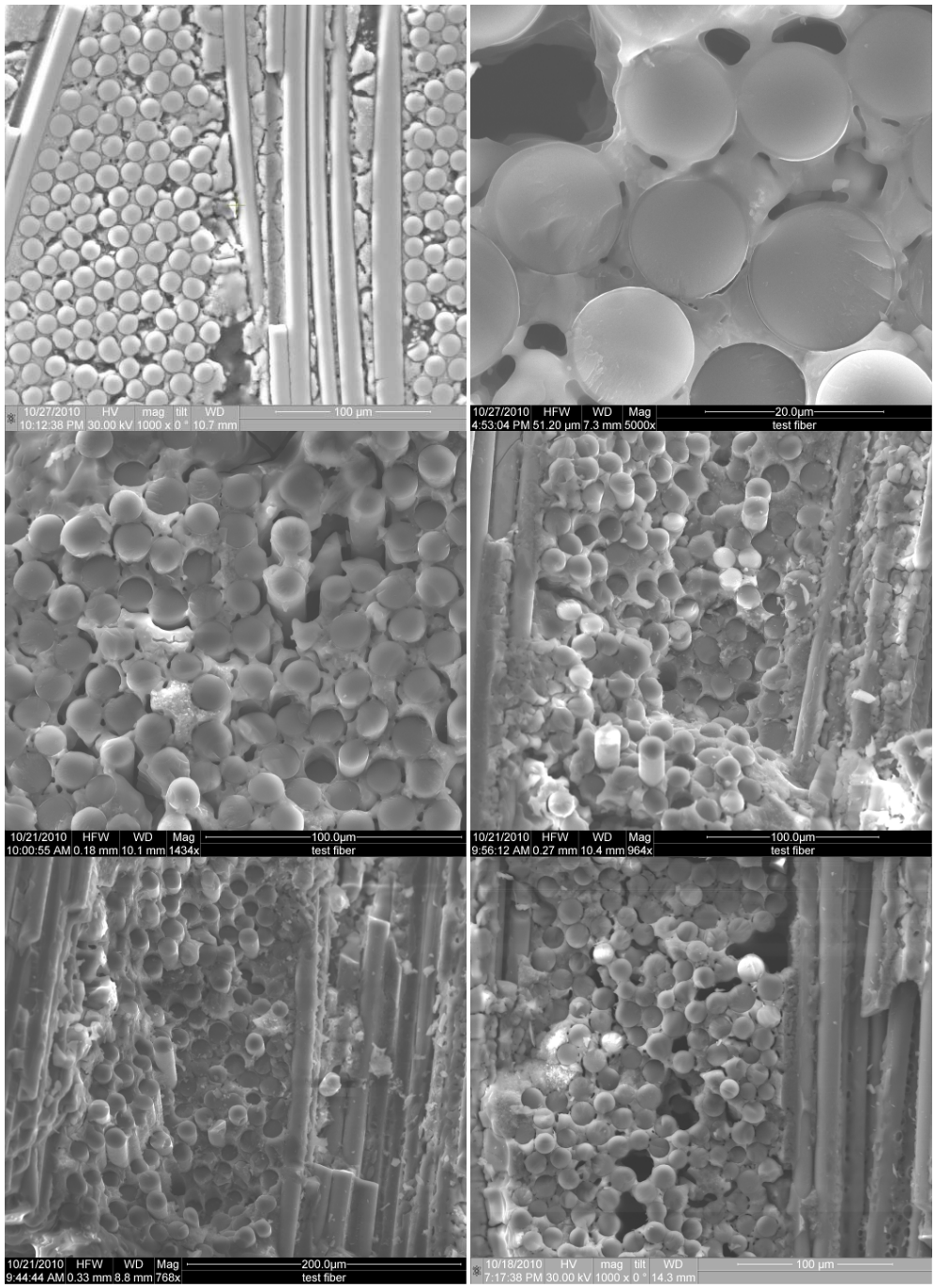

Figure 113: SEM micrographs of specimen S8E subjected to fatigue at 1000 °C in steam (f = 1.0 Hz, σ_{max} = 80 MPa, N_f = 46,621). Fracture surface normal to the applied load.

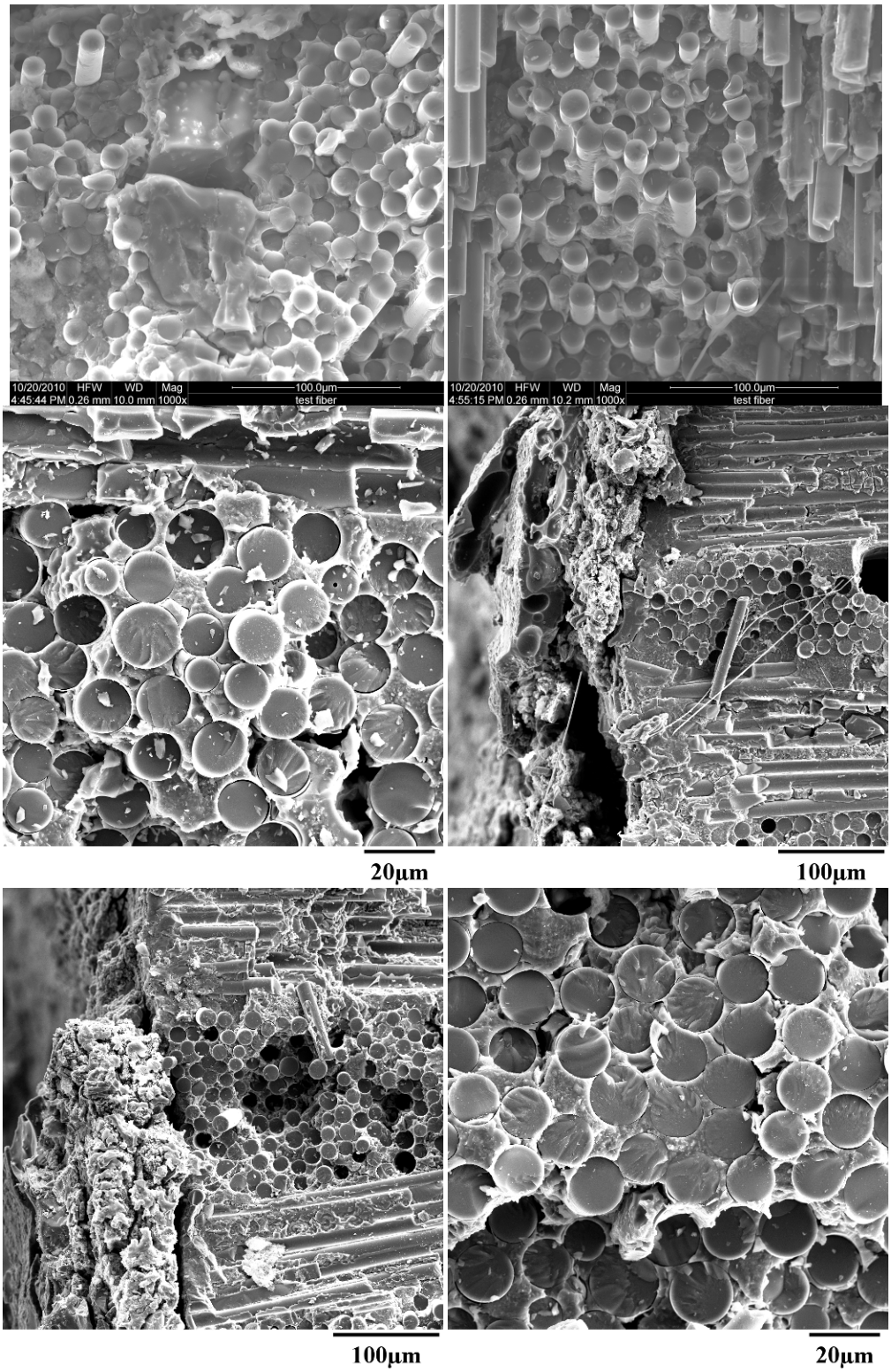

Figure 114: SEM micrographs of specimen S11C subjected to fatigue at 1000 °C in steam (f = 1.0 Hz, σ_{max} = 100 MPa, N_f = 17,587). Fracture surface normal to the applied load.

Bibliography

1. Brewer, David. *HSR/EPM Combustor Materials Development Program.* Cleveland, OH: Elsevier, 1999.

2. Campbell, F.C. *Manufactuing Technology for Aerospace Structural Materials.* Amsterdam: Elsevier, 2006.

3. Chawla, K.K. *Ceramic Matrix Composites.* Second Edition. Boston: Kluwer Academic Publishers, 2003.

4. Chawla, Nikhilesh, et al. *High-Frequency Fatigue Behavior of Woven Fiber Fabric Reinforced Polymer Derived Ceramic Matrix Composites.* Ann Arbor, MI: J Am Ceram Soc, 1998.

5. Christensen, Devon T. *Fatigue Behavior of an Advanced SiC/SiC Composite at Elevated Temperature in Air and Steam.* MS thesis, AFIT/GAE/ENY/09-D02. School of Engineering and Management, Air Force Institute of Technology (AU), Wright-Patterson AFB, OH, December 2009

6. Delapasse, Jacob. *Fatigue Behavior of an Advanced SiC/SiC Composite with an Oxidation Inhibited Matrix at 1200 °C in Air and Steam.* MS thesis, AFIT/GAE/ENY/10-M07. School of Engineering and Management, Air Force Institute of Technology (AU), Wright-Patterson AFB, OH, March 2010

7. DiCarlo, J.A., H-M Yun, G.N. Morscher and R.T. Bhatt. "SiC/SiC Composites for 1200 °C and Above." *Handbook of Ceramic Composites.* 2005.

8. Fair, G. E. Private Communication (2010).

9. Fuentes, M., J.M. Martinez-Esnaola and A.M. Daniel. *Ceramic and Metal Matrix Composite, CMMC 96, Part 1.* Totton, Hampshire, United Kingdom: Trans Tech Publications, Ltd., 1997.

10. Geels, Kay. *Metallographic and Materialographic Specimen Preparation, Light Microscopy, Image Analysis and Hardness Testing.* Lancaster, PA: ASTM Interanational, 2007.

11. Herakovich, Carl T. *Mechanics of Fibrous Composites.* New York: John Wiley and Sons, Inc., 1998.

12. *HI-NICALON™ Ceramic Fiber.* Magna, Utah: ATK Space Systems, 2006.

13. Jacobsen, Torben K. and Povl Bronsted. *Mechanical Properties of Two Plain-Woven Chemical Vapor Infiltrated Silicon Carbide-Matrix Composites.* Roskilde, Denmark: J Am Ceram Soc, 2001.

14. Jacobson, Nathan S. "Oxidation of Boron Nitride in Composites," *NASA Glenn Research Center Research and Technology 1997*, 1-2 (April 1998).

15. Jackson, P.R., M.B. Ruggles-Wrenn, S.S. Baek and K.A. Keller. *Compressive Creep Behavior of an Oxide-Oxide Ceramic Composite with Monazite Fiber Coating at Elevated Temperatures.* Wright-Patterson AFB, OH: Materials Science and Engineering, 2007.

16. *KDT Ceraset Polyureasilizane*. Huntingdon Valley, PA: KiON Defense Technologies Inc., no date.

17. Keller, Kristin A., George Jefferson and Ronald J. Kerans. "Oxide-Oxide Composites." *Handbook of Ceramic Composites.* 2005.

18. Kerans, Ronald J. and Triplicane A. Parthasarathy. *Crack Deflection in Ceramic Composites and Fiber Coating Design Criteria.* Wright-Patterson AFB, OH: Elsevier, 1999.

19. Kerans, Ronald J., et al. *Interface Design for Oxidation Resistant Ceramic Composites.* Wright-Patterson AFB, OH: J Am Ceram Soc, 2002.

20. *Low-Cost Net-Shape Processing of Ceramic Matrix Composites Utilizing Preceramic Polymer Processing.* Tuscon, AZ: MER Corporation, 2010.

21. McCauley, Ronald A. *Corrosion of Ceramic and Composite Materials.* Second Edition. New York: Marcel Dekker, Inc., 2004.

22. Mizno, Mineo, et al. *Cyclic-Fatigue Behavior of SiC/SiC Composites at Room and High Temperatures.* Tokyo: J Am Ceram Soc, 1996.

23. More, K.L., et al. *Exposure of Ceramics and Ceramic Matrix Composites in Simulated and Actual Combustor Environments.* New York: International Gas Turbine and Aeroengine Congress, 1999.

24. More, K.L., et al. *Observations of Accelerated Silicon Carbide Recession by Oxidation at High Water Vapor Pressures.* Oak Ridge, TN: J Am Ceram Soc, 2000.

25. Morscher, G.N. and J.D. Cawley. *Intermediate Temperature Strength Degradation in SiC/SiC Composites.* Clevland: Journal of the Eurpoean Ceramic Society, 2002.

26. Morscher, Gregory N. *Tensile Creep and Rupture of 2D Woven SiC/SiC Composites for High Temperature Applications.* Akron, OH: Elsevier, 2010.

27. Naslain, R. "Design, Preparation and Properties of Non-Oxide CMCs for Application in Enginers and Nuclear Reactors: an Overview." Pessac, France: Elsevier, 2003.

28. *NICALON™ Ceramic Fiber.* Magna, Utah: ATK Space Systems, 2006.

29. Oates, Gordon C. *Aerothermodynamics of Gas Turbine and Rocket Propulsion.* Third Edition. Reston, VA: AIAA, 1997.

30. Robinson, Raymond C. and James L. Smialek. *SiC Recession Caused by SiO_2 Scale Volatility Under Combustion Conditions: I, Experimental Results and Emperical Model.* Cleveland, OH: J Am Ceram Soc, 1999.

31. Ruggles-Wrenn, M.B., Private Communication (2010).

32. Ruggles-Wrenn, M.B. and V. Sharma. *Effects of Steam Environment on Fatigue Behavior of Two SiC/[SiC+Si_3N_4] Ceramic Composites at 1300 °C.* Wright-Patterson AFB, OH: Applied Composite Materials, In Press.

33. Shames, Irving H. and Francis A. Cozzarelli. *Elastic and Inelastic Stress Analysis.* Revised Printing. Philadelphia: Taylor & Francis, 1997.

REPORT DOCUMENTATION PAGE			Form Approved OMB No. 074-0188

PLEASE DO NOT RETURN YOUR FORM TO THE ABOVE ADDRESS.

1. REPORT DATE *(DD-MM-YYYY)*	**2. REPORT TYPE**	**3. DATES COVERED** *(From – To)*
12-23-2010	Master's Thesis	Sep 2009 – Dec 2010

4. TITLE AND SUBTITLE

Fatigue Behavior of a SiC/SiC Composite at 1000 °C in Air and in Steam

5a. CONTRACT NUMBER

5b. GRANT NUMBER

5c. PROGRAM ELEMENT NUMBER

6. AUTHOR(S)

Knauf, Michael W., Capt, USAF

5d. PROJECT NUMBER

5e. TASK NUMBER

5f. WORK UNIT NUMBER

7. PERFORMING ORGANIZATION NAMES(S) AND ADDRESS(S)
Air Force Institute of Technology
Graduate School of Engineering and Management (AFIT/EN)
2950 Hobson Way
WPAFB OH 45433-7765

8. PERFORMING ORGANIZATION REPORT NUMBER
AFIT/GAE/ENY/10-D01

9. SPONSORING/MONITORING AGENCY NAME(S) AND ADDRESS(ES)
Dr. Geoff Fair
Air Force Research Laboratory/Material and Manufacturing Directorate; Metals, Ceramics, and NDE Division
2230 Tenth Street, Bldg 655
WPAFB OH 45433-7765 DSN: 785-3232
geoff.fair@wpafb.af.mil

10. SPONSOR/MONITOR'S ACRONYM(S)
AFRL/RXLN

11. SPONSOR/MONITOR'S REPORT NUMBER(S)

12. DISTRIBUTION/AVAILABILITY STATEMENT
APPROVED FOR PUBLIC RELEASE; DISTRIBUTION UNLIMITED.

13. SUPPLEMENTARY NOTES

14. ABSTRACT

Tension-tension fatigue behavior of a prototype Silicon Carbide/Silicon Carbide (SiC/SiC) ceramic matrix composite (CMC) material was investigated at 1000 °C in laboratory air and in steam environments. The material consists of a SiC matrix reinforced with CG NICALON™ fibers woven in an eight harness satin weave (8HSW) and coated with a BN/SiC dual-layer interphase. The composite was manufactured by a Polymer Infiltration and Pyrolysis (PIP) process. A seal coat of SiC and elemental boron was applied to the test specimens after machining. The tensile stress-strain behavior was investigated and the tensile properties were measured at 1000 °C. Tension-tension fatigue behavior was studied for fatigue stresses ranging from 60 to 100 MPa. The fatigue limit (based on a run-out condition of 2 x 105 cycles) was 80 MPa, which is 59% of the Ultimate Tensile Strength (UTS). The material retained 82% of its tensile strength. The presence of steam significantly degraded the fatigue performance at 1000 °C. In steam the fatigue limit dropped below 60 MPa (44% UTS). Microstructural analysis revealed severe oxidation occurring in the specimens tested in steam, which resulted in accelerated damage development and failure. Through quantitative and qualitative analysis, the damage and premature failure of the composite in the steam environment is believed to be due to oxidation embrittlement. This material also showed considerably worse performance than similar SiC/SiC composites with a great deal of variability between specimens cut from different panels. The possibility exists that inadequate process control may be behind the degraded performance of the material and the panel-to-panel variability in performance.

15. SUBJECT TERMS
Ceramic Matrix Composite (CMC), Silicon Carbide/Silicon Carbide Composite (SiC/SiC), Boron Nitride (BN), Chemical Vapor Infiltration (CVI), Fatigue Test, Tensile Properties, Environment

16. SECURITY CLASSIFICATION OF:			**17. LIMITATION OF ABSTRACT**	**18. NUMBER OF PAGES**	**19a. NAME OF RESPONSIBLE PERSON**
REPORT	**ABSTRACT**	**c. THIS PAGE**			Dr. Marina B. Ruggles-Wrenn
U	**U**	**U**	**UU**	166	**19b. TELEPHONE NUMBER** *(Include area code)* (937) 785-3636, ext 4641 Email: marina.ruggles-wrenn@afit.edu

Standard Form 298 (Rev: 8-98)
Prescribed by ANSI Std. Z39-18